

High-Resolution NMR Studies of Nano-Cages

Nikki Jade Cookson

Submitted in accordance with the requirements for the degree of
Doctor of Philosophy

The University of Leeds
School of Chemistry

May 2016

The candidate confirms that the work submitted is his/her own, except where work which has formed part of jointly-authored publications has been included. The contribution of the candidate and the other authors to this work has been explicitly indicated below. The candidate confirms that appropriate credit has been given within the thesis where reference has been made to the work of others.

N.J. Cookson, J.J. Henkelis, R.J. Ansell, C.W.G. Fishwick, M.J. Hardie and J. Fisher, 'Encapsulation of Sodium Alkyl Sulfates by the Cyclotrimeratrylene-Based, [Pd6L8]¹²⁺ Stella Octangula Cage', *Dalton Transactions*, **2014**, 43, 5657-5661.

This copy has been supplied on the understanding that it is copyright material and that no quotation from the thesis may be published without proper acknowledgement.

The right of Nikki Cookson to be identified as Author of this work has been asserted by her in accordance with the Copyright, Designs and Patents Act 1988.

Acknowledgements

First and foremost I would like to thank both of my supervisors, Dr Julie Fisher and Professor Michael Hardie. Both have provided excellent guidance and support throughout my PhD. It has been a true pleasure and privilege to work with both of them. I feel I have been incredibly fortunate to have had two smashing supervisors. I would particularly like to thank Julie for believing in me and Michael for seeing it through and making sure that I got my PhD finished.

I would like to thank the past members of the Fisher group for their advice and continued support, particularly Cassey McRae, Kathryn Evans and Warren Yabsley. Although our time together was short, I will always remember it with such fondness. Thanks as well to the Hardie group past and present, in particular James Henkelis for making all of the ligands and interesting chats about supramolecular chemistry! I would also like to thank the Fishwick group, particularly Ricky Cain and Sarah Narramore. I've really enjoyed getting to know you guys over the years.

I would also like to thank Simon Barrett for additional NMR support, Martin Huscroft for trying to resolve our ligands, even though they didn't want to be resolved.

I have really enjoyed my time at Leeds, particularly the time well-spent with the post-graduate chemistry committee, so a big cheers to Dave Yeo for talking me into joining whilst drunk and a special shout out to Sam Hill, Irène Arrata and James Green for letting me keep my role as "Queen of Cake and Coffee" and putting up with my gobbiness in meetings! It's been an absolute pleasure testing out my bakes on the department. Cheers to anyone who ate one (or two, or more!). I've also had a blast helping to organise and attending events of merriment/debauchery that help bring the department together – cheers to everyone who came.

It would be remiss not to mention Dan Moon, Rob Woodward-Massey, Neil Howes, Sam Greatorex and Steven Chowny. Cheers for being my pub companions; we had a really special time! Much love to Becs Hoyle for all the much needed tea and cake sessions, cheers for always cracking out the posh Betty's tea!

A special mention to my family; Mum, Mark, Ross, Brett, Elisha, Maria and Bonzo and to Dan's parents Chris and Tim – thank you for your unyielding support.

And finally, I would like to thank Dr Daniel Binks for his steadfast support, encouragement and his excellent holiday booking skills!

In memory of Dr Julie Fisher

A most excellent supervisor, scientist and NMR spectroscopist, who is sorely missed.

Abstract

This thesis concerns the NMR investigations of supramolecular metallo-nanocages as hosts for host-guest chemistry. The research is based on metallo-nanocages constructed from cyclotrimeratrylene (CTV)-derivatives

The host-guest interaction between the $[\text{Pd}_6(\text{L1})_8] \cdot 12(\text{BF}_4)$ stella octangula cage and sodium alkyl sulfate guests have been characterised by ^1H 1-D, DOSY and 2-D ROESY NMR and ESI-MS. The host-guest stoichiometry was determined at 1:2 by Job's plot analysis. The shorter the length of the guest's alkyl tail, the more tightly bound it was to the host cage. The self-assembly and self-sorting of the $[\text{Pd}_6(\text{L1})_8] \cdot 12(\text{BF}_4)$ stella octangula cage were also investigated. d_6 -DMSO competed with the L1 ligand for the palladium(II) cation. The rate of self-sorting of the $[\text{Pd}_6(\text{L1})_8] \cdot 12(\text{BF}_4)$ stella octangula cage was found to be affected by concentration, with lower concentrations resulting in cage systems that self-sorted in to homochiral cages at a faster rate.

The novel FL1 ligand was characterised by ^1H and ^{19}F NMR spectroscopy in d_6 -DMSO and d_3 -MeCN and was used to produce stella octangula cage assemblies. The self-assembly of this system in d_6 -DMSO was observed and found to require an excess of palladium to form. This FL1 system was also investigated for host-guest interactions with sodium dodecyl sulfate (SDS). It formed a system that exhibited weaker binding than L1. The FL1 ligand formed quantitative cages in d_3 -MeCN. This system was characterised by ^1H and ^{19}F NMR spectroscopy, 2-D ROESY NMR, ESI-MS and X-ray crystallography.

The **L1** and **FL1** ligands were used to form cryptophanes with [1,3-bis(diphenylphosphino)propane] in d_6 -DMSO, d_3 -MeCN and d_3 -MeNO₂. These were characterised by ¹H, ¹⁹F, ³¹P NMR spectroscopy, 2-D ROESY NMR, ESI-MS and X-ray crystallography. Both ligands showed a strong preference for *anti* cryptophane isomers in solution, although a small amount of *syn* isomer was observed in the **L1** systems. The *syn* isomer was predominant species in the solid state.

Table of Contents

Acknowledgements.....	iii
Abstract	vii
Table of Contents	ix
List of Figures	xiv
List of Tables	xxviii
Abbreviations.....	xxix
Chapter 1 Introduction	1
1.1 Overview	1
1.2 Supramolecular Chemistry	1
1.2.1 Self-Assembly.....	3
1.2.2 Host-Guest Chemistry.....	4
1.2.3 Metallo-Supramolecular Chemistry	6
1.3 Cyclotrimeratrylene (CTV)	7
1.3.1 Applications of Cyclotrimeratrylene and its Analogues	14
1.3.2 Cryptophanes	23
1.3.3 Metallo-Cryptophanes.....	31
1.4 Metallo-Nanocages	39
1.4.1 Molecular Squares.....	39
1.4.2 Tetrahedral M_4L_6 and M_4L_4 Metallo-Nanocages	40
1.4.3 Octahedral M_6L_4 Metallo-Nanocages.....	46
1.4.4 Stella Octangula and Other M_6L_8 Metallo-Nanocages	49
1.4.5 Fujita's Larger Supramolecular Metallo-Nanocages.....	51
1.5 Project Outline.....	57
Chapter 2 Encapsulation of Sodium Alkyl Sulfate Salts by the $[Pd_6(L1)_8] \cdot 12(BF_4)$ Stella Octangula Cage	59
2.1 Introduction	59
2.1.1 Ligand L1 : Tris(isonicotinoyl)cyclotriguaiacylene.....	59

2.1.2 The $[\text{Pd}_6(\text{L1})_8] \cdot 12(\text{NO}_3)$ Stella Octangula Cage	61
2.1.3 Sodium Alkyl Sulfate Guests	63
2.2 Producing a Single Species of Cage	66
2.2.1 Choice of Palladium Salt	66
2.2.2 Self-Assembly of the $[\text{Pd}_6(\text{L1})_8] \cdot 12(\text{BF}_4)$ Stella Octangula Cage	69
2.2.2.1 Self-Assembly at Low Concentrations with the $[\text{Pd}_6(\text{L1})_8] \cdot 12(\text{BF}_4)$ Stella Octangula Cage	70
2.2.2.2 Effect of Concentration on Self-Assembly of $[\text{Pd}_6(\text{L1})_8] \cdot 12(\text{BF}_4)$ Stella Octangula Cage	73
2.2.2.3 Samples Prepared with Aged Stocks	79
2.2.2.4 $[\text{Pd}_6(\text{L1})_8] \cdot 12(\text{BF}_4)$ Stella Octangula Cage in Acetonitrile	81
2.3 Results	83
2.3.1 Solution Properties of Sodium Dodecyl Sulfate (SDS)	83
2.3.2 Investigation of Stoichiometry of the $[\text{Pd}_6(\text{L1})_8] \cdot 12(\text{BF}_4)$ Stella Octangula Cage and Sodium Alkyl Sulfate Host-Guest Complexes	85
2.3.3 ^1H NMR Titration Studies of Stella Octangula Cage and Sodium Alkyl Sulfate Guest Complexes	88
2.3.3.1 Determination of Association Constants for the $[\text{Pd}_6(\text{L1})_8] \cdot 12(\text{BF}_4)$ Stella Octangula Cage and Sodium Alkyl Sulfate Guest Host-Guest Complexes	93
2.3.4 Investigation of Association Using Diffusion Coefficients of the $[\text{Pd}_6(\text{L1})_8] \cdot 12(\text{BF}_4)$ Stella Octangula Cage and Sodium Dodecyl Sulfate Host-Guest Complex	95
2.3.5 Through-Space Connections in the $[\text{Pd}_6(\text{L1})_8] \cdot 12(\text{BF}_4)$ Stella Octangula Cage and Sodium Alkyl Sulfate Host-Guest Complex	96
2.3.6 Mass Spectroscopic Analysis of the Stella Octangula Cage and SDS Host-Guest Complex	100
2.4 Discussion	101
2.4.1 Self-Assembly of the $[\text{Pd}_6(\text{L1})_8] \cdot 12(\text{BF}_4)$ Stella Octangula Cage	101
2.4.2 Stoichiometry of Host-Guest Systems & Association Constants	104
2.4.3 Nature of the Host-Guest Interaction	105

2.5 Conclusions.....	106
Chapter 3 Investigation of ¹⁹ F-labelled Ligand FL1	107
3.1 Introduction	107
3.1.1 FL1 Ligand.....	108
3.1.2 Solubility of the FL1 Ligand.....	108
3.1.3 FL1 Ligand Characterisation.....	111
3.2 Results.....	119
3.2.1 FL1 Stella Octangula Cage in <i>d</i> ₆ -DMSO	119
3.2.2 Host-Guest Studies with the FL1 Stella Octangula Cage in <i>d</i> ₆ -DMSO.....	127
3.2.3 FL1 Stella Octangula Cage in <i>d</i> ₃ -Acetonitrile	139
3.2.4 Host-Guest Studies with the FL1 Stella Octangula Cage in <i>d</i> ₃ -Acetonitrile.....	146
3.3 Discussion.....	147
3.3.1 FL1 Ligand.....	147
3.3.2 FL1 Stella Octangula Cage in <i>d</i> ₆ -DMSO	148
3.3.3 Host-Guest Studies with FL1 Stella Octangula Cage in <i>d</i> ₆ -DMSO	149
3.3.4 FL1 Stella Octangula Cage in <i>d</i> ₃ -Acetonitrile	151
3.4 Conclusions.....	151
Chapter 4 Cryptophanes.....	153
4.1 Introduction	153
4.2 Initial Investigations	153
4.2.1 (Ethylenediamine)palladium(II) Dinitrate	153
4.2.2 Bis(acetonitrile)-{1,1'-methylenebis(3-benzyl-imidazol-2-ylidene)}palla dium(II) tetrafluoroborate.....	156
4.2.2.1 L1 and [Pd ₃ (bis-NHC-b) ₃].2(BF ₄) cryptophanes	160
4.2.3 [1,3-Bis(diphenylphosphino)propane]palladium(II)triflate.....	171
4.3 Results.....	172
4.3.1 ¹ H NMR Analysis of [Pd(dppp)] ²⁺	172

4.3.2 L1 + [Pd(dppp)] ²⁺ Cryptophanes.....	181
4.3.2.1 L1 + [Pd(dppp)] ²⁺ Cryptophanes in <i>d</i> ₆ -DMSO	182
4.3.2.2 L1 + [Pd(dppp)] ²⁺ Cryptophanes in <i>d</i> ₃ -MeCN.....	191
4.3.2.3 L1 + [Pd(dppp)] ²⁺ Cryptophanes in <i>d</i> ₃ -MeNO ₂	198
4.3.3 FL1 + [Pd(dppp)] ²⁺	202
4.3.3.1 FL1 + [Pd(dppp)] ²⁺ Cryptophanes in <i>d</i> ₆ -DMSO	203
4.3.3.2 FL1 + [Pd(dppp)] ²⁺ Cryptophanes in <i>d</i> ₃ -MeCN.....	211
4.3.3.3 FL1 + [Pd(dppp)] ²⁺ Cryptophanes in <i>d</i> ₃ -MeNO ₂	218
4.3.4 L1 + [Pd(dppp)] ²⁺ Cryptophane Host-Guest Investigations.....	223
4.4 Discussion.....	224
4.4.1 [Pd(dppp)] ²⁺	224
4.4.2 L1 Cryptophanes.....	225
4.4.3 FL1 Cryptophanes	229
4.5 Conclusions.....	232
Chapter 5 Conclusions.....	235
5.1 L1 Stella Octangula Cage.....	235
5.2 FL1 Stella Octangula Cage.....	236
5.3 Cryptophanes	237
5.4 Future Work.....	238
Chapter 6 Experimental	241
6.1 NMR Sample Preparation.....	241
6.1.1 Ligand Samples	241
6.1.2 Cage Samples	241
6.1.3 Reagents	243
6.2 NMR Experiments	243
6.2.1 ¹ H NMR Experiments	244
6.2.1.1 Diffusion-Ordered Spectroscopy Experiments	244
6.2.1.2 Rotational Overhauser Spectroscopy Experiments.....	244
6.2.2 ¹⁹ F NMR Experiments.....	245

6.2.3 ³¹ P NMR Experiments	245
6.2.4 Data Processing	245
6.3 Mass Spectroscopy	246
6.4 X-ray Crystallography	246
6.4.1 FL1 Stella Octangula Cage in Acetonitrile	246
6.4.2 [Pd ₃ (dppp) ₃ (FL1) ₂] ₂ ·6(OTf) Cryptophane in Acetonitrile	248
6.4.3 X-ray Crystallography Sample Preparation	250
Appendix	251
A.1 L1 + [Pd(dppp)] ²⁺ Cryptophane in <i>d</i> ₆ -DMSO ¹ H COSY	251
A.2 L1 & [Pd(dppp)] ²⁺ in <i>d</i> ₃ -MeNO ₂ ¹ H- ¹³ C HMQC	253
A.3 FL1 & [Pd(dppp)] ²⁺ in <i>d</i> ₃ -MeNO ₂ ¹ H- ¹³ C HMQC	255
References	257

List of Figures

Figure 1.1 Examples of crown ethers: a) [18]crown-6, b) dibenzo[18]crown-6, and cryptands: c) [2.1.1] cryptand, d) [2.2.1] cryptand, and e) [2.2.2] cryptand. ³ ...	5
Figure 1.2 2,3,6,7-Tetramethoxy-9,10-dihydroanthracene. ³⁷	8
Figure 1.3 Cyclotrimeratrylene. ³⁸	8
Figure 1.4 CTV conformations and NMR spectra. a) CTV saddle conformation, b) neat saddle isomer NMR spectrum (400 MHz, CDCl ₃), c) CTV saddle conformation and d) neat crown isomer NMR spectrum (400 MHz, CDCl ₃). b) and d) adapted with permission from H. Zimmermann, P. Tolstoy, H.-H. Limbach, R. Poupko and Z. Luz, 'The Saddle Form of Cyclotrimeratrylene', The Journal of Physical Chemistry B, 2004, 108, 18772-18778. Copyright (2004) American Chemical Society.	9
Figure 1.5 Cyclotrimeratrylene with two of the H _a protons and two of the H _e protons indicated.....	10
Figure 1.6 Top: structures of the unstable (C _s symmetry) saddle form (centre) and the corresponding right and left twisted stable conformations (C ₂ symmetry) (right and left sides). The C ₂ axes in both forms are indicated. Bottom: (reduced) pseudorotation cycle of the saddle isomer. Each entry corresponds to an average of a right and left twisted conformer (hence having C _s symmetry). The six entries correspond to the red, green, and blue benzene rings pointing to (from top clockwise) udd, udu, ddu, duu, dud, and uud, where u and d stand for "up" and "down", respectively. Reprinted with permission from H. Zimmermann, P. Tolstoy, H.-H. Limbach, R. Poupko and Z. Luz, 'The Saddle Form of Cyclotrimeratrylene', The Journal of Physical Chemistry B, 2004, 108, 18772-18778. Copyright (2004) American Chemical Society.	12
Figure 1.7 Cyclotrimeratrylene derivatives demonstrating chirality ⁴³	13
Figure 1.8 Ball and socket motif of CTV:C ₆₀ inclusion complex. ⁵⁷	15
Figure 1.9 a) CTV-Br and b) CTV with aryl moiety. ⁵⁸	16
Figure 1.10 CTV derivatised with 4-ureidopyrimidione. ⁵⁸	17
Figure 1.11 Complex formed between CTV, C ₇₀ and <i>o</i> -carborane. Hydrogen bonds shown in red. ⁶³	18
Figure 1.12 CTG derivative tris(4-pyridylmethylamino)cyclotrimeratrylene	19

Figure 1.13	CTG derivative tris[4-(3-pyridyl)phenylester]cyclotriguaiacylene. ⁶⁶	20
Figure 1.14	a) CTV-derivative tris(4-[2,2',6',2''-terpyridyl]-benzyl)cyclotriguaiacylene and b) schematic illustrating the dimeric handshake motif, with coloured ovals to represent the upper rim modified groups. ⁶⁷	21
Figure 1.15	a) L1 tris(isonicotinoyl)cyclotriguaiacylene and b) L2 tris(isonicotinoyl)-tris(propyl)-cyclotricatechylene.	22
Figure 1.16	a) M and P CTV-type molecules, b) achiral syn-linked meso cryptophanes and c) chiral anti-linked cryptophane isomers.	23
Figure 1.17	Part of the 500 MHz ¹ H NMR spectra of cryptophane-E and cryptophane-F in CDCl ₃ showing the differences between anti and syn isomers. a) is anti isomer (cryptophane-E) and b) is syn isomer (cryptophane-F). ⁷² Reproduced in part from Ref 72 with permission of The Royal Society of Chemistry.	24
Figure 1.18	Endo-carboxylic acid functionalised cryptophane. ⁷⁵	26
Figure 1.19	Cryptophane-E. ⁵³	27
Figure 1.20	Disulfide-linked cryptophane. ⁷⁸	28
Figure 1.21	Cryptophane-A. ⁵³	29
Figure 1.22	Cryptophane-A biosensor. Cryptophane-A is shown in black, xenon in red, avidin in green and biotin in orange. ^{80, 81}	30
Figure 1.23	a) Photochemical de-metalation of Atwood's aryl extended metalated CTV derivatives, b) syn and c) anti aryl-bridged cryptophanes. ⁸²	31
Figure 1.24	Yamaguchi and co-workers metallo-cryptophane, meso isomer. ⁷¹	32
Figure 1.25	Espinosa's metallo-cryptophane, anti isomer. ⁸³	33
Figure 1.26	Carboxylic acid functionalised CTV. ⁸⁴	34
Figure 1.27	Taken from the crystal structure of Hardie's bow-tie cryptophane. One carboxylic acid functionalised CTV in grey and one in green for clarity. ⁸⁴	34
Figure 1.28	a) tris(3-(3-pyridyl)phenylester)cyclotriguaiacylene ligand and b) taken from the crystal structure of Hardie's "Solomon's Cube". The loops of the complex are colour-coded to show the interlocking components. ⁸⁶	36

Figure 1.29 a) taken from the crystal structure of Hardie's triply interlocked [2]catenane. Chemically independent components distinguished by colour and b) schematic of one individual cryptophane. ⁸⁷	37
Figure 1.30 Taken from the crystal structure of Hardie's bis-N-heterocyclic carbene cryptophane. CTV-derivatives in grey and bis-N-heterocyclic carbene in green. ⁸⁸	38
Figure 1.31 Fujita's Molecular square. ⁹⁰	40
Figure 1.32 Schematic of the Nitschke group M ₄ L ₆ metallo-nanocage. The grey lines represent the ligands and the blue spheres represent the Fe(II) ions. ¹⁸	42
Figure 1.33 Schematic of the Nitschke group M ₄ L ₄ metallo-nanocage. The grey lines represent the tetrahedral shape of the metallo-nanocage, one ligand is illustrated and the purple spheres represent the Fe(II) ions. ⁹⁵	43
Figure 1.34 Raymond and Berman's M ₄ L ₆ metallo-nanocage. a) Schematic view, the grey lines represent the ligands and the red circles represent the gallium atoms. b) Taken from the crystal structure. The orange lines between the gallium(III) centres indicate the tetrahedral framework. ⁹⁶	45
Figure 1.35 The tridentate ligand 2,4,6-tri(pyridine-4-yl)-1,3,5-triazine used by the Fujita group to produce octahedral M ₆ L ₄ metallo-nanocages. ⁹⁸	46
Figure 1.36 Crystal structures of Fujita's M ₆ L ₄ cage. a) with no guest present, and b) with four adamantyl carboxylate ions shown in light blue. ⁹⁹	47
Figure 1.37 Stella octangula [Pd ₆ (L1) ₈] ¹²⁺ metallo-nanocage, a) from the crystal structure, b) space filling model and c) schematic of with only one L1 ligand shown for clarity. ¹¹⁰	51
Figure 1.38 Ligand 4,4'-(dibenzo[b,d]furan-2,8-diyl)diethyne-2,1-diyl)dipyridine. ¹¹⁷	52
Figure 1.39 Bidentate ligand from the Fujita group, with MMA units. ¹²⁰	53
Figure 1.40 Cage-in-a-cage bidentate ligand from the Fujita group. ¹²¹	54
Figure 1.41 FL1 ligand.	58
Figure 2.1 a) Tris(isonicotinoyl)cyclotriguaiacylene in the crown conformation, b) annotated section of ligand showing unique protons.	60
Figure 2.2 ¹ H NMR spectrum of tris(isonicotinoyl)cyclotriguaiacylene L1 with assignments and integration. (293 K, 500 MHz, d ₆ -DMSO)	61
Figure 2.3 The [Pd ₆ (L1) ₈].12(NO ₃) stella octangula cage a) space filling model and b) wireframe model.....	62

Figure 2.4 ¹ H NMR spectra of ligand L1 in red and [Pd ₆ (L1) ₈] · 12(BF ₄) in black. Integration shown for [Pd ₆ (L1) ₈] · 12(BF ₄). (293 K, 500 MHz, <i>d</i> ₆ -DMSO).....	63
Figure 2.5 a) Sodium dodecyl sulfate (SDS), b) the annotation used to describe the NMR spectrum of the sodium alkyl sulfate guests, the annotation is the same for all three guests.....	65
Figure 2.6 ¹ H NMR spectra of sodium alkyl guests a) SOS, b) SDS, c) STS.....	65
Figure 2.7 Downfield region of [Pd ₆ (L1) ₈] · 12(NO ₃) stella octangula cage with integrals, * indicate cage peaks and ♦ indicate unbound ligand. (293 K, 500 MHz, <i>d</i> ₆ -DMSO)	67
Figure 2.8 ¹ H NMR spectrum of the cage complex produced using tetrakis(acetonitrile)palladium(II)tetrafluoroborate with integration. The red arrow indicates the acetonitrile of the palladium salt and the blue-ringed peak indicates the contaminant present in the new palladium salt. (293 K, 500 MHz, <i>d</i> ₆ -DMSO)	68
Figure 2.9 ¹ H NMR spectra of [Pd ₆ (L1) ₈] · 12(BF ₄) stella octangula cage assemblies, a) heterochiral, b) homochiral. (293 K, 500 MHz, <i>d</i> ₆ -DMSO)	70
Figure 2.10 [Pd ₆ (L1) ₈] · 12(BF ₄) Stella octangula cages after 0 hours a) 0.1 mM, b) 0.2 mM, c) 0.3 mM, d) 0.4 mM and e) 0.5 mM. (293 K, 500 MHz, <i>d</i> ₆ -DMSO).....	71
Figure 2.11 [Pd ₆ (L1) ₈] · 12(BF ₄) Stella octangula cages after 24 hours a) 0.1 mM, b) 0.2 mM, c) 0.3 mM, d) 0.4 mM and e) 0.5 mM. Shown above is an expansion of the aromatic region of the 0.1 mM sample, indicating the low signal-to-noise ratio. (293 K, 500 MHz, <i>d</i> ₆ -DMSO)	72
Figure 2.12 2.5 mM [Pd ₆ (L1) ₈] · 12(BF ₄) stella octangula cage monitored over 748 hours. (293 K, 500 MHz, <i>d</i> ₆ -DMSO, referenced to TMS at 0.00 ppm)	75
Figure 2.13 1.0 mM [Pd ₆ (L1) ₈] · 12(BF ₄) stella octangula cage monitored over 343 hours. (293 K, 500 MHz, <i>d</i> ₆ -DMSO, referenced to TMS at 0.00 ppm)	76
Figure 2.14 0.5 mM [Pd ₆ (L1) ₈] · 12(BF ₄) stella octangula cage monitored over 255 hours. (293 K, 500, MHz <i>d</i> ₆ -DMSO, referenced to TMS at 0.00 ppm)	77
Figure 2.15 2.5 mM [Pd ₆ (L1) ₈] · 12(BF ₄) stella octangula cage produced with old stocks monitored over time. a) is 144 H, b) is 48 H, c) is 24 H and d) is 0 H.	79
Figure 2.16 2.5 mM [Pd ₆ (L1) ₈] · 12(BF ₄) stella octangula cage produced with old Pd stock and fresh ligand stock. a) is 24 H and b) is 0 H. (293 K, 500MHz, <i>d</i> ₆ -DMSO)	80

Figure 2.17 2.5 mM $[\text{Pd}_6(\text{L1})_8] \cdot 12(\text{BF}_4)$ stella octangula cage produced with heated Pd and fresh ligand L1 monitored over time, a) is 24 H and b) is 0 H. (293 K, 500 MHz, d_6 -DMSO)	81
Figure 2.18 ^1H NMR spectra of $[\text{Pd}_6(\text{L1})_8] \cdot 12(\text{BF}_4)$ stella octangula cage.	83
Figure 2.19 Job's plots for the $[\text{Pd}_6(\text{L1})_8] \cdot 12(\text{BF}_4)$ stella octangula cage & sodium alkyl guest systems. Legends show chemical shifts plotted. a) SOS, b) SDS and c) STS.	87
Figure 2.20 Comparison of Job's plots for the $[\text{Pd}_6(\text{L1})_8] \cdot 12(\text{BF}_4)$ stella octangula cage & sodium alkyl guest systems for of all three guests using the plot of the methyl tail group proton shifts with a line to indicate the 0.33 maximum. 88	
Figure 2.21 ^1H NMR spectra of $[\text{Pd}_6(\text{L1})_8] \cdot 12(\text{BF}_4)$ stella octangula cage:SOS titration study, (*) asterisk indicates methyl H4 peak. (293 K, 500 MHz, d_6 -DMSO).....	89
Figure 2.22 ^1H NMR spectra of $[\text{Pd}_6(\text{L1})_8] \cdot 12(\text{BF}_4)$ stella octangula cage:SDS titration study, (*) asterisk indicates methyl H4 peak. (293 K, 500 MHz, d_6 -DMSO).....	90
Figure 2.23 ^1H NMR spectra of $[\text{Pd}_6(\text{L1})_8] \cdot 12(\text{BF}_4)$ stella octangula cage:STS titration study, (*) asterisk indicates methyl H4 peak. (293 K, 500 MHz, d_6 -DMSO).....	91
Figure 2.24 Fitting of the ^1H NMR titration data for the $[\text{Pd}_6(\text{L1})_8]^{12+}$ stella octangula cage and sodium alkyl sulfate guests. Fitting shown is for the Ha/a' proton. a) SOS, b) SDS, c) STS, d) legend for plots.....	94
Figure 2.25 Plot of diffusion coefficient against the concentration ratio $[\text{H}]/[\text{G}]$ for the $[\text{Pd}_6(\text{L1})_8] \cdot 12(\text{BF}_4)$ stella octangula cage and SDS complex.....	96
Figure 2.26 the $[\text{Pd}_6(\text{L1})_8]^{12+}$ cage, with only one ligand illustrated to demonstrate the orientation of the pyridyl, aryl and methoxy groups with regards to the cavity. The cavity is indicated by the green oval.	97
Figure 2.27 Section of a 2-D ROESY spectrum for a 1:10 cage:SDS mixture with through space connections in red and exchange peaks in blue. (293 K, 500 MHz, d_6 -DMSO)	98
Figure 2.28 Section of a 2-D ROESY spectrum for a 1:20 cage:SOS mixture with through space connections in red and exchange peaks in blue. (293 K, 500 MHz, d_6 -DMSO)	99

Figure 2.29 ESI-MS of $[\text{Pd}_6(\text{L1})_8] \cdot 12(\text{BF}_4)$ stella octangula cage with 10 equivalents of SDS	100
Figure 3.1 a) FL1 ligand, b) L1 ligand.	107
Figure 3.2 a) FL1 in $d_3\text{-MeCN}$, b) tetrakis(acetonitrile)palladium(II)tetrafluoroborate in $d_3\text{-MeCN}$ and c) $[\text{Pd}_6(\text{FL1})_8] \cdot 12(\text{BF}_4)$ in $d_3\text{-MeCN}$	110
Figure 3.3 ^1H NMR spectrum of $[\text{Pd}_6(\text{FL1})_8] \cdot 12(\text{BF}_4)$ cage complex.	111
Figure 3.4 Annotated section of FL1 ligand, showing unique protons.....	112
Figure 3.5 ^1H NMR spectrum of FL1 ligand, with expansions of the peaks at 7.98 and 8.69 ppm and integrations. (293 K, 500 MHz, $d_6\text{-DMSO}$)	113
Figure 3.6 ^1H NMR spectrum of FL1 ligand, with expansions of the peaks at 7.92 and 8.62 ppm and integrations. (293 K, 500 MHz, $d_3\text{-MeCN}$).....	113
Figure 3.7 ^{19}F NMR spectra of FL1 ligand a) 298 K, b) 329 K. (471 MHz, $d_3\text{-MeCN}$)	117
Figure 3.8 ^{19}F NMR broadband decoupled spectrum of FL1 ligand. (296 K, 282 MHz, $d_3\text{-MeCN}$).....	117
Figure 3.9 ^{19}F NMR spectra of FL1 ligand. (297 K, 471 MHz, $d_6\text{-DMSO}$)	118
Figure 3.10 ^{19}F NMR spectra of FL1 ligand. (297 K, 471 MHz, $d_3\text{-MeNO}_2$)	118
Figure 3.11 ^1H NMR spectrum of FL1 stella octangula cage after 5 months, ★ indicates free ligand. (293 K, 500 MHz, $d_6\text{-DMSO}$).....	119
Figure 3.12 ^1H NMR spectra of $[\text{Pd}_6\text{FL1}_8] \cdot 12(\text{BF}_4)$ stella octangula palladium titration after 24 hours. ★ indicate free ligand. (293 K, 500 MHz, $d_6\text{-DMSO}$).....	121
Figure 3.13 ^1H NMR spectra of $[\text{Pd}_6\text{FL1}_8] \cdot 12(\text{BF}_4)$ stella octangula cage over time, $1.0 \times \text{Pd}$. (293 K, 500 MHz, $d_6\text{-DMSO}$)	122
Figure 3.14 ^1H NMR spectra of $[\text{Pd}_6\text{FL1}_8] \cdot 12(\text{BF}_4)$ stella octangula cage over time, $2.0 \times \text{Pd}$. (293 K, 500 MHz, $d_6\text{-DMSO}$)	123
Figure 3.15 ^1H NMR spectra of $[\text{Pd}_6\text{FL1}_8] \cdot 12(\text{BF}_4)$ stella octangula cage over time, $3.0 \times \text{Pd}$. (293 K, 500 MHz, $d_6\text{-DMSO}$)	124
Figure 3.16 ^1H NMR spectra of $[\text{Pd}_6\text{FL1}_8] \cdot 12(\text{BF}_4)$ stella octangula cage over time, $4.0 \times \text{Pd}$. (293 K, 500 MHz, $d_6\text{-DMSO}$)	125

Figure 3.17 ¹ H NMR spectra of [Pd ₆ FL1 ₈] ₁₂ (BF ₄) stella octangula palladium titration after 672 hours for samples 1.0 - 3.0 × Pd and 648 hours for 3.5 and 4.0 × Pd.....	126
Figure 3.18 ¹⁹ F NMR spectra of [Pd ₆ FL1 ₈] ₁₂ (BF ₄) stella octangula palladium.	127
Figure 3.19 ¹ H NMR spectra of [Pd ₆ FL1 ₈] ₁₂ (BF ₄) stella octangula. a) 4.0 × Pd, b) 1.0 × Pd. (293 K, 500 MHz, <i>d</i> ₆ -DMSO).....	128
Figure 3.20 ¹ H NMR spectra of 1.0 × Pd [Pd ₆ (FL1) ₈] ₁₂ (BF ₄) with a) 10.0 mM SDS, b) 1.0 mM SDS and c) no guest – aromatic region. Free ligand peaks are indicated by ★.....	129
Figure 3.21 ¹ H NMR spectra of SDS and 1.0 × Pd [Pd ₆ (FL1) ₈] ₁₂ (BF ₄) with SDS. a) SDS, b) 1.0 Pd [Pd ₆ (FL1) ₈] ₁₂ (BF ₄) with 1.0 mM SDS and c) 1.0 × Pd [Pd ₆ (FL1) ₈] ₁₂ (BF ₄) with 10.0 mM SDS – upfield regions showing SDS peaks. Expansions of the SDS H1 and H4 peaks are shown. (293 K, 500 MHz, <i>d</i> ₆ -DMSO)	130
Figure 3.22 ¹ H NMR spectra of 4.0 × Pd [Pd ₆ (FL1) ₈] ₁₂ (BF ₄) with a) 10.0 mM SDS, b) 1.0 mM SDS and c) no guest – aromatic region. (293 K, 500 MHz, <i>d</i> ₆ -DMSO)	131
Figure 3.23 ¹ H NMR spectra of SDS and 4.0 × Pd [Pd ₆ (FL1) ₈] ₁₂ (BF ₄) with SDS. a) SDS, b) 4.0 × Pd [Pd ₆ (FL1) ₈] ₁₂ (BF ₄) with 1.0 mM SDS and c) 4.0 × Pd [Pd ₆ (FL1) ₈] ₁₂ (BF ₄) with 10.0 mM SDS – upfield regions showing SDS peaks. Expansions of the SDS H1 and H4 peaks are shown. (293 K, 500 MHz, <i>d</i> ₆ -DMSO)	131
Figure 3.24 ¹ H NMR spectra of 0.5 mM 1.0 × Pd [Pd ₆ (FL1) ₈] ₁₂ (BF ₄) SDS with 10.0 mM at the bottom and 0.5 mM at the top, b) superimposed stacked plot of SDS H3 and H4 peaks.....	133
Figure 3.25 ¹ H NMR spectra of 0.5 mM 4.0 × Pd [Pd ₆ (FL1) ₈] ₁₂ (BF ₄) SDS with 10.0 mM at the bottom and 0.5 mM at the top, b) superimposed stacked plot of SDS H3 and H4 peaks.....	135
Figure 3.26 Fitting of the ¹ H NMR titration data for the 4.0 × Pd [Pd ₆ (FL1) ₈] ₁₂ ⁺ stella octangula cage and SDS, shown for protons: a) Hb, b) H4, c) H3, d) H2, e) H1 and f) legend for plots.	137
Figure 3.27 Job's plots for [Pd ₆ (FL1) ₈] ₁₂ (BF ₄) and SDS. Legends show guest chemical shifts plotted. a) 1.0 × Pd and b) 4.0 × Pd.	138
Figure 3.28 [Pd ₆ (FL1) ₈] ₁₂ (BF ₄) stella octangula cage with integrations.....	139

Figure 3.29 ^{19}F NMR spectrum of FL1 ligand. (296 K, 282 MHz, d_3 -MeCN).....	140
Figure 3.30 ^1H NMR DOSY spectrum of $[\text{Pd}_6(\text{FL1})_8]\cdot 12(\text{BF}_4)$ stella octangula cage.....	140
Figure 3.31 ESI-MS of $[\text{Pd}_6(\text{FL1})_8]\cdot 12(\text{BF}_4)$ stella octangula cage showing various	141
Figure 3.32 Section of 2-D ROESY spectrum for 0.5 mM $[\text{Pd}_6(\text{FL1})_8]\cdot 12(\text{BF}_4)$ stella octangula cage with through space connections in black and exchange peaks in pink.....	143
Figure 3.33 Optical microscopy images of $[\text{Pd}_6(\text{FL1})_8]\cdot 12(\text{BF}_4)$ stella octangula cage, b)-d) are polarised images.....	144
Figure 3.34 a) From the asymmetric unit of $[\text{Pd}_6(\text{FL1})_8]\cdot 12(\text{BF}_4)$, with carbon atoms in grey, oxygen atoms in red, nitrogen in dark blue, fluorine in blue and palladium in light blue, b) from the crystal structure of $[\text{Pd}_6(\text{FL1})_8]\cdot 12(\text{BF}_4)$, showing the two disordered enantiomers of the FL1 ligands in each $[\text{Pd}_6(\text{FL1})_8]\cdot 12(\text{BF}_4)$ cage. Individual ligand enantiomers are distinguished by colour.....	145
Figure 3.35 From the crystal structure of $[\text{Pd}_6(\text{FL1})_8]\cdot 12(\text{BF}_4)$ a) and b) from above and c) from the side. One ligand is coloured green.....	146
Figure 4.1 (Ethylenediamine)palladium(II) dinitrate.....	153
Figure 4.2 Rearrangement of $[\text{Pd}_3(\text{en})_3(\text{L2})_2]^{6+}$ to $[\text{Pd}_6(\text{L2})_8]^{12+}$. ⁸⁸	154
Figure 4.3 ^1H NMR spectra of a) FL1 and $\text{Pd}(\text{en})(\text{NO}_3)_2$ at 2:3 ratio, b) $\text{Pd}(\text{en})(\text{NO}_3)_2$ and c) FL1 (293 K, 500 MHz, d_6 -DMSO) Inset spectrum: ^{19}F NMR spectrum of FL1 + $\text{Pd}(\text{en})(\text{NO}_3)_2$ at 2:3 ratio. (296 K, 282 MHz, d_6 -DMSO)	155
Figure 4.4 ^1H NMR DOSY spectrum of FL1 and $\text{Pd}(\text{en})(\text{NO}_3)_2$ at a 2:3 ratio. The FL1 ligand components are highlighted in blue and the $\text{Pd}(\text{en})(\text{NO}_3)_2$ components are highlighted in green.	156
Figure 4.5 a) Tecton bis(acetonitrile)-{1,1'-methylenebis(3-benzyl-imidazol-2-ylidene)}palladium(I)tetrafluoroborate, b) annotated section of $[\text{Pd}(\text{bis-NHC-b})]$ showing unique protons, dashed line indicates a line of 2-fold symmetry.	158
Figure 4.6 ^1H NMR spectrum of $[\text{Pd}(\text{bis-NHC-b})(\text{MeCN})_2]\cdot 2(\text{BF}_4)$ with assignments and integrations. (293 K, 500 MHz, d_6 -DMSO)	159

Figure 4.7 ^1H NMR spectrum of $[\text{Pd}(\text{bis-NHC-b})(\text{MeCN})_2]\cdot 2(\text{BF}_4)$ with assignments and integrations. (293 K, 500 MHz, $d_3\text{-MeNO}_2$)	159
Figure 4.8 $[\text{Pd}_3(\text{bis-NHC-b})_3(\text{L1})_2]\cdot 6(\text{BF}_4)$	160
Figure 4.9 ^1H NMR spectra of a) $[\text{Pd}_3(\text{bis-NHC-b})_3(\text{L1})_2]^{6+}$, b) $\text{Pd}(\text{bis-NHC-b})(\text{MeCN})_2\cdot 2(\text{BF}_4)$ and c) L1 . (293 K, 500 MHz, $d_6\text{-DMSO}$).....	161
Figure 4.10 ^1H NMR spectra of a) $[\text{Pd}_3(\text{bis-NHC-b})_3(\text{L1})_2]^{6+}$, b) $\text{Pd}(\text{bis-NHC-b})(\text{MeCN})_2\cdot 2(\text{BF}_4)$ and c) L1 . (293 K, 500 MHz, $d_3\text{-MeNO}_2$).....	162
Figure 4.11 ^1H NMR DOSY spectrum of $[\text{Pd}_3(\text{bis-NHC-b})_3(\text{L1})_2]^{6+}$. (293 K, 500 MHz, $d_6\text{-DMSO}$)	164
Figure 4.12 ^1H NMR DOSY spectrum of $[\text{Pd}_3(\text{bis-NHC-b})_3(\text{L1})_2]^{6+}$. (293 K, 500 MHz, $d_3\text{-MeNO}_2$)	164
Figure 4.13 ^1H NMR spectrum of $[\text{Pd}_3(\text{bis-NHC-b})_3(\text{L1})_2]^{6+}$ at 293 - 333 K. The top spectrum was recorded after the sample had cooled to 20°C after heating. (500 MHz, $d_6\text{-DMSO}$)	166
Figure 4.14 ^1H NMR spectrum of $[\text{Pd}_3(\text{bis-NHC-b})_3(\text{L1})_2]^{6+}$ at 293 - 333 K. The top spectrum was recorded after the sample had cooled to 20°C after heating. (500 MHz, $d_3\text{-MeNO}_2$)	167
Figure 4.15 ^1H NMR DQF-COSY spectrum of $[\text{Pd}_3(\text{bis-NHC-b})_3(\text{L1})_2]^{6+}$. The blue box indicates intramolecular coupling between the CTG-bowl methylene protons. The red box indicates intramolecular coupling of the Ha/a' protons of the L1 ligand. (293 K, 500 MHz, $d_6\text{-DMSO}$)	168
Figure 4.16 ^1H NMR DQF-COSY spectrum of $[\text{Pd}_3(\text{bis-NHC-b})_3(\text{L1})_2]^{6+}$. The blue box indicates intramolecular coupling between the CTG-bowl methylene protons. The red box indicates intramolecular coupling of the Ha/a' protons of the L1 ligand. (293 K, 500 MHz, $d_3\text{-MeNO}_2$)	169
Figure 4.17 ^1H NMR ROESY spectrum of $[\text{Pd}_3(\text{bis-NHC-b})_3(\text{L1})_2]^{6+}$ exchange peaks in pink and through-space connections in black. (293 K, 500 MHz, $d_6\text{-DMSO}$)	170
Figure 4.18 ^1H NMR ROESY spectrum of $[\text{Pd}_3(\text{bis-NHC-b})_3(\text{L1})_2]^{6+}$ exchange peaks in pink and through-space connections in black. (293 K, 500 MHz, $d_3\text{-MeNO}_2$).....	170
Figure 4.19 [1,3-Bis(diphenylphosphino)propane]palladium(II)triflate.	171

Figure 4.20	[1,3-Bis(diphenylphosphino)propane]palladium(II), annotated to show unique protons, 5 proton environments.	173
Figure 4.21	¹ H NMR spectrum of [1,3-bis(diphenylphosphino)propane]palladium(II)triflate with integrations. Inset spectra show the aromatic peaks and the propyl bridge peaks at 2.9 and 1.9 ppm. (293 K, 500 MHz, <i>d</i> ₆ -DMSO)	173
Figure 4.22	¹ H NMR spectrum of [1,3-bis(diphenylphosphino)propane]palladium(II)triflate with integrations. Inset spectra showing the aromatic peaks and the propyl bridge peaks at 2.9 and 2.4 ppm. (293 K, 500 MHz, <i>d</i> ₃ -MeNO ₂)	174
Figure 4.23	¹ H NMR spectra of [1,3-bis(diphenylphosphino)propane]palladium(II)triflate with integrations. Inset spectra showing the aromatic peaks and the propyl bridge peaks at 2.9 and 2.2 ppm. (293 K, 500 MHz, <i>d</i> ₃ -MeCN).....	175
Figure 4.24	¹ H NMR spectra of [1,3-bis(diphenylphosphino)propane]palladium(II)triflate in acetonitrile at 0.5 – 5.0 mM, showing the aromatic peaks. (293 K, 500 MHz, <i>d</i> ₃ -MeCN)	176
Figure 4.25	¹ H NMR spectra of [1,3-Bis(diphenylphosphino)propane]palladium(II)triflate	177
Figure 4.26	Chair conformations of [1,3-Bis(diphenylphosphino)propane]palladium(II)triflate, a) axial moieties in red, b) after interconversion the red moieties are now in the equatorial position.	177
Figure 4.27	³¹ P NMR spectra of [1,3-Bis(diphenylphosphino)propane]palladium(II)triflate 0.5 – 5.0 mM, shown as a superimposed stacked plot, solvent contaminant marked with a black dot.....	178
Figure 4.28	¹ H NMR spectra of 5.0 mM [1,3-Bis(diphenylphosphino)propane]palladium(II)triflate at 298 - 348 K. The top spectrum was recorded after the sample had cooled to 25°C after heating. (293 K, 500 MHz, <i>d</i> ₆ -DMSO).....	179
Figure 4.29	¹ H NMR spectra of 0.5 mM [1,3-Bis(diphenylphosphino)propane]palladium(II)triflate at 298 - 348 K. The top spectrum was recorded after the sample had cooled to 25°C after heating. (293 K, 500 MHz, <i>d</i> ₆ -DMSO).....	180
Figure 4.30	[Pd ₃ (dppp) ₃ (L1) ₂]-6(OTf) cryptophane.	182

- Figure 4.31 ^1H NMR spectra of a) green trace, $[\text{Pd}_3(\text{dppp})_3(\text{L1})_2]^{6+}$, b) red trace, [1,3-bis(diphenylphosphino)propane]palladium(II)triflate, c) black trace, L1. Integrations are shown for $[\text{Pd}_3(\text{dppp})_3(\text{L1})_2]^{6+}$. (293 K, 500 MHz, d_6 -DMSO) 183
- Figure 4.32 Section of ^1H NMR ROESY spectrum of $[\text{Pd}_3(\text{dppp})_3(\text{L1})_2]^{6+}$, aromatic region showing weak through-space connections between the Ha/a' proton of the L1 pyridyl group and Hb protons of the phenyl arms of $[\text{Pd}(\text{dppp})]^{2+}$. Exchange peaks are in blue and rOes are in black..... 184
- Figure 4.33 $[\text{Pd}_3(\text{dppp})_3(\text{L1})_2] \cdot 6(\text{OTf})$ cryptophane in DMSO, with one $[\text{Pd}(\text{dppp})]^{2+}$ group drawn fully to show the through-space connections between Ha/a' of the L1 ligand and Hb of $[\text{Pd}(\text{dppp})]^{2+}$, which are indicated by the blue arrows..... 185
- Figure 4.34 ^1H NMR spectra of $[\text{Pd}_3(\text{dppp})_3(\text{L1})_2]^{6+}$ at 0.5 – 5.0 mM. (293 K, 500 MHz, d_6 -DMSO) 186
- Figure 4.35 ^1H NMR spectra of $[\text{Pd}_3(\text{dppp})_3(\text{L1})_2]^{6+}$ Hd $[\text{Pd}(\text{dppp})]^{2+}$ resonance with 5.0 mM at the bottom and 0.5 mM at the top. a) stacked plot, b) superimposed stacked plot, (•) black dot indicates contaminant in L1 ligand, (*) blue asterisk indicates Hd anti resonance, (♦) red diamond indicates Hd syn resonance. (293 K, 500 MHz, d_6 -DMSO) 187
- Figure 4.36 ^{31}P NMR spectra of $[\text{Pd}_3(\text{dppp})_3(\text{L1})_2]^{6+}$ at 0.5 – 5.0 mM. (•) black dot indicates contaminant in d_6 -DMSO. (300 K, 121 MHz, d_6 -DMSO) 188
- Figure 4.37 ^1H NMR spectra of 0.5 mM $[\text{Pd}_3(\text{dppp})_3(\text{L1})_2]^{6+}$ at 298 - 348 K. The top spectrum was recorded after the sample had cooled to 25°C after heating. The box highlights the $[\text{Pd}(\text{dppp})]^{2+}$ Hd peaks. (500 MHz, d_6 -DMSO)..... 189
- Figure 4.38 ^1H NMR spectra of 5.0 mM $[\text{Pd}_3(\text{dppp})_3(\text{L1})_2]^{6+}$ at 298 - 348 K. The top spectrum was recorded after the sample had cooled to 25°C after heating. The box shows an expansion of the Hd peaks of $[\text{Pd}(\text{dppp})]^{2+}$. (500 MHz, d_6 -DMSO) 191
- Figure 4.39 ^1H NMR spectra of a) pink trace, $[\text{Pd}_3(\text{dppp})_3(\text{L1})_2]^{6+}$, b) red trace, [1,3-bis(diphenylphosphino)propane]palladium(II)triflate, c) black trace, L1. Integrations are shown for $[\text{Pd}_3(\text{dppp})_3(\text{L1})_2]^{6+}$. (293 K, 500 MHz, d_3 -MeCN) 192
- Figure 4.40 ^1H NMR ROESY spectrum of $[\text{Pd}_3(\text{dppp})_3(\text{L1})_2]^{6+}$, Exchange peaks are in pink and rOes are in black. (293 K, 500 MHz, d_3 -MeCN) 193

Figure 4.41 Section of ^1H NMR ROESY spectrum of $[\text{Pd}_3(\text{dppp})_3(\text{L1})_2]^{6+}$, aromatic region showing through-space connections between the Ha/a' proton of the L1 pyridyl group and Hb and Hc protons of the phenyl arms of $[\text{Pd}(\text{dppp})]^{2+}$. Exchange peaks are in pink and rOes are in black. (293 K, 500 MHz, d_3 -MeCN).....	193
Figure 4.42 $[\text{Pd}_3(\text{dppp})_3(\text{L1})_2] \cdot 6(\text{OTf})$ cryptophane in MeCN, with one $[\text{Pd}(\text{dppp})]^{2+}$ group drawn fully to show the through-space connections between Ha/a' of the L1 ligand and Hb and Hc of $[\text{Pd}(\text{dppp})]^{2+}$, which are indicated by the pink arrows.	194
Figure 4.43 ^1H NMR spectra of $[\text{Pd}_3(\text{dppp})_3(\text{L1})_2]^{6+}$ at 0.5 – 5.0 mM.....	196
Figure 4.44 ^{31}P NMR spectra of $[\text{Pd}_3(\text{dppp})_3(\text{L1})_2]^{6+}$ at 0.5 – 5.0 mM.....	197
Figure 4.45 ^1H NMR spectra of $[\text{Pd}_3(\text{dppp})_3(\text{L1})_2]^{6+}$ with 5.0 mM at the bottom and 0.5 mM at the top a) Ha/a' peaks, b) H_{endo} peaks and c) Hd syn peaks.	197
Figure 4.46 ^1H NMR spectra of a) purple trace, $[\text{Pd}_3(\text{dppp})_3(\text{L1})_2]^{6+}$, b) red trace, [1,3-bis(diphenylphosphino)propane]palladium(II)triflate, c) black trace, L1. Inset spectrum shows expansion of $[\text{Pd}_3(\text{dppp})_3(\text{L1})_2]^{6+}$ Hd peaks. (293 K, 500 MHz, d_3 -MeNO ₂)	198
Figure 4.47 ^1H NMR ROESY spectrum of $[\text{Pd}_3(\text{dppp})_3(\text{L1})_2]^{6+}$. Exchange peaks are in purple and rOes are in black. (293 K, 500 MHz, d_3 -MeNO ₂).....	199
Figure 4.48 $[\text{Pd}_3(\text{dppp})_3(\text{L1})_2] \cdot 6(\text{OTf})$ cryptophane in MeNO ₂ , with one $[\text{Pd}(\text{dppp})]^{2+}$ group drawn fully to show the through-space connections between Ha/a' of the L1 ligand and Hb of $[\text{Pd}(\text{dppp})]^{2+}$, which are indicated by the purple arrows.....	200
Figure 4.49 ^1H NMR spectra of $[\text{Pd}_3(\text{dppp})_3(\text{L1})_2]^{6+}$ at 0.5 – 5.0 mM.....	201
Figure 4.50 ^{31}P NMR spectra of $[\text{Pd}_3(\text{dppp})_3(\text{L1})_2]^{6+}$ at 0.5 – 4.5 mM.....	202
Figure 4.51 ^1H NMR spectra of a) green trace, $[\text{Pd}_3(\text{dppp})_3(\text{FL1})_2]^{6+}$, b) red trace, [1,3-bis(diphenylphosphino)propane]palladium(II)triflate, c) black trace, FL1. Integrations are shown for $[\text{Pd}_3(\text{dppp})_3(\text{FL1})_2]^{6+}$. (293 K, 500 MHz, d_6 -DMSO)	203
Figure 4.52 Section of ^1H NMR ROESY spectrum of $[\text{Pd}_3(\text{dppp})_3(\text{FL1})_2]^{6+}$, aromatic region showing a weak through-space connections between the Ha and Hb protons of the FL1 pyridyl group and Hb protons of the phenyl arms of $[\text{Pd}(\text{dppp})]^{2+}$. Exchange peaks are in blue and rOes are in black. (293 K, 500 MHz, d_6 -DMSO).....	204

Figure 4.53 Pd ₃ (dppp) ₃ (FL1) ₂ ·6(OTf) cryptophane in DMSO, with one [Pd(dppp)] ²⁺ group drawn fully to show the through-space connections between Ha/Hb of the FL1 ligand and Hb of [Pd(dppp)] ²⁺ , which are indicated by the blue arrows.....	205
Figure 4.54 ESI-MS of Pd ₃ (dppp) ₃ (FL1) ₂ ·6(CF ₃ SO ₃) cryptophane.	206
Figure 4.55 ¹ H NMR spectra of [Pd ₃ (dppp) ₃ (FL1) ₂] ⁶⁺ at 0.5 – 5.0 mM. Inset spectra show the superimposed stacked plot of the Hd peaks. (293 K, 500 MHz, d ₆ -DMSO)	208
Figure 4.56 ¹⁹ F NMR spectra of [Pd ₃ (dppp) ₃ (FL1) ₂] ⁶⁺ at 0.5 – 5.0 mM.....	209
Figure 4.57 ³¹ P NMR spectra of [Pd ₃ (dppp) ₃ (FL1) ₂] ⁶⁺ at 0.5 – 5.0 mM. (•) black dot indicates contaminant in d ₆ -DMSO. (300 K, 121 MHz, d ₆ -DMSO)	210
Figure 4.58 ¹ H NMR spectra of 0.5 mM [Pd ₃ (dppp) ₃ (FL1) ₂] ⁶⁺ at 298 - 348 K. The top spectrum was recorded after the sample had cooled to 25°C after heating. (500 MHz, d ₆ -DMSO).....	211
Figure 4.59 ¹ H NMR spectra of a) pink trace, [Pd ₃ (dppp) ₃ (FL1) ₂] ⁶⁺ , b) red trace, [1,3-bis(diphenylphosphino)propane]palladium(II)triflate, c) black trace, FL1. Integrations are shown for [Pd ₃ (dppp) ₃ (FL1) ₂] ⁶⁺ . (293 K, 500 MHz, d ₃ -MeCN)	212
Figure 4.60 ¹ H NMR spectra of [Pd ₃ (dppp) ₃ (FL1) ₂] ⁶⁺ at 0.5 – 5.0 mM.....	213
Figure 4.61 ¹⁹ F – { ¹ H} NMR spectra of [Pd ₃ (dppp) ₃ (FL1) ₂] ⁶⁺ at 0.5 – 5.0 mM.	214
Figure 4.62 ³¹ P NMR spectra of [Pd ₃ (dppp) ₃ (FL1) ₂] ⁶⁺ at 0.5 – 5.0 mM.....	215
Figure 4.63 From the crystal structure of complex [Pd ₃ (dppp) ₃ (FL1) ₂ ·6(OTf), FL1 ligands in grey and [Pd(dppp)] ²⁺ shown in purple, a) as viewed from the top, b) as viewed from the top with the four triflate anions that have been located, c) as viewed from the side.	216
Figure 4.64 From the crystal structure of complex [Pd ₃ (dppp) ₃ (FL1) ₂ ·6(OTf). One [Pd(dppp)] ²⁺ arm showing the second-sphere coordination between the triflate anion and palladium(II) centres.....	217
Figure 4.65 a) From the crystal structure of [Pd ₃ (dppp) ₃ (FL1) ₂ ·6(OTf), a) side view displaying the large cavity. The FL1 ligand is shown in grey and [Pd(dppp)] ²⁺ in purple, b) packing diagram of [Pd ₃ (dppp) ₃ (FL1) ₂ ·6(OTf). The cryptophane is displayed in space-filling mode, with solvent and OTf anions omitted for clarity.....	218

Figure 4.66 ^1H NMR spectra of a) purple trace, $[\text{Pd}_3(\text{dppp})_3(\text{FL1})_2]^{6+}$, b) red trace, $[\text{1,3-bis(diphenylphosphino)propane}]_{\text{palladium(II)triflate}}$, c) black trace, FL1 .	219
Figure 4.67 ^1H NMR ROESY spectrum of $[\text{Pd}_3(\text{dppp})_3(\text{FL1})_2]^{6+}$. Exchange peaks are in purple and rOes are in black. (293 K, 500 MHz, $d_3\text{-MeNO}_2$)	220
Figure 4.68 $\text{Pd}_3(\text{dppp})_3(\text{FL1})_2 \cdot 6(\text{OTf})$ cryptophane in MeNO_2 , with one $[\text{Pd}(\text{dppp})]^{2+}$ group drawn fully to show the through-space connections between Hb of the FL1 ligand and Hb of $[\text{Pd}(\text{dppp})]^{2+}$, which are indicated by the purple arrows.	221
Figure 4.69 ^1H NMR spectra of $[\text{Pd}_3(\text{dppp})_3(\text{FL1})_2]^{6+}$ at 0.5 – 5.0 mM.	222
Figure 4.70 ^{31}P NMR spectra of $[\text{Pd}_3(\text{dppp})_3(\text{FL1})_2]^{6+}$ at 0.5 – 5.0 mM.	222
Figure 4.71 ^{19}F $\{^1\text{H}\}$ NMR spectra of $[\text{Pd}_3(\text{dppp})_3(\text{FL1})_2]^{6+}$ at 0.5 – 5.0 mM.	223
Figure 4.72 CTBs used by Espinosa and co-workers. ⁸³	226
Figure 6.1 Schematic of Pd stella octangula cage host-guest synthesis.	242

List of Tables

Table 2.1 Solvent Properties for DMSO and Acetonitrile	82
Table 2.2 Fitted cumulative association constants for the host-guest systems.	94
Table 3.1 Solubility of FL1 and Pd salt ligand in deuterated solvents.	109
Table 3.2 Table of peak assignments for FL1 ligand in MeCN and DMSO at 500 MHz.	115
Table 3.3 Table to show results of selective homonuclear decoupling experiments for FL1 ligand. (296 K, 500 MHz, <i>d</i> ₃ -MeCN).....	116
Table 3.4 Fitted cumulative association constants for 4.0 × Pd [Pd ₆ (FL1) ₈].12(BF ₄) and SDS host- guest systems.	136
Table 3.5 Table to show calculated and observed <i>m/z</i> for the [Pd ₆ (FL1) ₈].12(BF ₄) stella octangula cage.	142
Table 3.6 Table of through-space connections and assignments for [Pd ₆ (FL1) ₈].12(BF ₄) stella octangula cage.	143
Table 4.1 Diffusion Coefficients of L1 , Pd(bis-NHC-b)(MeCN) ₂ .2(BF ₄) and [Pd ₃ (bis-NHC-b) ₃ (L1) ₂] ⁶⁺	163
Table 4.2 Table of through-space connections and assignments for [Pd ₃ (dppp) ₃ (L1) ₂].(OTf) ₆ cryptophane in <i>d</i> ₃ -MeCN. L1 listed in black and [Pd(dppp)] ²⁺ listed in red.....	195
Table 4.3 Table to show calculated and observed <i>m/z</i> for the [Pd ₃ (dppp) ₃ (FL1) ₂].6(CF ₃ SO ₃) cryptophane in DMSO.....	207
Table 4.4 Table of through-space connections and assignments for [Pd ₃ (dppp) ₃ (FL1) ₂].(OTf) ₆ cryptophane in <i>d</i> ₃ -MeNO ₂ . L1 listed on black and [Pd(dppp)] ²⁺ listed in red.....	220
Table 6.1 Crystal data and structure refinement for the FL1 stella octangula cage	248
Table 6.2 Crystal data and structure refinement for [Pd ₃ (dppp) ₃ (FL1) ₂].6(OTf) Cryptophane in Acetonitrile	250

Abbreviations

Å	ångström
Ar	aryl group
BF ₄ ⁻	tetrafluoroborate anion
°C	degrees Celsius
<i>ca.</i>	Circa (approximately)
CDCl ₃	deuterated chloroform
COSY	correlation ordered spectroscopy
CPK	Corey-Pauling-Koltun
CSI-TOF-MS	cold-spray ionisation time of flight mass spectroscopy
CTB	cyclotribenzylene
CTC	cyclotricatechylene
CTG	cyclotriguaiacylene
CTV	cyclotrivenatrylene
DCM	dichloromethane
DMF	dimethylformamide
DMSO	dimethyl sulfoxide
DNA	deoxyribonucleic acid

DOSY	diffusion ordered spectroscopy
dppe	[1,3-bis(diphenylphosphino)ethane]
dppp	[1,3-bis(diphenylphosphino)propane]
DQF-COSY	double quantum filtered correlation spectroscopy
EN	ethylenediamine
ESI-MS	electro-Spray Ionisation Mass Spectrometry
<i>et al.</i>	et alia (and others)
FL1	fluorinated ligand - (\pm)-2,7,12-trimethoxy-3,8,13- <i>tris</i> -(4-carboxy-3-fluoropyridyl)-10,15-dihydro-5 <i>H</i> -tribenzo[a,d,g]cyclononatriene
G	guest
H	host
HMQC	heteronuclear Multiple Quantum Coherence
HPLC	high-performance liquid chromatography
Hz	Hertz
<i>J</i>	coupling constant
K	Kelvin
kJ/mol	kilojoules per mole
L1	ligand 1 - tris(isonicotinoyl)cyclotriguaiacylene

L2	ligand 2 - tris(isonicotinoyl)-tris(propyl)-cyclotricatechylene
<i>M</i>	minus (left-handed screw chirality)
Me	methyl group
MeCN	acetonitrile
MeNO ₂	nitromethane
mM	millimole
MMA	methyl methacrylate
MOF	metal-organic framework
ms	milliseconds
<i>m/z</i>	mass to charge ratio
NHC	<i>N</i> -heterocyclic carbene
nm	nanometre
NMR	nuclear magnetic resonance
nOe	nuclear Overhauser effect
NOESY	nuclear Overhauser effect spectroscopy
<i>o</i> -	<i>ortho</i>
OAc	acetoxy group (CH ₃ CO ₂)
OMe	methoxy group

OPr	propoxy group
OTf	triflate anion (CF_3SO_3^-)
<i>P</i>	plus (right-handed screw chirality)
$[\text{Pd}(\text{dppp})]^{2+}$	[1,3-bis(diphenylphosphino)propane]palladium(II)triflate
PF_6^-	hexafluorophosphate anion
PFG	pulsed-field gradient
Ph	phenyl
pm	picometre
PMMA	polymethyl methacrylate
ppm	parts per million
rOe	rotating frame nuclear Overhauser effect
ROESY	rotational Overhauser effect spectroscopy
s	seconds
SDS	sodium dodecyl sulfate
SOS	sodium octyl sulfate
STS	sodium tetradecyl sulfate
TCE	tetrachloroethane

Tecton	molecules whose interactions are dominated by specific attractive forces that induce the assembly of aggregates with controlled geometries ¹
TMS	tetramethylsilane
VT	variable temperature

Chapter 1 Introduction

1.1 Overview

The work presented in this thesis details the NMR (nuclear magnetic resonance) spectroscopic investigations of metallo-nanocages formed from novel cyclotrimeratrylene (CTV) derivatives. This chapter will introduce the reader to the field of supramolecular chemistry. It will cover a brief history of self-assembly and host-guest systems, followed by the history of CTV and a brief review of its analogues and their applications. This will be succeeded by a discussion of the advances in metallo-nanocages to provide context and to demonstrate the significance of the research to be presented to the field of supramolecular chemistry.

1.2 Supramolecular Chemistry

The term comes from the Latin *supra*, meaning beyond. Supramolecular chemistry is the chemistry of the intermolecular bond, described by Lehn as “chemistry beyond the molecule”.² Steed divides supramolecular chemistry into two broad domains: self-assembly and host-guest chemistry.³ The first reports of “supramolecular” chemistry date back to the early 1960’s.³ Supramolecular chemistry is a vigorous area of scientific research, as it is a wide reaching multidisciplinary area of chemistry. Its beginnings were in organic chemistry, but it soon expanded into inorganic synthesis and physical chemistry; for experimental and theoretical investigations with an emphasis on biology and biochemistry.^{2, 4} As characterisation techniques have advanced with time, this has

enabled new methodologies to be developed for ever more subtle and delicate probing of supramolecular environments.

The term 'supramolecular' can be applied to systems involving aggregates of molecules or ions held together by non-covalent interactions, which include electrostatic interactions, hydrogen bonding, dispersion interactions and solvophobic effects.³

Inspiration for supramolecular chemistry comes from nature as a substantial endeavour of supramolecular chemistry is biomimicry.^{3, 5} The details of non-covalent binding in biomolecules can be exceedingly challenging to interpret due to their complexity. Supramolecular chemistry can aid the interpretation of biomolecular function by providing a simple model system as a basis for a more profound analysis.^{3, 5, 6}

Biological systems use a wide range of nanometre-scale assemblies formed from molecular components which interact in precise, well-defined protocols. An important factor in efficient operation of biological systems is their ability to self-assemble and self-replicate.⁷ Some examples from nature include the iron storage protein, apoferritin, composed of 24 non-covalently linked protein subunits forming a nearly spherical shell of octahedral symmetry;⁸ the globular protein actin, which self-assembles into filaments that make up the actuating components of muscle cells;⁹ and of course, the ultimate supramolecule, DNA, which is the central courier of information in cells, its double helices held together by hydrogen bonds.^{10, 11} Non-covalent self-assembly processes allow genetic information to be stored, retrieved, and transcribed.⁹ Information is routinely stored in biological systems in the shape, size and electronic properties of molecules. This information is read by the way molecules recognise and interact with each other, this is termed molecular recognition. ^{2, 10}

Supramolecular chemistry has been responsible for the development of exciting novel materials with functionalities such as; catalysis, attempting to match enzymes with their turnover rates^{5, 12-15} and gas storage, by sequestering hazardous agents such as noxious gases and pyrophoric white phosphorus.¹⁶⁻¹⁸

1.2.1 Self-Assembly

Self-assembly is the spontaneous and reversible association of molecules under equilibrium conditions into stable, structurally well-defined aggregates joined by non-covalent bonds.¹⁹⁻²¹

For the self-assembled structure to be stable and to have well-defined shape, the non-covalent bonds between molecules must be collectively stable. The strengths of individual van der Waals interactions and hydrogen bonds are relatively weak (0.3 to 20.0 kJ/mol)²² relative to typical covalent bonds (150.0 to 450.0 kJ/mol).³ Accordingly, to achieve the required stability, molecules in self-assembled systems need to be connected by many of these weak non-covalent interactions, or by multiple hydrogen bonds or perhaps even both.^{19, 23} The formation of self-assembled complexes is driven by a maximisation of site occupancy, as well as entropy. A consequence of this, the smallest number of components is chosen that can form a discrete supramolecular entity which satisfies the maximum site occupancy.^{24, 25}

A key feature in self-assembly is the ability to correct mistakes so that the final product is as desired. Weak non-covalent bonds allow for this to happen with relative ease as they are weak enough to permit rearrangement, which facilitates correction as required. This results in the conversion of unfavourable products and intermediates into a single product.⁷ When the constituent parts of the supramolecular construct exhibit mutual

molecular recognition properties this initiates self-sorting within the self-assembly process. Self-sorting occurs after the self-assembly process,²⁶ and is described by Wu and Isaacs²⁷ as “the high-fidelity recognition of self, from nonself”. They divide self-sorting into two types: thermodynamic self-sorting and kinetic self-sorting. A system is defined as being thermodynamically self-sorting if it has reached thermodynamic equilibrium and exhibits self-sorting. All other systems of self-sorting are considered to be kinetic self-sorting. As a result of this self-sorting, aided by the molecular recognition abilities of the constituent parts, it is unlikely that defective constituents will become incorporated into the self-assembled system.^{7, 19} As only a small number of types of molecules are normally involved in self-assembly (typically only two types of molecule), this results in a limited set of binding interactions needed to form the final assembly. This minimises the amount of information required for a particular structure, making it a very economical synthesis technique, giving rise to structures exhibiting a high degree of symmetry with quantitative yields ^{7, 9, 19}

1.2.2 Host-Guest Chemistry

Donald Cram defined hosts and guests as follows: the host constituent is an organic molecule or ion whose binding sites converge in the complex, whereas the guest is the converse of this.^{3, 28} A host and guest together form a complex, held together in solution by non-covalent bonds.²⁸ Steed refined this definition, describing host-guest chemistry as “the study of large ‘host’ molecules that are capable of enclosing smaller ‘guest’ molecules *via* non-covalent interactions.”³ The earliest host-guest systems were the crown ethers prepared by Pedersen in 1967^{29, 30} and the cryptands prepared by Lehn in 1969.³¹ Examples of these crown ethers and cryptands are shown in Figure

1.1. An example of a host-guest system in Nature would be an enzyme and its substrate, where the enzyme is the host and the substrate its guest.³

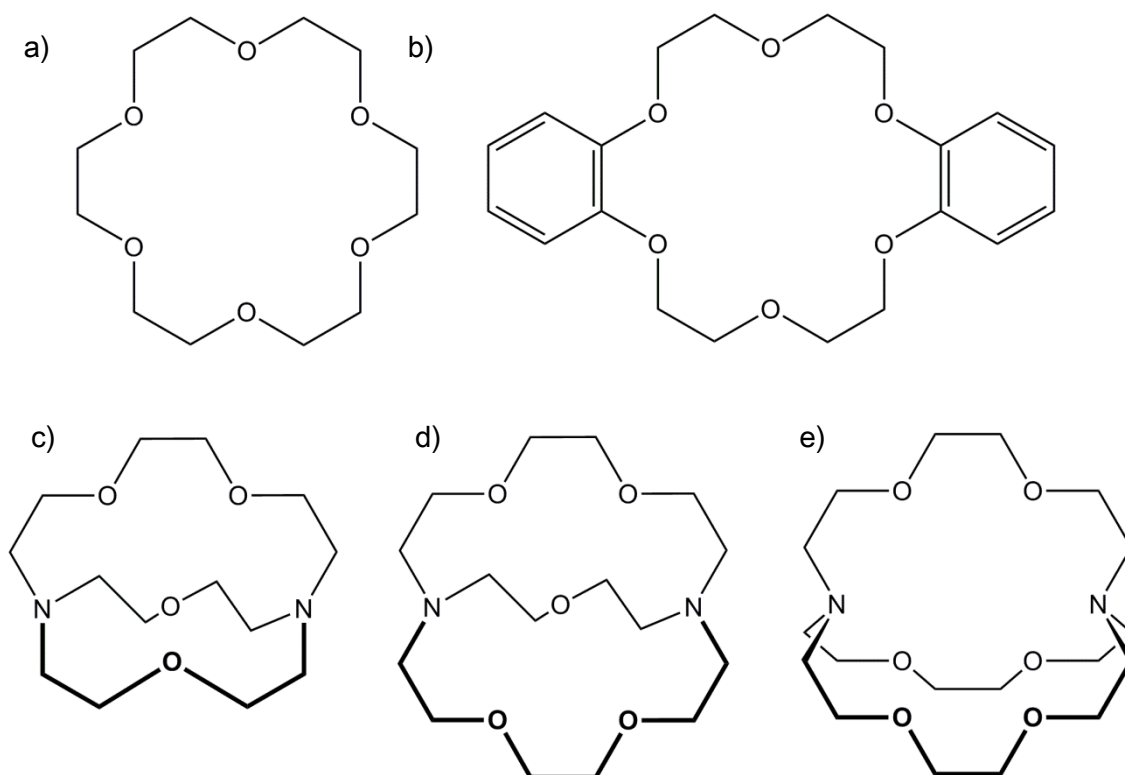


Figure 1.1 Examples of crown ethers: a) [18]crown-6, b) dibenzo[18]crown-6, and cryptands: c) [2.1.1] cryptand, d) [2.2.1] cryptand, and e) [2.2.2] cryptand.³

To determine the suitability of potential guests, the 55% rule was devised by Rebek and Mecozzi. They found that optimal host-guest binding was achieved when $55 \pm 9\%$ of the volume of the host cavity is occupied. When the packing coefficient is less than 45%, the intermolecular interactions between the host and the guest are similar to what the guest experiences in the bulk solvent. Packing coefficients above 65% restrict the movement of the guest, effectively trapping it within the host. This rule is often used to assess the binding between host and guest.³²

1.2.3 Metallo-Supramolecular Chemistry

Coordination-directed self-assembly is a powerful technique for the preparation of large metallo-supramolecular structures of defined shapes and sizes.³³ To synthesise large, discrete, rigid self-assembled structures requires the use of stronger bonds for thermodynamic reasons.^{9, 33} The Gibbs free energy of a metallo-supramolecular system favours coordinatively saturated complexes. This requires that all ligand and metal binding sites are used, fulfilling the needs for maximum site occupancy.²⁵

Coordination bonds are stronger than other types of non-covalent bonds and are highly directional.^{9, 33} Metallo-supramolecular chemistry takes advantage of dative coordinate bonds. This is often illustrated by utilising Pd-pyridine bonds, which facilitate the self-assembly process due to their being labile, this allows for self-sorting processes to occur after the self-assembly process. Whilst metal–ligand coordination bonds are strong compared to most other non-covalent interactions, they are still kinetically labile. Thus, coordination-driven self-assembly is a dynamic process carried out under thermodynamic control.^{8, 9}

The metal coordination geometry and the orientation of the sub-units in a ligand provide the instructions for the self-assembly of metallo-nanocages.⁸ These factors are governed by the geometry of the species used in the self-assembly process.³⁴ When linear sub-units are used in conjunction with “angled” sub-units, a variety of two-dimensional assemblies can be formed. For example, if the angled species has a 60° angle a triangle is formed, a 90° angle gives a square and a 108° angle gives a pentagon and so forth. However, if multidentate ligands are used in the place of bidentate sub-units, then a wide assortment of polygons and polyhedra can be

produced.³⁵ To produce these three-dimensional shapes, sub-units are required that have more than two coordination sites.³⁴ When the geometry of the ligand and the metal coordination are chosen wisely (i.e. that is, they fit each other appropriately), the metallo-nanocage should be the only stoichiometric product, satisfying the binding requirements of both the ligand and the metal ions.^{8, 21}

This research focuses on CTV-based complexes, there will be an introduction on the discovery of CTV and its properties will be discussed in depth. The discussion will focus on CTV and its derivatives and the complexes produced with them. The discussion will then cover cryptophanes, (complexes made from two CTV-like subunits) and more complicated and larger metallo-nanocages, exhibiting the most exciting and relevant examples.

1.3 Cyclotrimeratrylene (CTV)

CTV was first encountered by Robinson in 1915. Robinson was following up earlier work on the synthesis of anthracene derivatives. CTV was formed by the condensation reaction when veratrole alcohol was reacted with formaldehyde under acidic conditions. This gave a sparingly soluble crystalline product with a melting point of 227°C and the empirical formula $C_7H_{10}O_2$. However, the product was incorrectly identified as 2,3,6,7-tetramethoxy-9,10-dihydroanthracene (Figure 1.2),^{4, 36} the dimer of the intermediate veratryl cation. Robinson was misled in her assessment of her results by earlier work by Ewins³⁷, in which he too, had misidentified the reaction product as 2,3,6,7-tetramethoxy-9,10-dihydroanthracene.³⁷

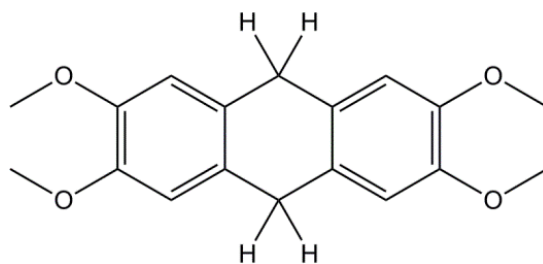


Figure 1.2 2,3,6,7-Tetramethoxy-9,10-dihydroanthracene.³⁷

It was not until the 1960's when the inception of a variety of modern techniques helped to finally establish the correct trimeric formula.⁴ In 1965, Lindsey undertook a detailed study of the reaction between veratrole alcohol and formaldehyde, performing molecular-weight determinations, infrared absorption spectroscopy, ultraviolet absorption spectroscopy and proton NMR. These analyses revealed that the reaction product was actually a cyclic trimer, as opposed to the dimer originally postulated by Robinson and Ewins. Lindsey established that the product was actually 10,15-dihydro-2,3,7,8,12,13-hexamethoxy-5*H*-tribenzo[*a,d,g*]cyclonone which for convenience he named cyclotrimeratrylene,³⁸ shown below in Figure 1.3.³⁸

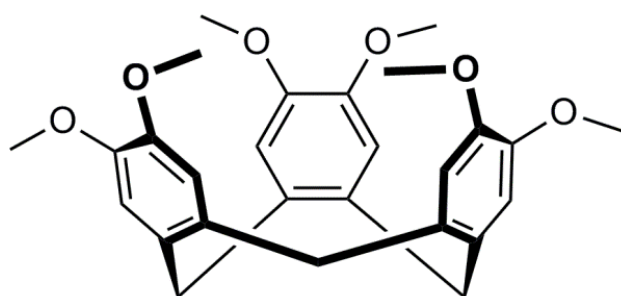


Figure 1.3 Cyclotrimeratrylene.³⁸

CTV can exist in two conformations; the crown and the saddle, illustrated in Figure 1.4. The most stable conformation is the rigid crown which has C_{3v} symmetry.³⁹ This conformation provides an electron-rich, hydrophobic molecular cavity in which guests can be bound in a non-covalent fashion. Because of these attributes, CTV is thought of

as a molecular host.^{40, 41} The crown conformation is also the stable conformer of the parent molecule cyclononatriene.⁴²

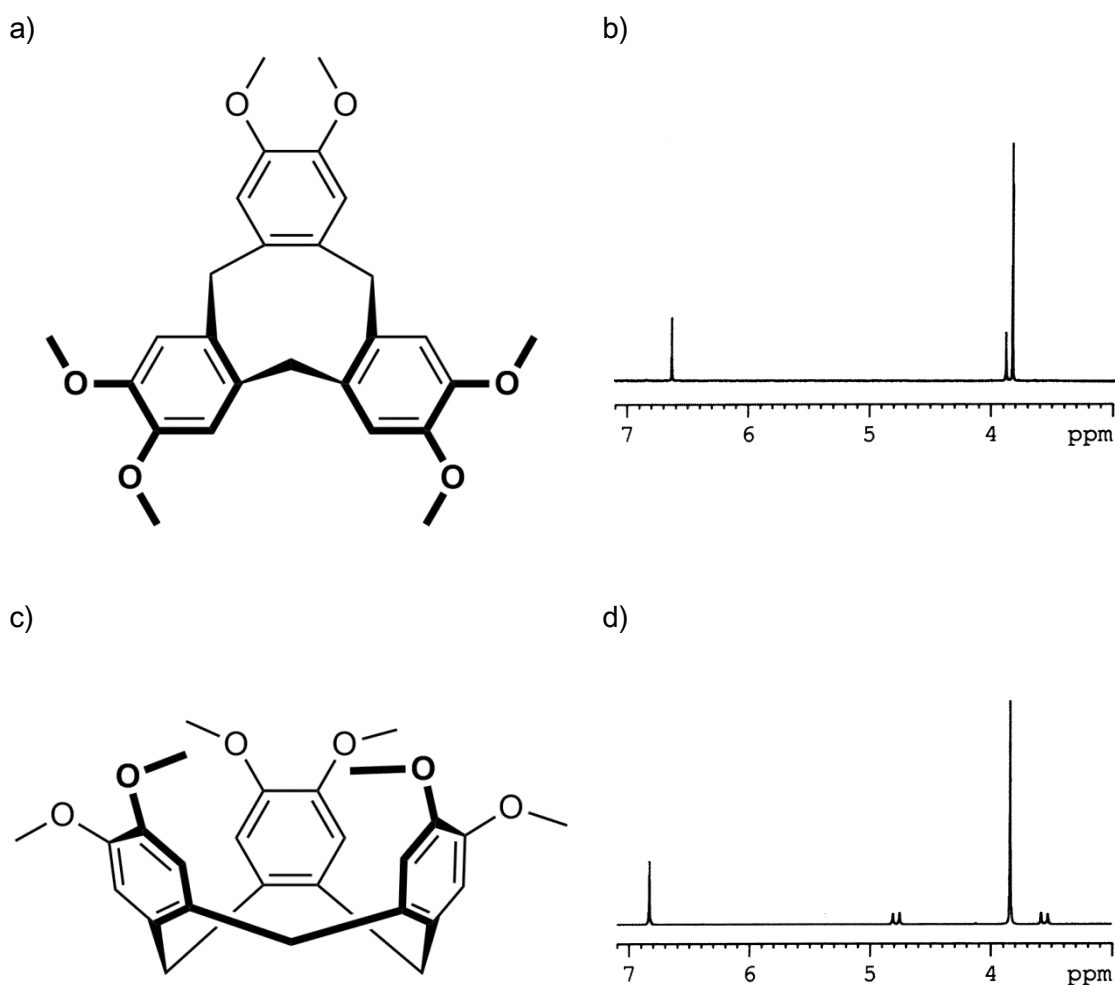


Figure 1.4 CTV conformations and NMR spectra. *a) CTV saddle conformation, b) neat saddle isomer NMR spectrum (400 MHz, CDCl₃), c) CTV saddle conformation and d) neat crown isomer NMR spectrum (400 MHz, CDCl₃). b) and d) adapted with permission from H. Zimmermann, P. Tolstoy, H.-H. Limbach, R. Poupko and Z. Luz, 'The Saddle Form of Cyclotrivenatrylene', *The Journal of Physical Chemistry B*, 2004, 108, 18772-18778. Copyright (2004) American Chemical Society.*

The crown conformation of CTV is characterised by the two doublet resonances of the methylene bridge protons in its ¹H NMR spectrum. These protons are labelled H_a and H_e illustrated in Figure 1.5, which correspond to the quasi-axial (the inner or *endo* proton) and quasi-equatorial (outer or *exo* proton).^{43, 44} This pair of doublets is caused

by the three equivalent pairs of quasi-axial and quasi-equatorial hydrogens. The *endo* protons resonate 1.2 ppm downfield from the *exo* protons. The reason for this large downfield shift of the *endo* protons is that they are strongly deshielded, which is explained by the steric compression effect, caused by overcrowding at the crown base.^{45, 46} The *endo* protons of the methylene bridge are only separated from each other by ~210 pm. This causes steric compression, which means that there is effectively no hole at the base of the crown.⁴⁷ These steric requirements that favour the crown conformation lead to an essentially pyramidal structure, where the benzene rings form the pyramid sides and the methylene bridge protons form the tip.³⁸

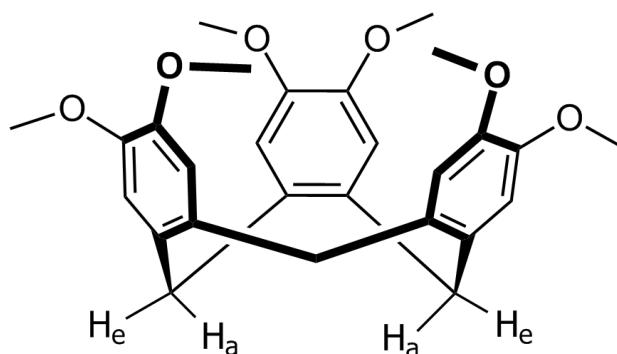
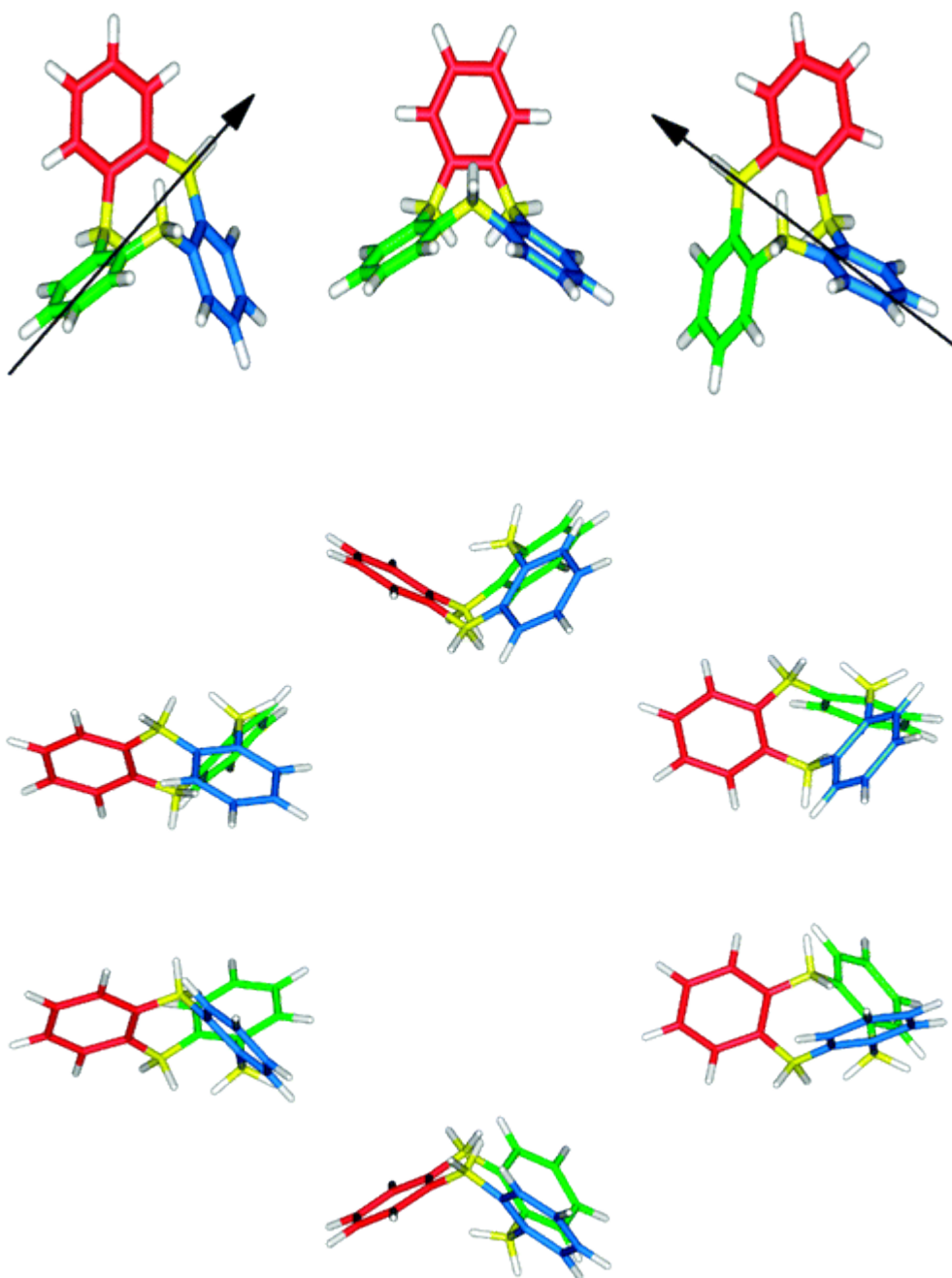


Figure 1.5 Cyclotrimeratrylene with two of the H_a protons and two of the H_e protons indicated.

The saddle conformation of CTV [Figure 1.4 a)] is highly flexible and difficult to isolate due to its lower thermodynamic stability. However, rapid quenching of a hot solution or high-temperature melt to below room temperature can be used to isolate this isomer of CTV.⁴⁸ The relative instability of the saddle form is due to repulsive interactions between the inward pointing methylene hydrogen and the opposite benzene ring. The energy minimum of the saddle corresponds to a twisted rather than symmetric (C_3) structure.⁴⁸ The open structure and highly flexible nature of the saddle form simultaneously increase its entropy and lower its free energy in solution at high

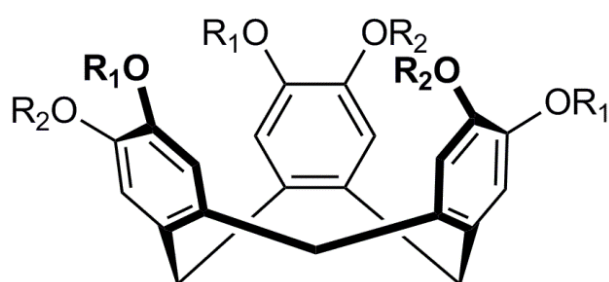
temperatures, so that in these conditions, an equilibrium develops between crown and saddle forms that greatly favours the saddle isomer.⁴⁹

The quenching study performed by Zimmerman and co-workers enabled them to isolate the saddle form of CTV and they were able to produce a ¹H NMR spectrum in CDCl₃. This spectrum showed three singlets at 6.62, 3.38 and 3.82 ppm, which were identified as the aromatic ring protons, the methylene protons and the methoxy protons of the saddle isomer respectively. The simplicity of this spectrum reflects the averaging effect of the pseudorotation process, which renders the different types of hydrogens equivalent. The spectrum effectively corresponds to a tribenzocyclononatriene core with *D*_{3h} symmetry.⁴⁸ The lifetime in the saddle form is of the order of hours. During this period, it undergoes billions of pseudorotation cycles (pseudorotation is; stereoisomerisation resulting in a structure that has the appearance of being produced by rotation of the entire molecule⁵⁰) (Figure 1.6), so that when it reconverts to the crown form it has a 50% chance of ending up in the opposite chirality of the starting configuration.⁴⁸ A force field calculation showed that the minimum-energy structure of the twisted form actually has approximate *C*₂ symmetry, with the *C*₂ axis bisecting one of the side benzene rings and passing through the opposite methylene bridge carbon. There are two such structures corresponding to a right and a left twist, giving six average conformations (with average *C*_s symmetry) obtained by flipping each benzene ring alternatively “up” and “down”. In reality, each entry corresponds to a rapidly interconverting pair of right and left twisted conformers.⁴⁸ Thus it might be expected that at least a small amount of the saddle isomer is present at equilibrium with the crown form in solution. However, so far there are no reports claiming the observation of the saddle conformer in solutions of CTV derivatives.⁴⁸



*Figure 1.6 Top: structures of the unstable (C_s symmetry) saddle form (centre) and the corresponding right and left twisted stable conformations (C_2 symmetry) (right and left sides). The C_2 axes in both forms are indicated. Bottom: (reduced) pseudorotation cycle of the saddle isomer. Each entry corresponds to an average of a right and left twisted conformer (hence having C_s symmetry). The six entries correspond to the red, green, and blue benzene rings pointing to (from top clockwise) *udd*, *udu*, *ddu*, *duu*, *dud*, and *uud*, where *u* and *d* stand for “up” and “down”, respectively. Reprinted with permission from H. Zimmermann, P. Tolstoy, H.-H. Limbach, R. Poupko and Z. Luz, ‘The Saddle Form of Cyclotriveratrylene’, *The Journal of Physical Chemistry B*, 2004, 108, 18772-18778. Copyright (2004) American Chemical Society.*

CTV is achiral; however, it is possible to produce chiral derivatives, which occur when all R groups are not the same. CTV is typically modified by appending side-arms to the upper rim, this can be done in one of two ways; either in a C_3 -symmetric style ($R_1 \neq R_2$), which is sometimes referred to as a trimeric derivatisation or in hexameric fashion ($R_1 = R_2$),⁵¹ as illustrated in Figure 1.7. The enantiomers of CTV analogues are stereoisomers that are designated according to the *P* or *M* helicity of their preferred conformations.^{43, 52}



CTV, $R_1 = R_2 = \text{Me}$ (achiral)

CTC, $R_1 = R_2 = \text{H}$ (achiral)

CTG, $R_1 = \text{Me}, R_2 = \text{H}$ (*P*)(-)

$R_1 = \text{Me}, R_2 = \text{COCH}_3$ (*M*)(-)

Figure 1.7 Cyclotrimeric crown ether derivatives demonstrating chirality⁴³

Chiral CTV analogues can undergo racemisation, a process that is understood to proceed *via* the saddle form.⁴⁸ The racemisation proceeds by slow interconversion between two identical CTV or enantiomeric crown conformers in a racemic mixture.⁴¹ The mechanism of the conformational inversion in these compounds is similar to that of cyclohexane. It is assumed that inversion takes place *via* a flexible conformer readily pseudo-rotating between enantiomeric saddle and twist forms which are about 15-25 kJ/mol less stable than the crown form.⁴⁷ The activation barrier for the crown-to-crown interconversion in CTV analogues has been found to be relatively uniform and of the order of 110-120 kJ/mol.^{4, 47, 53} This activation barrier corresponds to the rate-determining step and represents the passage from the crown to the flexible saddle-twist form, a process which might involve either the flipping of one phenyl ring or that of a methylene bridge; consequently, the transition state is not planar. The intermediate

saddle-twist form (equivalent to the boat-twist form of cyclohexane) is destabilised with respect to the crown by the existence of repulsive interaction between the inward hydrogen atom of the methylene bridge pointing into the ring and the opposite benzene ring.⁴⁷ The inversion half-life is approximately one month at 20°C, but less than 0.1 s at 200°C.⁴

1.3.1 Applications of Cyclotrimeratrylene and its Analogues

The ability of CTV to form inclusion compounds with small molecules was first noted in 1931 by Bhagwat et al,^{54, 55} who found that the reaction product they created crystallised with a mixture of water and benzene. These inclusion compounds are only formed in the solid state as due to the trigonal symmetry of CTV, the crystals do not pack closely and can accommodate small guests within the voids of its lattice.⁵⁶ CTV can form a ball and socket motif with the fullerenes C₆₀ and C₇₀, where the fullerene sits in the CTV bowl as a 1:1 complex, shown in Figure 1.8. This was initially discovered in 1994 by Steed and co-workers, who used CTV to separate the fullerenes from a fullerite solution.⁵⁷ The CTV:C₆₀ inclusion complex has both steric and electronic complementarity, as the radius of fullerene C₆₀ is similar to that of the CTV cavity and CTV is very electron-rich due to aryl rings in its tribenzo[*a,d,g*]cyclononatriene core, and fullerene is electron-deficient.⁴

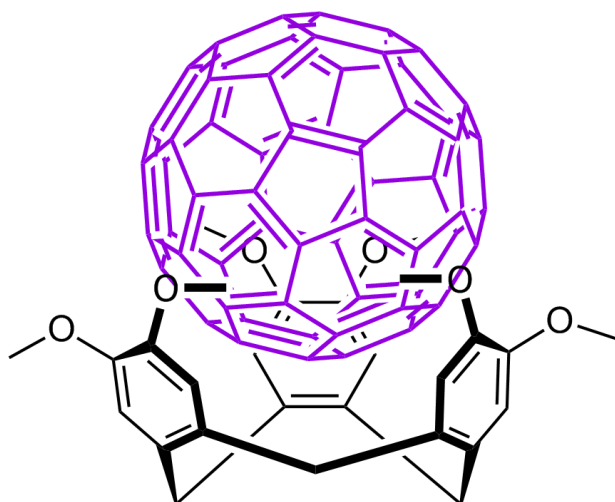
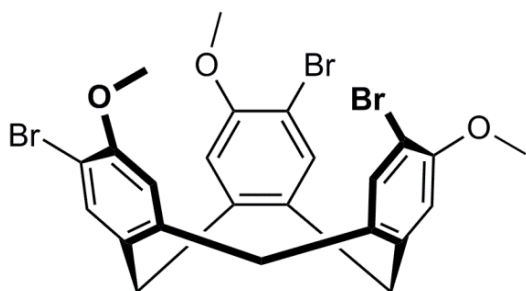


Figure 1.8 Ball and socket motif of CTV:C₆₀ inclusion complex.⁵⁷

To improve upon this function of CTV, Zheng and co-workers extended the upper rim of CTV in a C_3 symmetric fashion with aryl groups, which provide better recognition potential due to their rigidity. In order to provide the required rigidity, the aryl moieties were attached directly to the tribenzo[*a,d,g*]cyclononatriene core, achieved by derivatising a brominated CTV derivative (Figure 1.9), where the R₁ group does not have a methoxy group attached to it, but a bromine instead. If a CTV derivative with the methoxy groups had been utilised, this would have provided free rotation around the oxygen, meaning that the methoxy groups can bend inside the bowl, preventing guest recognition. With this new rigid analogue of CTV, a high binding constant was achieved whilst maintaining the 1:1 host-guest ratio seen by Steed and co-workers.⁵⁸ It has also been noted that the interaction with CTV can lead to the polarisation of C₆₀, if the CTV is saturated in toluene. This polarisation of C₆₀ can lead to aggregation of the fullerenes, giving polymeric arrays in the solid state.⁵⁹

a)



b)

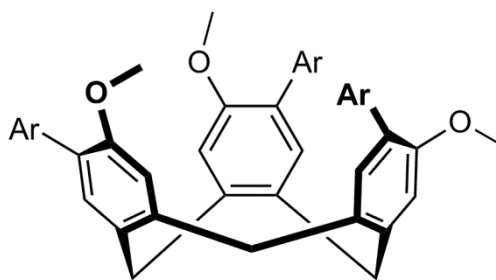


Figure 1.9 a) CTV-Br and b) CTV with aryl moiety.⁵⁸

Mendoza and colleagues derivatised CTV in a tri-substituted manner with 4-ureidopyrimidinone as shown in Figure 1.10, greatly extending the size of the cavity available and providing hydrogen bonding capabilities. These ligands arrange into a dimer around the fullerenes, but unlike other cryptophanes, the two CTV-based ligands are not joined by linker units, but by hydrogen bonding. This capsule has an inner volume of ca. 790 Å³ and has shown selective binding for both C₇₀ and the larger C₈₄. This allows for easy separation of fullerene mixtures or crude soot without the need for expensive and time-consuming HPLC separation techniques. For C₇₀, a purity level of 97% was obtained from fullerite by employing a simple solid-liquid extraction.^{60, 61}

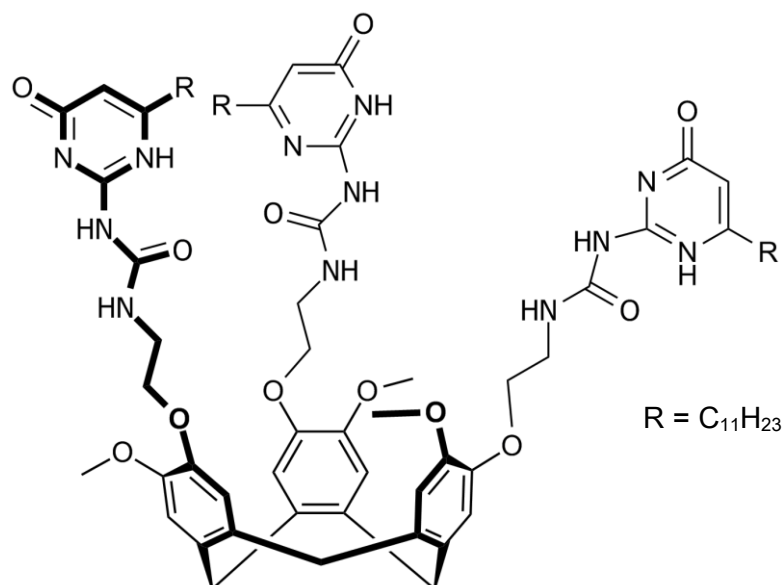
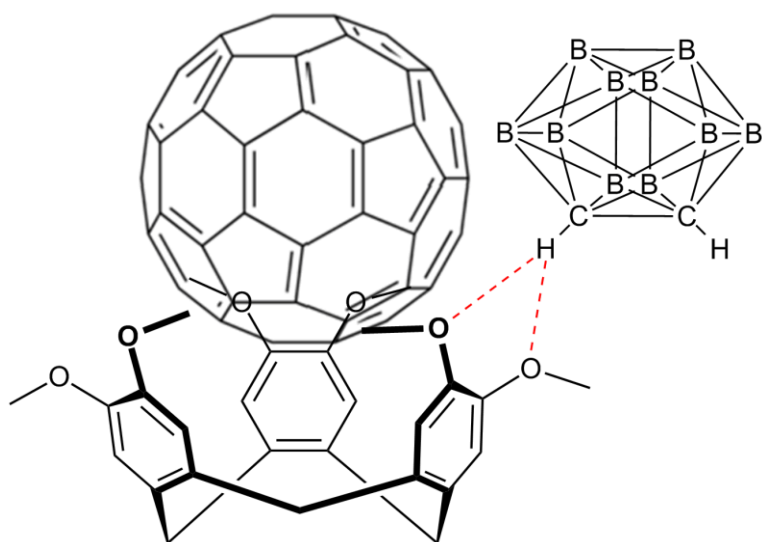


Figure 1.10 CTV derivatised with 4-ureidopyrimidione.⁵⁸

CTV and its analogues have been known to form inclusion complexes with α -carboranes. This was initially reported in 1997 by Raston and co-workers, who concluded that a 2:1 host-guest complex was formed in solid and liquid states. They deduced that although two CTV units were involved in the complex formation, only one of the CTV units was bound to the α -carborane. They also noted that the α -carborane could be bound in either the *endo* or *exo* fashion with regards to the CTV cavity. α -Carborane has a similar diameter to fullerene C_{60} ; at 8 Å compared to 10 Å. The ball and socket motif formed with CTV and fullerene C_{60} complexes was previously known, so it seemed reasonable to assume that complexes between CTV and α -carborane would form. They described the cavity of CTV as shallow, and the motif formed as a “perching” complex, however, it seemed very similar to the ball and socket motif described previously.^{57, 62} A further study in this area by Hardie and Raston found a 1:2 host-guest complex could be formed between CTV and α -carborane, where one α -carborane is inside the cavity in a much more secure fashion than the 2:1 complex and the other carborane is held by hydrogen bonds to three CTV units. They also showed that a complex could be formed between CTV, α -carborane and C_{70} , shown in

Figure 1.11. They found that in the absence of *o*-carborane, C₇₀ does not complex with CTV, in contrast to C₆₀ which can form two different complexes with CTV. The complex formed between *o*-carborane, C₇₀ and CTV forms a helical array, with each *o*-carborane interacting with two CTV units and each CTV hydrogen-bonded to two *o*-carboranes. The helices formed are chiral, with the CTV cavities pointing outwards from the helix, forming built-in receptor sites. These receptor sites bind the C₇₀ to form the recognisable ball and socket motif seen in the discrete structures formed between CTV and fullerenes.^{57, 62-64}



*Figure 1.11 Complex formed between CTV, C₇₀ and *o*-carborane. Hydrogen bonds shown in red.⁶³*

They also investigated how a similar ligand, CTG (cyclotriguaiacylene) derivative tris(4-pyridylmethylamino)cyclotriguaiacylene (Figure 1.12). When cage formation was attempted with Cd(OAc)₂ as the metal ion and in the presence of the *o*-carborane as a guest molecule, these sub-units formed a 1:1:1 complex as an overall 2-D coordination polymer. However, when this system was prepared without the presence of *o*-carborane, a different product was created that was postulated to be a cryptophane-like complex where the two CTV-like subunits are connected by dimers of the cadmium

complex, creating what the authors refer to as paddlewheel-linked CTV-capsule.⁶⁵ The evidence for this complex is weak, but the investigation in general did provide interesting insight on how the presence of a guest can direct the formation of discrete entities or coordination polymers. When this same ligand was complexed with Ag(I) salts, it formed a tetrahedral M_4L_4 coordination cage. When glutaronitrile was introduced to the reaction mixture as a potential guest, discrete tetrahedral cages were no longer produced and instead a 2-D coordination polymer was produced. The rationalisation for this observation was that when this large guest occupied the cavity of the CTV-like subunit, it became sterically incompatible with the formation of a tetrahedral cage.⁶⁵ These findings show the versatility of CTV-like ligands and demonstrate that intercavity guest binding motifs also occur in crystalline assemblies.

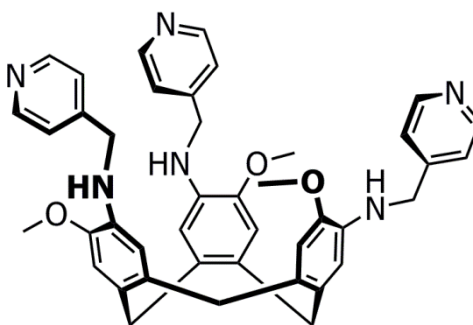


Figure 1.12 CTG derivative tris(4-pyridylmethylamino)cyclotriguaiacylene

Hardie and co-workers modified CTG (Figure 1.7), a chiral analogue of CTV by appending 4-(3-pyridyl)phenylester, shown in Figure 1.13.⁶⁶ This ligand forms a 2-D hydrogen bonded network, with the CTG derivatives in a head-to-head arrangement, forming capsules around pairs of $CHCl_3$ molecules. When Ag(I) salts are reacted with the ligand, a 2-D coordination polymer with metallo-capsules is formed.⁶⁶

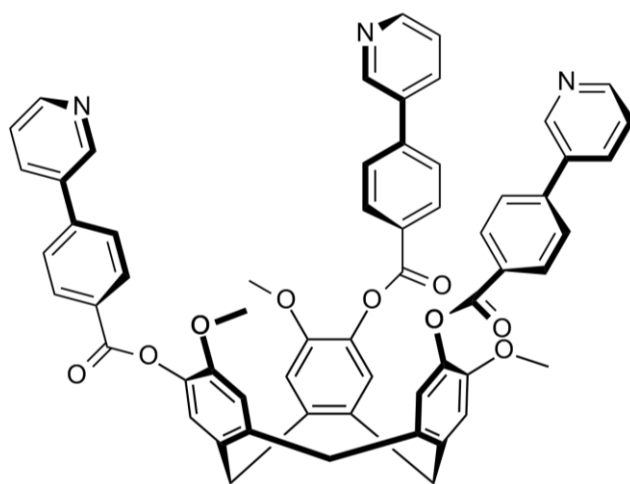


Figure 1.13 CTG derivative tris[4-(3-pyridyl)phenylester]cyclotriguaiacylene.⁶⁶

When CTG is modified on the upper rim with large pyridine-containing groups such as 2,2',6',2''-terpyridyl, dimeric “hand-shake” motifs can be formed where one arm of each ligand becomes the guest in the other ligand (Figure 1.14). With this particular ligand, it was also possible to complex three Cu(II) ions to each ligand, as the copper ions were able to complex with the terpyridyl groups of the ligands.⁶⁷

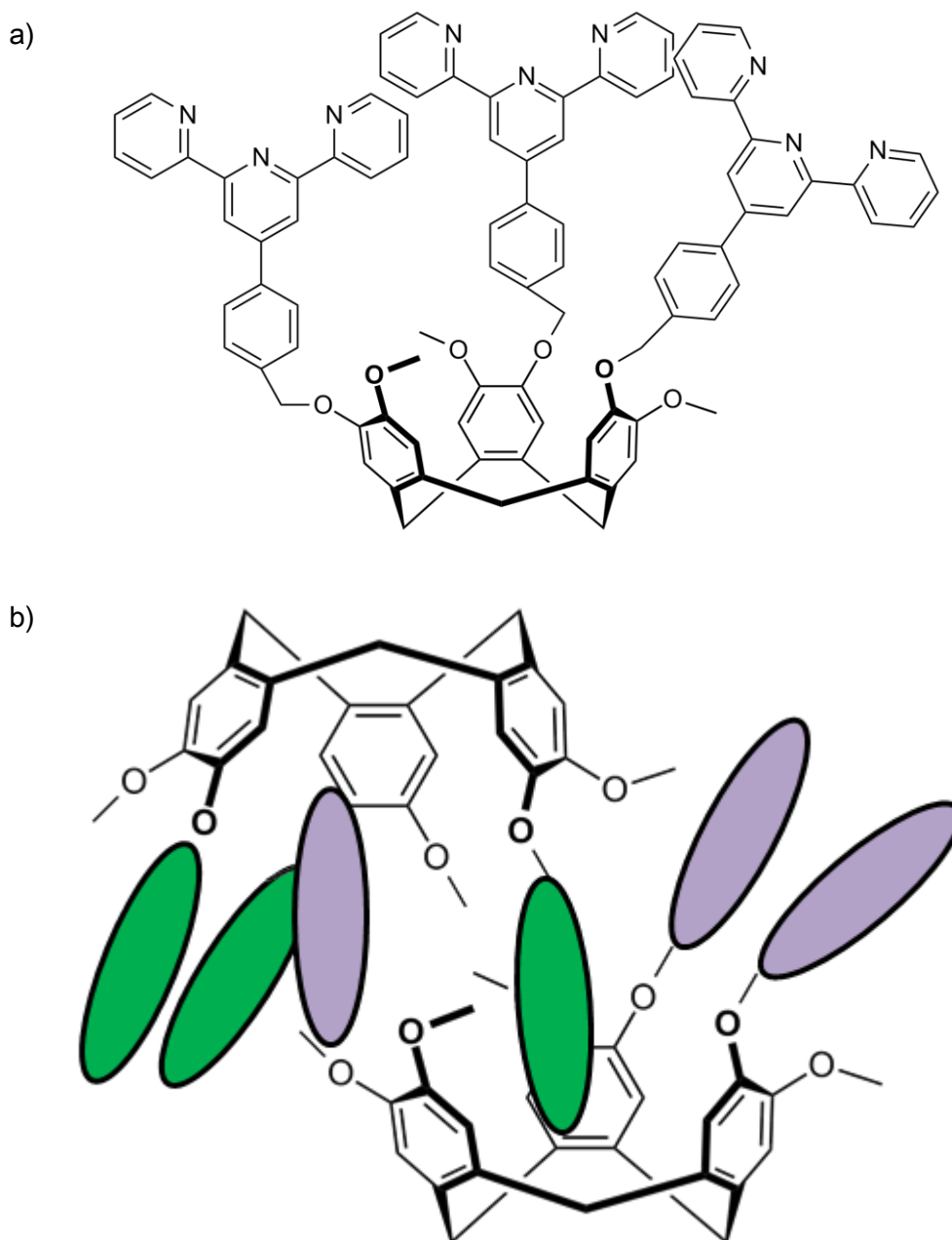


Figure 1.14 a) CTV-derivative tris(4-[2,2',6',2''-terpyridyl]-benzyl)cyclotriguiacylene and b) schematic illustrating the dimeric handshake motif, with coloured ovals to represent the upper rim modified groups.⁶⁷

When more than one pyridyl group per arm is incorporated into a CTV-like ligand, the ability to complex metals with geometries different from *cis*-capped square planar complexes becomes available. Hardie and colleagues took advantage of this to design a 3-D triply interlocked chiral [2]catenane. The ligand concerned was appended with 4-[4'-methyl-2,2'-bipyridyl] functional groups that formed octahedral complexes with

either Zn(II) or Co(II). Each metal ion was complexed to one arm of each CTV-like subunit, which has two coordinating pyridines. The individual cryptophane units contain both enantiomers of the ligand. When the [2]catenane is formed, all of the metal centres have the same chirality, causing the [2]catenane to be chiral.⁶⁸

Zheng and co-workers have used CTV modified on the upper rim in a trimeric fashion with carboxy-phenyl and copper complexes to create a metal-organic framework that they call a nanotube. They claim that this is the first example of a CTV-based metal-organic framework (MOF) with permanent porosity.⁶⁹

Henkelis and Hardie have investigated a range of modified CTV congeners based upon tris-(isonicotinoyl)cyclotriguaiacylene (Figure 1.15), in two different sets where the ligands were identical except for the length of the alkyl moiety attached to the CTV-core. **L1** has a methyl group and **L2** has a propyl group. They found that the propylated CTV ligands show different coordination chemistry to their methyl counterparts, due to their increased solubility. Their findings indicate that a slight change to the ligand structure can entirely change the way that it behaves.⁷⁰

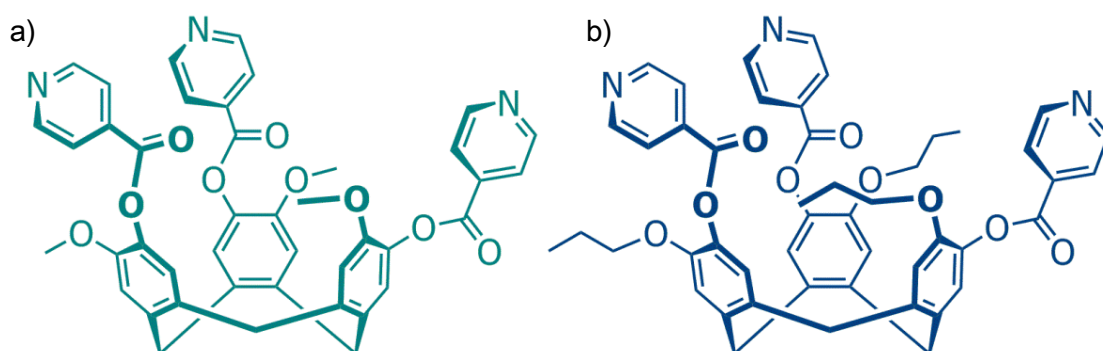


Figure 1.15 a) L1 tris(isonicotinoyl)cyclotriguaiacylene and b) L2 tris(isonicotinoyl)-tris(propyl)-cyclotriguaiacylene.

1.3.2 Cryptophanes

Two CTV molecules, joined together in a head-to-head-fashion by three bridges form what is termed a 'cryptophane' (Figure 1.16). These cryptophanes can exist in *anti* or *syn* forms. The *anti* form is chiral and the *syn* form is achiral.^{51, 56} *Anti* cryptophanes are formed when both CTV-derivatives in the cryptophane have the same chirality, that is *MM* or *PP*. *Syn* cryptophanes are formed if CTV-based derivatives of both chiralities are involved in the cryptophane formation, that is, *MP* or *PM*.^{52, 71}

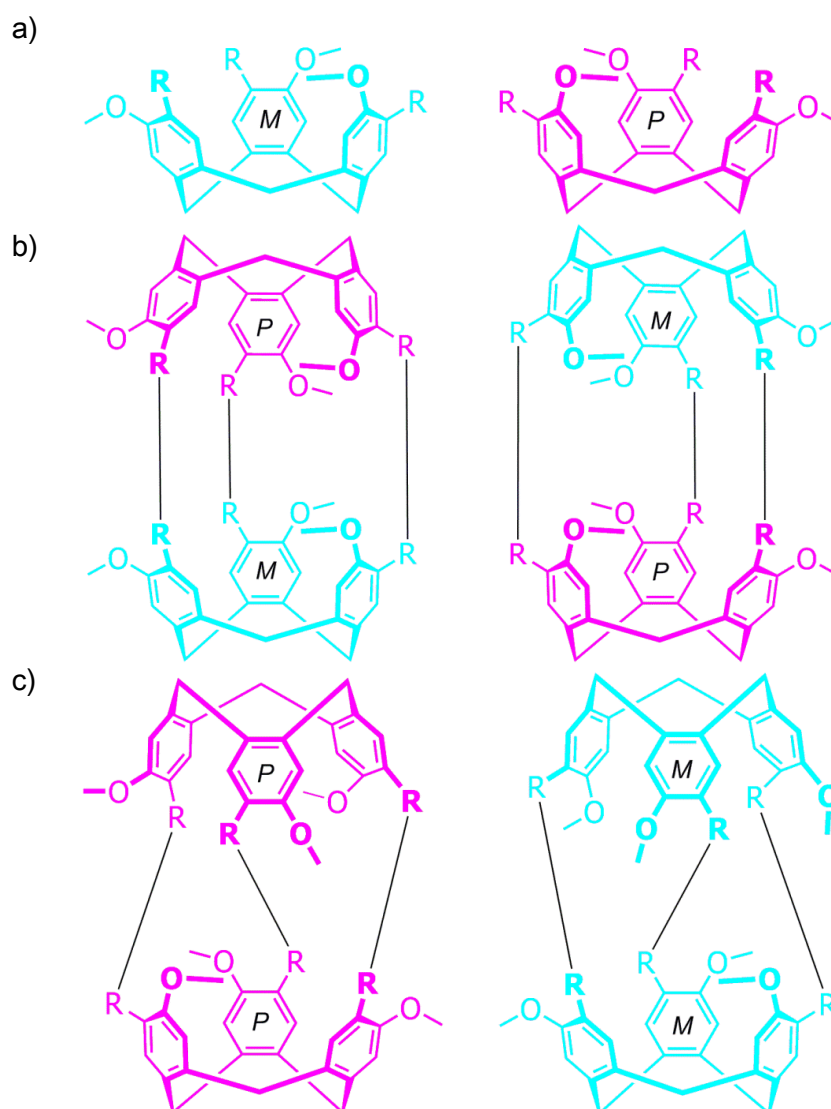


Figure 1.16 a) *M* and *P* CTV-type molecules, b) achiral *syn*-linked meso cryptophanes and c) chiral *anti*-linked cryptophane isomers.

Collet and co-workers were able to use ^1H NMR to provide evidence for cryptophane enantiomer determination when the cryptophanes were linked with alkyl chains. This was demonstrated by cryptophanes-E and -F. These sister cryptophanes have the same propyl linker. Cryptophane-E is the D_3 *anti*-linked isomer and displayed a broad singlet for the middle CH_2 protons of the propyl linker [Figure 1.17 a)]. This is because those CH_2 protons lie on a C_2 axis and the two hydrogens are homotopic. Cryptophane-F is the C_{3h} *syn*-linked isomer. The middle CH_2 protons in the *syn* isomer linker are diastereotopic and resonate as two separate signals [Figure 1.17 b)].⁷²

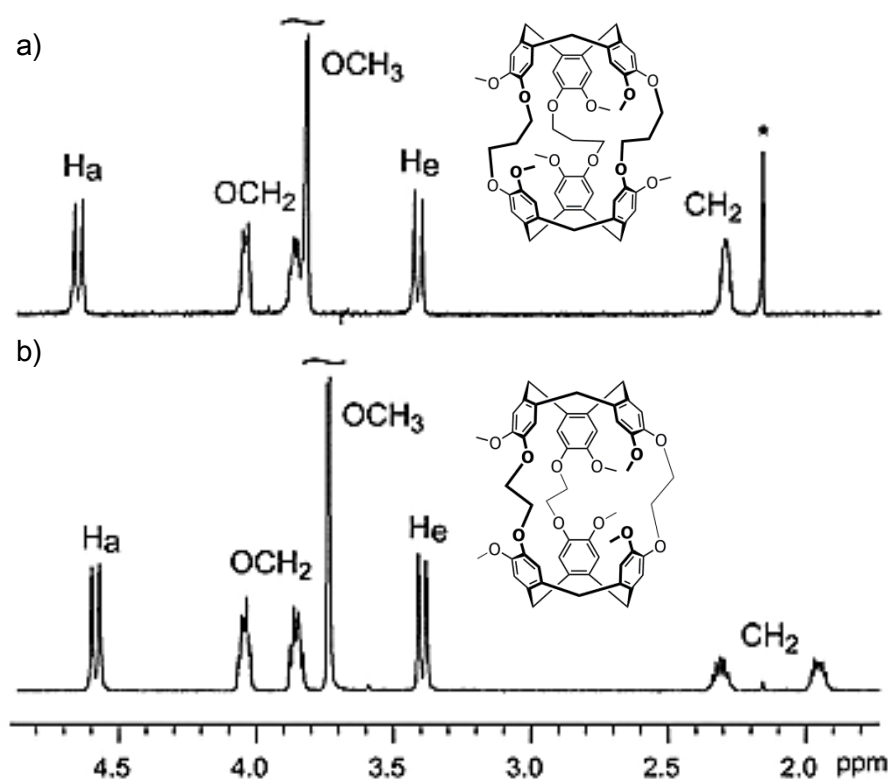


Figure 1.17 Part of the 500 MHz ^1H NMR spectra of cryptophane-E and cryptophane-F in CDCl_3 showing the differences between *anti* and *syn* isomers. a) is *anti* isomer (cryptophane-E) and b) is *syn* isomer (cryptophane-F).⁷² Reproduced in part from Ref 72 with permission of The Royal Society of Chemistry.

Cryptophanes have three windows that allow the inclusion of guest molecules. The size of the cryptophane cavity can be controlled by using linkers of differing size and

structure.⁵⁶ When cryptophanes were first synthesised, a system of nomenclature was devised by Collet and co-workers, based upon the chronology of their description. The first member of the cryptophane series had *anti* stereochemistry, and was thus called cryptophane-A and its corresponding *syn* isomer was termed cryptophane-B. This was followed by pairs C/D and so forth.⁵⁵ The study of cryptophanes, along with CTV, is a very active area of research with many reviews on the subject.^{47, 51, 55, 73}

Roesky *et al.* designed a new cryptophane which features three *endo*-carboxylic acid moieties on the linker groups (Figure 1.18). Although this type of functionality means that the cavity is very small compared to the traditional cryptophanes at only 28 Å³, (for example, cryptophane-A has a cavity of 81.5 Å³,⁷⁴) they were able to show complexation with small alcohols and the liquid-liquid extraction of different metal ions including sodium, caesium, magnesium, calcium, strontium, barium, europium and yttrium. The cavity of their cryptophane has a pre-organised coordination pattern with a nearly octahedral geometry which facilitates the complexation of these metal ions. They also noted that when the metals are complexed, the size of the cryptophane increases slightly.⁷⁵

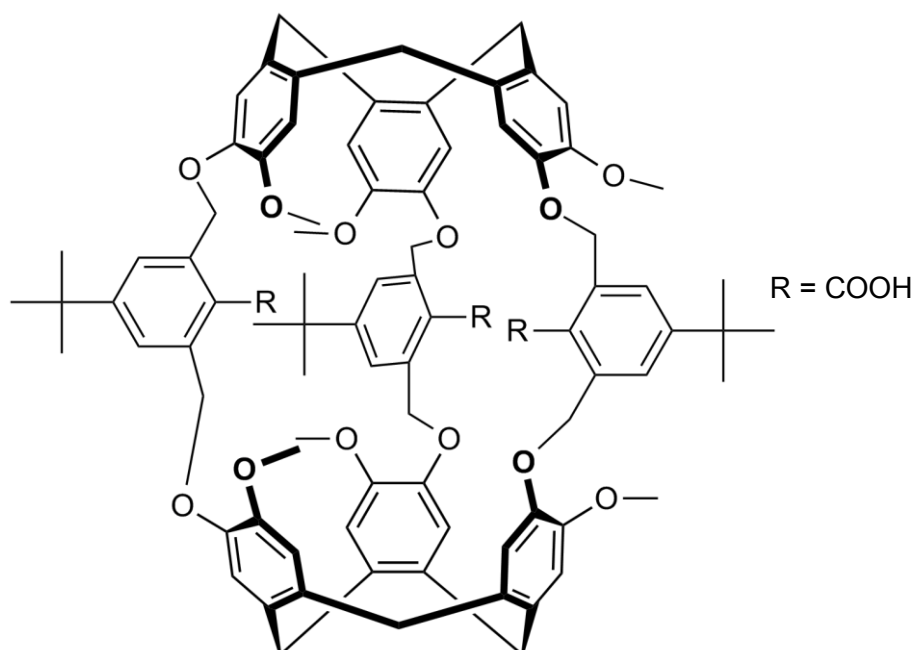


Figure 1.18 Endo-carboxylic acid functionalised cryptophane.⁷⁵

Cryptophane-E (Figure 1.19) has demonstrated strong binding of neutral molecules in lipophilic solvents, complexing chloroform with a binding constant of 470 M^{-1} at 300 K. Exchange processes for cryptophane-E are slow on the NMR timescale when compared to other cryptophane systems, for example, cryptophane-C.⁵⁵ Exchange rates are directly correlated with the size of the interior cavity of the cryptophane. As cryptophane-E has a larger cavity, it prefers a larger guest, (75 \AA^3 compared with 60 \AA^3 for the smaller cryptophane-C).^{32, 55, 76}

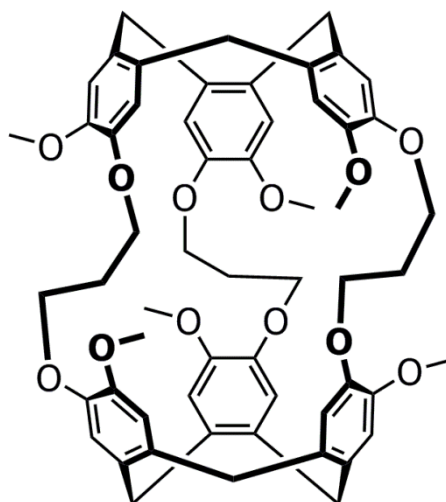


Figure 1.19 Cryptophane-E.⁵³

Recent studies by Bandmann and co-workers have challenged the scientific consensus on the binding abilities of cryptophane-E. When the cryptophanes were first studied, it was assumed that 1,1,2,2-tetrachloroethane was too large to fit within the cryptophane cavity and it was used as a non-competing solvent. Bandmann and co-workers have shown that this is not the case and previous binding constants have been underestimated by up to two orders of magnitude. They have also challenged the notion that if a solvent that is larger than the host cavity is used; the cavity will consequently be empty. They used quantum calculations and NMR VT (variable temperature) experiments to show that a cryptophane with an empty cavity is highly unstable and will either encapsulate a guest or turn into the more stable imploded cryptophane where it has a C_1 *out-saddle* conformation. This conformation fills the void space and is more energetically favourable than the empty void space.⁷⁷

Collet and colleagues modified cryptophane-E so that the methoxy groups were replaced with thiomethyl moieties to further study the host-guest binding behaviours of cryptophane-E with small neutral and cationic guests. The new cryptophane has a similar sized cavity to the original, but the SMe moieties are larger than the OMe

moieties, leading to greater obstruction of the cryptophane windows. It was found that the lifetime of the complexes dramatically increased, whereas the association constants and rate constants dramatically decreased and the barriers for association and dissociation increased by ~ 20 kJ/mol.⁷² Hardie and colleagues have also studied a cryptophane which has sulfur in its structure (Figure 1.20). In this case, the disulfide bonds were the linkers between the two CTV derivatives. This still provided a small cavity, which they estimated to be approximately 40 \AA^3 . This small cryptophane was found to bind reversibly with methane, which at 28 \AA^3 , was a good fit for the cavity space in accordance with the 55% rule.³² They were also able to conduct binding studies with small gas molecules, including nitrogen and hydrogen.⁷⁸

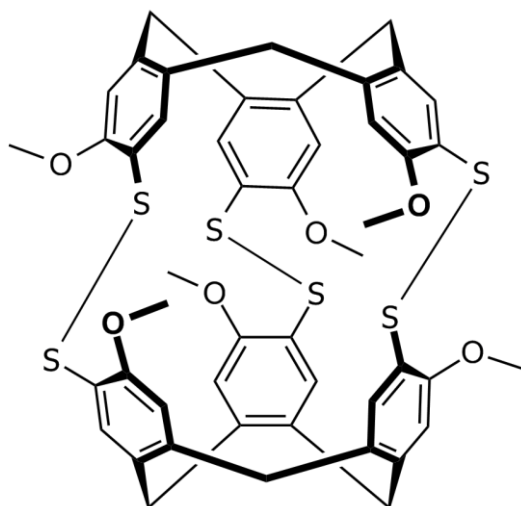
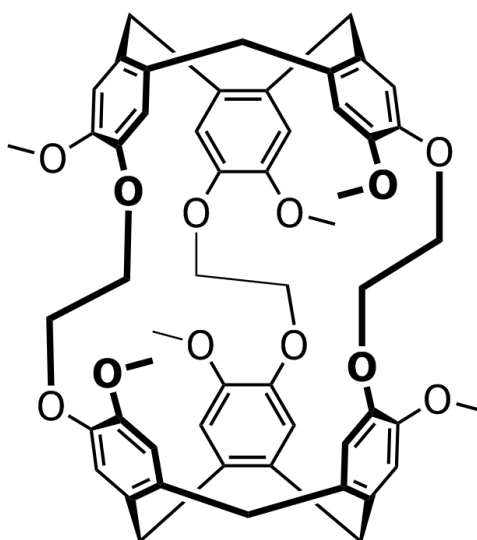


Figure 1.20 Disulfide-linked cryptophane.⁷⁸

Dmochowski and co-workers studied cryptophane-A (Figure 1.21) its triproparyl and triallyl derivatives and their host-guest properties. They found that the cavity volume increased by as much as 20% as the guest volume increased from methanol to chloroform, and that the packing coefficients varied from 0.39 – 0.73. In accordance with the 55% rule, methanol with a volume of 33 \AA^3 under fills the cavity with a packing coefficient of 0.39. Consequently, they postulated that it is energetically unfavourable

for the cavity to shrink any smaller than the 84 \AA^3 , as is seen when methanol is encapsulated within cryptophane-A. Chloroform, which is more than twice the size of methanol at 72 \AA^3 , stretches the cavity to 102 \AA^3 , with a packing coefficient of 0.71, (just outside of the 55% rule). This is quite a difference in size depending on the guest encapsulated. Modelling studies indicate that cryptophane-A can expand horizontally and vertically to accommodate chloroform as a guest.⁷⁹



*Figure 1.21 Cryptophane-A.*⁵³

Pines and co-workers modified a cryptophane-A cage to become an NMR biosensor (Figure 1.22). This was achieved by tethering a biotin ligand to cryptophane-A *via* a linker molecule on one of the CTV units of the cryptophane. They used this to functionalise xenon, which was possible due to a physical coupling between the encapsulated xenon and avidin (protein that binds to the biotin ligand).^{80, 81} Xenon (at 42 \AA^3) has a packing coefficient of 0.47 in a cavity that is 89 \AA^3 . This is consistent with the 55% rule, where the ideal packing coefficient is described as 0.55 ± 0.09 . This indicated that a favourable balance between the enthalpic and entropic forces had been found and explained the high affinity that is seen for xenon in cryptophane-A. This

functionalisation creates an NMR-based biosensor that can sensitively report on its local environment by means of its chemical shift and relaxation parameters.^{32, 79}

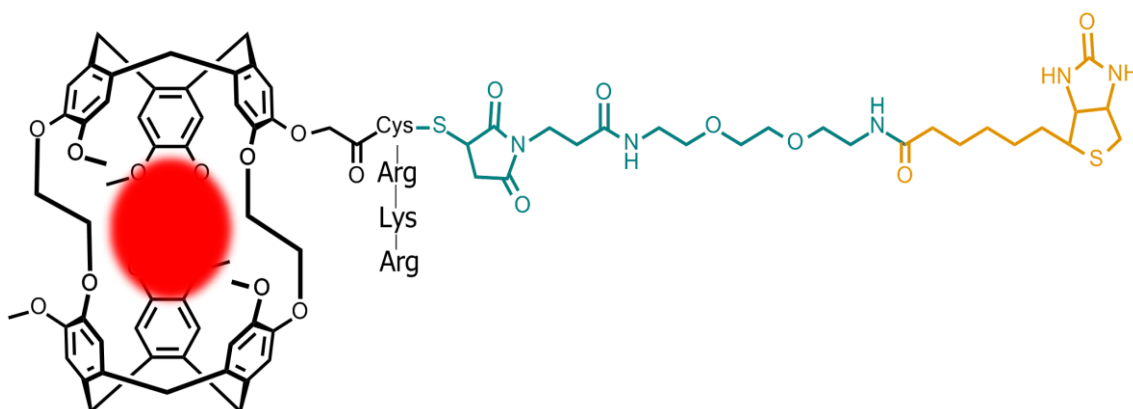


Figure 1.22 Cryptophane-A biosensor. Cryptophane-A is shown in black, xenon in red, avidin in green and biotin in orange.^{80, 81}

Atwood and co-workers developed aryl extended CTV derivatives and aryl-bridged cryptophanes. The CTV derivatives were able to bind the anions $[\text{BF}_4]^-$ and $[\text{PF}_6]^-$, showing a selectivity for the $[\text{BF}_4]^-$ anion. The cryptophanes were prepared in an unusual manner: photochemical de-metalation of the metalated CTV derivatives (Figure 1.23), followed by ‘capping’ the de-metaleed CTV derivative with CTG. They found no evidence for complexation between their cryptophanes and small guests in solution; however, they did find evidence of inclusion complexes being formed in the solid state. Using X-ray crystallography they were able to take “snapshots” of the molecular gating process, providing insights to guest-gating conformational processes of the methoxy arm of the tribenzylene core that are pivotal in allowing guests into the cryptophane cavity. They found that the size of the guest was of the utmost importance. For example, when they used chloroform as a guest, they found that one molecule of chloroform was entirely within the cavity, but that another was perched in one of the portals to allow the space to be fully utilised. This was termed the “open gate” structure. They were able to find an appropriately sized guest for the void and

found that this led to a “closed gate” structure, wherein all of the methoxy arms lie in the plane of their arene rings, meaning that the portals are effectively closed. They also discovered that the cryptophane can take up a conformation where it fills the majority of the internal void space in the absence of a guest. This may explain why inclusion complexes in solution were not revealed.⁸²

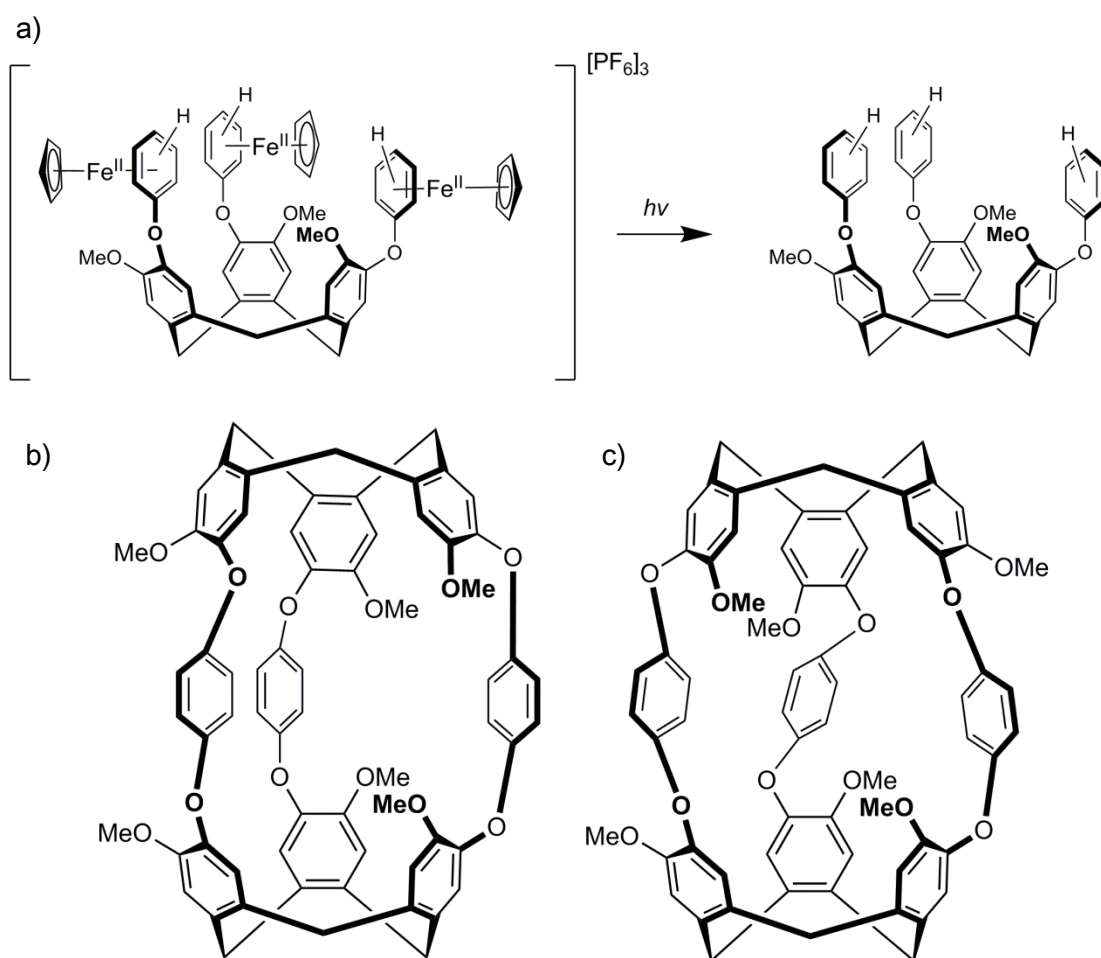


Figure 1.23 a) Photochemical de-metalation of Atwood's aryl extended metalated CTV derivatives, b) syn and c) anti aryl-bridged cryptophanes.⁸²

1.3.3 Metallo-Cryptophanes

The first example of a metallo-cryptophane was reported when Yamaguchi and co-workers developed various novel square-planar palladium(II) mediated cryptophanes

using a CTV derivative functionalised on the upper rim with a pyridyl group ($R_1 = \text{OMe}$, $R_2 = \text{Pyridyl}$). This resulted in a racemic mix of *anti*-chiral and *syn-meso* cryptophane isomers. They found that the *meso* isomer (Figure 1.24) was more stable than either the *M* or *P* isomers, and postulated that this was because the *meso* isomer had a smaller N-Pd-N bond angle, resulting in less steric crowding. They also found that if the *anti* isomers of the CTV derivative were optically resolved, they would only self-assemble into the chiral cryptophane.⁷¹

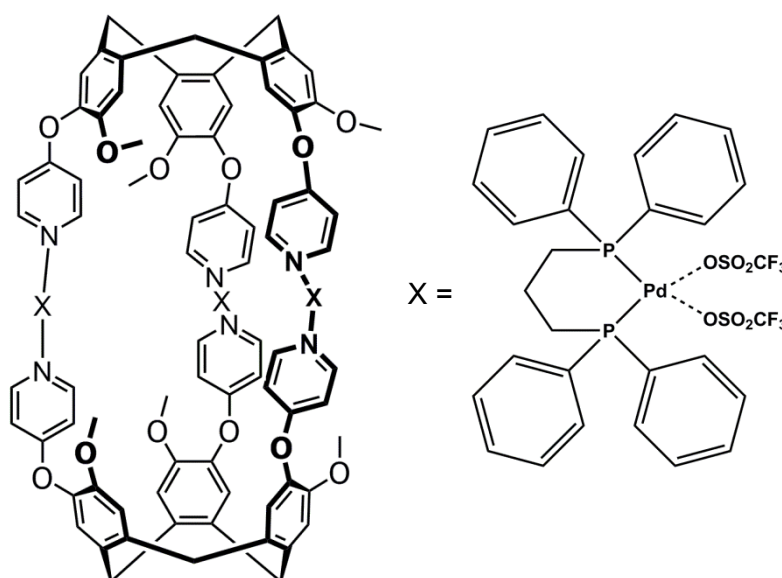


Figure 1.24 Yamaguchi and co-workers metallo-cryptophane, *meso* isomer.⁷¹

Espinosa and co-workers also created metallo-cryptophanes, using CTV analogues appended on the upper rim with nitrile groups (Figure 1.25). As the CTV derivatives were used as racemates, they expected a mix of *syn* and *anti* form cryptophanes. They found that the cryptophanes self-assembled stereoselectively and that only the *anti* form was observed. However, when the cryptophane was prepared in dichloromethane, broad signals were observed in its ^1H NMR spectrum at room temperature. This was further investigated by low temperature VT experiments. As the temperature was lowered, the signals from the *anti* cryptophane diminished and a new

set of signals attributed to the *syn* cryptophane were observed. They were able to assign the cryptophane conformers in the same way as cryptophanes-E and -F were assigned (section 1.3.2), as the propyl linker of the *cis*-protected palladium(II) salt experiences the same symmetry conditions, D_3 for the anti cryptophane and C_{3h} for the *syn* isomer.⁸³

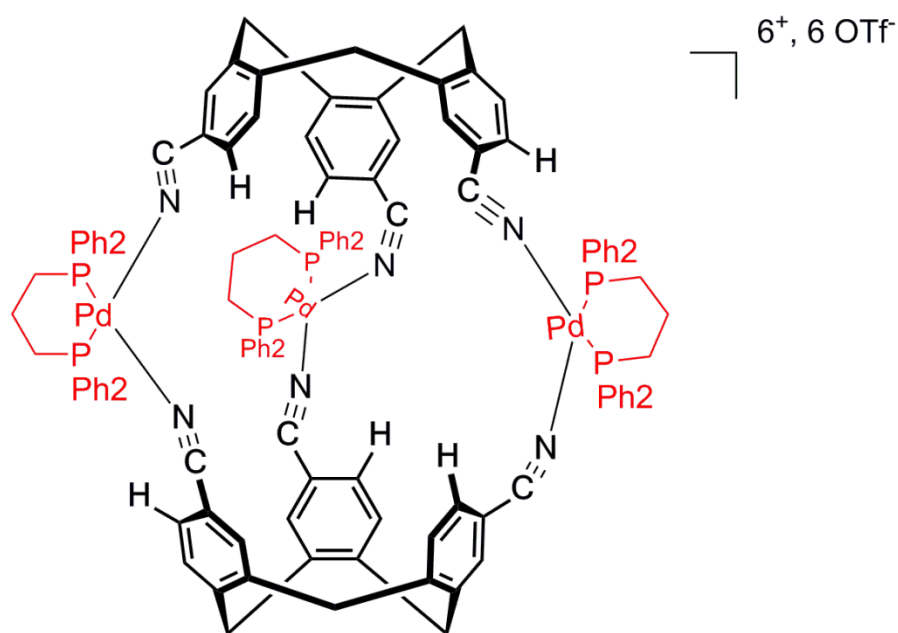


Figure 1.25 Espinosa's metallo-cryptophane, anti isomer.⁸³

Hardie and co-workers have produced a range of geometrically interesting CTV-based products including a bow-tie motif metallo-cryptophane produced from a carboxylic acid functionalised CTV unit. A novel approach was taken to functionalisation. There were three linker groups, where $R_1 \neq R_2$. Each linker group was attached to the R_2 of one of the crown benzene groups and also to the R_1 of the adjacent crown benzene, as shown in Figure 1.26. These modified cyclotricatechylene units were then formed into copper- or cobalt-based metallo-cryptophanes with a characteristic bow-tie configuration. This configuration has two small cavity spaces and not one large space, as seen in other cryptophanes.

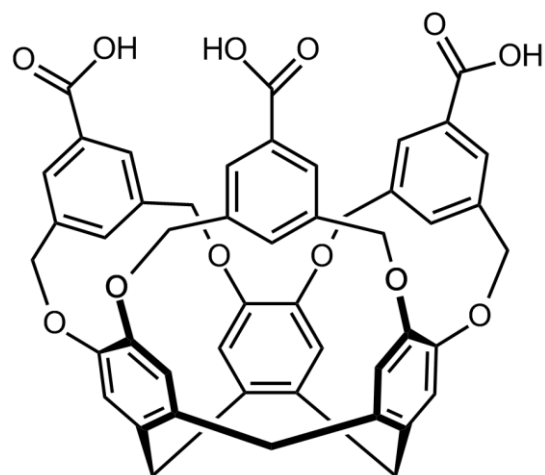


Figure 1.26 Carboxylic acid functionalised CTV.⁸⁴

These bow-tie cryptophanes (Figure 1.27) were also linked together by a bridging ligand, forming a dimer.⁸⁴ Hardie and co-workers have also produced an M_2L_2 type cryptophane from an upper-rim extended CTV unit, with functional groups appended in a trimeric fashion, where $R_1 = \text{OMe}$ and $R_2 =$ a pyridylmethylamino group. To form a cryptophane, each silver ion is coordinated to a terminal acetonitrile group and 3 pyridyl groups. This is highly unusual, as most cryptophanes are linked by three bridges, however, the silver ions still satisfy the requirement for maximum site occupancy.²⁵

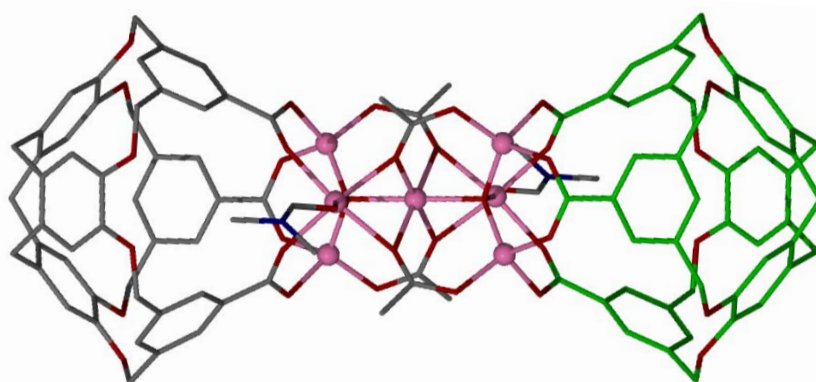


Figure 1.27 Taken from the crystal structure of Hardie's bow-tie cryptophane. One carboxylic acid functionalised CTV in grey and one in green for clarity.⁸⁴

If the pyridyl group of the CTV unit is changed from a 3-pyridyl to a 4-pyridyl then a remarkable change in product is observed. Instead of the cryptophane-like capsule, a tetrahedral M_4L_4 nanocage is formed, where the metal ions sit on the vertices of the tetrahedron and the ligands occupy the tetrahedron faces. Due to the convex shape of the CTV unit, the nanocages have a spiked-aspect. Again, this is an unusual arrangement, as tetrahedral nanocages typically take the form M_4L_6 , where the ligands occupy the edges of the tetrahedron.⁸⁵ The Hardie group have produced another M_4L_4 type structure with a different upper-rim functionalised CTV-unit. The CTV-unit was modified in a trimeric style, this time with (3-pyridyl)phenylester. Instead of forming a tetrahedron, this ligand, when combined with palladium(II) nitrate self-assembles into what they referred to as a “topologically complicated Solomon’s cube” (Figure 1.28). To fulfil the maximum site occupancy requirement, each palladium ion is coordinated to three of the four CTV-units and its remaining site is occupied with a nitrate group. What is remarkable about this complex is the way that the ligands are interlocked with each other; two of the ligands linked together form a figure of eight-like band. Even more remarkably, in the solid state, six of these Solomon’s cubes aggregate to form a much larger polyhedral assembly with an octahedral arrangement and a diameter that is larger than 4 nm.⁸⁶

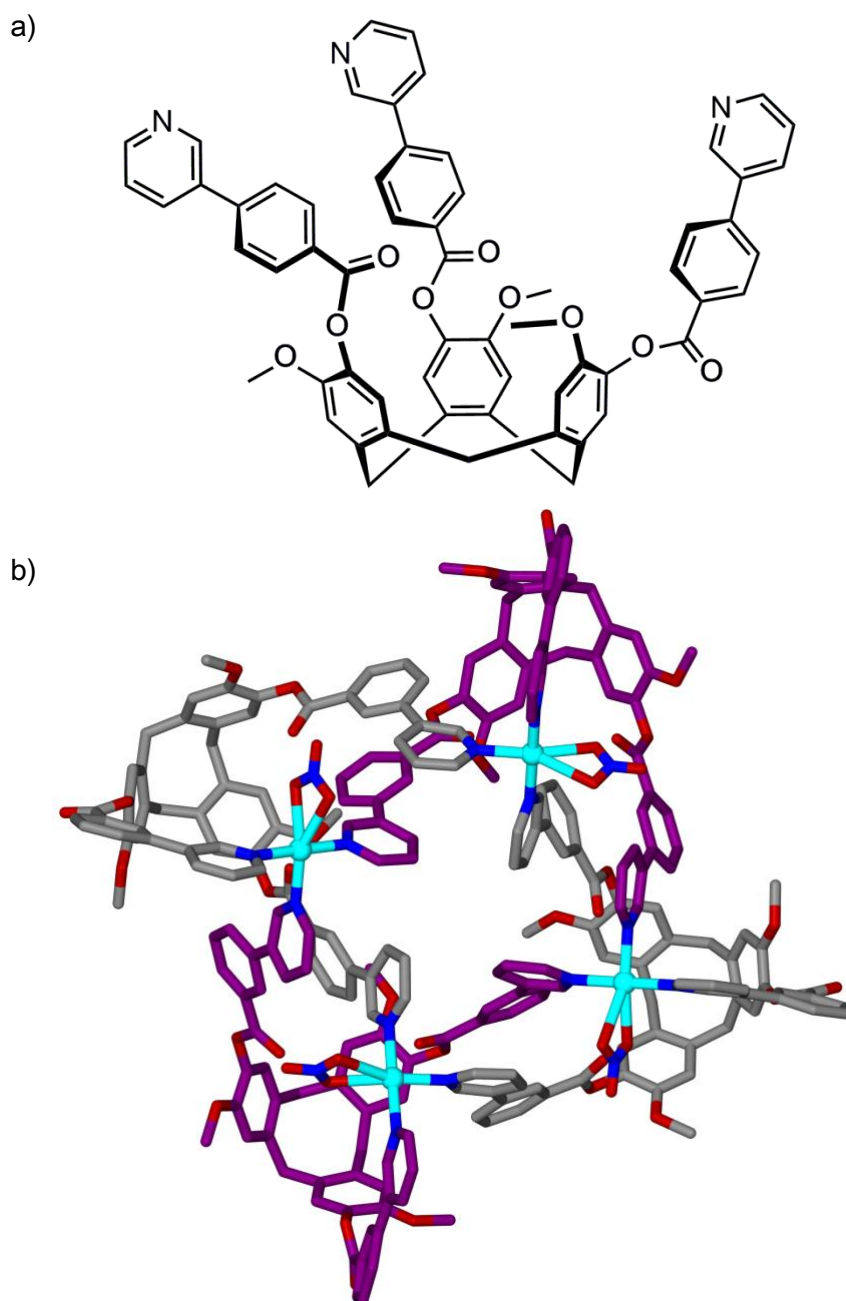


Figure 1.28 a) tris(3-(3-pyridyl)phenylester)cyclotrignaiacylene ligand and b) taken from the crystal structure of Hardie's "Solomon's Cube". The loops of the complex are colour-coded to show the interlocking components.⁸⁶

Continuing their work on [2]catenanes, Hardie and co-workers have also developed two additional M_3L_2 metallo-cryptophanes in addition to those discussed in section 1.3.1. The CTV cores were derivatised in a trimeric fashion with pyridyl and pyrimidine functionalities, both with the N-donor in the 3-position. The pyridyl derivative forms a triply interlocked [2]catenane (Figure 1.29), this time with silver as the coordinating

metal. Both the [2]catenane and the metallo-cryptophane described are *anti* isomers, being formed from the same enantiomer, which contrasts with the previously reported catenane. In these compounds the coordinating metal acts as a linear linker, which means that only the *anti* isomer can be formed because of steric considerations.⁸⁷

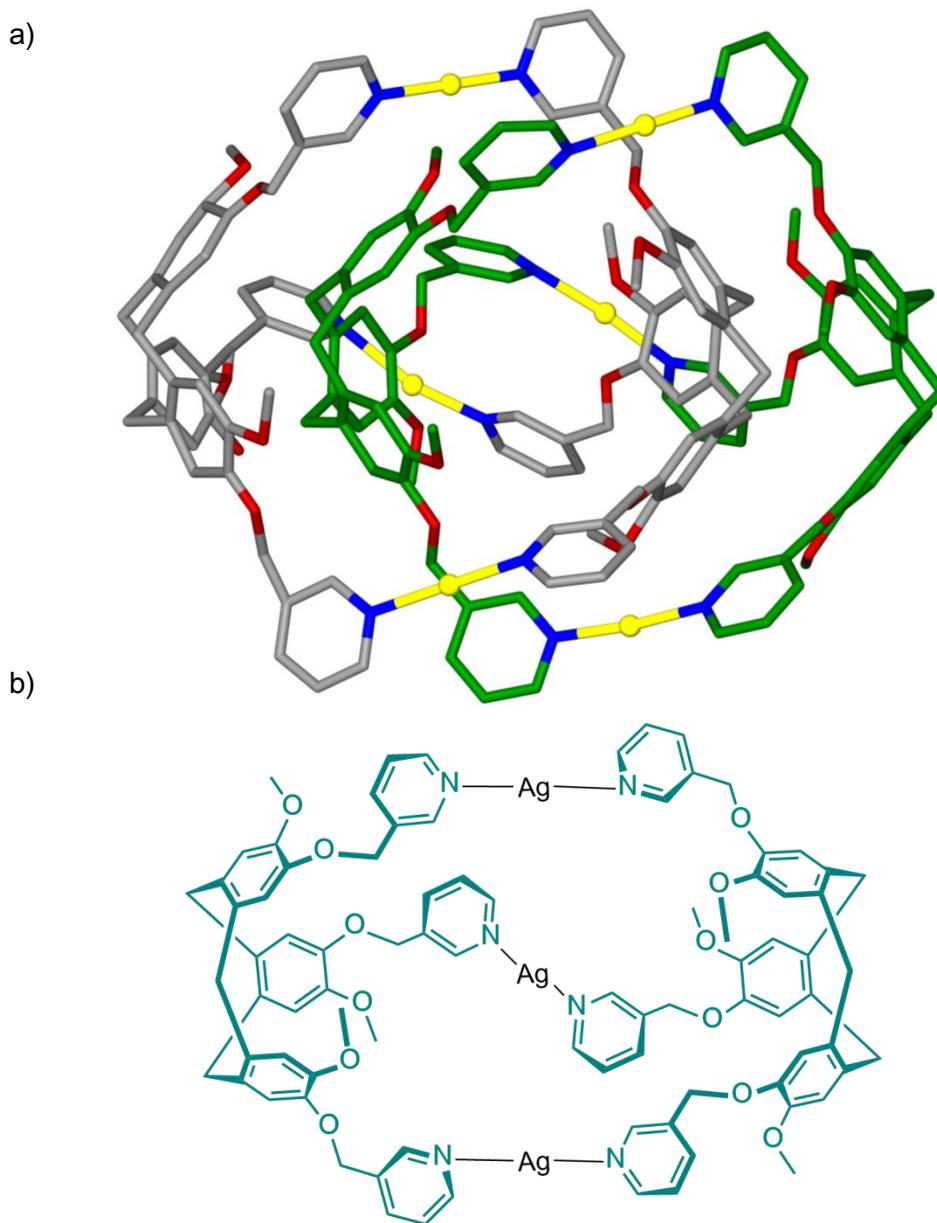


Figure 1.29 a) taken from the crystal structure of Hardie's triply interlocked [2]catenane. Chemically independent components distinguished by colour and b) schematic of one individual cryptophane.⁸⁷

Hardie and co-workers have also produced M_3L_2 cryptophanes using *cis*-protected palladium(II) salts. When they utilised tris(isonicotinoyl)-tris(propyl)-cyclotricatechylene

(L2) and (ethylenediamine)palladium(II) dinitrate, initially a M_3L_2 metallo-cryptophane was formed. However, after a period of two weeks, the product had rearranged into an M_6L_8 stella octangula cage assembly. This was also found to be the case when (2,2'-bipyridine)dichloropalladium(II) and (ethylenediamine)platinum(II) dinitrate were used. It is postulated that these rearrangements are entropically driven because the stella octangula system has higher symmetry than the cryptophane. If bis-*N*-heterocyclic carbene ligands are used, this problem is overcome. When metallo-cryptophanes are formed from the carbene protected palladium and the CTV derivative L2, a large internal cavity of 697 Å³ is formed. A similar sized complex is formed when the ligand tris(isonicotinoyl)cyclotriguaiacylene (L1) is used and this metallo-cryptophane has been shown to encapsulate three molecules of iodine. Once encapsulated, the I₂ is not easily extracted from the metallo-cryptophane, demonstrating the potential use as a sequestering agent.⁸⁸

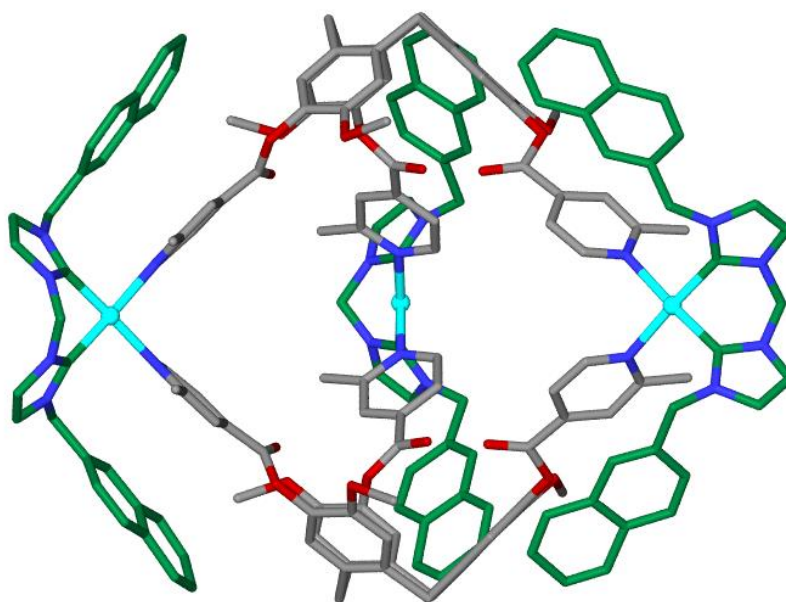


Figure 1.30 Taken from the crystal structure of Hardie's bis-N-heterocyclic carbene cryptophane. CTV-derivatives in grey and bis-N-heterocyclic carbene in green.⁸⁸

1.4 Metallo-Nanocages

1.4.1 Molecular Squares

In 1990 the Fujita group prepared the first well-defined square complex (Figure 1.31) by self-assembly. When square-planar *cis*-protected (ethylenediamine)palladium(II) dinitrate was mixed with the linear bidentate ligand 4,4'-bipyridine in a 1:1 ratio, they found that the molecular square was formed with a 91% yield. The ¹H NMR spectrum of the complex indicated that all the pyridine nuclei were equivalent. Due to the bond angles between the nitrogens of the pyridine groups and the palladium being at 90°, they concluded that no other complex could form, as this would incur tremendous ring strain. They noted that the complex was formed under thermodynamic control. CPK (Corey-Pauling-Koltun) modelling revealed that the molecular square had a cavity of 7.8 x 7.8 x 6.5 Å and that it was capable of binding 1,3,5-trimethoxybenzene in aqueous solution. The structure was later confirmed with X-ray crystallography.⁸⁹⁻⁹¹ The molecular square is a very elegant and simple design, demonstrating the ease with which self-assembly can be used to form host molecules. However, the cavity of the molecular square is very open with no means to encapsulate guest molecules for long periods of time.

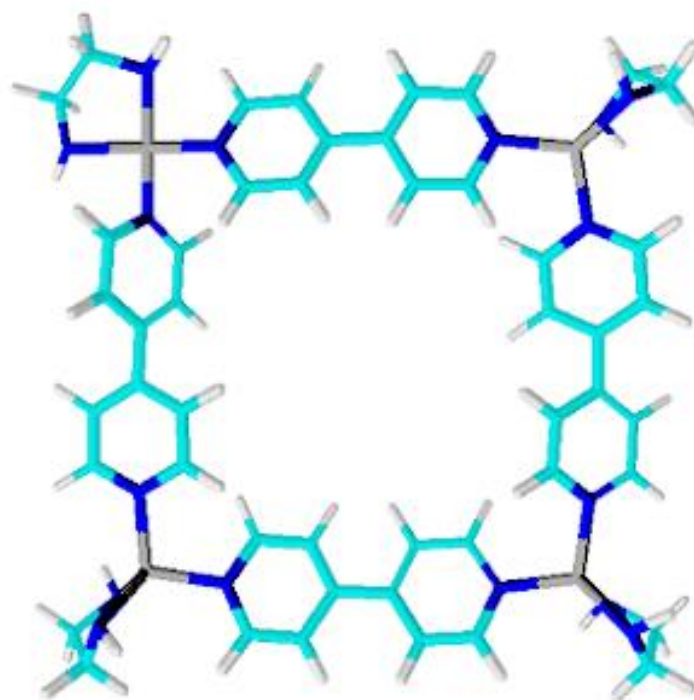


Figure 1.31 Fujita's Molecular square.⁹⁰

1.4.2 Tetrahedral M_4L_6 and M_4L_4 Metallo-Nanocages

Nitschke and co-workers constructed a tetrahedral M_4L_6 anionic cage from the self-assembly of 4,4'-diaminobiphenyl-2,2'-disulphonic acid, 2-formylpyridine and iron(II) with a cavity size of 141 \AA^3 (Figure 1.32). The iron(II) ions rest on the vertices and the ligands lie on the edges of the tetrahedral construct. This complex displayed tetrahedral symmetry in its ^1H NMR spectrum, where only one set of ligand resonances was detected. This cage was shown to selectively and tightly bind hydrophobic guest molecules in aqueous solutions. When cyclohexane was used as the guest molecule, a large upfield shift was noted in the NMR spectrum compared to the free guest in solution. Encapsulation of the guest also caused a shift of the cage resonances. A 1:1 host-guest complexation was observed, with cyclohexane having a packing coefficient of 0.61, indicating compliance with the 55% rule.³² Cyclopentane was also used as a guest, again resulting in a 1:1 host-guest ratio with a packing coefficient of 0.51. In a

competition experiment between these two guests, no selectivity was observed, which was attributed to the guests both being a good fit for the cavity size in accordance with the 55% rule.³² To form the host-guest complexes, the guest compounds were added at the time of cage formation. The high affinity seen for these guests was attributed to the portals of the cage being relatively small. The largest sphere that would be able to pass through in van der Waals contact would have a diameter of 2.04 Å, whereas the approximate van der Waals diameter of cyclohexane is 6 Å. This meant that the guest was effectively trapped. Consequently, two methods were developed to release the guests. One method involved reacting the host-guest system with tris(2-ethylamino)amine, which irreversibly unlocked the cage and released the guest. The other method entailed altering the pH of the solution, which enabled a reversible unlocking of the cage, where the cages could be reformed and re-used. This cage has also been used to sequester white phosphorus, a notoriously difficult and dangerous compound to handle due to its air-sensitive nature. When the cage was left in contact with solid white phosphorus, the phosphorus became encapsulated within the cage, clearly indicated by ¹H and ³¹P NMR and by X-ray crystallography. When the phosphorus was encapsulated within the cage, it became water-soluble and air-stable and these conditions could be maintained for at least four months. As previously noted, the portals of this cage system are small, and the X-ray crystallography data of the inclusion complex revealed a portal radius of 1.0 Å. Although this is marginally smaller than the radius of an oxygen molecule, it was expected that fluctuations in the portal size would allow oxygen into the cavity space. However, because the space in the cavity is so restricted, no reaction between the O₂ and P₄ can take place as the space is not sufficient to hold any reaction products. The removal of the phosphorus from the cage appears to be a relatively simple procedure. This was achieved by adding an

equal volume of benzene to the aqueous solution, where the benzene replaces the phosphorus as the encapsulated guest. Once extracted from the cage environment, the phosphorus regained its sensitivity to air and formed phosphoric acid in the aqueous phase of the reaction solution.^{16, 18, 92, 93}

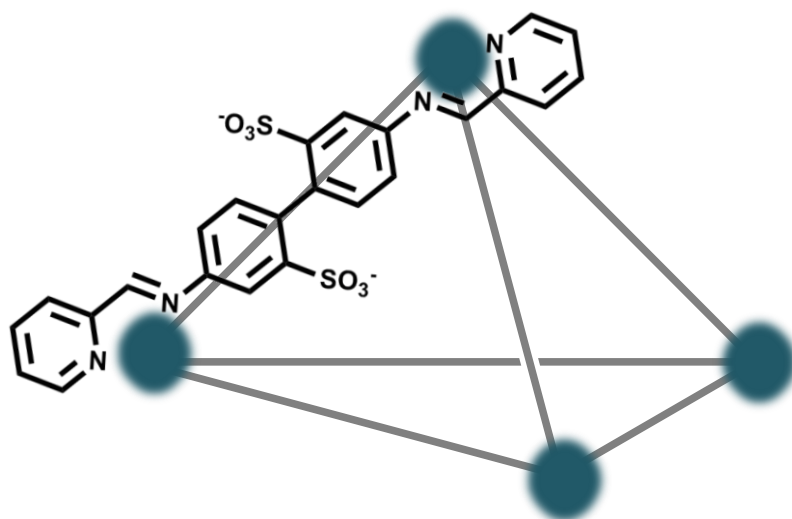


Figure 1.32 Schematic of the Nitschke group M_4L_6 metallo-nanocage. The grey lines represent the ligands and the blue spheres represent the Fe(II) ions.¹⁸

This cage from the Nitschke group is also capable of binding sulfur hexafluoride, a potent greenhouse gas. Sulfur hexafluoride is particularly difficult to sequester, due to its inert nature. When SF_6 is bubbled through an aqueous solution of the cage, it is encapsulated in a 1:1 host-guest ratio, as indicated by 1H and ^{19}F NMR. These spectra do not indicate complete encapsulation, with about 75% of the SF_6 being encapsulated. The host-guest complex was also unambiguously characterised by X-ray crystallography. The sulfur hexafluoride was found to have a packing coefficient of 0.53, which is larger than the reported optimal for a gas, which Rebek states is 0.40.⁹⁴ There is strong binding between SF_6 and the cage system, indicated by this high packing coefficient and its binding constant. As this cage is known not to bind to a variety of other gases including Xe, Ar, N_2 , O_2 , N_2O , methane and carbon dioxide, there is significant potential for this cage in the application of selectively binding sulfur hexafluoride from gaseous mixtures. The presence of the cage in aqueous solution

dramatically improves the solubility of SF₆ by 30 times and when encapsulated, it can be stored safely for at least a week. Three different methods were determined for releasing the guest: temperature induced guest desorption; addition of acid to open up the cage, releasing the guest; and the previously mentioned irreversible unlocking method.^{16, 93}

The Nitschke group have also developed a face-capped [Fe₄L₄]⁸⁺ tetrahedral cage constructed from a tridentate ligand with C₃ symmetry, 2-formylpyridine and iron(II) (Figure 1.33). These face-capped ligands have the ability to flex, causing the cage to adapt to different sized guests. This cage is soluble in both aqueous solution and acetonitrile and has a cavity size of 233 ± 2 Å³, which is larger than that of their M₄L₆ tetrahedral cages.

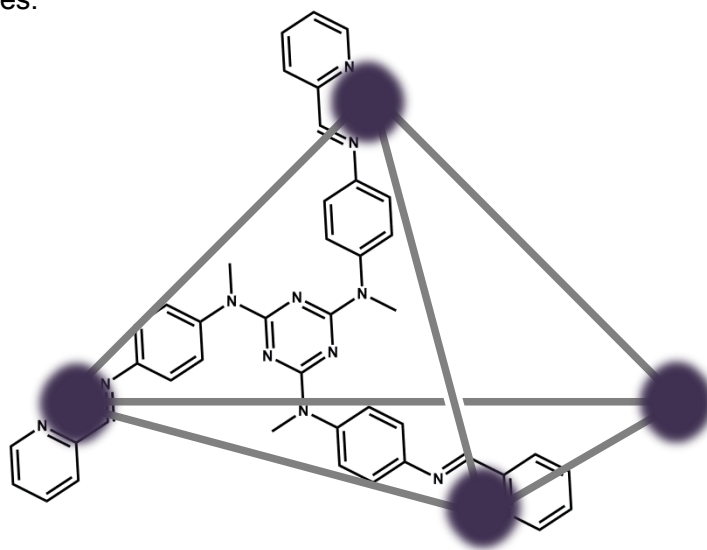


Figure 1.33 Schematic of the Nitschke group M₄L₄ metallo-nanocage. The grey lines represent the tetrahedral shape of the metallo-nanocage, one ligand is illustrated and the purple spheres represent the Fe(II) ions.⁹⁵

This Fe₄L₄ cage is capable of binding a wide range of guests in aqueous solution, but only a small subset of these guests in acetonitrile. For example, aromatic guests would only bind in water, as well as the larger guests trialled. The size of the guest also influenced the rate of exchange, with smaller guests showing rapid exchange and some larger guests requiring up to two weeks for equilibration. The host-guest binding

affinities were dependent on the size, shape and polarity of the guest molecules, with spherical guests like adamantane experiencing stronger binding than linear or flat molecules such as cyclopentane. This is postulated to be because of the good fit between the size and shape of the spherical molecules. Modelling of this cage with various guests indicated that when the guest was small, the phenylene rings contracted, lessening the amount of free rotation available to them. Conversely, with larger guests, the phenylene rings were forced apart. As a result of this ligand flexing, the size of the cavity was observed to vary from $261 \pm 2 \text{ \AA}^3$ for the guest pyridine to $347 \pm 1 \text{ \AA}^3$ for hexylthiophene. This flexing effect separates the guest molecules from the bulk solution and allows for observations that are not possible in bulk solution, like that of the hydroxyl proton of 1-adamantylmethanol. This proton is not observed in the ^1H NMR spectrum under bulk conditions due to the rapid proton exchange with the solvent. When 1-adamantylmethanol is encapsulated within the cage in acetonitrile, the hydroxyl group gives rise to a triplet peak, which arises due to coupling with the exocyclic methylene group. This is not observed when the system is in water, however, the methylene resonances are split in a manner consistent with coupling to the OD deuterium of 1-adamantylmethanol. These differences are attributed to water providing a greater sense of chirotopicity, because of stronger solvophobic interactions experienced by the cage when compared to acetonitrile.⁹⁵

Collaboration between the Bergman and Raymond groups led to a $[\text{Ga}_4\text{L}_6]^{12-}$ cage (Figure 1.34) with a multitude of uses. The ligand used was *N,N'*-bis(2,3-dihydroxybenzoyl)-1,5-diaminonaphthalene, a bis-bidentate ligand and formed an enantiomeric cage with *T* symmetry and a cavity of 450 \AA^3 .

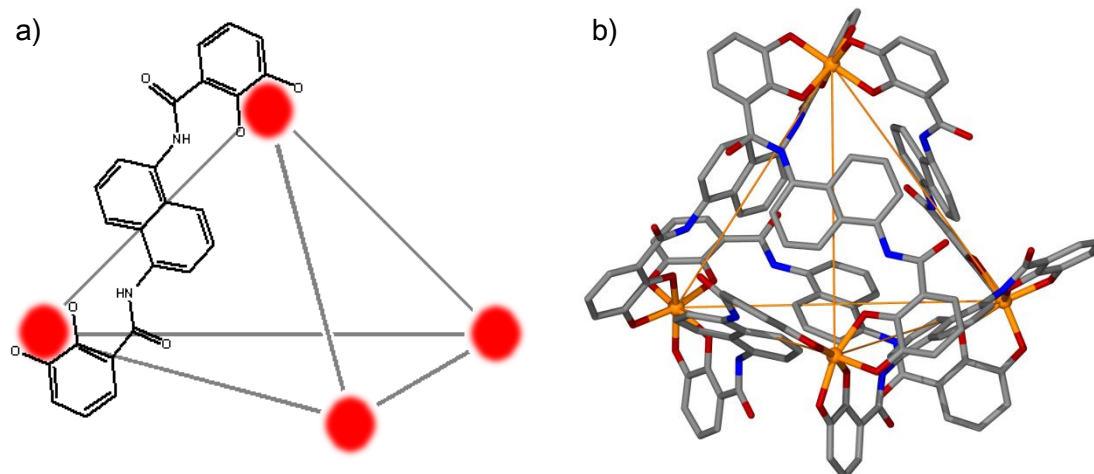


Figure 1.34 Raymond and Berman's M_4L_6 metallo-nanocage. *a) Schematic view, the grey lines represent the ligands and the red circles represent the gallium atoms. b) Taken from the crystal structure. The orange lines between the gallium(III) centres indicate the tetrahedral framework.*⁹⁶

This host system was able to encapsulate protonated guests and due to its tetrahedral symmetry, allowed the observation of guests with geminal *N*-methyl groups as they became desymmetrised in the host cavity. The catalysis of small orthoformates was also possible in this host, and was accelerated by a factor of 3900 compared to the corresponding uncatalysed reactions. However, the most impressive feat achieved by this cage concerns the catalysis of the Nazarov cyclisation reaction, where the reaction was accelerated by over a million-fold. This increase in the rate of reaction is similar to that found with enzymes and is due to a combination of various factors including pre-organisation of the complexed substrate, an increase in the basicity of the alcohol moiety upon encapsulation and the stabilisation of the transition state caused by constrictive binding.^{12, 97} This was a truly remarkable achievement and a great step forward in the aims of supramolecular chemistry with regards to biomimicry.

1.4.3 Octahedral M_6L_4 Metallo-Nanocages

In 1995 Fujita and co-workers synthesised a new metallo-nanocage from *cis*-protected palladium and rigid tridentate pyridine-containing ligands (Figure 1.35) in aqueous solution. This self-assembled to form a roughly spherical construct, approximately 2 nm in diameter, with four portals with a diameter of ~ 8 Å. They still continue to investigate this metallo-nanocage host-guest properties today, as it finds use in applications for catalysis and performing unusual reactions that do not proceed under normal conditions.⁹⁸

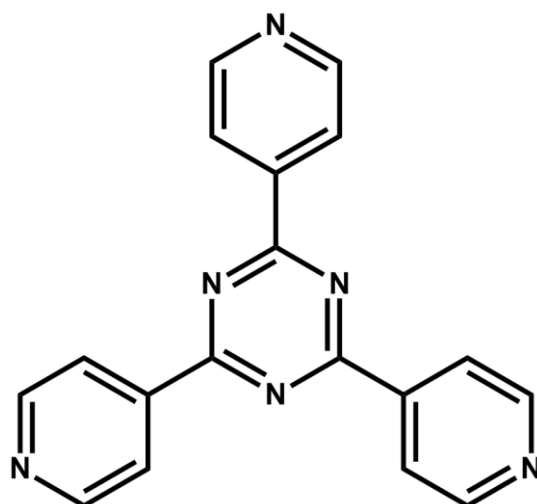


Figure 1.35 The tridentate ligand 2,4,6-tri(pyridine-4-yl)-1,3,5-triazine used by the Fujita group to produce octahedral M_6L_4 metallo-nanocages.⁹⁸

This cage exhibits T_d symmetry as the twelve pyridine rings are all equivalent. Consequently the ^1H NMR spectrum is very simple, showing only two peaks. This cage was found to form an inclusion complex with adamantyl carboxylate ions at a 1:4 host-guest ratio (Figure 1.36), as observed by X-ray crystallography and ^1H NMR titration studies. The X-ray crystallography analysis revealed that the hydrophilic carboxylate moieties of the guest sit outside the host cavity, whilst the hydrophobic adamantyl groups rest within the cavity.⁹⁹

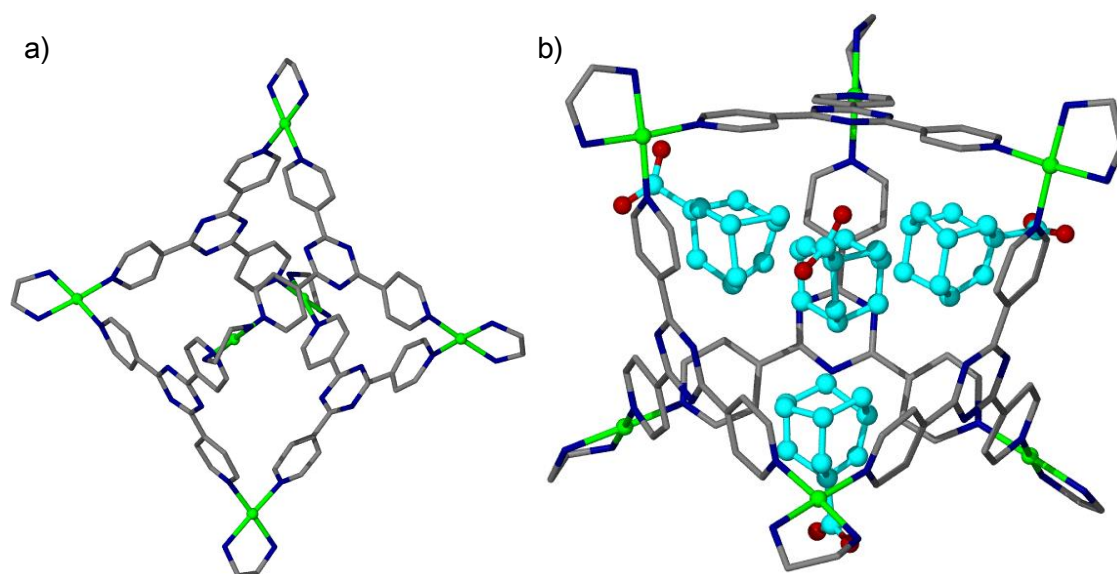


Figure 1.36 Crystal structures of Fujita's M_6L_4 cage. a) with no guest present, and b) with four adamantyl carboxylate ions shown in light blue.⁹⁹

Other guests have also been found to be encapsulated in this host at this ratio, including substituted benzenes and *o*-carborane. These guests aggregate along the tetrahedral axes of the host. Larger, flexible guests such as *cis*-stilbene and diphenylmethane bend to fit in the cavity, sitting orthogonal to each other. Guests larger than 8 Å, like tri-*tert*-butylbenzene form a 1:1 complex.⁹⁸ This cage has been used to accelerate the Diels-Alder reaction between naphthoquinone and isoprene by over 100 fold. This is suggested to occur due to the pre-organisation of the substrates within the cage cavity, which reduces the entropy cost of the pericyclic reaction. This technique has likewise been applied to Diels-Alder reactions with naphthalene with similar results.^{100, 101} It has also been used to conduct reverse phase-transfer catalysis of Wacker oxidation of olefins. Styrene and its derivatives were added to an aqueous solution of the cage with 10 mol% of the *cis*-protected palladium to promote the reaction. A control experiment found that the reaction did not proceed without the cage being present.¹⁰² Another reaction this cage system has performed is the highly stereoselective [2+2] photodimerisation of olefins. The cavity of the cage promoted the

photodimerisation of acenaphthylenes and naphthoquinones, which was shown not to occur under normal reaction conditions.¹⁰³ Furthermore, [2+2] photo and [2+4] thermal cycloadditions of highly stable arenes have been shown to occur within the cage cavity. These unusual reactions are proposed to happen because of the induced proximity of the guests within the cavity, which consequently reduces the entropic costs of the reaction.¹³

The Pt-analogue of this nanocage has been used to produce short-lived reaction intermediates. This was achieved by using the cavity space to generate the products *in situ*, forming them from smaller subunits that could fit through the cage, effectively preventing the products from leaving cage portals. This has been applied to trisilanols, intermediates of the polycondensation of trialkoxysilanes, also known as sol-gel condensation. This method of trapping these short-lived intermediates also increases their stability; they were found to remain intact after a month at room temperature.¹⁰⁴ A similar experiment, in the sense of trapping the guest, was applied to overcrowded alkenes. Overcrowded alkenes with *anti*-folded conformations could be converted to their twisted conformer within the cage cavity as the dimensions of the cavity were better suited to the twisted conformation. This guest could be easily removed from the cage by the addition of 4 equivalents of 1-adamantol, a more suitable guest for the cage. It was noted that the ejected overcrowded alkene was able to retain its new twisted conformation, implying that the conformation was “memorised”, although this memory was easily “erased” by heating the sample to 70°C for a short duration.¹⁰⁵ This cage system has been recently applied to alkyne activation, by allowing the pairwise selective recognition of transition metal complexes with linear organic compounds. These reactions only occur within the cavity, as it causes the reactants to be in close proximity to each other, activating the C(sp)—H bond. Hence, the reactions do not

require any harsh conditions. This mimics the behaviour of metalloenzymes, which bring substrates close to the metal in their binding pocket to perform chemical reactions at ambient temperatures.¹⁰⁶

1.4.4 Stella Octangula and Other M_6L_8 Metallo-Nanocages

Yamaguchi and co-workers developed a spherical metallo-nanocage with octahedral symmetry from 14 subunits. Square planar $Pd(NO_3)_2$ coordinates with the tridentate ligand 1,3,5-tris(4-pyridylmethyl)benzene to form a Pd_6L_8 construct with twelve windows. 1H NMR analysis indicated that the eight ligands were equivalent.^{107, 108}

Lah and colleagues devised an M_6L_8 cage from the self-assembly of N,N',N'' -tris(3-pyridinyl)-1,3,5-benzenetricarboxamide, a C_3 -symmetric tridentate ligand and $Pd(NO_3)_2$. It is the curvature in the ligand, which has a $\sim 120^\circ$ bend, combined with the C_4 -symmetric nature of the square planar palladium that provides the face-capped corner-linked truncated octahedral geometry to this 2.4 nm diameter complex. The complex has 12 portals with a cavity size of $\sim 1600 \text{ \AA}^3$.¹⁰⁹

Hardie and co-workers have synthesised a self-assembled Pd_6L_8 stellated octangula metallo-nanocage, (Figure 1.37) from the CTV-based tridentate ligand tris(isonicotinoyl)cyclotriguaiacylene (**L1**) discussed in section 1.3.1, and $Pd(NO_3)_2$. The stella octangula structure could also be formed using tetrakis(acetonitrile)palladium(II)tetrafluoroborate as the source of palladium(II) ions. A stella octangula assembly is the first and only stellation of an octahedron, which occurs when the edges of an octahedron are expanded until they intersect at points, which produces a starlike structure.¹¹⁰ The rigid cone shape of the CTV-like ligand allowed for a greater cavity volume when compared with planar analogues. The palladium(II) ions

occupy the corners of the octahedron whilst the ligands inhabit the faces of the octahedron, with the crown of the tribenzo[*a,d,g*]cyclononatriene core sticking out to form the stellation of the octangula. Tris(isonicotinoyl)cyclotriguaiacylene is a tris-substituted CTV derivate, a chiral ligand that results in chiral complexes. The Pd₆L₈ complexes self-assemble with eight ligands of the same chirality, resulting in a racemic solution of cages. The stella octangula cage has a diameter of approximately 3.1 nm and eight windows that are 7 x 9 Å, although the X-ray crystallography indicated that these windows were partly obscured by the OMe arms of the ligands. The cavity of this system is ~2050 Å³.¹¹⁰⁻¹¹² A stella octangula construct can also be formed with the similar ligand tris(isonicotinoyl)-tris(propyl)-cyclotricatechylene (**L2**). This ligand has an OPr arm in place of the OMe arm, resulting in better solubility properties. The **L1** cage is only soluble in DMSO, whereas the **L2** cage is soluble in DMSO, MeCN, MeNO₂ and DMF. It was noted that the ability of the **L2** cage to self-sort after self-assembly was noticeably affected by the choice of solvent, with the fastest self-sorting occurring in MeNO₂. It does not appear to reach a state where individual cages are homochiral with DMF and DMSO. It is possible to disassemble the **L2** cage by employing 24 equivalents of 4,4'-dimethylaminopyridine (DMAP). The cage can then be reformed by the addition of 24 equivalents of *para*-toluenesulfonic acid, demonstrating the ability of this stella octangula **L2** system to be used in cargo delivery.¹¹³

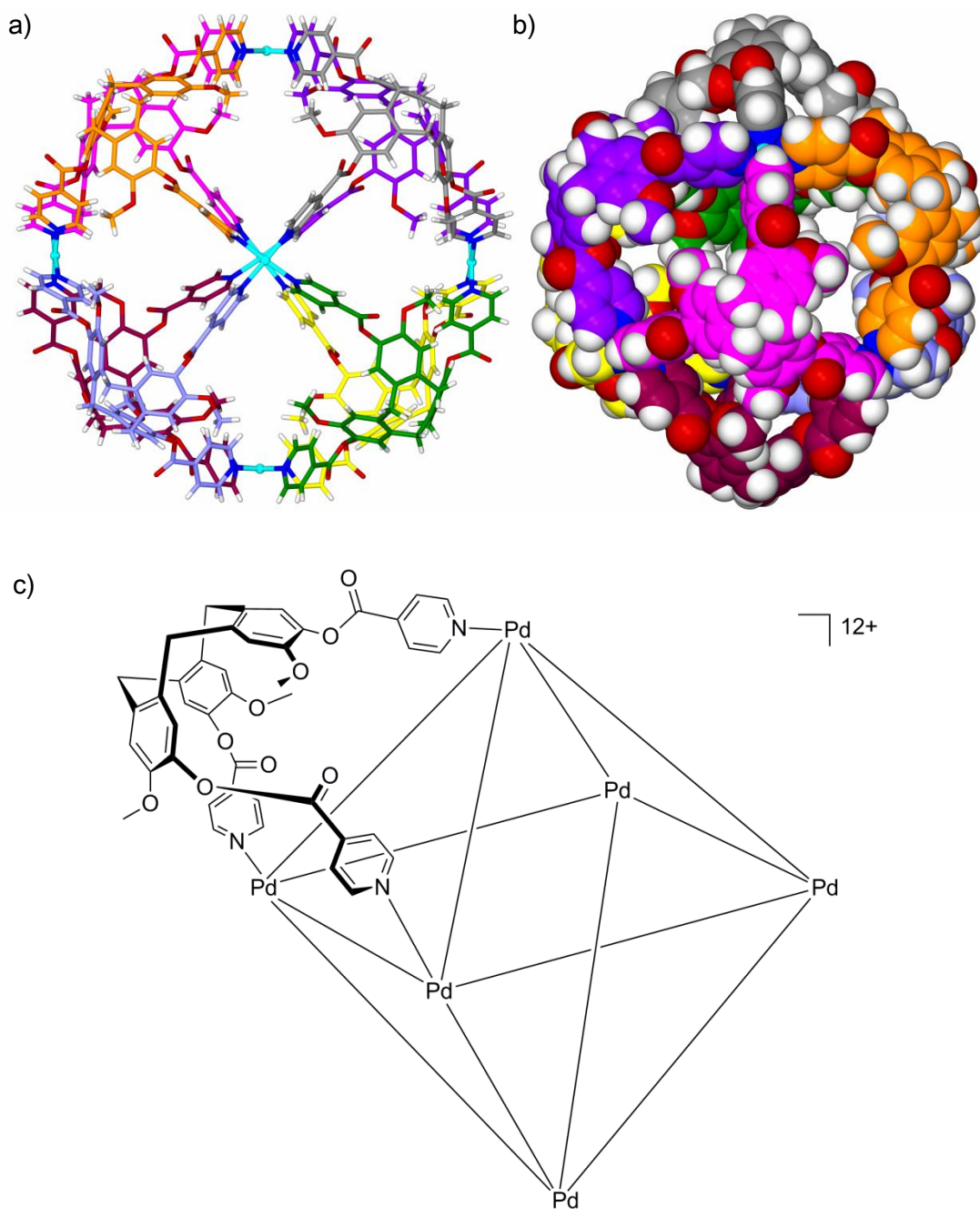
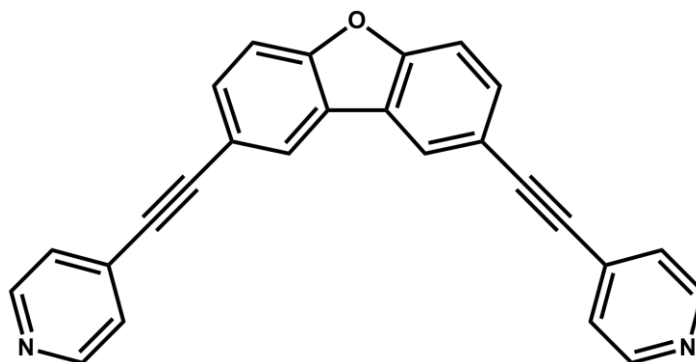


Figure 1.37 Stella octangula $[Pd_6(L1)_8]^{12+}$ metallo-nanocage, a) from the crystal structure, b) space filling model and c) schematic of with only one L1 ligand shown for clarity.¹¹⁰

1.4.5 Fujita's Larger Supramolecular Metallo-Nanocages

The Fujita group has a long history in synthesising supramolecular metallo-nanocages and they have been incredibly prolific in the variety and functionality of the systems that are produced in their laboratory.^{5, 114} They started small with the molecular squares

discussed in section 1.4.1 in 1990 and are currently working on complexes as large as $M_{24}L_{48}$.^{89, 115} In this section metallo-nanocages of sizes not covered in the previous sections will be discussed. The majority of the metallo-nanocages produced in the Fujita laboratories have the formula M_nL_{2n} .¹¹⁶ The smallest of these to be discussed in this section is an M_6L_{12} 3 x 3 x 3 nm cube. The cubic shape comes from the design of the ligand, 4,4'-(dibenzo[*b,d*]furan-2,8-diyl)diethyne-2,1-diyl)dipyridine, which has a 90° bend angle, (Figure 1.38). The ¹H NMR spectrum showed that all the ligands of this cage were equivalent, indicating a high degree of symmetry in the complex.¹¹⁷



*Figure 1.38 Ligand 4,4'-(dibenzo[*b,d*]furan-2,8-diyl)diethyne-2,1-diyl)dipyridine.¹¹⁷*

The next size in the range of Fujita nanocages is $M_{12}L_{24}$. These systems are exceptionally versatile and have been shown to be remarkably stable. The stability comes from the cooperation of the 48 Pd(II)—pyridine interactions.²⁶ These systems are formed from “banana-shaped” pyridine-capped bidentate ligands and square-planar metal complexes.^{118, 119} These ligands can be functionalised in such a manner that when they self-assemble into metallo-nanocages, the resulting system has endohedral functionalisation. This was achieved by applying methyl methacrylate (MMA) units to the ligands (Figure 1.39), resulting in a nanocage with a diameter of up to 4.6 nm, with 24 MMA units tethered to the interior of the cage. The MMA units were attached to the bidentate ligands by an oligo(ethylene oxide) linker. When longer linkers were used,

the MMA units were closer to the centre of the nanocage, as indicated by ^1H NMR. Radical polymerisation was performed within the nanocage, with 73% of the MMA being converted to polymethyl methacrylate (PMMA). Whilst the polymerisation was occurring, the integrity of the nanocage structure was maintained. A control experiment using uncoordinated ligands revealed that the reaction scarcely proceeded under those conditions, indicating that the nanocage efficiently promotes the polymerisation process.¹²⁰

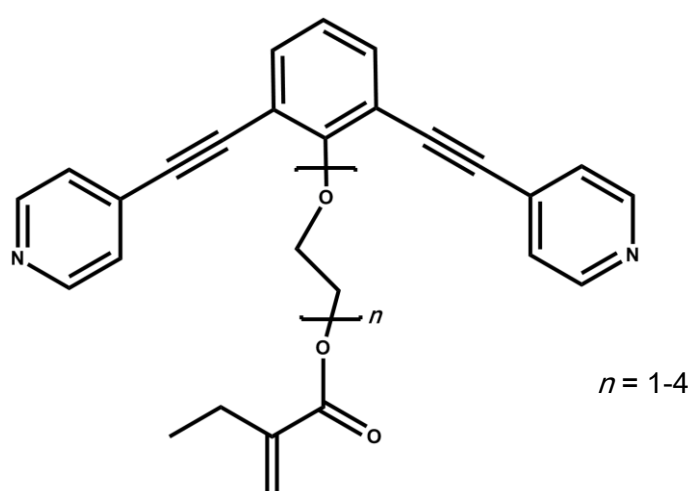


Figure 1.39 Bidentate ligand from the Fujita group, with MMA units.¹²⁰

The technique of modifying the ligands to endohedrally functionalise the interior has also been applied to fabricating a cage-within-a-cage structure. In this instance, the ligand is a dual linked bispyridinyl ligand, where the inner section has a smaller span than the outer section, as shown in Figure 1.40. The coordination sites are identical and when treated with $\text{Pd}(\text{NO}_3)_2$, a cage-within-a-cage with a cuboctahedral framework is formed from 24 ligands and 24 $\text{Pd}(\text{II})$ ions. This system was evidenced by cold-spray ionisation time-of-flight mass spectrometry (CSI-TOF-MS), X-ray crystallography, ^1H NMR and diffusion-ordered NMR spectroscopy (DOSY). The X-ray crystallography revealed that the inner cage had a diameter of 3.5 nm and the outer cage had a diameter of 6.5 nm. The inner cage was largely spherical, whilst the outer cage

displayed oval distortion. The formation of this $M_{24}L_{24}$ complex closely resembled protein assembly and it is the first artificial cage-within-a-cage molecule.¹²¹

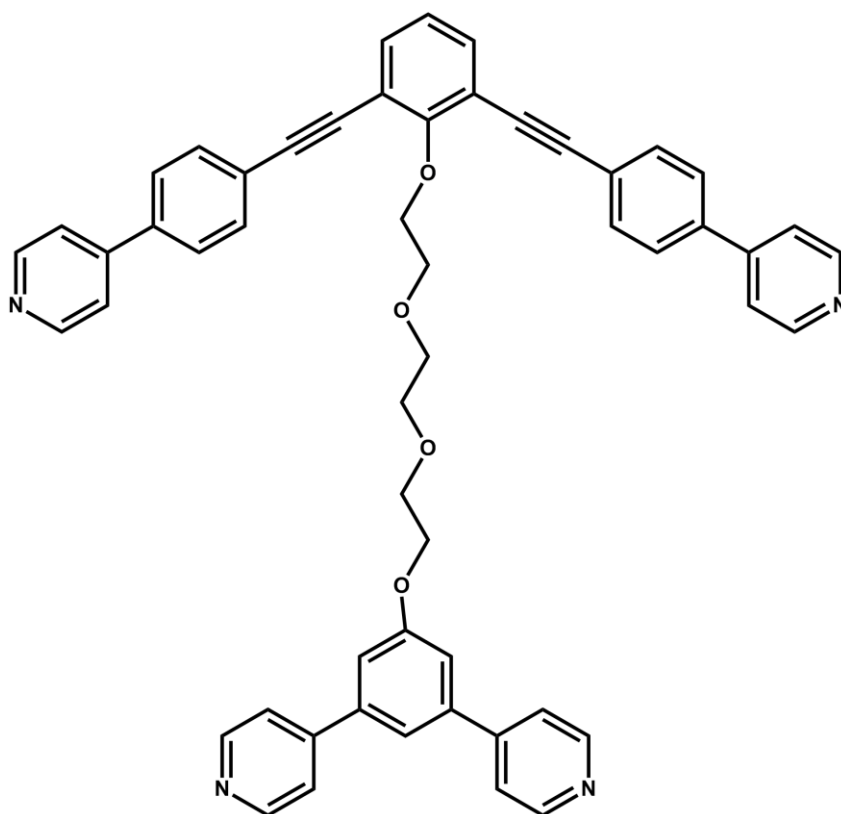


Figure 1.40 Cage-in-a-cage bidentate ligand from the Fujita group.¹²¹

In collaboration with the Stoddart group, an $M_{12}L_{24}$ cage was used as a “molecular flask” to conduct host-guest chemistry in its cavity. In this instance, bidentate bispyridinyl ligands were functionalised in a similar manner to the cage-in-a-cage system discussed above. The functionalisation for this system entailed tethering the guest molecule 1,5-dioxynaphthalene (DNP) to the central aryl ring of the ligand. Two different ligands were formulated, the only difference between them being the length of the linker. These ligands were then used to form a metallo-nanocage by the addition of $Pd(BF_4)_2$. These cages have two sets of windows, six square and eight triangular. The system with the shorter ligand has a radius of 2.4 nm with an internal volume of 44.4 nm^3 and the larger ligand provided a radius of 3.2 nm and a cavity size of

128 nm³. However, due to the endohedral ligand functionalisation, 17.5 nm³ and 21.1 nm³ of the cavity space was already occupied, respectively. The smaller of the two cages has an aperture width of 1.8 nm, whilst the larger cage has windows of 2.3 nm. Even the smallest of these apertures, at 1.8 x 1.8 nm² is much larger than the intended cyclophane host molecule, cyclobis(paraquat-*p*-phenylene) (CBPQT⁴⁺) which measured 1.10 x 0.65 nm². With the DNP, a pseudorotaxane host-guest complex was formed between the DNP and CBPQT⁴⁺. When the CBPQT⁴⁺ was added to the cage solution, no interaction between them is seen. When a tetrabutylammonium salt was added to the solution, the Coulombic barrier between the host and guest was lowered and the cage portals “opened” to allow the guest into the cage cavity. The system has become a stimulus-responsive system, displaying an emergent property, as neither of the subunits were observed to respond to this stimuli independently. It was also noted, that if the ligand and CBPQT⁴⁺ were reacted to form the pseudorotaxane host-guest complex and then the palladium(II) was introduced to the reaction mixture, the palladium(II) ejects the CBPQT⁴⁺ hosts from the cage system, indicating a hierarchy between the subunits. This system is a good model for a transmembrane ion channel, where the nanocage shell acts as a gate that is only opened in response to an applied stimulus.¹²²

The Fujita group have also used the endohedral ligand functionalisation method to encapsulate the protein ubiquitin within an M₁₂L₂₄ nanocage. To achieve this, a bidentate bispyridinyl was modified in a similar way to the ligand used in the “molecular flask” example discussed above. However, this time it was a molecule of ubiquitin that was tethered to the central aryl ring. The cage is essentially formed around the ubiquitin, so it is not the encapsulation of a free protein unit. The cage was formed from one functionalised ligand, twenty-three unfunctionalised ligands and twelve

palladium(II) ions to generate the $M_{12}L_{24}$ construct. The large size of ubiquitin (~3-4 nm in diameter) prevents more than one protein unit being encapsulated within the cage. This system was characterised by ^1H NMR, DOSY NMR and X-ray crystallography. This was the first incidence of a protein being encapsulated within a metallo-nanocage, or any other kind of synthetic host molecule.¹²³

The final $M_{12}L_{24}$ nanocage from the Fujita group to be discussed is the most recent and possibly the most impressive. This time the nanocage was designed to mimic a histone-octamer. Histone is a protein that packages DNA from an elongated conformation to a more compact form. To achieve this impressive feat, the nanocage was coated in peptides to create a system that is of a similar size and surface charge density to the histone octamer. The resulting complex had a 3.5 nm organometallic core that was covered in 24 peptide chains in the sequence Arg-Lys-Leu-Pro-Asp-Ala giving a complex with a diameter of 8.4 nm. This complex mediated the folding of a single DNA duplex *via* three different forms: I, the “beads-on-a-string”; form, II, the “multistrand aggregation”; and finally III, a compact globule form. This assembly was characterised by atomic force microscopy (AFM) and dynamic light scattering (DLS) and is a superb example of supramolecular chemistry providing models of complex biological systems.¹²⁴

The final systems from the Fujita group to be discussed are the $M_{24}L_{48}$ polyhedra. It was realised that the number of components in a M_nL_{2n} metallo-nanocage is directly related to the bend angle of the ligand when using square-planar metal ions and bidentate ligands. In an ideal cuboctahedron, represented by the $M_{12}L_{24}$, the edges have angles of 120° . In an ideal rhombicuboctahedron, represented by the $M_{24}L_{48}$, the edges have angles of 135° . Experimentally, it was found that a bend angle of 127°

produced a $M_{12}L_{24}$ complex, whilst bend angles of 135, 143, 147 and 149° all produced $M_{24}L_{48}$ complexes. These complexes were characterised by ^1H NMR, CSI-MS and X-ray crystallography. The $M_{24}L_{48}$ has a cavity space of 23,000 Å³.^{115, 125}

1.5 Project Outline

The aims of this research were to characterise host-guest chemistry for CTV-derivative-based metallo-nanocages. The CTV-derivatives were produced *in situ* by the Hardie group. The resulting metallo-nanocages were subjected to detailed examination predominantly by ^1H NMR spectroscopy, utilising 1-D, DOSY and 2-D ROESY techniques. These investigations were supported by mass spectrometry and X-ray crystallography to provide a full characterisation of novel host-guest systems.

This work began with the investigation of the host-guest chemistry between the Pd_6L_8 stella octangula system and sodium alkyl sulfate salts. The stoichiometry and the nature of the interaction between host and guest were characterised. This was followed with work on the novel **FL1** ligand shown in Figure 1.41. This ligand is similar to **L1**. The only difference is that of one of the pyridyl protons, which is been substituted for fluorine. This allows for systems with the **FL1** ligand to be investigated with ^{19}F NMR spectroscopy. When the work on stella octangula systems and their host-guest chemistry have been completed, the **L1** and **FL1** ligands were applied to forming cryptophanes with *cis*-protected palladium(II) salts and investigations were made into the host-guest properties of the cryptophanes produced.

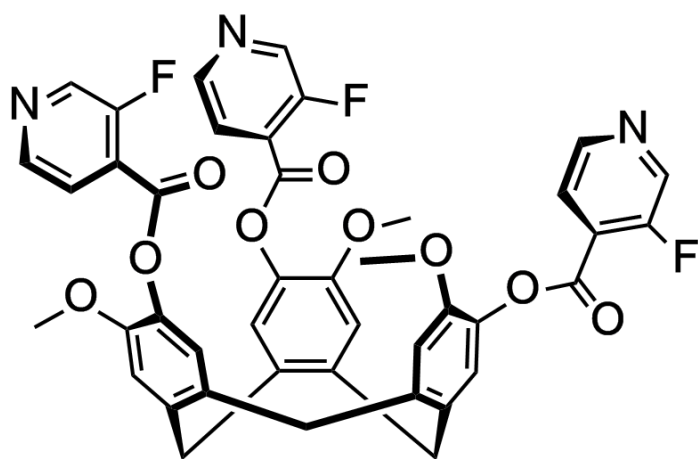


Figure 1.41 FL1 ligand.

Chapter 2 Encapsulation of Sodium Alkyl Sulfate Salts by the [Pd₆(L1)₈]·12(BF₄) Stella Octangula Cage

2.1 Introduction

In this chapter, the investigation of the host-guest relationship between the [Pd₆(L1)₈]·12(BF₄) stella octangula cage and sodium alkyl sulfate guests is described. The solution and solid phase properties of the stella octangula cage have previously been reported¹¹⁰ and it is known that not only is there a large inner void, there are also sizable portals into this inner void. The purpose of this investigation was to establish that a guest could be accommodated within this inner void and to characterise any host:guest complexes formed.

2.1.1 Ligand L1: Tris(isonicotinoyl)cyclotrivaicylene

The tris(isonicotinoyl)cyclotrivaicylene ligand [referred to as L1 from here on and shown in Figure 2.1 a)] is a tri-substituted cyclotrivaicylene (CTV) derivative. It is produced by the reaction of cyclotrivaicylene (CTG) with isonicotinoyl chloride hydrochloride, which results in a racemic mix of L1 *M* and *P* diastereoisomers.^{43, 126} The L1 ligand retains the crown conformation of CTV, resulting in a rigid molecule with C₃ symmetry. The L1 ligand is functionalised with pyridyl donors appended to the upper rim of the CTG core which enables the molecule to coordinate with three transition metals and extends the cavity of the CTG core.¹²⁶

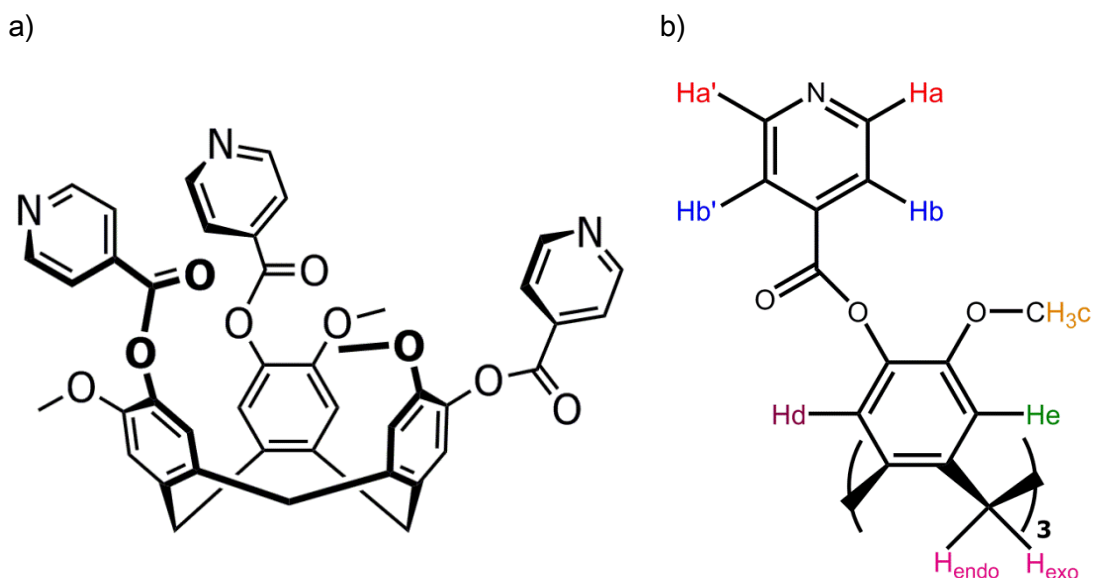


Figure 2.1 a) Tris(isonicotinoyl)cyclotriguaiacylene in the crown conformation, b) annotated section of ligand showing unique protons.

Due to the high symmetry of the ligand, there are only 7 resolvable proton environments, which give a simple ^1H NMR spectrum (Figure 2.2). All of the protons exhibit sharp peaks at 500 MHz. The two protons on the CTV-derivative bowl are chemically inequivalent and resonate as a pair of doublets;⁴³ the endo protons (annotated as H_{endo}) resonates further downfield by over 1 ppm compared to its exo neighbour. This is because its chemical environment is drastically different as it points into the bowl of the CTV-derivative where it is strongly deshielded due to the steric compression of the cyclononatriene ring of the CTV-core.^{45, 46} The exo proton points away from the CTV-derivative bowl, and is not affected by the deshielding region of the ligand. The left-hand peak of the exo doublet is under the singlet for the Hc protons.

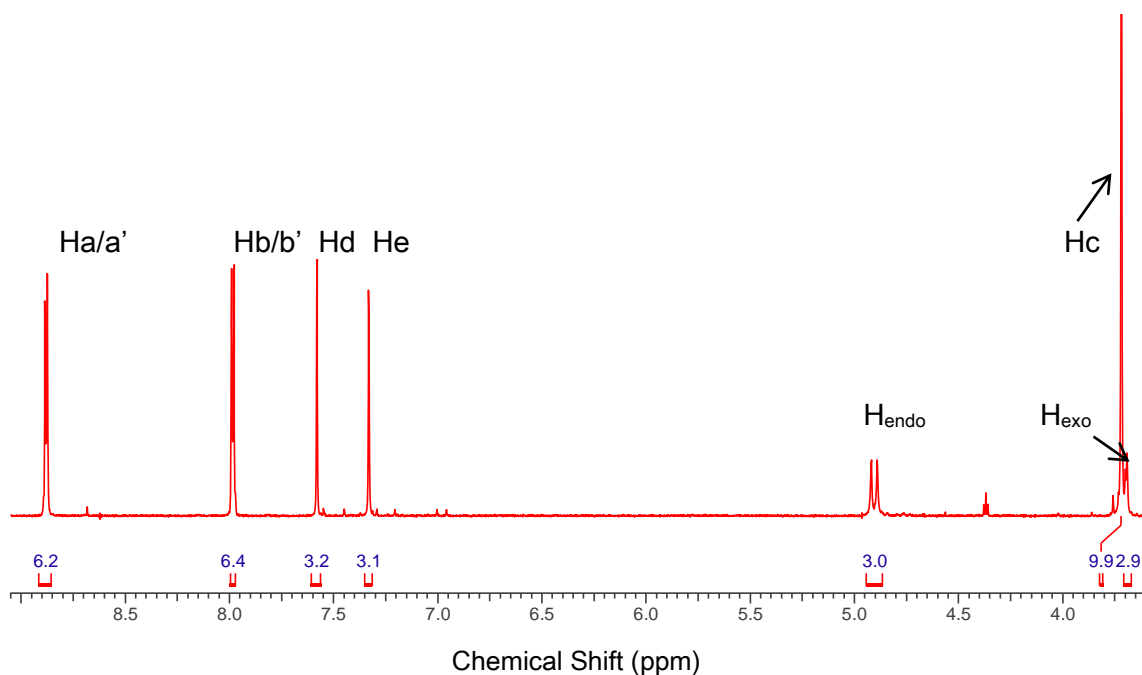


Figure 2.2 ^1H NMR spectrum of tris(isonicotinoyl)cyclotriguaiacylene **L1** with assignments and integration. (293 K, 500 MHz, d_6 -DMSO)

2.1.2 The $[\text{Pd}_6(\text{L1})_8]\cdot 12(\text{NO}_3)$ Stella Octangula Cage

The $[\text{Pd}_6(\text{L1})_8]\cdot 12(\text{NO}_3)$ stella octangula cage is obtained from the self-assembly of six “naked” Pd(II) ions with eight tris(isonicotinoyl)cyclotriguaiacylene (**L1**) molecules in d_6 -DMSO. The formation of this cage, shown in Figure 2.3, was first reported by Ronson *et al.*¹¹⁰ X-ray diffraction analysis of the cage revealed that it crystallises in an asymmetric tetragonal unit cell. The Pd(II) centres of the cage complex are arranged in an octahedron with respect to each other. Each ligand coordinates to three different Pd sites. The Pd sites exhibit square planar geometry, as each Pd is attached to four different ligands. The overall dimension of the cage was reported as roughly 3.1 nm^3 , when measured from the basal hydrogen atoms of the $-(\text{CH}_2)-$ planes for diametrically opposed ligands.¹¹⁰ The cage has eight windows on its surface, which each have an area of approximately 60 \AA^2 .

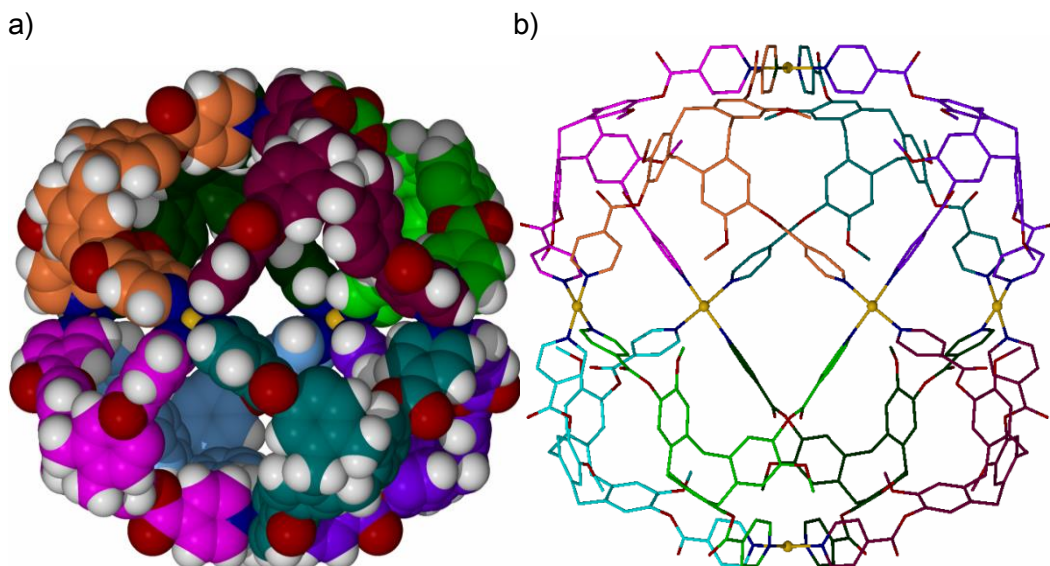


Figure 2.3 The $[Pd_6(L1)_8] \cdot 12(NO_3)$ stella octangula cage a) space filling model and b) wireframe model.

NMR-based diffusion studies were performed on the ligand and the cage complex, which permitted the hydrodynamic radius to be estimated. A diffusion coefficient of $0.555 \times 10^{-10} \text{ m}^2 \text{ s}^{-1}$ was measured for the cage in d_6 -DMSO, compared to $1.284 \times 10^{-10} \text{ m}^2 \text{ s}^{-1}$ for the ligand d_6 -DMSO.¹¹⁰ Thus, a hydrodynamic radius of 19.4 Å was derived using the Stokes-Einstein relationship.¹²⁷

For this investigation, a different palladium(II) salt - with a (BF_4^-) counter ion - was used. The reasons for this are discussed in section 2.2.1. All cage samples were prepared in d_6 -DMSO as this is the only solvent that the cage is soluble in. The $[Pd_6(L1)_8] \cdot 12(BF_4)$ stella octangula cage is produced by mixing fresh stock solutions in molar quantities. After the samples were made, the remaining stock solutions were stored under ambient conditions. The 1H NMR spectrum for the $[Pd_6(L1)_8] \cdot 12(BF_4)$ stella octangula cage is shown in Figure 2.4 with the spectrum of L1 for comparison. Despite the different counter ion, the spectrum appears the same as that for the (NO_3^-) counter ion. The spectrum of the cage is similar to that of the ligand, again it shows 7 different proton environments. However, the peaks are broader than those seen for

uncomplexed **L1**, which is indicative of the complexation of the **L1** ligand with palladium ions.¹²⁸ The pyridine peaks are shifted down field as a result of complexation, whereas the aryl peaks and the peak for the methoxy group (Hc) are shifted slightly upfield. The methylene bridge protons show no change in chemical shift, but are broadened. The notation for the protons of the stella octangula cage spectrum is the same as for the ligand, which is shown in Figure 2.1 b).

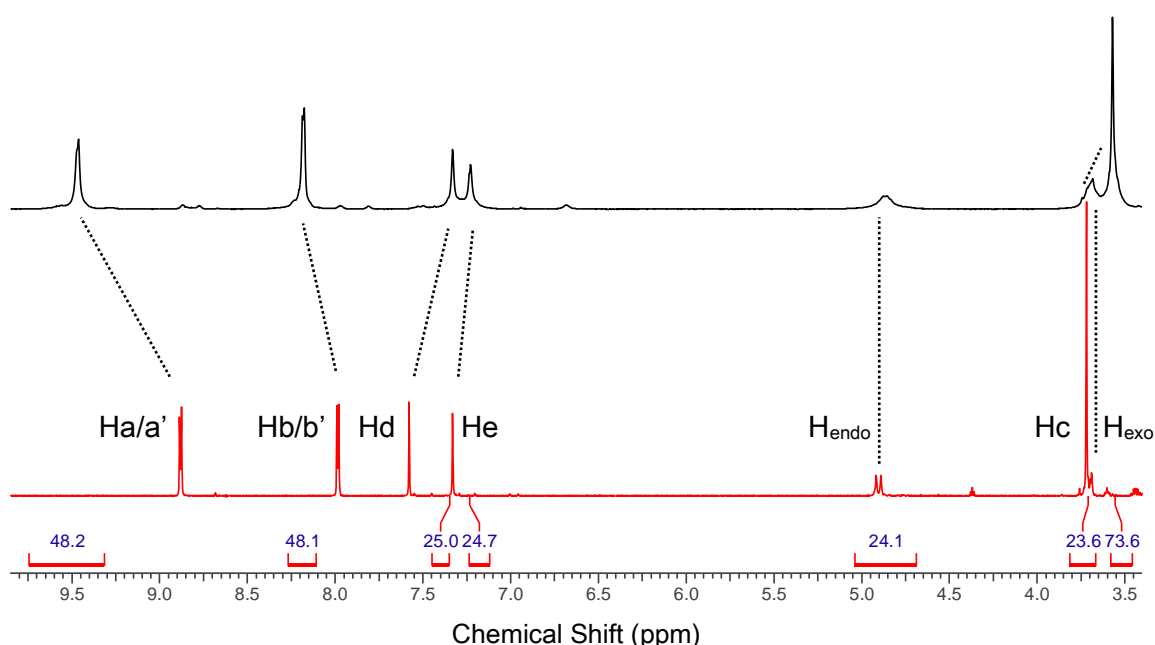


Figure 2.4 ^1H NMR spectra of ligand **L1** in red and $[\text{Pd}_6(\text{L1})_8] \cdot 12(\text{BF}_4)$ in black. Integration shown for $[\text{Pd}_6(\text{L1})_8] \cdot 12(\text{BF}_4)$. (293 K, 500 MHz, d_6 -DMSO)

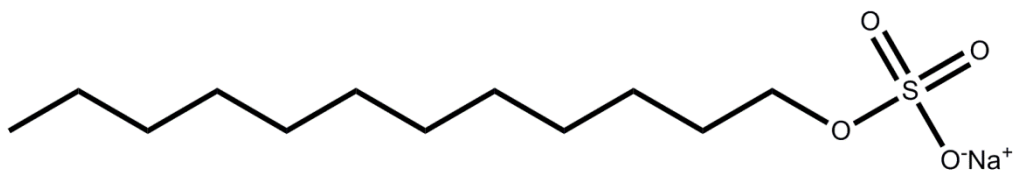
2.1.3 Sodium Alkyl Sulfate Guests

Studies performed within the group¹²⁹ prior to this investigation assessed a few small molecules as potential guests for the stella octangula cage. These potential guests included adamantane, *o*-carborane and sodium dodecyl sulfate (SDS). The only one of these potential guests that gave any indication of a host-guest interaction with the cage was SDS.¹²⁹ As a part of this investigation, molecules including 2-bromoadamantane,

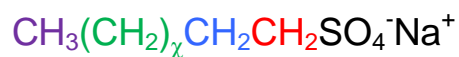
adamantane-1-carboxylic acid, biphenyl and *D*-camphor were also probed for their suitability as guests. However, no evidence of any interaction between the cage and the guests could be seen in the ¹H NMR spectra.

SDS is an anionic surfactant with a polar head moiety and a 12 carbon aliphatic tail giving the molecule amphiphilic properties. SDS is an unbranched molecule and simple size estimates indicate that it should fit through the cage portals. As SDS has surfactant properties, it can spontaneously form micelles when the concentration is above its critical micelle concentration (CMC). In DMSO solution, this concentration is approximately 30 mM.¹³⁰ This is higher than the CMC of SDS in pure water, which is approximately 8 mM.¹³¹ This is because the aggregation of the SDS molecules is inhibited by the DMSO. Related molecules were available with different length carbon tails. Two of these were selected: sodium tetradecyl sulfate (STS), which has a 14 carbon tail; and sodium octyl sulfate (SOS), which has an 8 carbon tail chain. SDS is shown in Figure 2.5, along with the notation for its ¹H NMR spectra. The spectra for all three guest molecules are shown in Figure 2.6. All three guests exhibit identical spectra, with the only difference being the integration of the H3 peak, which integrates for 12, 18 and 24 protons, for SOS, SDS and STS respectively, as the aliphatic chain length increases. Consequently the notation is the same for all three guests, which exhibit four resolvable proton environments at 500 MHz.

a)



b)



5, SOS



$\chi = 9$, SDS

14, STS

Figure 2.5 a) Sodium dodecyl sulfate (SDS), b) the annotation used to describe the NMR spectrum of the sodium alkyl sulfate guests, the annotation is the same for all three guests.

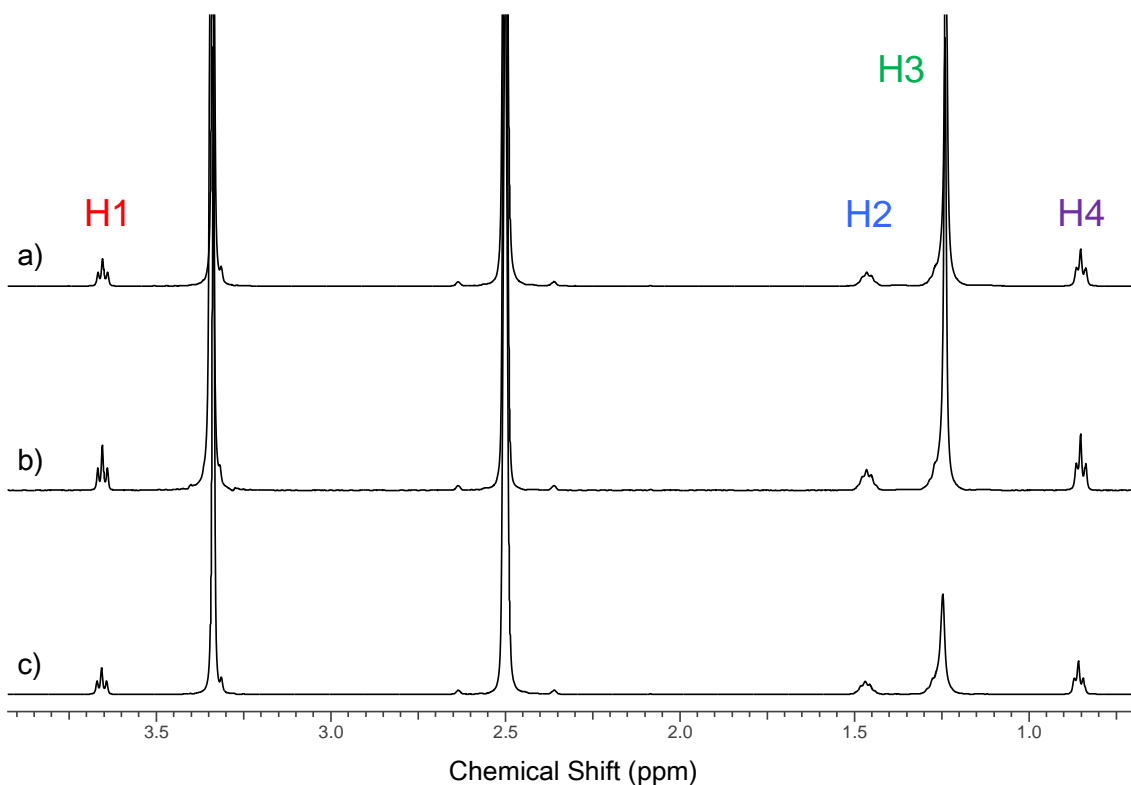


Figure 2.6 ^1H NMR spectra of sodium alkyl guests a) SOS, b) SDS, c) STS. (293 K, 500 MHz d_6 -DMSO, referenced to TMS at 0.00 ppm)

2.2 Producing a Single Species of Cage

Prior to describing the results of the host-guest study, some observations made whilst preparing the stella octangula cage will be discussed. The first observation arose early in the investigation; an issue with free ligand which was traced back to the palladium nitrate used as the source of “naked” palladium ions. This issue was resolved relatively quickly and easily by changing the palladium salt used. This is discussed in section 2.2.1. The second issue concerned the self-assembly of the stella octangula cage system. This issue took longer to resolve and for a short period of time became the main focus of the investigation and is detailed in section 2.2.2.

2.2.1 Choice of Palladium Salt

During the initial studies for this investigation, it was observed that the $[\text{Pd}_6(\text{L1})_8] \cdot 12(\text{NO}_3)$ stella octangula cage samples contained a large quantity of unbound (free) ligand, as shown by the integrated spectrum in Figure 2.7. Palladium(II) nitrate was used to make these cage samples as this was the palladium salt used to obtain the X-ray crystallography data.¹¹⁰ Reasons that were considered for the free ligand present in the samples included: the variability of the palladium(II) nitrate hydrate salt, which is highly hygroscopic, and always seemed damp when the bottle was opened; and the possibility that the palladium salt contained some palladium(0) as well as palladium(II), which would not react with the L1 ligand. When the palladium(II) nitrate was used to produce cages, despite many attempts, a “complete” cage solution (that is, where all of the ligand has reacted with all of the available palladium to form a quantitative product) was never achieved. The first approach to solving this problem

was to add an excess of palladium to the cage samples. This excess was approximately three times the amount of palladium(II) nitrate required to prepare stoichiometrically correct cage samples. This does alleviate the problem of free ligand, but causes problems calculating accurate cage concentrations. Purification of the palladium nitrate was then considered, but discounted due to the highly hygroscopic nature of the compound.

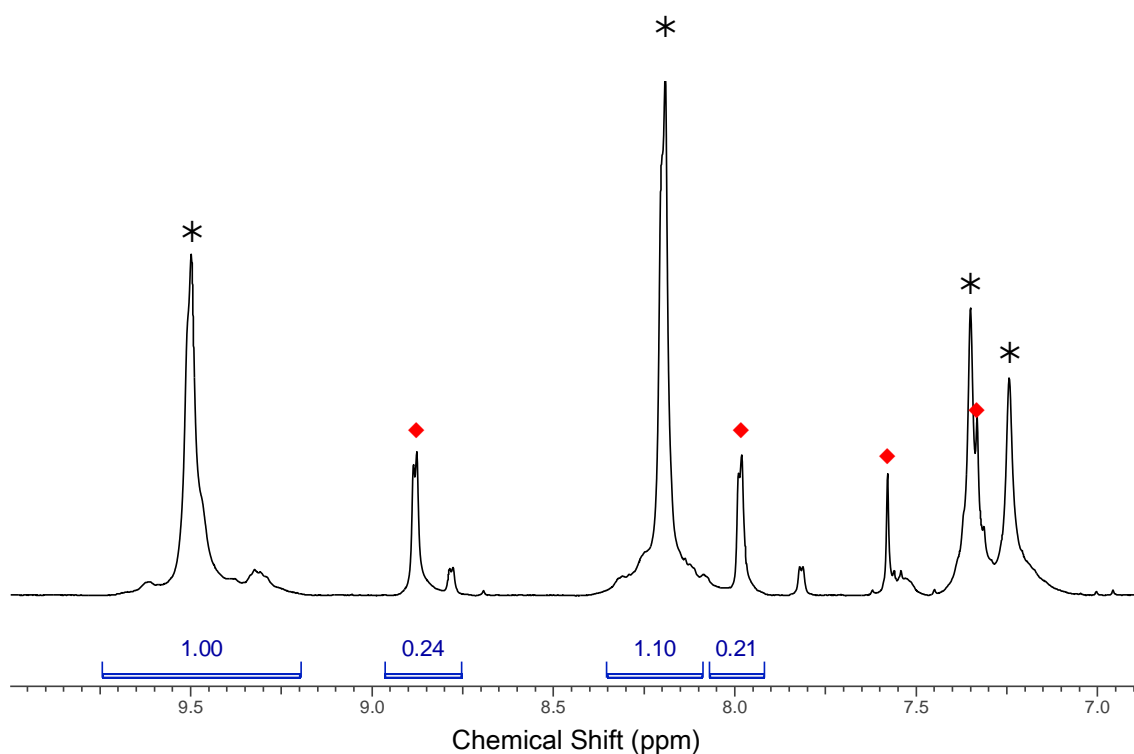


Figure 2.7 Downfield region of $[Pd_6(L1)_8] \cdot 12(NO_3)$ stella octangula cage with integrals, * indicate cage peaks and ♦ indicate unbound ligand. (293 K, 500 MHz, d_6 -DMSO)

The problem was solved by using a different palladium source: tetrakis(acetonitrile)palladium(II)tetrafluoroborate. This mustard yellow crystalline salt is obtained dry, unlike the palladium nitrate, which had a damp appearance. This made it considerably easier to work with, as it was easier to measure out accurately and it dissolved faster than the nitrate salt. The resulting solutions were a lighter shade of yellow when compared to the nitrate salt solutions. The 1H NMR spectrum of the $[Pd_6(L1)_8] \cdot 12(BF_4)$ cage is identical to those made with the nitrate salt. The acetonitrile

component of the new palladium salt is detected at 2.08 ppm, together with a contaminant at 1.75 ppm. These peaks are illustrated in Figure 2.8 with the acetonitrile peak shown in red and the contaminant peak is shown ringed in blue. When the tetrakis(acetonitrile)palladium(II)tetrafluoroborate was purchased from Acros Organics, the contaminant peak was not present in the spectrum. Neither of these peaks caused any overlap problems with either the cage complex or the guest molecules.

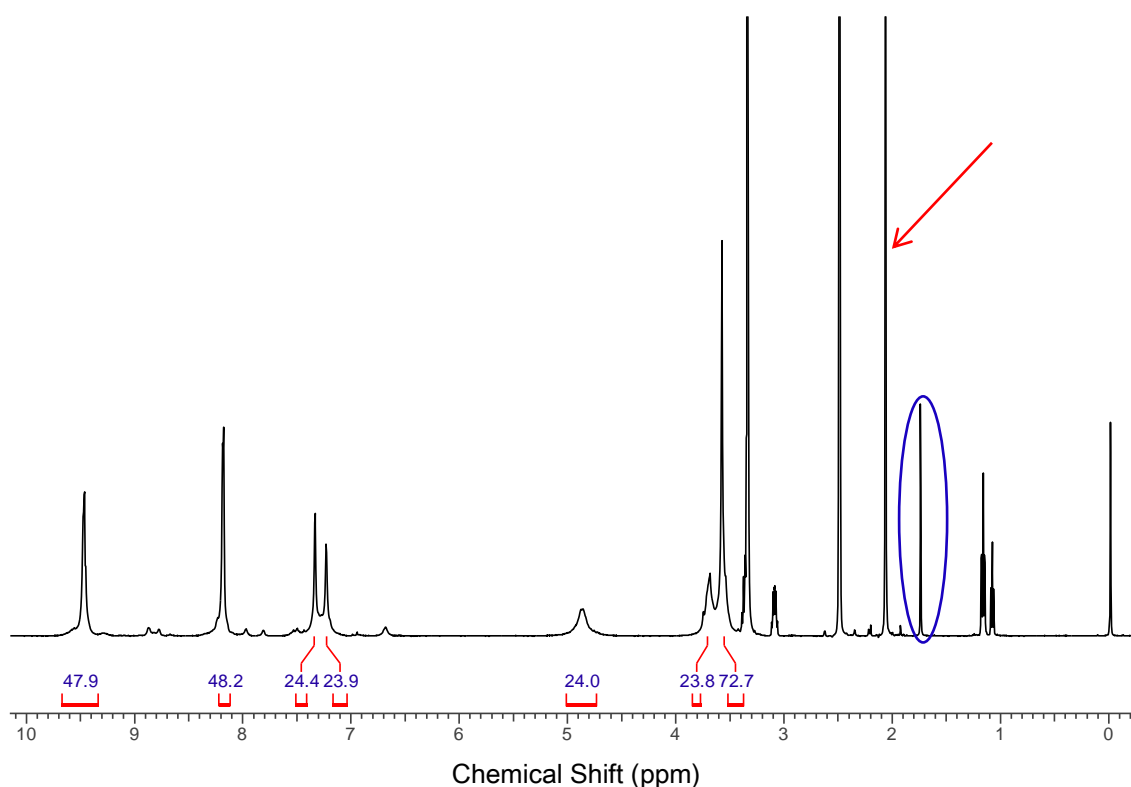


Figure 2.8 ^1H NMR spectrum of the cage complex produced using tetrakis(acetonitrile)palladium(II)tetrafluoroborate with integration. The red arrow indicates the acetonitrile of the palladium salt and the blue-ringed peak indicates the contaminant present in the new palladium salt. (293 K, 500 MHz, d_6 -DMSO)

The Fujita group use both palladium(II) nitrate and tetrakis(acetonitrile)palladium(II)tetrafluoroborate to form their large metallo-nanocages in DMSO.^{26, 107, 115, 117, 118, 120, 123, 132, 133} Despite searching the literature, no record of problems using palladium(II) nitrate as a coordinating metal in DMSO was discovered. However, such problems have been noted by the Hardie group.¹¹³

2.2.2 Self-Assembly of the $[\text{Pd}_6(\text{L1})_8]\cdot 12(\text{BF}_4)$ Stella Octangula Cage

Self-assembly is the spontaneous and reversible association of molecular species to form a larger supramolecular entity.³ After a complex has self-assembled, self-organisation, (otherwise known as self-sorting) can occur to correct mistakes and ensure that the most thermodynamically stable product is reached.^{3, 134} In some cases, self-sorting can take the form of “self-resolution”, which results in the formation of homochiral assemblies formed from racemic components.¹³⁴ The most stable result for this system is the formation of all *M* or *P* cages and hence a racemic mix of stella octangula assemblies. This racemic mix is termed the “homochiral cage”, as each individual cage is formed from ligands that have one helicity, resulting in a chiral assembly.¹¹⁰ The expression “heterochiral cage” is applied when cages are formed with a mix of *M* and *P* ligands, resulting in cage isomers with lower symmetry.

Although self-assembly is usually instantaneous, some cage samples produced in this study were observed to take a considerable time to self-sort into homochiral cages. The most thermodynamically stable $[\text{Pd}_6(\text{L1})_8]\cdot 12(\text{BF}_4)$ stella octangula cage had a well-resolved ^1H NMR spectrum. However, if the most thermodynamically stable species had not been fully realised, then a more complex, broader ^1H NMR spectrum was observed. This is illustrated in Figure 2.9. These observations led to an investigation into the rate of self-sorting of the stella octangula cage. The investigations were carried out in three different ways: in samples with very low concentrations (section 2.2.2.1); in samples at varying concentrations over the course of one month (section 2.2.2.2); and in samples made from old stocks (section 2.2.2.3). The purpose of these investigations was to discover what was causing the slow rate of self-sorting.

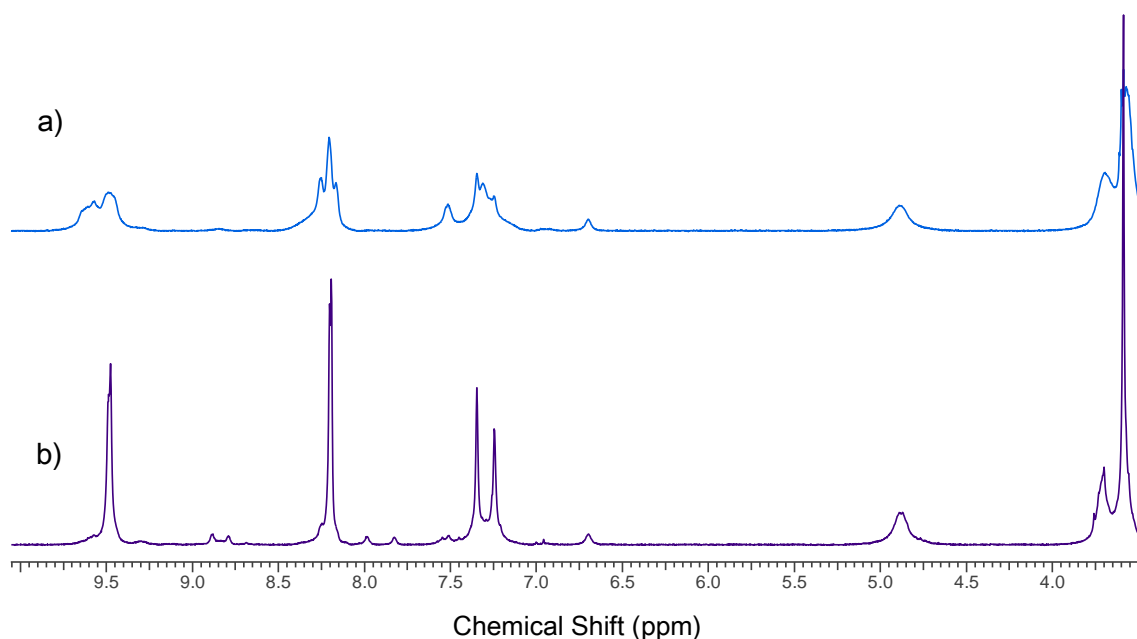


Figure 2.9 ^1H NMR spectra of $[\text{Pd}_6(\text{L}1)_8] \cdot 12(\text{BF}_4)$ stella octangula cage assemblies, *a)* heterochiral, *b)* homochiral. (293 K, 500 MHz, d_6 -DMSO)

2.2.2.1 Self-Assembly at Low Concentrations with the $[\text{Pd}_6(\text{L}1)_8] \cdot 12(\text{BF}_4)$ Stella Octangula Cage

A series of varying, low concentration host-guest samples was prepared with SDS as the guest. These samples were prepared from a stock solution of 0.5 mM cage that was then diluted to prepare the other samples in this series. When these samples were analysed, the two lowest cage concentrations (0.1 and 0.2 mM) were found to have a considerable amount of free ligand and proportionally very little cage present. To probe this further and see if this result was reproducible, two more sets of samples were prepared. The first set was identical to the original set; that is a series of host-guest samples. The second set contained the stella octangula cage with no guest present, but at the same concentrations as the first set. This was done to investigate if the guest was causing the incomplete cage formation not. However, the cage peaks were at the

same stage of self-assembly in both of these sets of spectra, ruling out the guest as the cause of incomplete cage formation.

These two new sets of samples were analysed immediately, which led to the discovery that the stella octangula cage does not self-sort instantaneously, as shown in Figure 2.10 as the spectra of the samples did not display homochiral cage spectra, but instead indicated heterochiral cages with free ligand present.

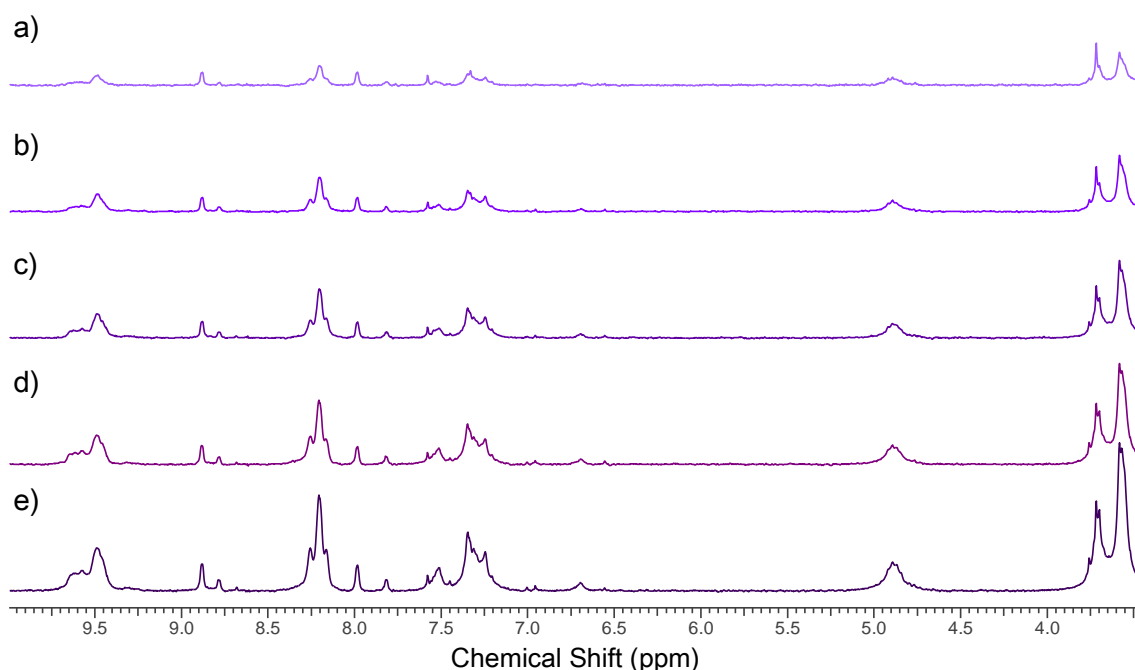


Figure 2.10 $[Pd_6(L1)_8] \cdot 12(BF_4)$ Stella octangula cages after 0 hours a) 0.1 mM, b) 0.2 mM, c) 0.3 mM, d) 0.4 mM and e) 0.5 mM. (293 K, 500 MHz, d_6 -DMSO)

When these same samples were analysed again 24 hours later, shown in Figure 2.11, the spectra now had the appearance of homochiral cages, indicating that the heterochiral cages had self-sorted into the more thermodynamically stable homochiral assemblies. The lowest concentration sample did not appear as well sorted as those of a higher concentration, but it is hard to gauge due to the low intensity of the spectrum

It was decided at this point that future cage samplers would be prepared at higher concentrations than 0.2 mM. This would ensure that future samples would be formed at the correct stoichiometry and would make analysis of samples easier. Samples of

lower concentration (e.g. 0.1 mM) are more difficult to analyse due to low signal intensity arising from the low concentration of cage. Low signal intensity increases the level of error in detecting any change in chemical shift. Furthermore, the signal-to-noise ratio is much smaller for the low concentration samples. When measured for the methoxy (H_c) peak in the series shown below, the sample at 0.5 mM had a signal to noise-ratio of 409, whereas the 0.1 mM sample had a signal-to-noise ratio of 71. For the H_{endo} peak (a low intensity peak) the signal-to-noise ratio is even lower, at just 12 (compared to 37 for the 0.5 mM sample).

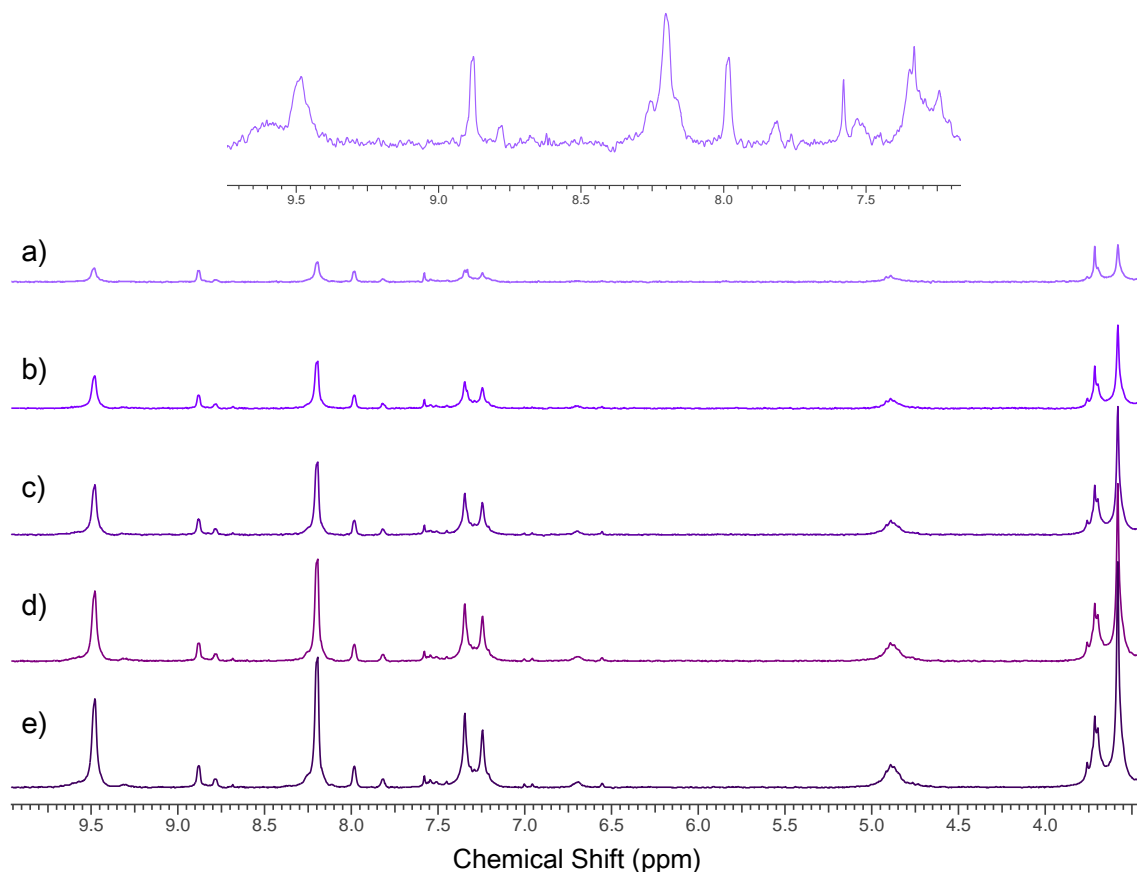


Figure 2.11 $[\text{Pd}_6(\text{L1})_6] \cdot 12(\text{BF}_4)$ Stella octangula cages after 24 hours a) 0.1 mM, b) 0.2 mM, c) 0.3 mM, d) 0.4 mM and e) 0.5 mM. Shown above is an expansion of the aromatic region of the 0.1 mM sample, indicating the low signal-to-noise ratio. (293 K, 500 MHz, *d*₆-DMSO)

2.2.2.2 Effect of Concentration on Self-Assembly of $[\text{Pd}_6(\text{L1})_8] \cdot 12(\text{BF}_4)$ Stella Octangula Cage

The self-sorting phase of the self-assembly of the stella octangula cage was found to be inconsistent. When the process was slow (that is, taking longer than 24 hours), samples were monitored to see how long it took them to become homochiral. To examine if the self-assembly was a kinetically driven process, a sample of the stella octangula cage was heated to 60°C for 5 minutes and then analysed, ^1H NMR showed that the rate of self-assembly was unaffected.

Samples of different concentrations (2.5, 1.0 & 0.5 mM) were prepared and monitored by ^1H NMR for 32 days. The 2.5 mM sample is shown over the course of one month in Figure 2.12. The peaks in the aromatic region were very broad to begin with, which is an indication of exchange processes occurring. The Ha/a' peak appeared as two broad resonances covering the region from 9.35 to 9.72 ppm. The Hb/b' resonance had the appearance of a triplet, however it was actually three broad singlets, with the central peak at 8.20 ppm corresponding to homochiral assemblies present and the side peaks at 8.16 and 8.25 ppm representing the heterochiral assemblies present in the solution. The Hd and He peaks for homochiral assemblies were present at 7.35 and 7.25 ppm respectively, however, they were less intense when compared to a spectrum of only homochiral assemblies. Also present were broad peaks at 7.51 and 7.31 ppm representing the heterochiral assemblies present.

With the passage of time, the spectra slowly became more symmetrical in appearance, that is, the sharp peaks, characteristic of the homochiral cage became more intense and the side peaks attributed to heterochiral cages receded as the cage molecules

became more symmetrical. A trend was observed relating to the concentration of the cage samples and the rate of achieving the final self-assembled product. After 32 days (748 hours) the 2.5 mM cage still showed signs of self-sorting, although by 14 days (325 hours), it showed mostly homochiral characteristics. The 1.0 mM (Figure 2.13) cage showed a fully homochiral spectrum after 15 days (343 hours). The 0.5 mM cage (Figure 2.14) was fully homochiral by 11 days (255 hours), although by 7 days (153 hours) is showed mostly homochiral characteristics.

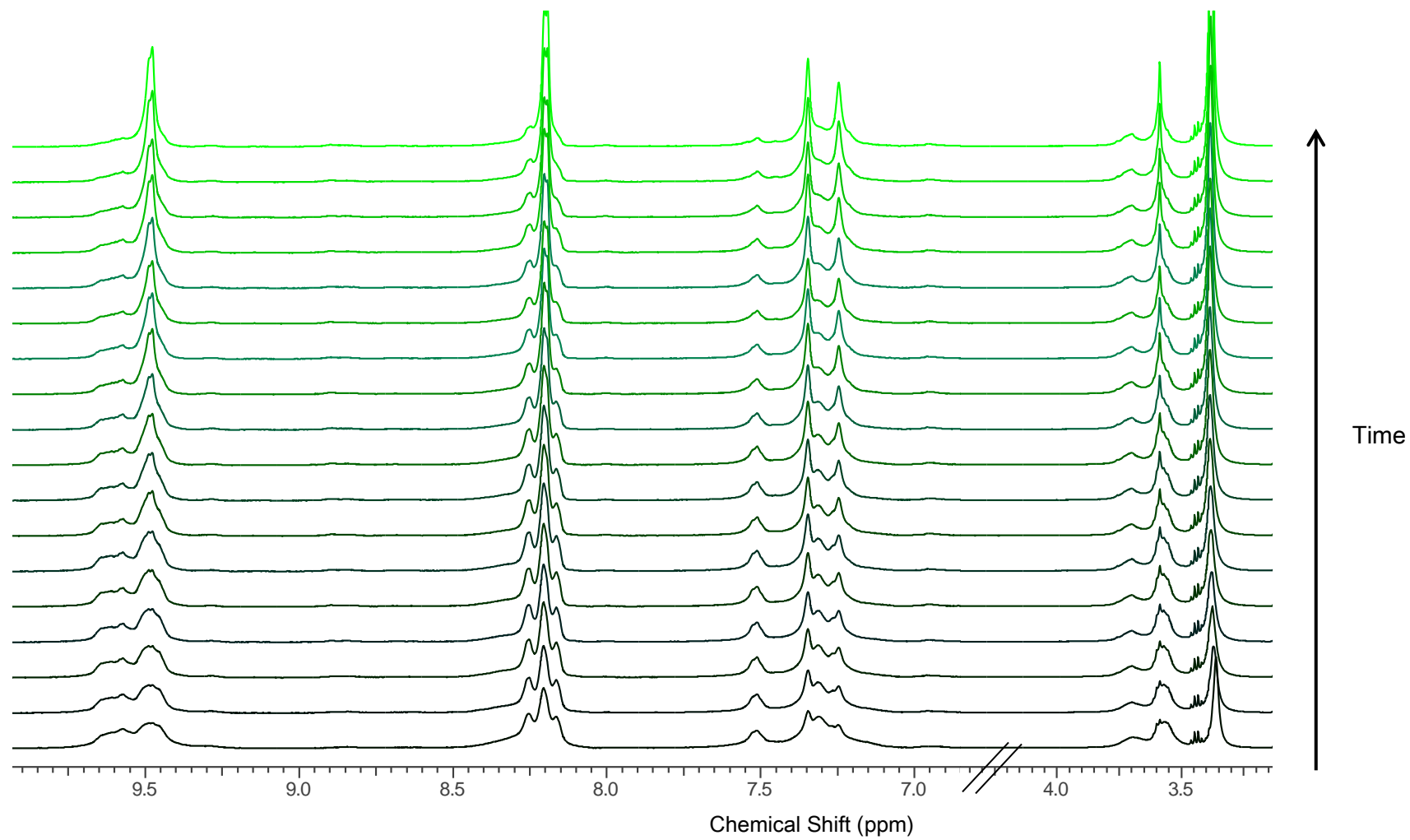


Figure 2.12 2.5 mM [Pd₆(L1)₈]₁₂(BF₄) stella octangula cage monitored over 748 hours. (293 K, 500 MHz, d₆-DMSO, referenced to TMS at 0.00 ppm)

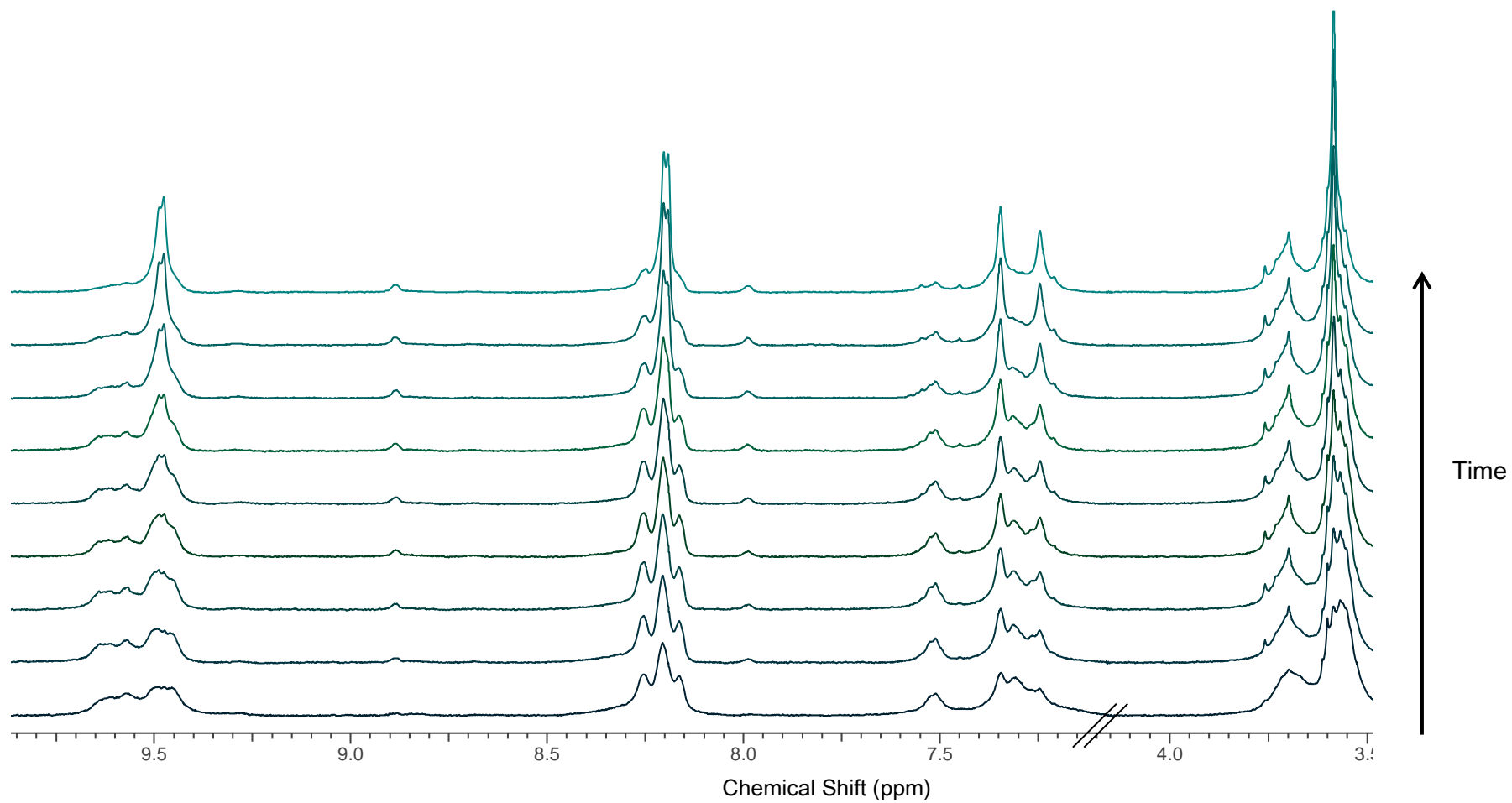


Figure 2.13 1.0 mM [Pd₆(L1)₈]₂·12(BF₄) stella octangula cage monitored over 343 hours. (293 K, 500 MHz, d₆-DMSO, referenced to TMS at 0.00 ppm)

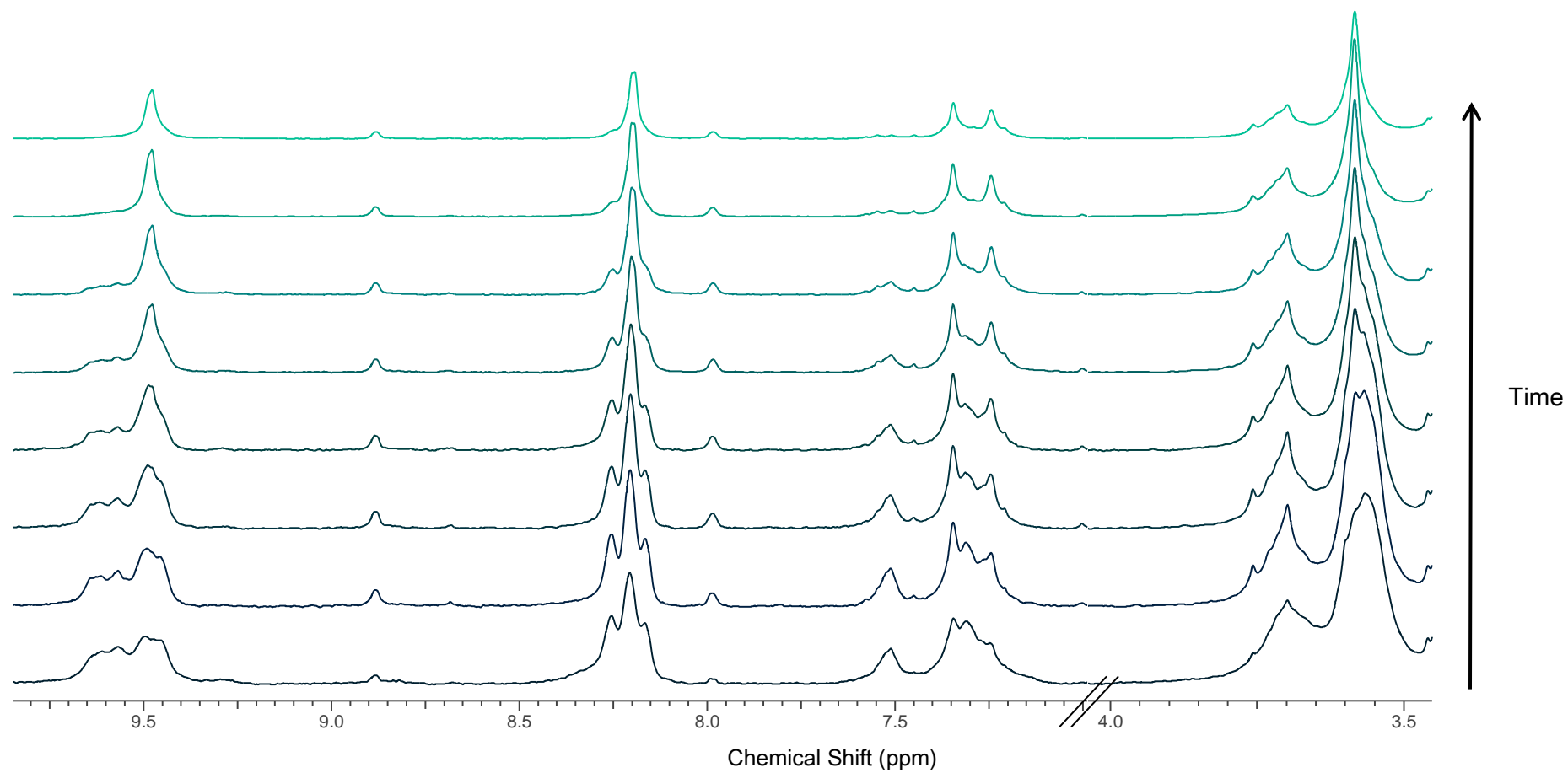


Figure 2.14 0.5 mM [Pd₆(L1)₄]-12(BF₄) stella octangula cage monitored over 255 hours. (293 K, 500, MHz d₆-DMSO, referenced to TMS at 0.00 ppm)

Blank Page

2.2.2.3 Samples Prepared with Aged Stocks

As discussed in section 2.1.2, the $[\text{Pd}_6(\text{L1})_8] \cdot 12(\text{BF}_4)$ stella octangula cage samples were produced by mixing fresh stock solutions in molar quantities. After the samples were made, any remaining stocks were stored under ambient conditions.

Several of these stock solutions that had been stored were originally used to prepare cage samples that became homochiral within 24 hours. This was prior to the issues arising with self-assembly documented in sections 2.2.2.1 and 2.2.2.2. Where there was a sufficient amount of stock solution remaining, samples were reproduced as two series of samples. The first was made with old stock solutions of both tetrakis(acetonitrile)palladium(II)tetrafluoroborate and L1 and its ^1H NMR spectrum is shown below in Figure 2.15.

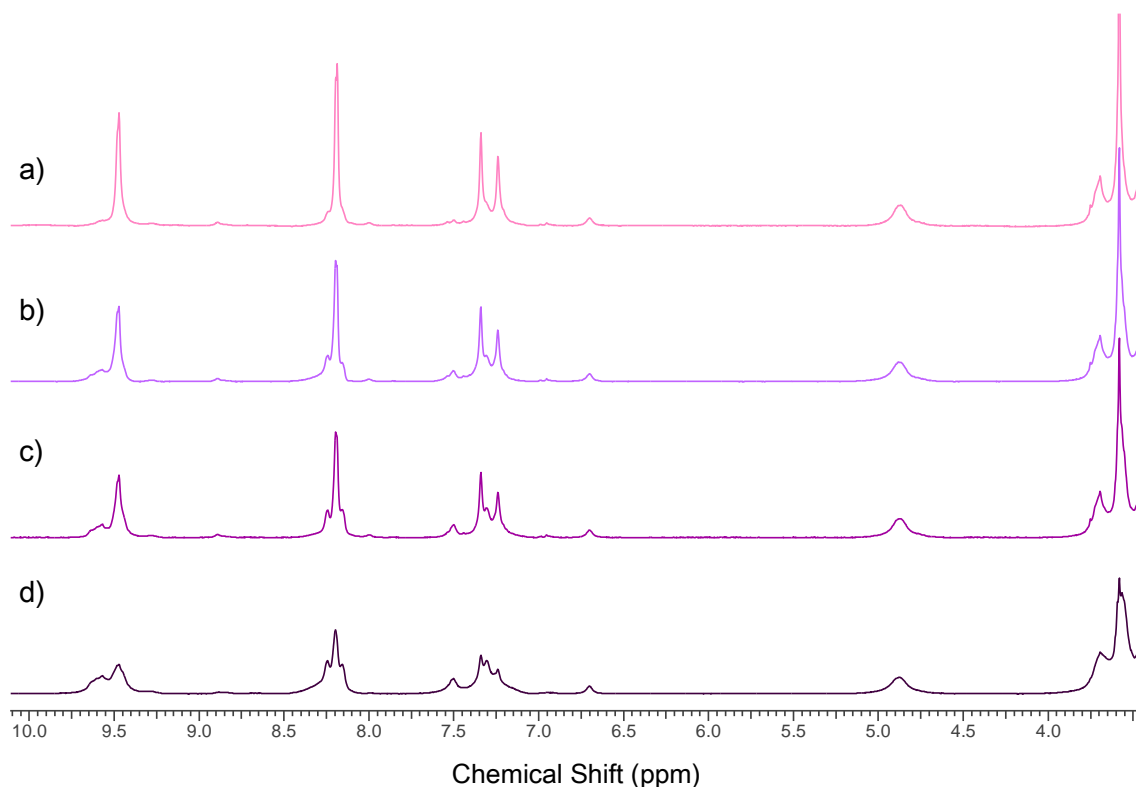


Figure 2.15 2.5 mM $[\text{Pd}_6(\text{L1})_8] \cdot 12(\text{BF}_4)$ stella octangula cage produced with old stocks monitored over time. a) is 144 H, b) is 48 H, c) is 24 H and d) is 0 H. (293 K, 500MHz, d_6 -DMSO)

The second set was made with an old stock solution of tetrakis(acetonitrile)palladium(II)tetrafluoroborate and a fresh L1 stock solution, ^1H NMR spectrum shown in Figure 2.16. These experiments were conducted to see if the problem rested with the ligand or the palladium solution. Both of these cage samples self-sorted into homochiral cages much faster than those made with fresh palladium stocks, that is, within one week. When the fresh ligand was used with the old palladium stocks, the homochiral cage was formed within 24 hours.

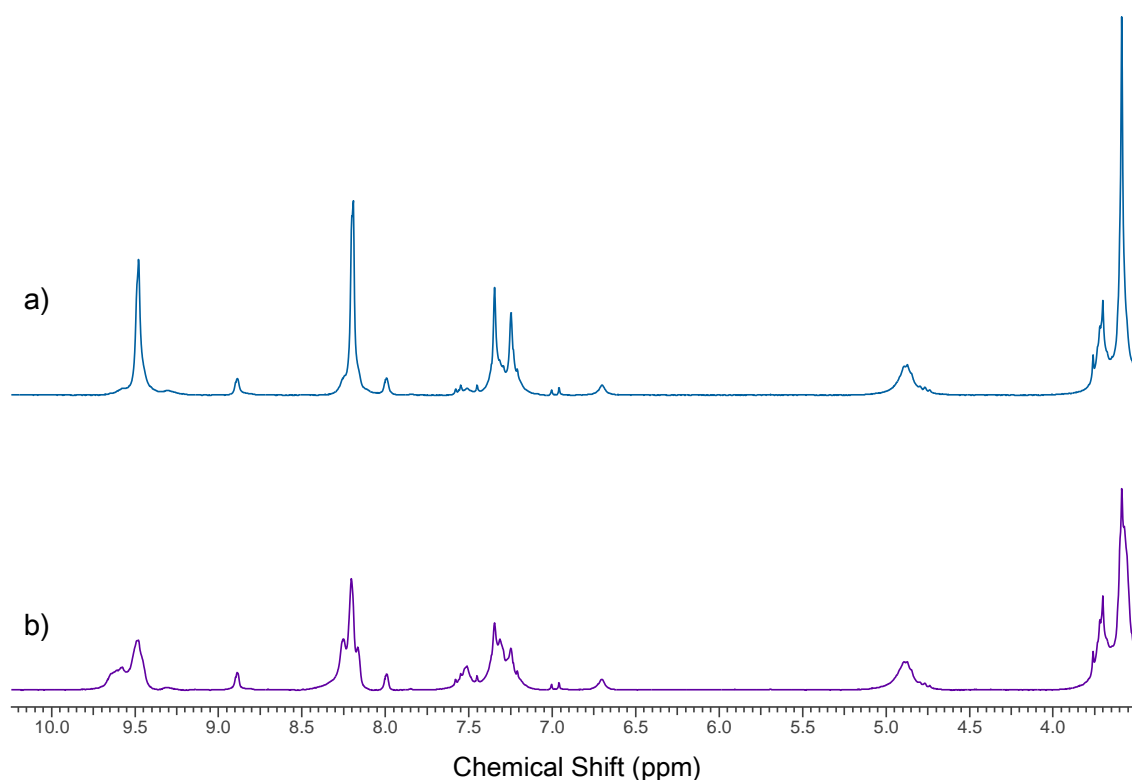


Figure 2.16 2.5 mM $[\text{Pd}_6(\text{L}1)_6] \cdot 12(\text{BF}_4)$ stella octangula cage produced with old Pd stock and fresh ligand stock. a) is 24 H and b) is 0 H. (293 K, 500MHz, d_6 -DMSO)

After consulting the literature, it was noted that the Fujita group had made use of the same palladium salt, but their approach to cage formation always involved heating the cage samples for a minimum of 90 minutes.^{107, 116, 123, 132} As heating solutions of cage, (solutions containing molar amounts of L1 ligand and palladium salt) had proven to be ineffectual (section 2.2.2.2), it was decided to see if heating the palladium salt alone, prior to mixing with the ligand, would enable the formation of homochiral assemblies. A

fresh stock solution of tetrakis(acetonitrile)palladium(II)tetrafluoroborate was heated to 90°C for 90 minutes and allowed to cool to room temperature before being added to some freshly prepared ligand stock and analysed. After 24 hours a spectrum was recorded which demonstrated formation of a homochiral cage, shown in Figure 2.17. However, it was noted that there was still some free ligand present and that the homochiral peaks shown in trace a) of Figure 2.17 are slightly broadened at their bases.

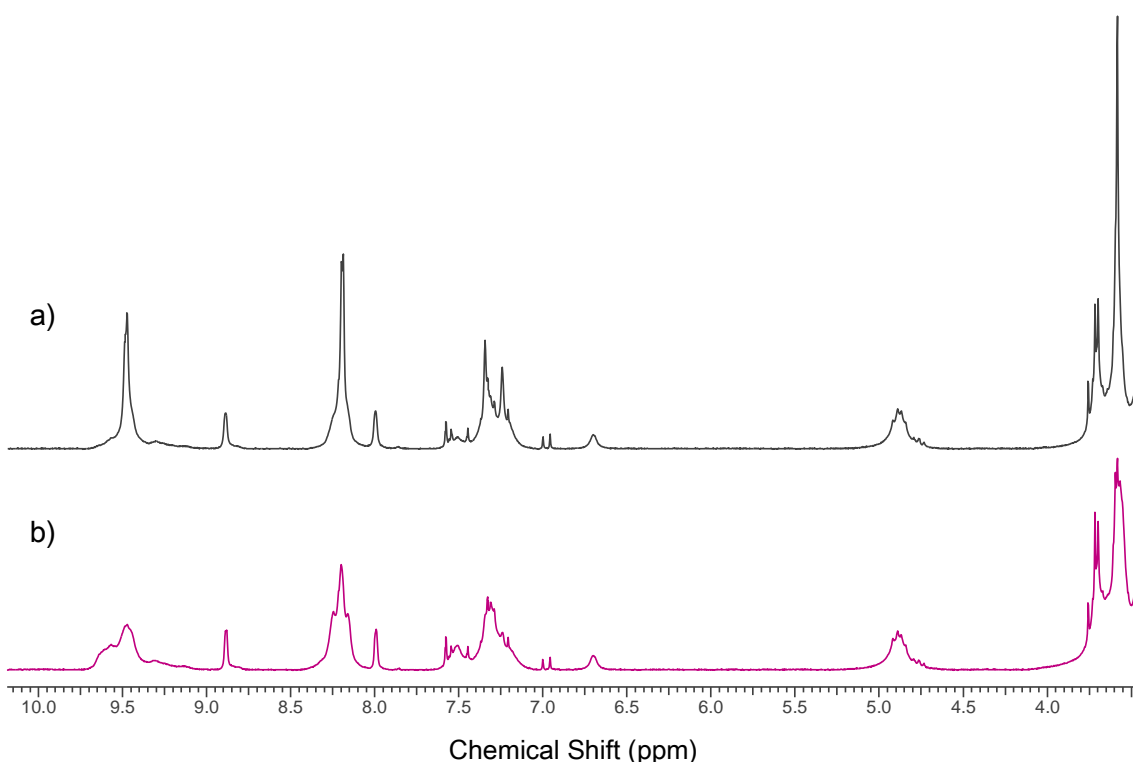


Figure 2.17 2.5 mM $[Pd_6(L1)_8] \cdot 12(BF_4)$ stella octangula cage produced with heated Pd and fresh ligand L1 monitored over time, a) is 24 H and b) is 0 H. (293 K, 500 MHz, d_6 -DMSO)

2.2.2.4 $[Pd_6(L1)_8] \cdot 12(BF_4)$ Stella Octangula Cage in Acetonitrile

To investigate the possibility that DMSO solvent was in competition with the ligand for the palladium cation, a sample of cage was prepared in α -acetonitrile. Acetonitrile was chosen as it is also a polar aprotic solvent like DMSO, but has a lower donor number (DN). The DN is a measure of nucleophilic behaviour. The DN of acetonitrile is 14.1

compared to 29.8 for DMSO.¹³⁵ It was hoped that the small difference between the solvents would have an effect on the self-assembly process of the stella octangula cage system and indicate if the DMSO was inhibiting the self-sorting of the cage.

Table 2.1 Solvent Properties for DMSO and Acetonitrile

Solvent	Dielectric Constant ¹³⁶	Dipole Moment ¹³⁷	Density	Donor Number ¹³⁵	Acceptor Number ¹³⁵
	ϵ_r	$\mu \cdot 10^{30}/\text{Cm}$	$\rho \text{ g cm}^3$	DN	AN
DMSO	46.7	13.0	1.1000 ¹³⁸	29.8	19.3
Acetonitrile	37.5	13.5	0.7767 ¹³⁹	14.1	19.3

This investigation indicated that DMSO was in competition with the L1 for the palladium(II) cation, as the ¹H NMR spectrum of [Pd₆(L1)₈]·12(BF₄) stella octangula cage in *d*₃-MeCN does not show any evidence of self-sorting over time. The spectrum (Figure 2.18), is asymmetric, indicating that the product formed is not as symmetrical as the most thermodynamically stable product formed in DMSO. When compared to the ¹H NMR spectrum of the [Pd₆(L1)₈]·12(BF₄) stella octangula cage in *d*₆-DMSO shown in Figure 2.4, it can be seen that all of the cage peaks were considerably broadened (the pyridine peaks in particular) and are not indicative of the highly symmetrical environment of a homochiral cage system. A mass spectrum was recorded for this sample which was highly indicative of a [Pd₆(L1)₈]·12(BF₄) stella octangula cage system in the gaseous phase. However, because of the appearance of the ¹H NMR spectrum, it was decided not to pursue this system in this solvent, as the system was not homochiral.

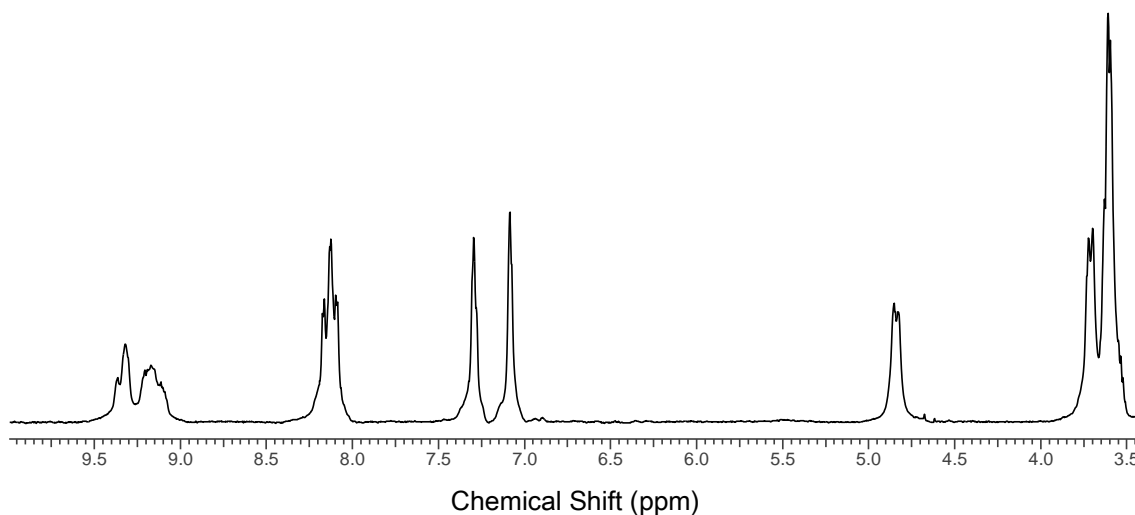


Figure 2.18 ^1H NMR spectra of $[\text{Pd}_6(\text{L1})_8] \cdot 12(\text{BF}_4)$ stella octangula cage.
(293 K, 500 MHz, d_3 -MeCN)

With the problems surrounding the production of a single species of cage resolved, the stella octangula cage system could now be used to investigate the host-guest interaction between the cage and sodium alkyl sulfate guests.

2.3 Results

2.3.1 Solution Properties of Sodium Dodecyl Sulfate (SDS)

Prior to the encapsulation studies, the solution properties of SDS in d_6 -DMSO alone were investigated. The aim of this was to learn about the solution properties of SDS, to gather data to provide comparison to host-guest samples and to ensure that any interactions that were observed with the cage complex were due to cage complex-SDS interactions. This involved a ^1H NMR titration study, a temperature variation study, diffusion measurements performed with DOSY NMR and two Job's plot type analyses, one with SDS and the L1 ligand and the other with SDS and tetrakis(acetonitrile)palladium(II)tetrafluoroborate.

In the titration study, no chemical shift change was observed with increasing concentration. SDS was found to be stable up to 60°C. Although the peaks at 60°C were not as well defined as those at the lower temperatures; the multiplicities of the peaks were maintained, implying that the molecule had not broken up with the increase in temperature. The diffusion coefficient of SDS at 1 mM was recorded at $2.483 \pm 0.008 \times 10^{-10} \text{ m}^2 \text{ s}^{-1}$ in d_6 -DMSO at 293 K. In the two Job's plot type analyses, the ^1H NMR data was recorded; however, the Job's treatment was not applied to these data, as no change in chemical shift was observed. This strongly suggested that SDS did not interact with free ligand in solution and nor did it interact with the palladium salt.

Of the four different proton environments shown in the SDS spectrum [Figure 2.6 b)], the H4 peak of the methyl tail group, at 0.85 ppm is considered to be the most useful. The H2 signal at 1.47 ppm does not have well defined multiplicity and is the lowest intensity signal of all four proton environments, meaning that the error associated with the chemical shift change for this multiplet would be greatest of the four signals. The signals at 3.66 and 1.24 ppm unfortunately overlap with signals in the cage complex spectrum, with the endo proton of the CTV bowl and a contaminant in the ligand respectively.

After concluding these studies into the solution properties of SDS, a considerable amount has been ascertained about handling this compound and its behaviour in d_6 -DMSO solution. These data were also used in comparison with the host-guest complexes.

2.3.2 Investigation of Stoichiometry of the $[\text{Pd}_6(\text{L1})_8] \cdot 12(\text{BF}_4)$ Stella Octangula Cage and Sodium Alkyl Sulfate Host-Guest Complexes

To firmly establish the stoichiometry of the host-guest systems, fresh samples were prepared to perform a Job's plot analysis. A Job's plot requires the sum of the $[\text{H}]_0$ and $[\text{G}]_0$ to be kept constant, whilst systematically varying the ratios of host to guest.⁶ To perform a Job's plot for NMR data, chemical shift is plotted against the volume fraction of the host, that is $[\text{H}]_0/([\text{H}]_0+[\text{G}]_0)$, when $[\text{H}]_0$ is the host concentration and $[\text{G}]_0$ is the guest concentration. The maximum or minimum occurs at a ratio of $[\text{H}]_0/([\text{H}]_0+[\text{G}]_0)$ corresponding to the combining ratio of host to guest, which expresses the host-guest ratio.^{6, 140}

If the concentration of the host-guest complex cannot be measured directly, the y-axis of the Job's plot can be replaced with a parameter that is proportional to the host-guest system. This is the case for the stella octangula cage:SDS system. Therefore, the corrected guest chemical shift multiplied by the molar fraction of the guest was plotted, as this is representative of the cage:SDS system. For the cage:SOS system, SOS peaks H1, H2 and H4 were plotted. For cage systems with SDS and STS guests, all four guest peaks were used.

For each sodium alkyl guest, 11 samples were prepared with a total fixed concentration of 2.5 mM. This concentration was selected as the total fixed concentration because at cage concentrations below 0.2 mM the spectra become difficult to analyse accurately, as demonstrated in section 2.2.2.1. If 2.5 mM total fixed concentration is used, then the lowest cage concentration is 0.25 mM, avoiding any associated issues with analysing these spectra.

The Job's plots are shown below in Figure 2.19. The Job's plots for all three sodium alkyl guests show the same maximum at 0.33. This is indicated by the line in Figure 2.20. If the maximum is at 0.33, it indicates a three-part system, and in this instance there is 1 host molecule to 2 guest molecules. Although the results from the Job's plot are highly consistent, Job's plots for stoichiometries other than 1:1 are not considered reliable.¹⁴¹ As a consequence of this, other methods including the fitting of association constants and diffusion measurements were used to verify the information provided from the Job's plot analysis.

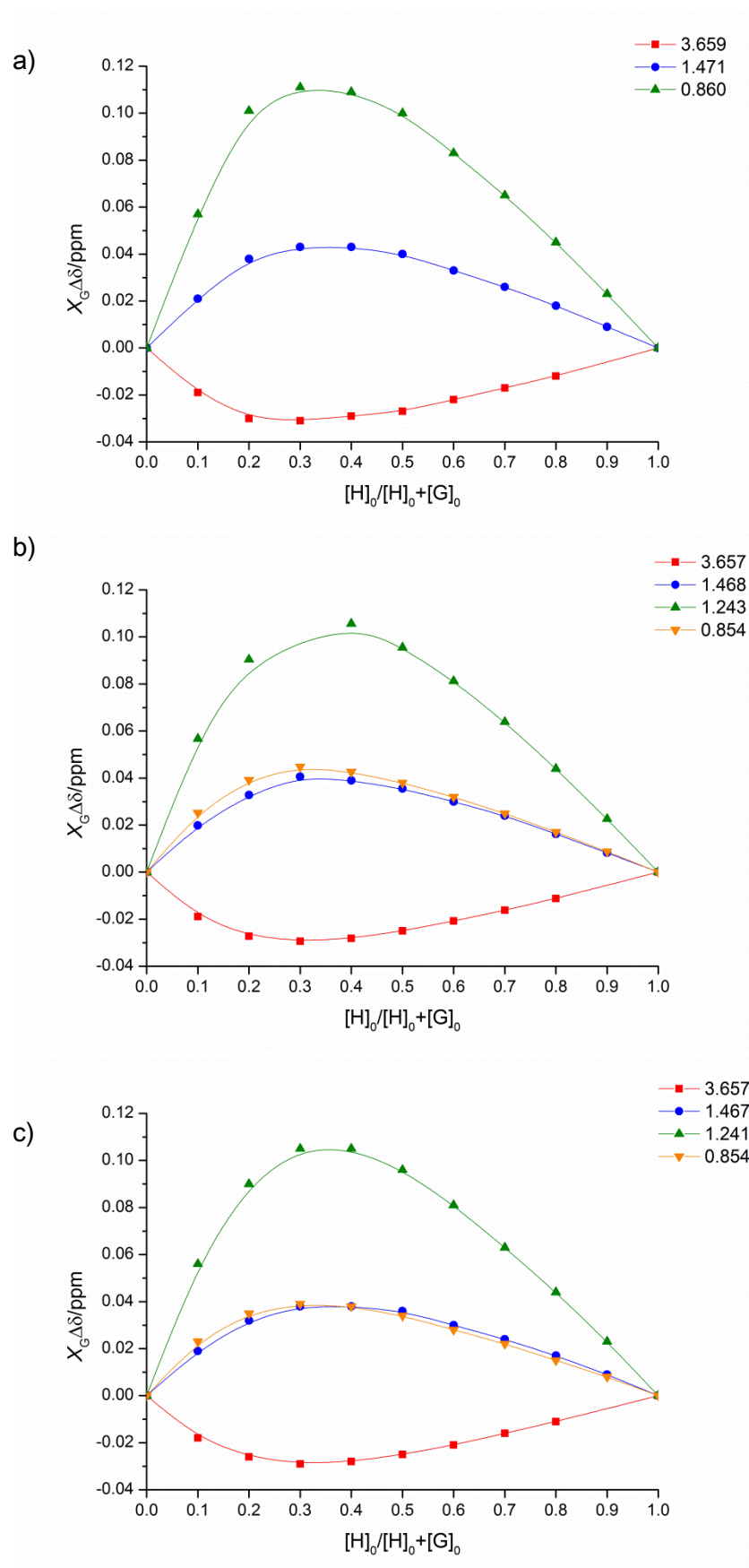


Figure 2.19 Job's plots for the $[Pd_6(L)_6]-12(BF_4)_x$ stella octangula cage & sodium alkyl guest systems. Legends show chemical shifts plotted. a) SOS, b) SDS and c) STS.

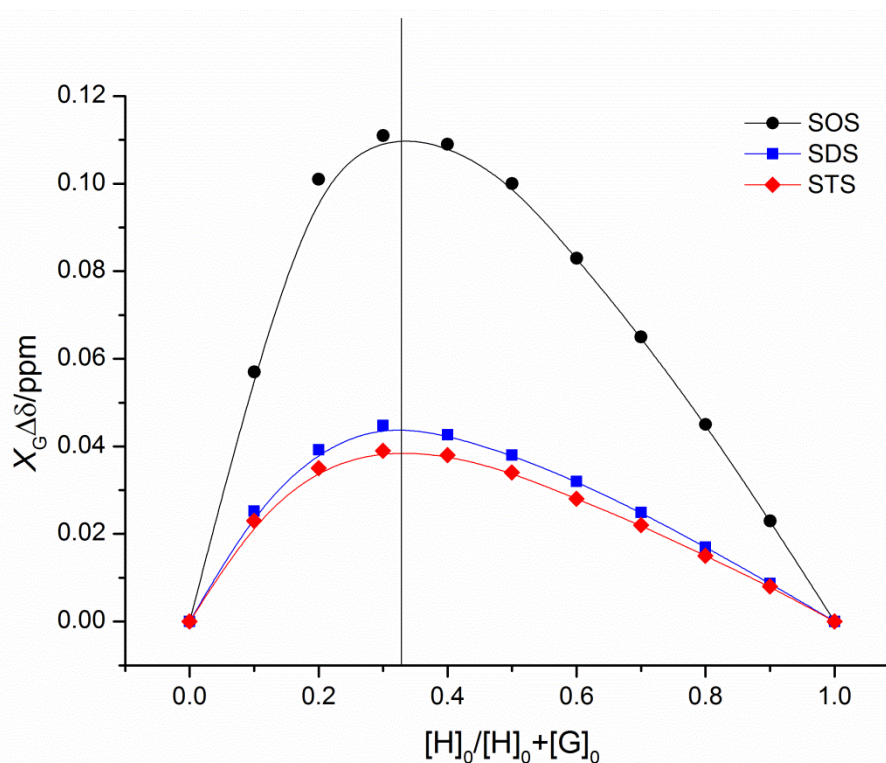


Figure 2.20 Comparison of Job's plots for the $[Pd_6(L1)_8] \cdot 12(BF_4)$ stella octangula cage & sodium alkyl guest systems for of all three guests using the plot of the methyl tail group proton shifts with a line to indicate the 0.33 maximum.

2.3.3 ¹H NMR Titration Studies of Stella Octangula Cage and Sodium Alkyl Sulfate Guest Complexes

Three sets of samples with the host concentration fixed at 0.5 mM were prepared to study with ¹H NMR spectroscopy, one set for each guest. Each set contained seven samples with guest concentrations ranging from 0.5 - 10.0 mM. The data from these analyses were used to fit binding constants for the host-guest systems and samples from this series were also used to collect DOSY and ROESY data. The ¹H NMR spectra from these experiments are shown in Figure 2.21 - Figure 2.23. Sodium octyl sulfate showed the largest change in chemical shift, this was seen for the methyl H4 peak, which had a shift difference of 0.15 ppm when compared with SOS with no cage present

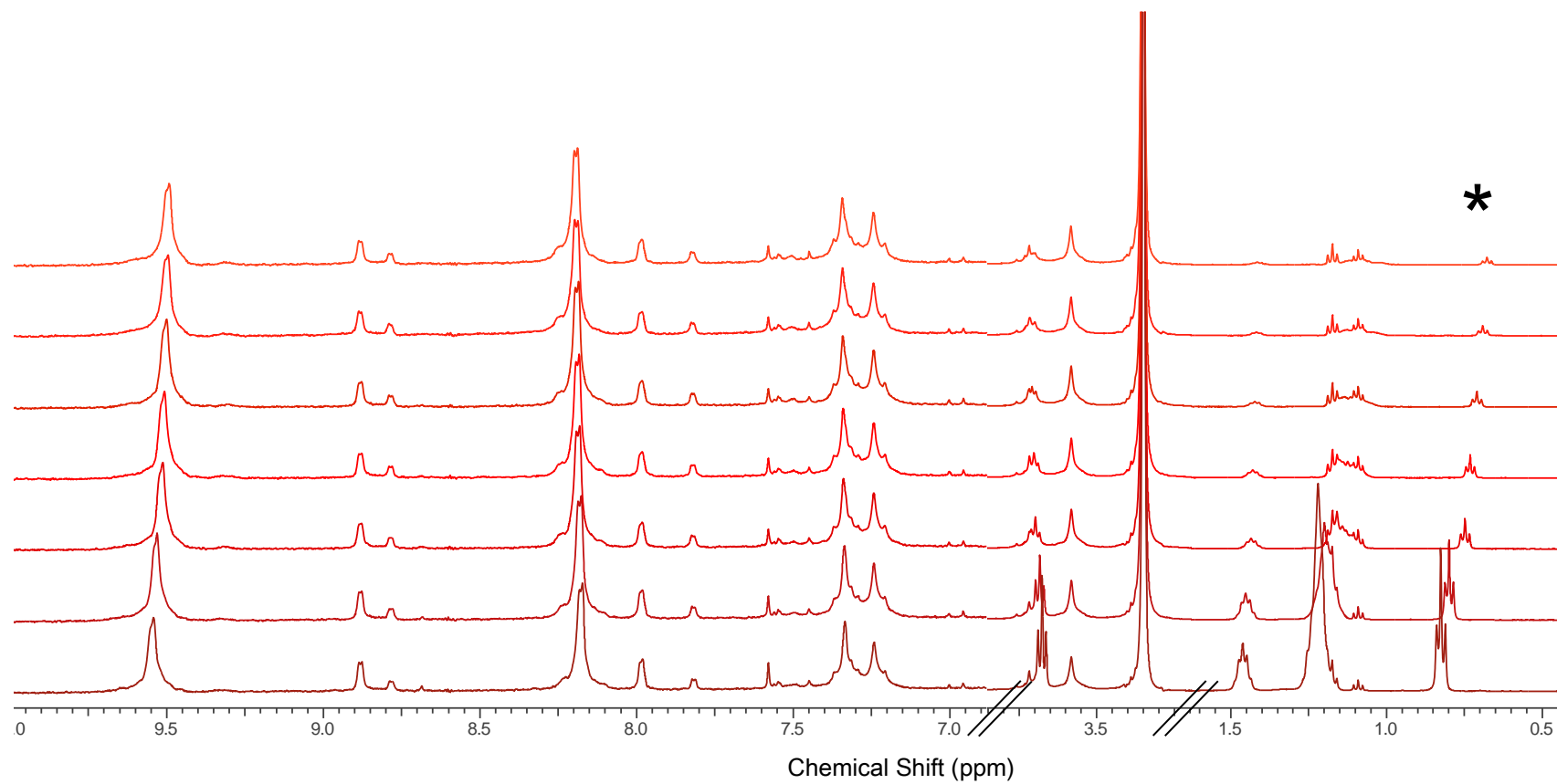


Figure 2.21 ¹H NMR spectra of [Pd₆(L1)₈]-12(BF₄) stella octangula cage:SOS titration study, () asterisk indicates methyl H4 peak. (293 K, 500 MHz, d₆-DMSO)*

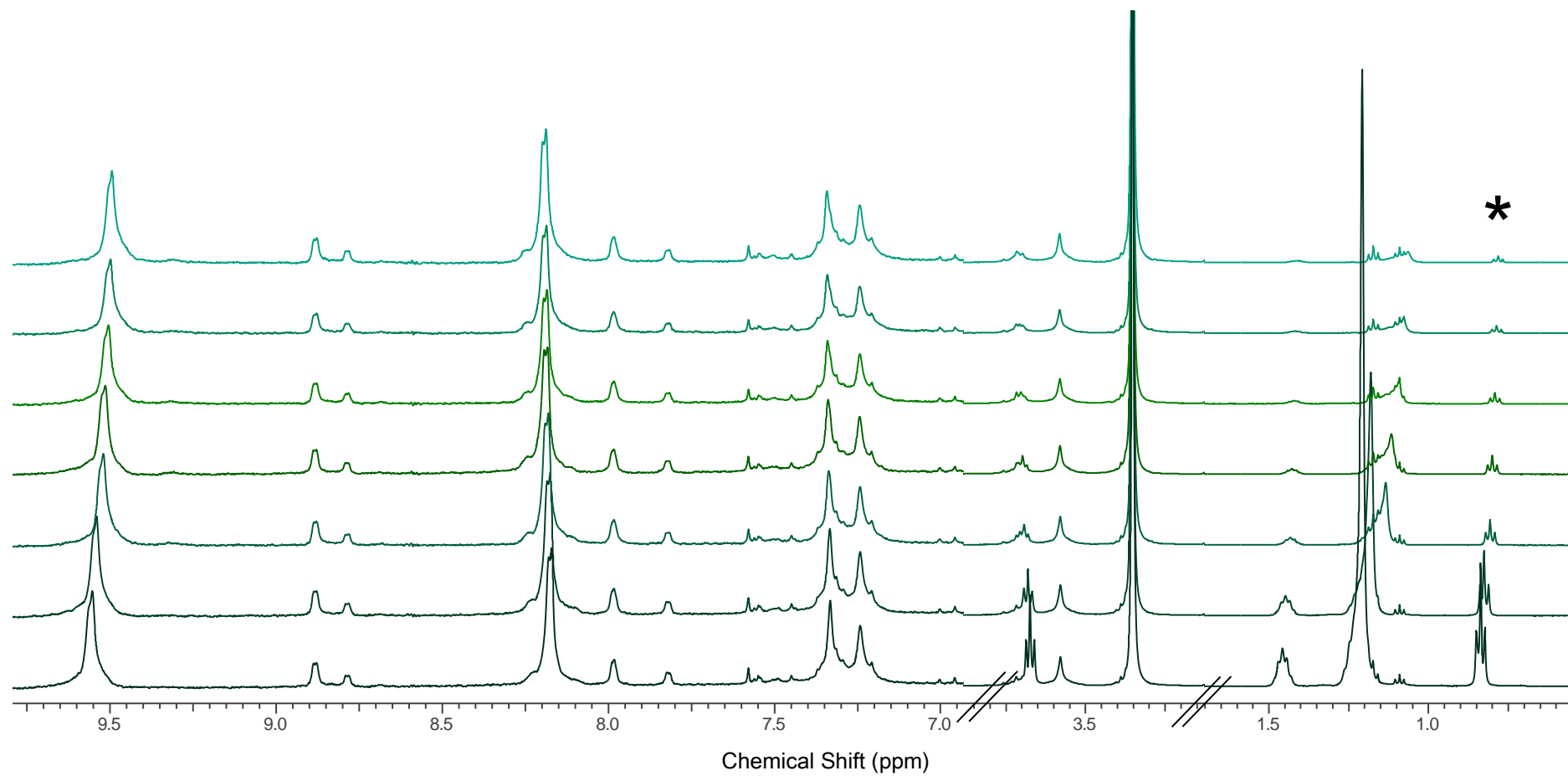


Figure 2.22 ^1H NMR spectra of $[\text{Pd}_6(\text{L}1)_8] \cdot 12(\text{BF}_4)$ stella octangula cage: SDS titration study, (*) asterisk indicates methyl H4 peak. (293 K, 500 MHz, d_6 -DMSO)

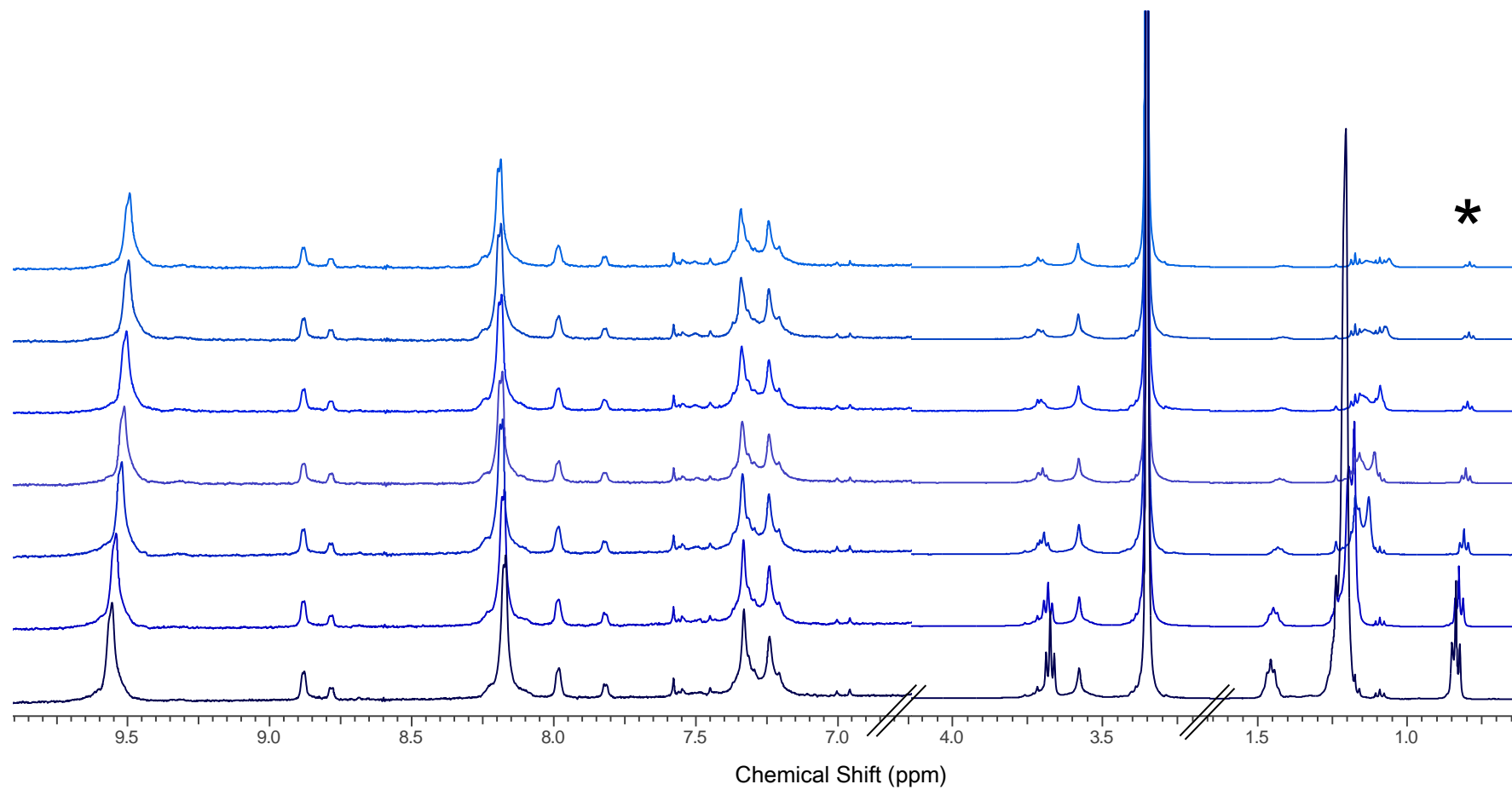


Figure 2.23 ¹H NMR spectra of [Pd₆(L1)₆]-12(BF₄) stella octangula cage:STS titration study, (*) asterisk indicates methyl H4 peak. (293 K, 500 MHz, d₆-DMSO)

Blank Page

2.3.3.1 Determination of Association Constants for the [Pd₆(L1)₈]·12(BF₄) Stella Octangula Cage and Sodium Alkyl Sulfate Guest Host-Guest Complexes

The binding constants of the host-guest systems were fitted using the HypNMR 2008¹⁴² programme. The chemical shift data of the titration studies were used for these calculations. Both cage and guest chemical shifts were used, as it was imperative to use as many data points as feasibly possible, to achieve the best fit. The peaks used were Ha/a' and Hb/b' of the host molecule and all four peaks of the guest molecules. For SDS and STS, the Hd peak of the cage complex was also used. The fitted cumulative association constants β are listed in Table 2.2. It is important to note that the β_2 is a cumulative association constant, not a stepwise constant. The first association constant ($K_{a1} = \beta_1$) for all three guests were higher (ca. 10^4 M^{-1}) than that of the second stepwise constant K_{a2} , which can be roughly calculated by dividing β_2/β_1 . This gives small K_{a2} values of approximately 10^2 M^{-1} .

To achieve fitting, the HypNMR software needs to be instructed as to the stoichiometry of the reaction it is fitting for. For these systems, attempts were made at fitting 1:1 and 1:3 host-guest ratio. However, fitting could not be achieved with these stoichiometries; it could only be achieved for the 1:2 host-guest ratio, lending further support to the hypothesis of a 1:2 host-guest interaction. Figure 2.24 shows the fitting for the Ha/a' proton of the host-guest systems. These plots indicated that although there are 1:2 host-guest complexes, most of the guest was free in solution

Table 2.2 Fitted cumulative association constants for the host-guest systems.

Guest	β_1/M^{-1} (H+G \leftrightarrow HG)	β_2/M^{-2} (H+2G \leftrightarrow HG ₂)
SOS	$(5.0 \pm 0.4) \times 10^3$	$(10.0 \pm 1.3) \times 10^5$
SDS	$(2.0 \pm 0.7) \times 10^3$	$(5.0 \pm 0.3) \times 10^5$
STS	$(1.0 \pm 0.6) \times 10^3$	$(1.3 \pm 0.2) \times 10^5$

The uncertainties are estimates of the standard deviation calculated by HypNMR¹⁴²

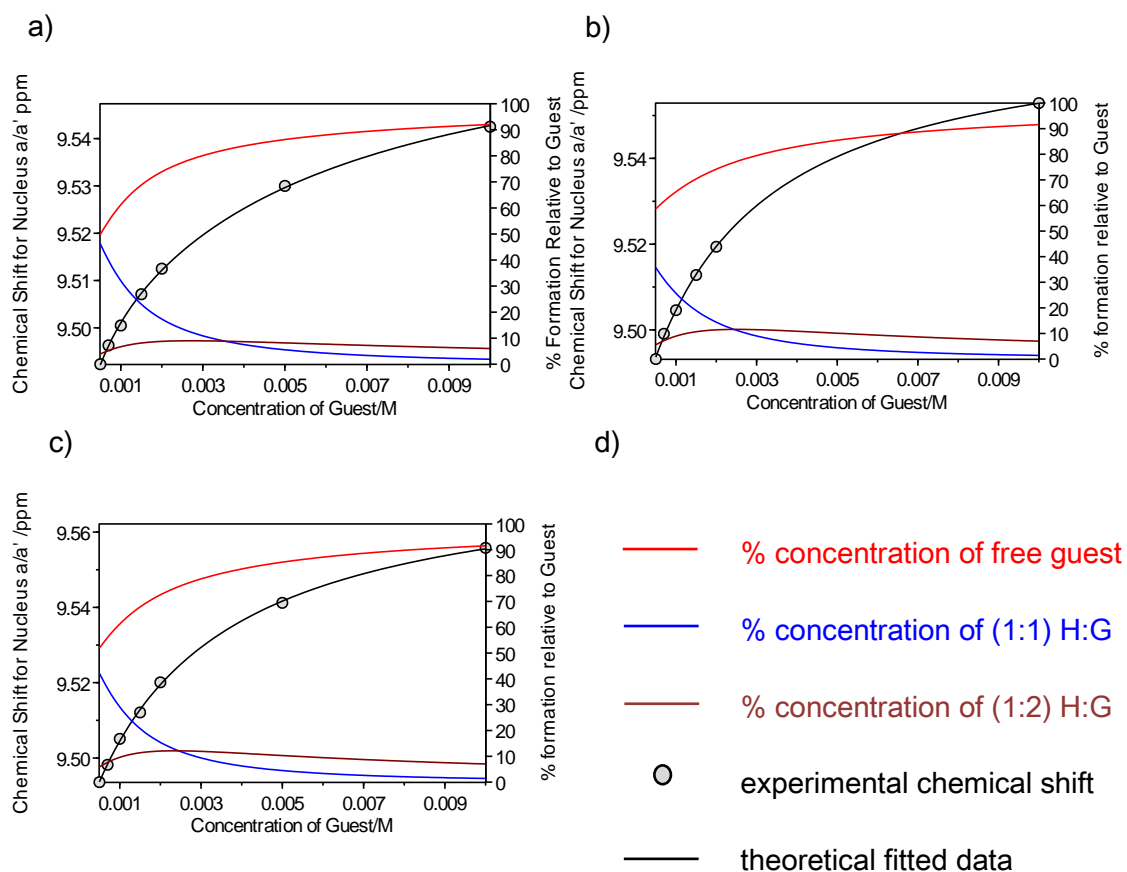


Figure 2.24 Fitting of the ¹H NMR titration data for the [Pd₆(L1)₈]¹²⁺ stella octangula cage and sodium alkyl sulfate guests. Fitting shown is for the Ha/a' proton. a) SOS, b) SDS, c) STS, d) legend for plots.

2.3.4 Investigation of Association Using Diffusion Coefficients of the [Pd₆(L1)₈].12(BF₄) Stella Octangula Cage and Sodium Dodecyl Sulfate Host-Guest Complex

Diffusion measurements were recorded for a variety of [Pd₆(L1)₈].12(BF₄) stella octangula cage and SDS complexes. It was anticipated that the diffusion coefficient measured for the cage would be unaffected with the change in SDS concentration and this was borne out by the experimental results. The diffusion coefficient for SDS however, changed substantially from $2.483 \pm 0.008 \times 10^{-10} \text{ m}^2 \text{ s}^{-1}$ when measured in isolation from the cage to as low as $1.387 \pm 0.019 \times 10^{-10} \text{ m}^2 \text{ s}^{-1}$ for the highest host-guest ratio. The plot of diffusion coefficient against the host-guest ratio is shown in Figure 2.25. It can be seen from the plot that the diffusion coefficient for the SDS reached a plateau as the saturation point of the cage was reached. This saturation point was at the [H]/[G] ratio of 0.5, which again indicated a 1:2 host-guest stoichiometry. When the concentration of SDS was high, its diffusion coefficient was nearly the same as the isolated SDS. It was not exactly the same because a small amount of the SDS present in solution will be interacting with the cage system and the diffusion coefficient is a time-averaged signal of the free SDS and the encapsulated SDS. If all the SDS were unbound then its diffusion coefficient would be the same as for isolated SDS.

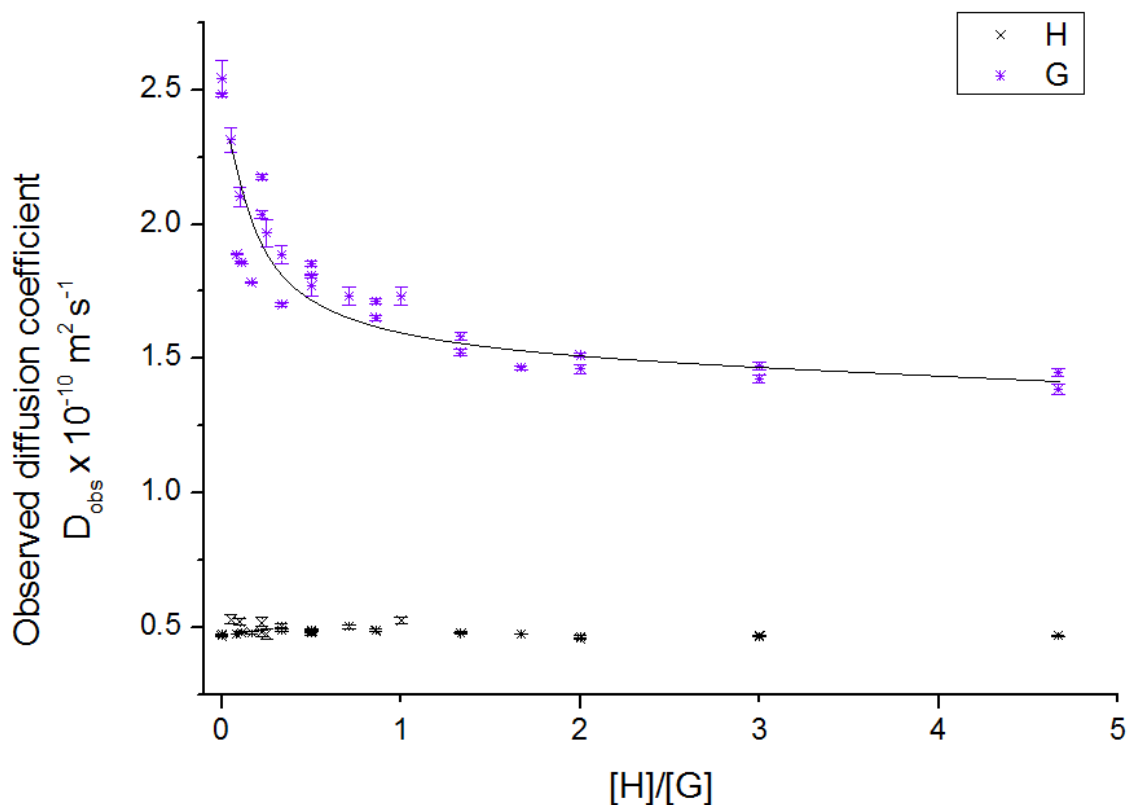


Figure 2.25 Plot of diffusion coefficient against the concentration ratio $[H]/[G]$ for the $[Pd_6(L1)_8] \cdot 12(BF_4)$ stella octangula cage and SDS complex.

2.3.5 Through-Space Connections in the $[Pd_6(L1)_8] \cdot 12(BF_4)$ Stella Octangula Cage and Sodium Alkyl Sulfate Host-Guest Complex

The ROESY experiment examines rotating-frame nOes, which provide information regarding the spatial proximity between protons.¹⁴³ ROESY experiments were performed on a sample of cage and samples of cage:SDS and cage:SOS. These analyses were performed to investigate how the sodium alkyl sulfates interacted with the $[Pd_6(L1)_8] \cdot 12(BF_4)$ stella octangula cage. Because although a 1:2 host-guest “association” has been firmly established, the nature of the interaction has not yet been determined; i.e. that is, whether the interaction is one with the exterior of the cage or with the interior of the cage cavity.

The $[Pd_6(L1)_8] \cdot 12(BF_4)$ stella octangula cage is configured such that the hydrogens of the pyridyl groups are pointing into and out of the cage (due to rotation around the CO-C bond between the ester linkage and the pyridyl group) lying perpendicular to the palladium and the hydrogens of the methyl linkers of the CTV bowl are pointing outwards, away from the internal cavity, as shown in Figure 2.26 below.

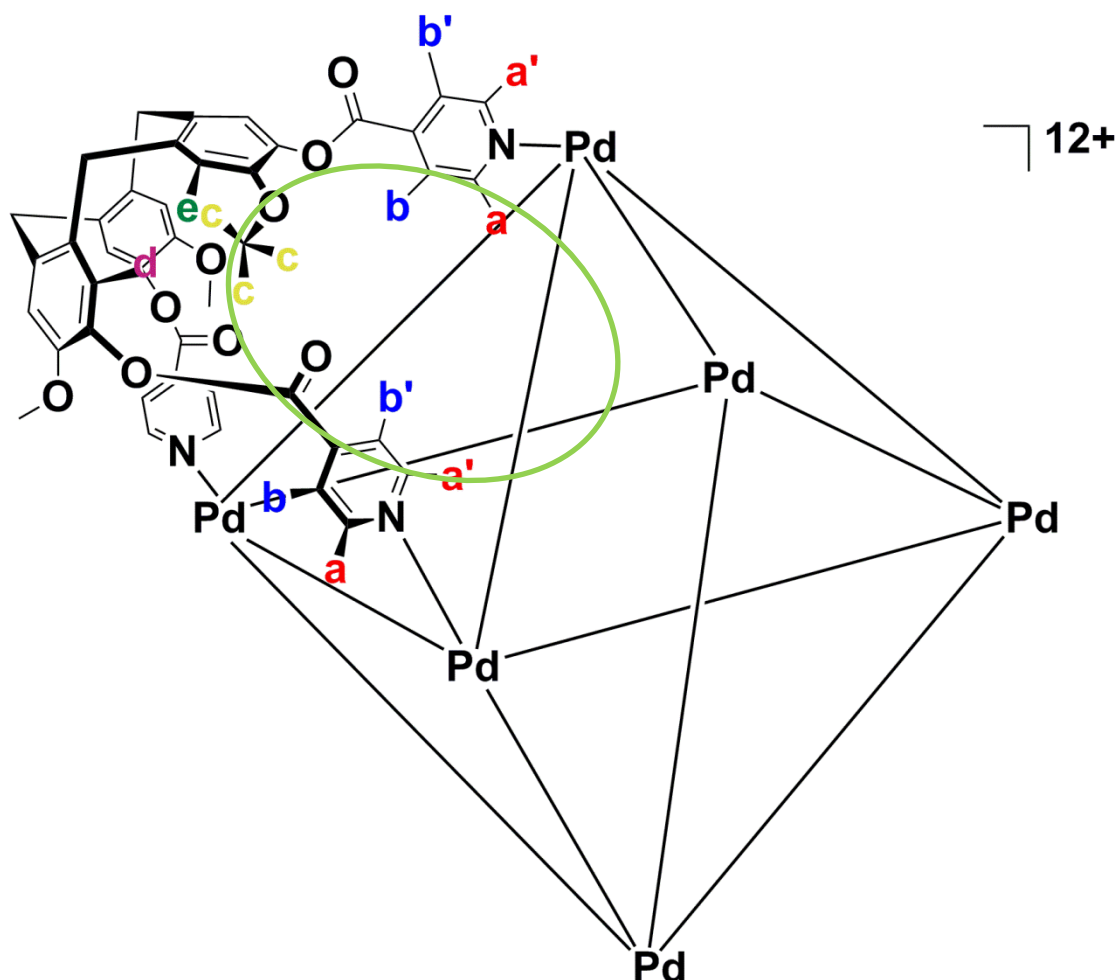


Figure 2.26 the $[Pd_6(L1)_8]^{12+}$ cage, with only one ligand illustrated to demonstrate the orientation of the pyridyl, aryl and methoxy groups with regards to the cavity. The cavity is indicated by the green oval.

The ROESY spectra in Figure 2.27 showed interactions between SDS and the pyridyl group of the cage. This was a definite indication of the SDS being inside the cage cavity. If the SDS was interacting with the external surface of the cage, through-space connections would be expected between SDS and the CTV bowl of the cage. It would

also be expected that if the SDS was interacting by charge attraction outside the cage, then the hydrophobic chain portion of the SDS would be moving freely in solution; if there was any residence time near the cage, than nOes would be expected to connect the SDS to the aryl group, However, a through-space connection was seen between Hd and H1 (a proton of the benzene ring of **L1** and the methylene group closest to the polar head of SDS respectively). These through-space connections with the aryl protons were rationalised as being indicative of the guests passing into the cage windows, since those protons can be considered as part of the window. Interactions were also seen between all of the SDS protons and the Hb/b' protons of the cage. Through-space connections could also be seen with Ha/a', Hd and He protons of the cage system, but no through-space connections were seen between the guest molecules and the CTV-bowl of the cage.

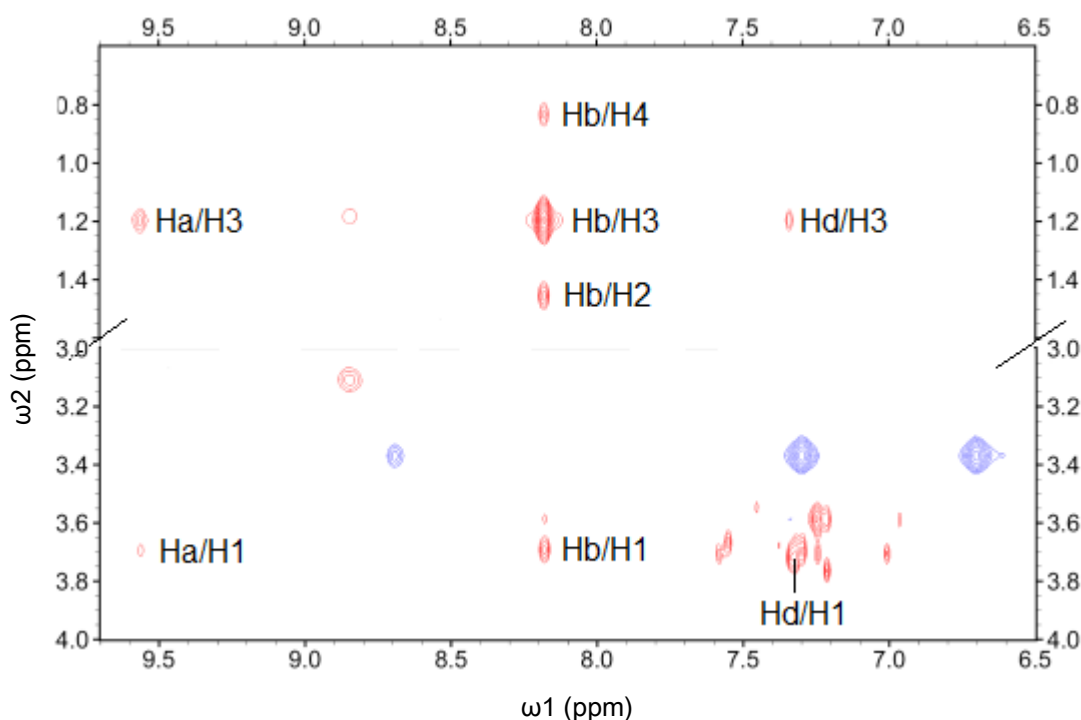


Figure 2.27 Section of a 2-D ROESY spectrum for a 1:10 cage:SDS mixture with through space connections in red and exchange peaks in blue. (293 K, 500 MHz, d_6 -DMSO)

The spectrum for the cage:SOS host-guest system is shown in Figure 2.28, this spectrum was very similar to that of the cage:SDS system, which strongly implied that the guests were behaving in the same manner. For the cage:SOS spectrum a connection was observed between the H2 and H3 protons of the SOS and the Hc protons of the cage. The Hc protons are the methoxy group attached to the aryl ring of the cage system, which as can be seen in Figure 2.26 is in the cage portal opening. It was established in section 2.3.1 that there was no interaction between SDS (and presumably SOS and STS) and the ligand, this was further confirmed by the ROESY analyses, which showed no through-space connections between the small amounts of free ligand present in the samples and the guest molecules.

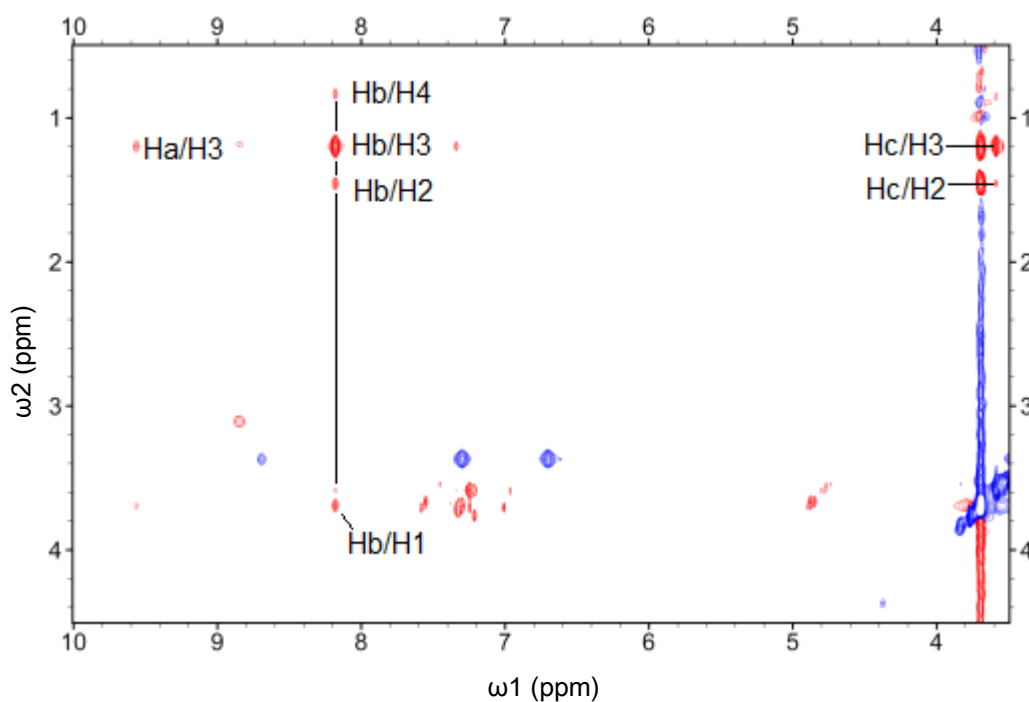


Figure 2.28 Section of a 2-D ROESY spectrum for a 1:20 cage:SOS mixture with through space connections in red and exchange peaks in blue. (293 K, 500 MHz, d_6 -DMSO)

2.3.6 Mass Spectroscopic Analysis of the Stella Octangula Cage and SDS

Host-Guest Complex

Electrospray ionisation mass spectroscopy (ESI-MS) was also used to verify that the cage and the host-guest complex with SDS had been formed in solution. Ronson and co-workers also used this technique to provide the same evidence for the $[\text{Pd}_6(\text{L1})_8] \cdot 12(\text{NO}_3)$ stella octangula cage.¹¹⁰ Taking into account the different anions, the ESI-MS spectrum of the $[\text{Pd}_6(\text{L1})_8] \cdot 12(\text{BF}_4)$ stella octangula cage was identical to the spectrum recorded by Ronson and co-workers. A series of signals at m/z 1780.6, 1407.2, 1158.0, 979.5 and 846.1 can be assigned to $[\{\text{Pd}_6(\text{L1})_8\}(\text{BF}_4)_{(12-x)}]^{x+}$ (where $x = 4, 5, 6, 7, 8$). These signals resulted from the octahedral core of the stella octangula cage, but with different numbers of anions present. Figure 2.29 shows the ESI-MS of the $[\text{Pd}_6(\text{L1})_8] \cdot 12(\text{BF}_4)$ stella octangula cage with 10 equivalents of SDS guest present. Various adducts containing SDS can be seen, providing more evidence for a host-guest interaction between the $[\text{Pd}_6(\text{L1})_8] \cdot 12(\text{BF}_4)$ stella octangula cage and SDS.¹¹¹

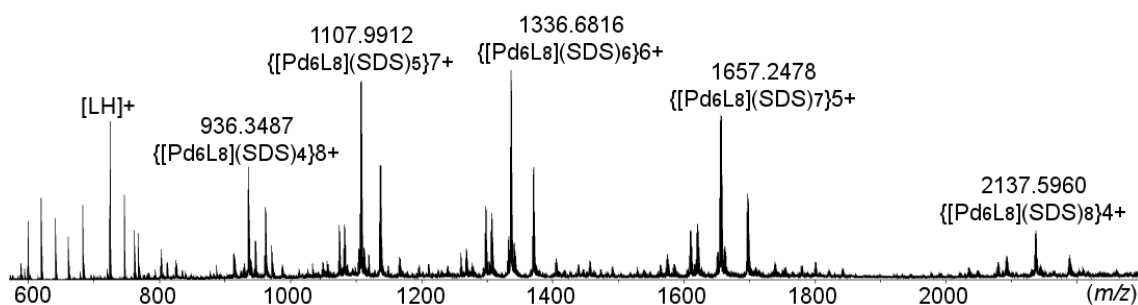


Figure 2.29 ESI-MS of $[\text{Pd}_6(\text{L1})_8] \cdot 12(\text{BF}_4)$ stella octangula cage with 10 equivalents of SDS

2.4 Discussion

2.4.1 Self-Assembly of the $[\text{Pd}_6(\text{L1})_8] \cdot 12(\text{BF}_4)$ Stella Octangula Cage

Although self-assembly is a rapid process,^{3, 4} the $[\text{Pd}_6(\text{L1})_8] \cdot 12(\text{BF}_4)$ stella octangula cage, it sometimes took a considerable amount of time for the cage to “sort” itself chirally and this process was dependent on cage concentration.

Self-assembly is the spontaneous association of molecules and/or ions to create larger aggregate species.^{3, 134} One important aspect of self-assembly is the ability of these constructs to correct errors during their formation and develop into being the most thermodynamically stable product.³ The L1 ligand is a tris-substituted CTV derivative. Tris-substitution results in a chiral ligand and when used to for cage formation results in a chiral cage complex. The most thermodynamically stable arrangement for the stella octangula cage is when each individual $[\text{Pd}_6(\text{L1})_8]^{12+}$ stella octangula cage self-assembles with eight ligand molecules of the same chirality. This results in a racemic mixture of both cage enantiomers.¹¹⁰

After the experiments detailed in section 2.2.2.1 were analysed, samples with cage concentrations below 0.2 mM were no longer produced as those samples contained a significant amount of free ligand and the quality of the ^1H NMR data was not suitable for high-resolution studies. The small quantity of free ligand present in the samples from section 2.2.2.1 was not affected by the presence of a guest and did not change when the samples had self-sorted. It is postulated that degradation of the tetrakis(acetonitrile)palladium(II)tetrafluoroborate could be responsible for this, which is discussed in more detail in this section.

When the stella octangula cage samples of different concentrations were monitored in section 2.2.2.2, the lowest concentration (0.5 mM) self-sorted the fastest, followed by the 1.0 mM sample and the 2.5 mM sample, which took 32 days to reach a state of homochirality. These results show that the rate of self-sorting of the cage was affected by cage concentration. It is possible that there is an optimum amount of material in solution to enable the self-sorting of the stella octangula cage. The data from section 2.2.2.1 indicate that this is above 0.2 mM and the data from section 2.2.2.2 indicate that it is not higher than 0.5 mM. That is, the optimum concentration for self-sorting is between 0.2 and 0.5 mM.

The problem associated with the duration of self-sorting seemed to be also related to the tetrakis(acetonitrile)palladium(II)tetrafluoroborate. After consulting the literature from the Fujita group, who also use both of the palladium salts used in this study, it was noted that they always heated their samples to at least 60°C and for at least 90 minutes.^{107, 116, 123, 132} When a $[\text{Pd}_6(\text{L1})_8] \cdot 12(\text{BF}_4)$ stella octangula cage was heated, no effect on self-sorting was seen. However, when the palladium salt (section 2.2.2.3) was heated individually, the self-assembly and self-sorting of the homochiral cage was achieved within the desired time. The same effect was seen when old palladium stock solutions were used to produce cage samples. It is possible that the acetonitrile component of the palladium salt competes with the labile nitrogens of the ligand pyridyl group and that the heating process allows the acetonitrile groups to dissociate from the palladium, which in turns reacts with the labile nitrogens of the ligand.

It is also possible that the DMSO solvent was in competition with the ligand for the palladium cation. DMSO has previously been shown to act as a ligand.^{138, 144, 145} With this in consideration, an attempt was made to produce a cage in d_3 -acetonitrile, also a

polar aprotic solvent, to see if this would have any effect on the self-assembly processes of the stella octangula cage system. This investigation was successful; the ^1H NMR spectrum of the $[\text{Pd}_6(\text{L1})_8]\cdot 12(\text{BF}_4)$ stella octangula cage in d_3 -MeCN showed a complex that formed instantly and showed no evidence of self-sorting after the initial self-assembly. When compared to the ^1H NMR spectrum of the $[\text{Pd}_6(\text{L1})_8]\cdot 12(\text{BF}_4)$ stella octangula cage in d_6 -DMSO shown in Figure 2.4, it can be seen that all of the cage peaks were considerably broadened and the pyridine peaks especially were not indicative of a highly symmetrical environment of a homochiral cage system. The mass spectrum was recorded for this sample and was highly indicative of a $[\text{Pd}_6(\text{L1})_8]\cdot 12(\text{BF}_4)$ stella octangula cage system in the gaseous phase. However, because of the appearance of the ^1H NMR spectrum, it was decided not to pursue this system in this solvent, as the system was not homochiral.

When Henkelis studied the self-assembly of the $[\text{Pd}_6(\text{L2})_8]^{12+}$ stella octangula cage in d_6 -DMSO, further self-sorting after the initial self-assembly process was not observed and the crystal structure revealed a disordered assembly comprised of a mixture of *M* and *P* **L2** enantiomers.^{113, 146} This was in contrast to the **L1** stella octangula cage, where each cage featured a single *M* or *P* **L1** ligand enantiomer.¹¹⁰ Interestingly, Henkelis also observed that the self-assembly of the **L2** stella octangula cage in d_3 -acetonitrile and d_3 -nitromethane facilitated ligand exchange toward enantiopure assemblies.^{113, 146} When **L1** stella octangula cages were studied in d_3 -acetonitrile, no further changes were observed in its ^1H NMR spectrum, indicating that any self-sorting occurred during the initial self-assembly process.

2.4.2 Stoichiometry of Host-Guest Systems & Association Constants

Job's plot analyses^{6, 140} were performed to ascertain the host-guest stoichiometry. The host:guest stoichiometry was established at 1:2. Although a Job's plot can indicate a multitude of stoichiometries, they are assumed to be most accurate in determining 1:1 stoichiometries.¹⁴¹ As a consequence of this, other techniques were used to confirm the result of the Job's analysis. When it came to fitting the ¹H NMR chemical shift data (section 2.3.3.1) using the HypNMR 2008 software, a fit could not be achieved unless the software was instructed as to the stoichiometry of the complex for which the binding constants are being fitted. 1:1 and 1:3 stoichiometries were investigated, but fitting could not be achieved for those stoichiometries at all, which supports the theory that the cage:sodium alkyl sulfate guests have a 1:2 stoichiometry. Diffusion coefficient data for the [Pd₆(L1)₈]₁₂(BF₄):SDS system was plotted against the [H]/[G] ratio and this plot again indicated a 1:2 host-guest stoichiometry. All three of these techniques are in definite agreement about the stoichiometry of the [Pd₆(L1)₈]¹²⁺ cage:sodium alkyl guest system, which is established at 1 host to 2 guests.

A trend was observed that related the length of the guest to the tightness of the binding with stella octangula cage, as the shortest guest, SOS displayed the tightest binding for both the first and second cumulative association constant. The fitting programme also demonstrated that most of the guest present in the samples was free in solution. Rebek's³² paper on optimal host-guest binding states that optimal binding is achieved when a complex has a packing coefficient of 0.55 ± 0.09 . The stella octangula cage:SDS system does not achieve this; its packing coefficients were calculated at 0.10 for 1 encapsulated guest and 0.21 for 2 encapsulated guests.¹¹¹ This suggests

that the packing is not at all optimal and explains why so much of the guest is free in solution.

2.4.3 Nature of the Host-Guest Interaction

During the analysis of the stoichiometry, an interaction between the $[\text{Pd}_6(\text{L1})_8] \cdot 12(\text{BF}_4)$ stella octangula cage and the sodium alkyl guests was evident. However, the analysis up to that point did not provide any information about the nature of the interaction and to establish that the system was interacting like a host-guest system, it needed to be confirmed that the guest was indeed inside the host. The guests in question are anionic with a polar head moiety, which suggests that they could have been interacting with the exterior of the cage, as the cage system is positively charged. To investigate the nature of the interaction, 2-D ROESY experiments were performed on cage systems with SDS and SOS present (see section 2.3.5). These experiments proved conclusively that the sodium alkyl guest were interacting with the cage interior, as through-space connections could only be seen between the protons in the cage portal openings and the guest molecules. If the guests were interacting with the exterior of the cage, it would be expected that through-space connections would be seen between the guests and the CTV-bowl protons; these were not seen. In Figure 2.27 and Figure 2.28, it can be seen that the Hb/b' protons are interacting with all of the protons in the guest molecules. At first inspection this seems unintuitive, however, this observation has been made with other host-guest systems by Kulasekharan *et al.*,¹⁴⁷ who developed a model in which the guest molecule rotates around its long axis over the timescale of the Overhauser measurement. The dimensions of the $[\text{Pd}_6(\text{L1})_8] \cdot 12(\text{BF}_4)$ stella octangula cage do allow for this.

2.5 Conclusions

In conclusion, this investigation has gone exceedingly well. It has been established that guests can be accommodated within the inner void of the stella octangula cage and the stoichiometry of the $[\text{Pd}_6(\text{L1})_8]^{12+}$ cage:SDS complex has been firmly established using a Job's plot analysis, the fitting of the association constants and with the diffusion data. Following on from this the nature of the interaction between the $[\text{Pd}_6(\text{L1})_8]^{12+}$ cage and SDS has also been established using ROESY spectroscopy, confirming that the guest is indeed inside the host. This host-guest interaction has also been established for two other sodium alkyl guests (SOS and STS) which appear to behave in the same manner as SDS. However, the tightness of binding does appear to be related to the length of the guest. Problems that have arisen during this investigation have been satisfactorily solved. The only issue has been the duration of this project and solving the problems has had an impact on this. One of the aims of this research was to ready this study for publication and this has also been achieved. The work has been accepted by the RSC journal "Dalton Transactions".¹¹¹ Familiarity has been achieved with the research and the techniques used to investigate host-guest solution phase chemistry and these skills will now be utilised in the next section of research; host-guest studies of a new stella octangula cage that is very similar to the one formed with **L1**. The new ligand, **FL1** is a ^{19}F labelled version of the **L1** ligand. This ligand has been devised to follow the self-assembly processes of the stella octangula cage with ^{19}F NMR. **FL1** has one fluorine on each of its pyridine groups, replacing one of the Hb/b' protons. It is also anticipated that **FL1** may be more soluble than **L1**, which will lead to working in solvents other than d_6 -DMSO, which was shown by Henkelis to have a detrimental effect on the self-assembly of stella octangula systems.¹¹³

Chapter 3 Investigation of ^{19}F -labelled Ligand FL1

3.1 Introduction

This chapter describes the investigations into the ^{19}F -labelled ligand **FL1**. This ligand was derived to follow the self-assembly of the stella octangula M_6L_8 system with ^{19}F NMR spectroscopy, enabling further understanding of the self-assembly of the $[\text{Pd}_6\text{L}_1]_8$ stella octangula cage in solution. This ligand is analogous to the **L1** ligand. The only difference is that a fluorine has been appended at the 3-position on the pyridyl ring, as illustrated in Figure 3.1.

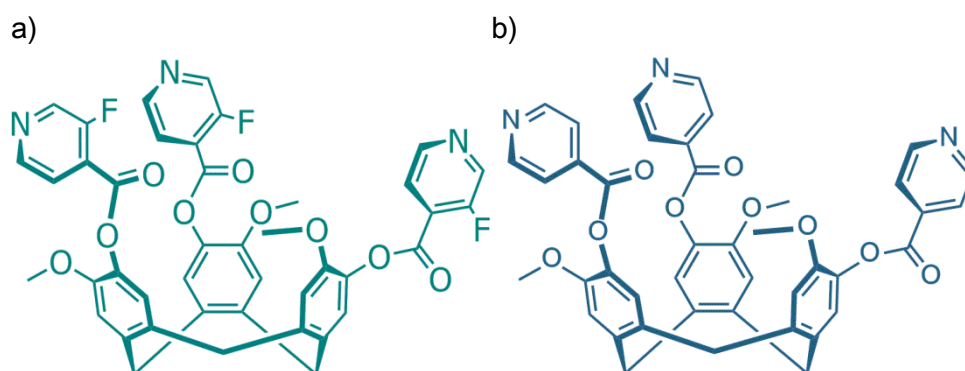


Figure 3.1 a) FL1 ligand, b) L1 ligand.

Investigations with this novel ligand included probing the self-assembly of the $[\text{Pd}_6(\text{FL1})_8]^{12+}$ stella octangula cage with ^1H and ^{19}F NMR spectroscopy. Evaluation of the solubility of the ligand and its complexes and their host:guest properties were also performed.

3.1.1 FL1 Ligand

This novel ligand, (\pm)-2,7,12-trimethoxy-3,8,13-*tris*-(4-carboxy-3-fluoropyridyl)-10,15-dihydro-5*H*-tribenzo[a,d,g]cyclononatriene (**FL1**) was produced in-house by the Hardie group. This ligand, like **L1**, is a tri-substituted cyclotrimeratrylene (CTV) derivative. As with **L1**, **FL1** retains the crown conformation of CTV, again resulting in a rigid molecule with C_3 symmetry. The **FL1** ligand is also functionalised with pyridyl donors appended to the upper rim of the CTG core, which enables the molecule to coordinate with three transition metals and extends the cavity of the CTG core.¹²⁶ Introducing a highly electronegative fluorine to the pyridyl ring of the ligand will change the solubility properties of the ligand; this is discussed in the next section.

3.1.2 Solubility of the FL1 Ligand

The solubility of the **FL1** ligand was evaluated in a variety of solvents, along with the palladium compound tetrakis(acetonitrile)palladium(II)tetrafluoroborate, as this is the palladium salt that will be used to form the $[\text{Pd}_6(\text{FL1})_8]^{12+}$ stella octangula cage. The results of this are shown in Table 3.1.

It was expected that the **FL1** ligand would be soluble in d_6 -DMSO as **L1** was soluble in d_6 -DMSO, as was the $[\text{Pd}_6(\text{L1})_8]^{12+}$ stella octangula cage. However, it was desired that the **FL1** ligand would also be soluble in other solvents, as d_6 -DMSO was not considered to be an ideal solvent in which to perform host:guest studies. This was due to its ability to strongly compete with ligands for metal-ion coordination¹⁴⁸ and the slow self-sorting experienced with **L1** in section 2.2.

Table 3.1 Solubility of FL1 and Pd salt ligand in deuterated solvents.

Solvent	Solvent Type	FL1 ligand	Pd(CH ₃ CN) ₄ (BF ₄) ₂
Chloroform- <i>d</i>	Non-polar	✓	✗
Toluene- <i>d</i> ₇	Non-polar	✓	✗
DCM- <i>d</i> ₂ (Dichloromethane)	Non-polar	✓	
DMSO- <i>d</i> ₆ (Dimethyl sulfoxide)	Polar aprotic	✓	✓
MeCN- <i>d</i> ₃ (Acetonitrile)	Polar aprotic	✓†	✓
Acetone- <i>d</i> ₃	Polar aprotic	✓†	✓
MeNO ₂ - <i>d</i> ₃ (Nitromethane)	Polar aprotic	✓	✓
D ₂ O	Polar protic	✗	✓
Methanol- <i>d</i> ₃	Polar protic	✗	✗

✓ indicates compound is soluble, ✗ indicates compound is insoluble

† Soluble, but rapidly precipitates out

Although the ligand was soluble in the non-polar solvents *d*-chloroform, *d*₇-toluene and *d*₂-dichloromethane, the palladium salt was not, ruling out these solvents for cage studies. Neither the ligand nor the palladium dissolved in *d*₃-methanol and the ligand did not dissolve in D₂O, ruling out both of these as potential solvents. The FL1 ligand does dissolve in *d*₃-nitromethane; however, Henkelis and co-workers found that stella octangula cages formed in *d*₃-nitromethane with the propylated ligand L2, did not form quantitatively, but did self-sort rapidly.¹¹³ This makes *d*₃-nitromethane a less than ideal

solvent to perform host:guest studies in, as any free ligand in solution could potentially interfere with host:guest interactions. When the ligand was dissolved in the polar aprotic solvents d_3 -acetonitrile and d_3 -acetone, the resulting solutions were cream-coloured cloudy suspensions. When the palladium salt solution was added to these cloudy suspensions, the resulting solutions became clear, with a very pale yellow hue, as shown in Figure 3.2, where the cloudy suspension of a solution of **FL1** in d_3 -acetonitrile can be seen in. Figure 3.2 c) shows a cage sample in acetonitrile that had been briefly vortexed after the **FL1** and Pd stock solutions were mixed together. The resulting clear solution remained stable at room temperature for at least 4 months.

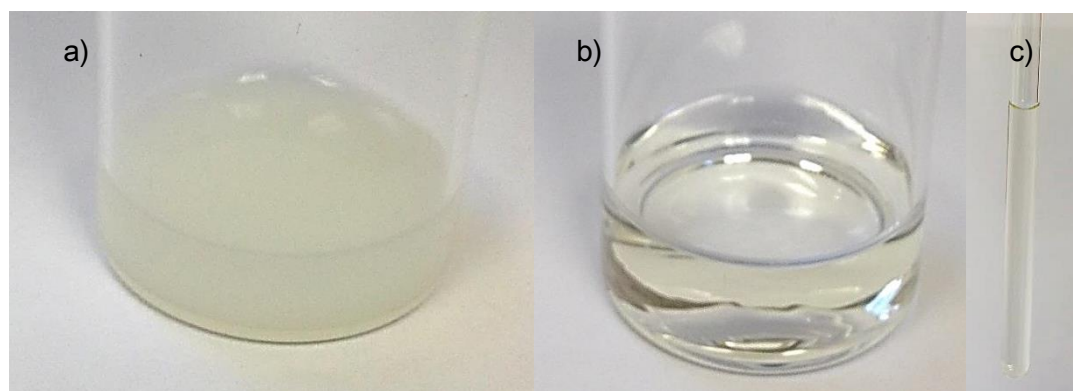


Figure 3.2 a) FL1 in d_3 -MeCN, b) tetrakis(acetonitrile)palladium(II)tetrafluoroborate in d_3 -MeCN and c) $[Pd_6(FL1)_8]_{12}(BF_4)$ in d_3 -MeCN.

When the **FL1** ligand was dissolved in acetone the solution was very cloudy and a 1H NMR proton spectrum could not be recorded. A spectrum of the cage in d_3 -acetone is shown in Figure 3.3.

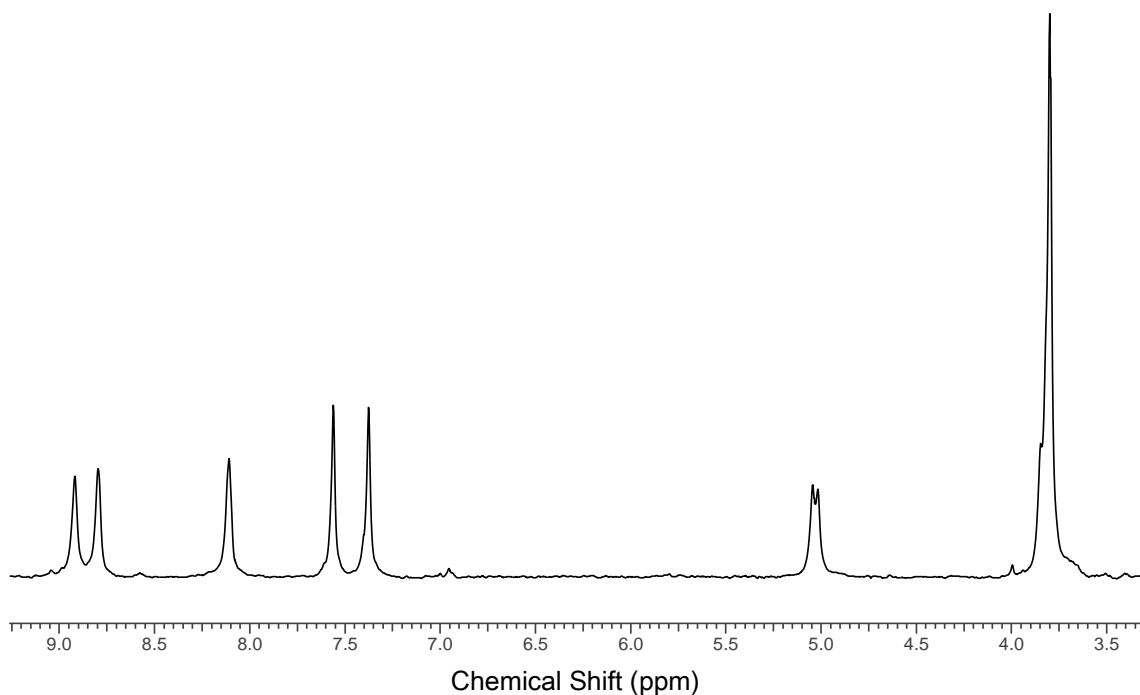


Figure 3.3 ^1H NMR spectrum of $[\text{Pd}_6(\text{FL1})_8] \cdot 12(\text{BF}_4)$ cage complex.
(293 K, 500 MHz, d_6 -acetone)

The spectrum in d_3 -acetone (Figure 3.3) had poorly defined peaks. The spectrum appeared to show a cage complex as opposed to free ligand, as the pyridyl and aryl peaks had shifted downfield and broadened in a way indicative of cage formation.^{110, 111, 113} After two days, this sample precipitated out and did not show any signs of self-sorting. Thus, this solvent was not pursued any further.

3.1.3 FL1 Ligand Characterisation

The **FL1** ligand has eight resolvable proton environments at 500 MHz in both d_6 -DMSO and d_3 -acetonitrile. These are illustrated below in Figure 3.4 There is an additional proton environment when compared with **L1**, as the fluorine atom has replaced a Hb/b' atom, rendering the protons labelled as Ha/a' in **L1** magnetically inequivalent.

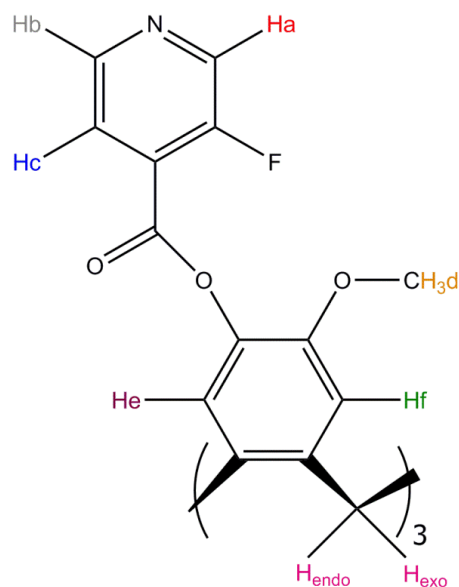


Figure 3.4 Annotated section of FL1 ligand, showing unique protons.

As discussed in section 3.1.2, the **FL1** ligand is soluble in the polar aprotic solvents d_6 -DMSO and d_3 -acetonitrile. The spectra for both are shown in Figure 3.5 and Figure 3.6 respectively, with the chemical shift assignments detailed in Table 3.2. The spectrum recorded in d_6 -DMSO is better defined than that recorded in d_3 -acetonitrile, with sharper peaks and clearer separation of the multiplets present. However, the two different solvents do reveal similar spectra. As can be seen in Figure 3.5 and Figure 3.6, both spectra of the **FL1** ligand exhibit a pair of doublets for the protons on the CTV-derivative bowl.⁴³ The pair of doublets are separated by over 1 ppm, which is characteristic of the ligand retaining the crown conformation, as described in section 1.3. The protons labelled d, e and f for the **FL1** ligand are largely unaffected by the addition of fluorine to the ligand and resonate with the same spectral pattern as seen for **L1**.

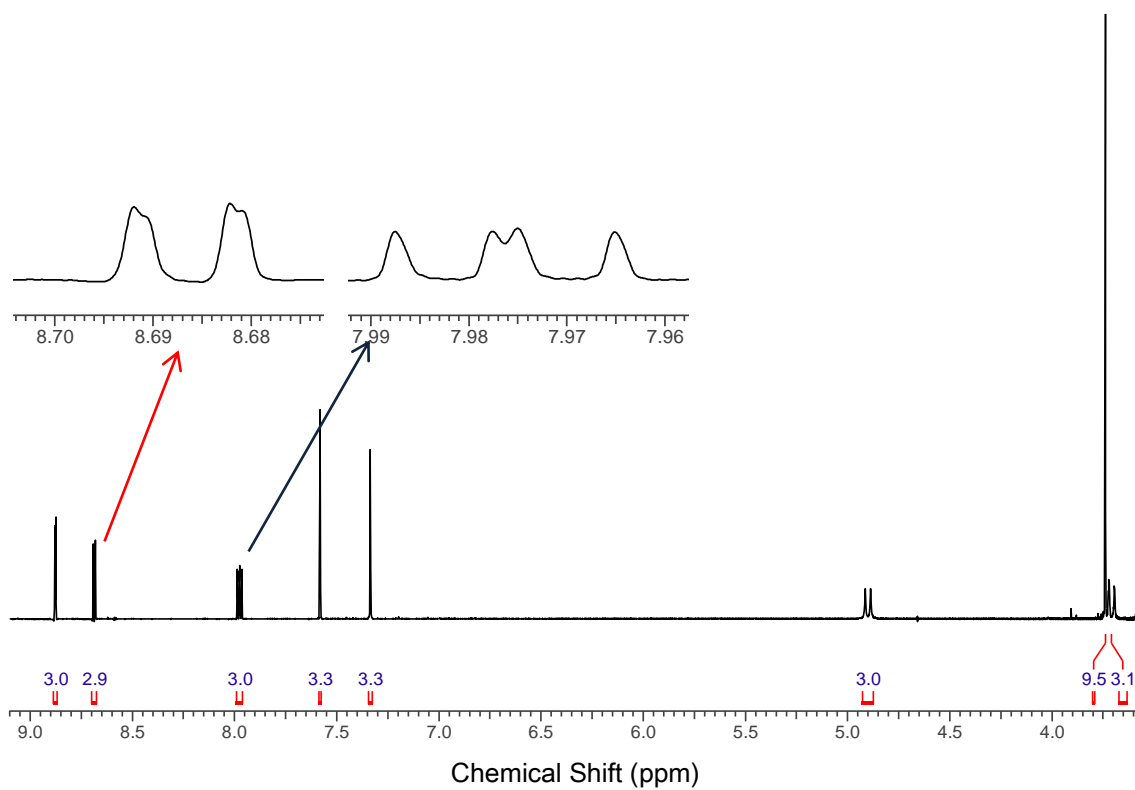


Figure 3.5 ^1H NMR spectrum of FL1 ligand, with expansions of the peaks at 7.98 and 8.69 ppm and integrations. (293 K, 500 MHz, d_6 -DMSO)

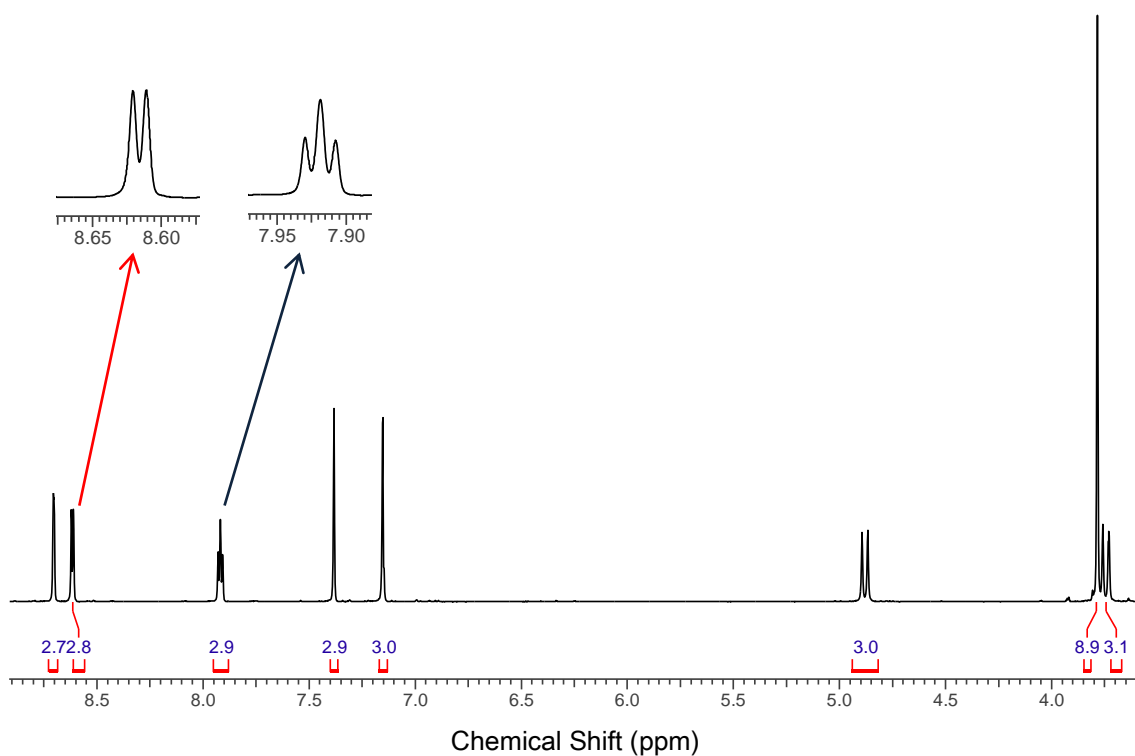


Figure 3.6 ^1H NMR spectrum of FL1 ligand, with expansions of the peaks at 7.92 and 8.62 ppm and integrations. (293 K, 500 MHz, d_3 -MeCN)

The pyridyl proton assignment is slightly complicated by the addition of the fluorine to the pyridyl ring as the fluorine can also couple with the protons on the ring. To ascertain the correct assignment of the pyridyl protons, homonuclear selective decoupling was applied to each of the pyridyl protons individually. The results of this are displayed in Table 3.3

Proton Ha resonated furthest downfield at 8.70 and 8.88 ppm in α_3 -acetonitrile and α_6 -DMSO respectively, as it is the least shielded of the pyridyl protons in its position between the highly electronegative fluorine and the pyridyl nitrogen. The peak for the Ha proton is a doublet split by the adjacent fluorine atom with a coupling constant of $J_{\text{Ha,F}} = 2.3$ Hz. When the Ha resonance was selectively decoupled, the resonances for Hb and Hc were unchanged.

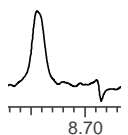
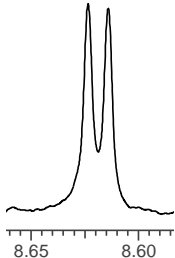
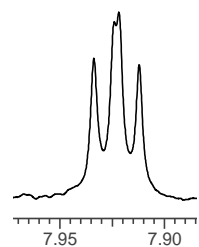
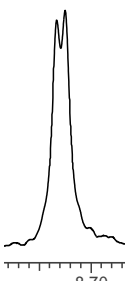
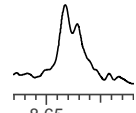
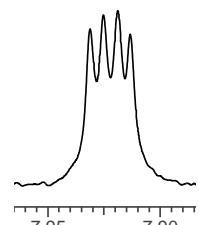
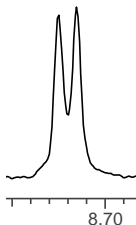
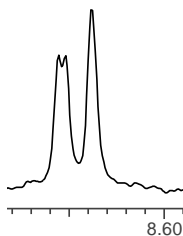
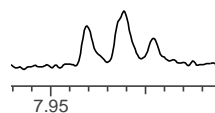
The Hb peak (8.69 and 8.62 ppm in α_3 -acetonitrile and α_6 -DMSO respectively) was seen as a broad doublet in α_3 -acetonitrile and as a double doublet in α_6 -DMSO. The couplings determined from the α_6 -DMSO spectrum were a 4.9 Hz coupling to the Hc proton and a smaller coupling of 0.8 Hz caused by the Ha proton. This was established by the selective homonuclear decoupling experiments. When the Hc proton was irradiated, the coupling between Hb and Hc was no longer present, revealing a doublet with a coupling constant of $J_{\text{Ha,Hb}} = 0.8$ Hz and a singlet. The reason that there were two peaks for the Hb proton was due to the pyridyl protons being magnetically inequivalent. The doublet is caused by coupling to the Ha proton and the singlet was due to the collapsed signal caused by the Hc proton. The 0.8 Hz coupling constant of Ha-Hb was not seen in either of the Ha resonances as their $\frac{1}{2}$ height line widths were wider than 0.8 Hz, meaning that this coupling was not observed in those resonances.

The Hc proton appeared to resonate as a triplet in acetonitrile at 7.92 ppm, whilst in d_6 -DMSO this peak was a double doublet, showing a 4-bond coupling to the fluorine of 6.3 Hz and the 3-bond coupling to the Hb proton. The assignments for the **FL1** are summarised below in Table 3.2.

Table 3.2 Table of peak assignments for FL1 ligand in MeCN and DMSO at 500 MHz.

Peak/ppm d_3 -MeCN	Multiplicity/Hz d_3 -MeCN	Peak/ppm d_6 -DMSO	Multiplicity/Hz d_6 -DMSO	Assignment
8.704	d ($J_{\text{Ha,F}}$ 2.3)	8.887	d ($J_{\text{Ha,F}}$ 2.3)	Ha
8.616	d ($J_{\text{Hb,Hc}}$ 4.9)	8.686	dd ($J_{\text{Hb,Hc}}$ 4.9, $J_{\text{Ha,Hb}}$ 0.8)	Hb
7.919	t (5.5, 5.5)	7.976	dd ($J_{\text{Hc,F}}$ 6.3, $J_{\text{Hb,Hc}}$ 4.9)	Hc
7.382	s	7.582	s	He
7.152	s	7.336	s	Hf
4.880	d ($J_{\text{Hendo,Hexo}}$ 13.7)	4.900	d ($J_{\text{Hendo,Hexo}}$ 13.3)	H _{endo}
3.784	s	3.739	s	Hd
3.744	d ($J_{\text{Hendo,Hexo}}$ 13.7)	3.708	d ($J_{\text{Hendo,Hexo}}$ 13.3)	H _{exo}

Table 3.3 Table to show results of selective homonuclear decoupling experiments for FL1 ligand. (296 K, 500 MHz, d_3 -MeCN)

Peak irradiated	Ha peak	Hb peak	Hc peak
Ha	Irradiated peak 	bd, 4.8 Hz 	dd, 6.1, 4.9 Hz 
Hb	bd, 2.3 Hz 	Irradiated peak 	dd, 6.3, 2.9 Hz 
Hc	d, 2.4 Hz 	d, 0.8 Hz, s 	Irradiated peak 

In the ^{19}F NMR spectrum of FL1 in d_3 -acetonitrile, [Figure 3.7a)] a doublet of doublets can be seen. These peaks are broad at room temperature, and sharper at 56°C (Figure 3.7 b). Couplings seen in this spectrum were between Ha and F, and between Hc and F. When broadband decoupling (Figure 3.8) was applied to the ^{19}F NMR spectrum, the signal collapsed down to a singlet, indicating that there was only one fluorine environment in the FL1 ligand.

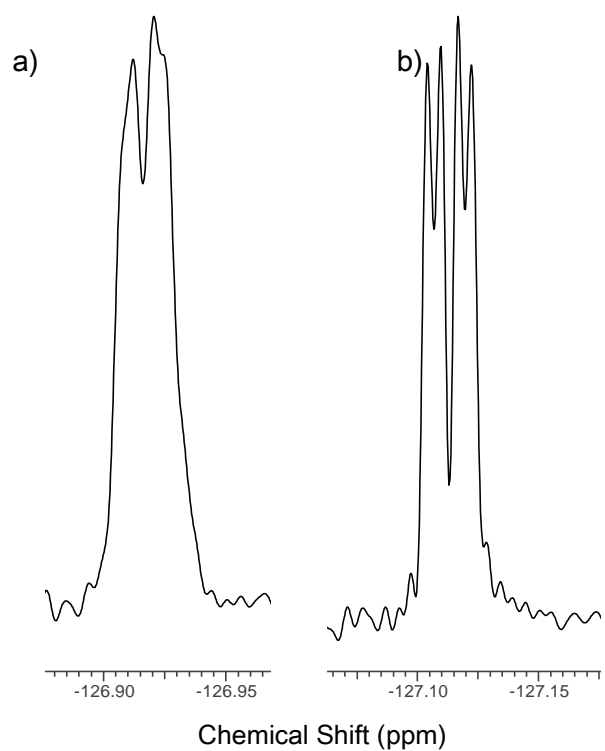


Figure 3.7 ^{19}F NMR spectra of FL1 ligand a) 298 K, b) 329 K. (471 MHz, d_3 -MeCN)

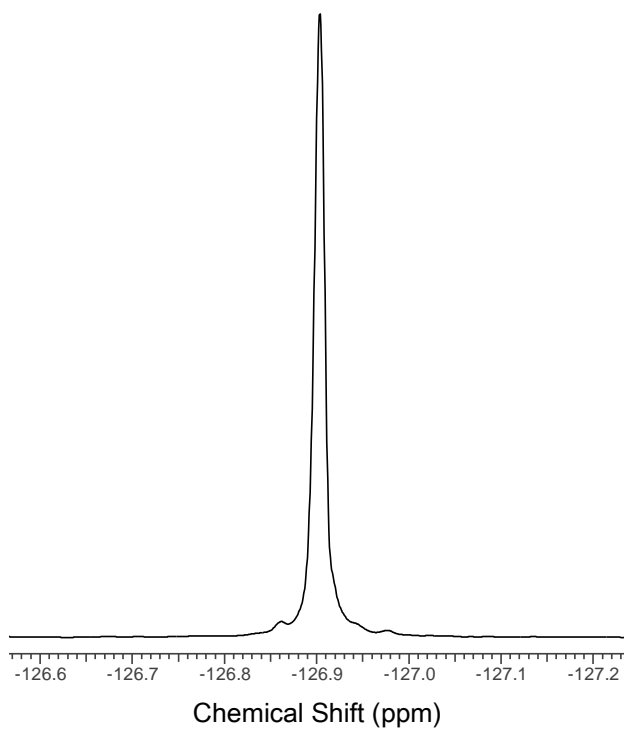


Figure 3.8 ^{19}F NMR broadband decoupled spectrum of FL1 ligand. (296 K, 282 MHz, d_3 -MeCN)

^{19}F NMR data were also recorded for FL1 in d_6 -DMSO and d_3 -nitromethane and the spectra are shown below in Figure 3.9 and Figure 3.10 respectively. The spectra both showed a doublet of doublets as was seen with d_6 -MeCN, although the peaks in d_3 -MeNO₂ were better resolved than those in d_6 -DMSO. When broadband decoupling was applied to FL1 in d_6 -DMSO and d_3 -MeNO₂, the same change was seen; that is, the doublet of doublets collapsed down to a singlet, as the couplings seen in the ^{19}F NMR spectra were a result of coupling to the pyridyl protons.

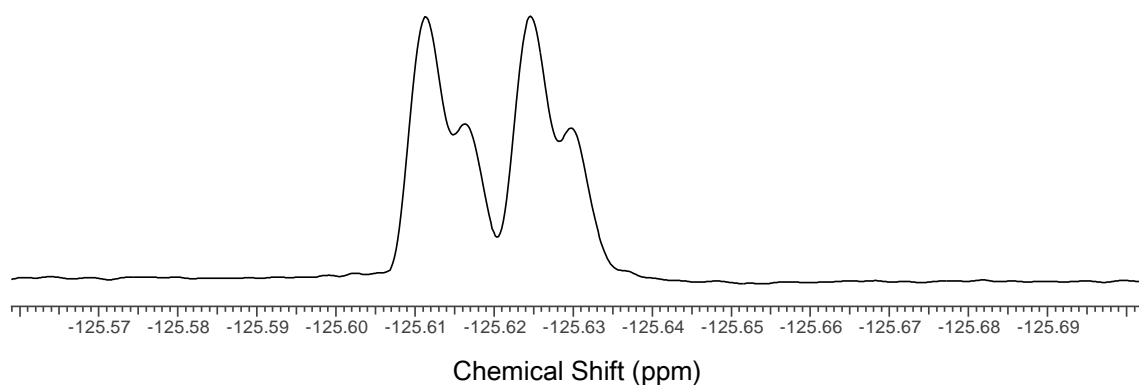


Figure 3.9 ^{19}F NMR spectra of FL1 ligand. (297 K, 471 MHz, d_6 -DMSO)

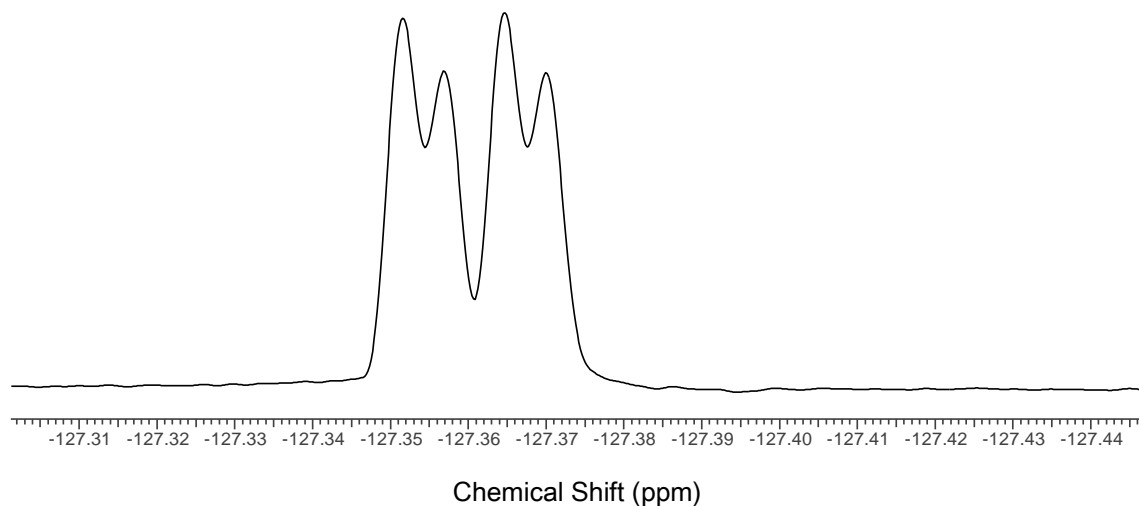


Figure 3.10 ^{19}F NMR spectra of FL1 ligand. (297 K, 471 MHz, d_3 -MeNO₂)

3.2 Results

3.2.1 FL1 Stella Octangula Cage in d_6 -DMSO

The intention of this study was to monitor the self-assembly of stella octangula cages. To this end a sample of $[\text{Pd}_6\text{FL1}_8]\cdot 12(\text{BF}_4)$ was prepared in d_6 -DMSO and analysed. This sample was analysed after 5 months and still contained a large amount of free ligand, as illustrated in Figure 3.11, where the pyridyl and aryl free ligand are highlighted. There are also free ligand peaks present for the methylene bridge of the CTV bowl and for the methoxy group. However these peaks have a very similar chemical shift to that of the cage complex, with the free ligand and cage peaks overlapping, making them harder to differentiate. The large amount of free ligand present indicated that although a small amount of complex was produced, the majority of the FL1 preferred to stay free in solution.

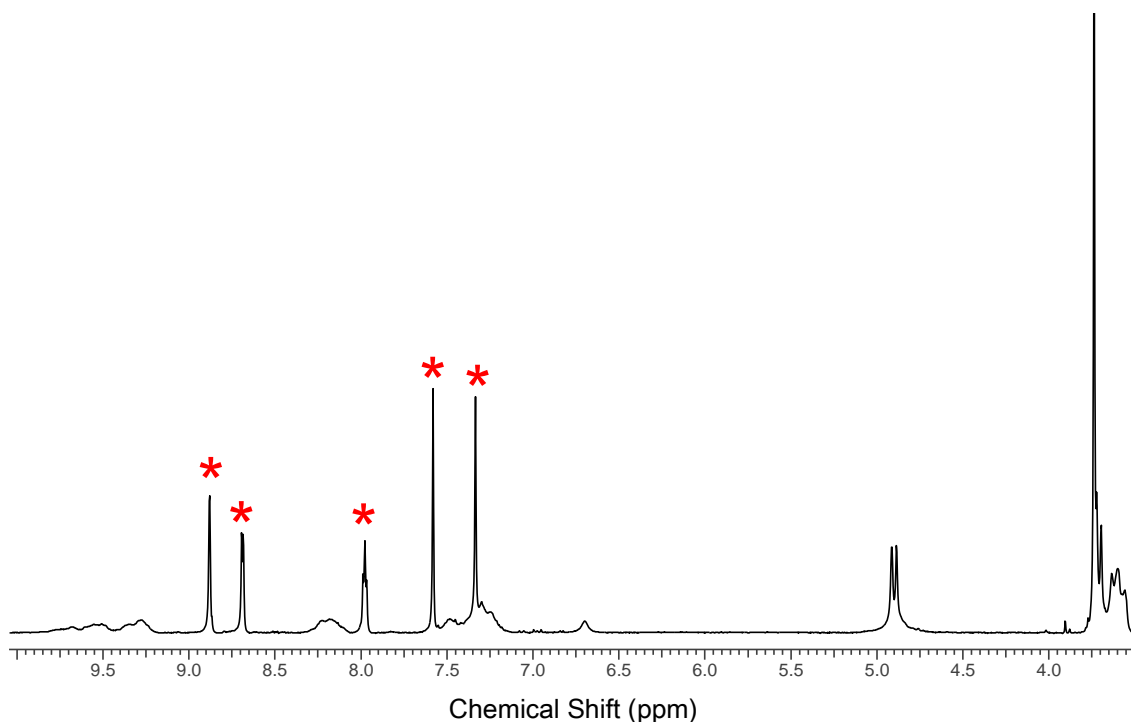


Figure 3.11 ^1H NMR spectrum of FL1 stella octangula cage after 5 months, * indicates free ligand. (293 K, 500 MHz, d_6 -DMSO)

Fresh samples were prepared and analysed, and despite using several heating methods to encourage the self-assembly of the $[\text{Pd}_6\text{FL1}_8]\cdot 12(\text{BF}_4)$ complex in d_6 -DMSO, these were unsuccessful. At this juncture, a palladium titration experiment was devised to see if additional palladium present in solution would aid the formation of stella octangula cage assemblies, as it was shown to in section 2.2.1. A new bottle of tetrakis(acetonitrile)palladium(II)tetrafluoroborate was acquired from Sigma Aldrich for this experiment. A series of seven samples was prepared, starting with a stoichiometrically correct ratio of metal to ligand. The correct ratio is six metals to eight ligands and this was termed the $1.0 \times \text{Pd}$ sample. Six more samples were produced in $0.5 \times$ increments up to $4.0 \times \text{Pd}$, which had 24 equivalents of metal to 8 equivalents of ligand. These samples were then monitored over a period of 28 days to follow the self-sorting of the stella octangula cages.

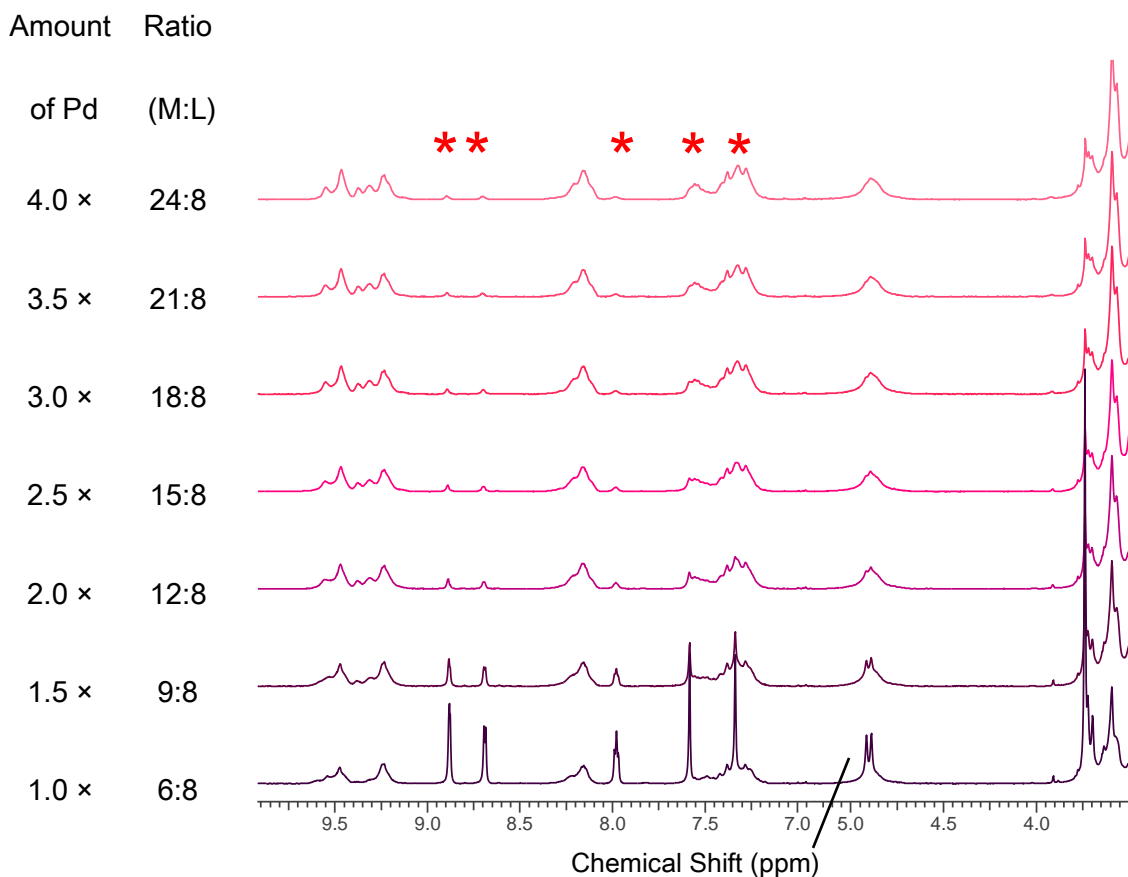


Figure 3.12 ^1H NMR spectra of $[\text{Pd}_6\text{FL}1\text{a}]\cdot 12(\text{BF}_4)$ stella octangula palladium titration after 24 hours. * indicate free ligand. (293 K, 500 MHz, d_6 -DMSO)

After 24 hours, as shown in Figure 3.12, it could be seen that the more palladium that was present in the sample, the less free ligand was present. The cage complex peaks were also sharper. The trace for 1.0 × Pd in Figure 3.12 was very similar to that shown in Figure 3.11. When the amount of palladium present is 3.0 × and above, there appeared to be very little free ligand present, and the top three spectra in Figure 3.12 had a very similar appearance. The sample made at the correct stoichiometric ratio, that is six metals to eight ligands, showed a small amount of change in the appearance of its spectrum after ten days, but after this point, no further changes were seen. The cage complex peaks in these spectra, shown in Figure 3.13 were broad, indicative of heterochiral assemblies.¹¹³

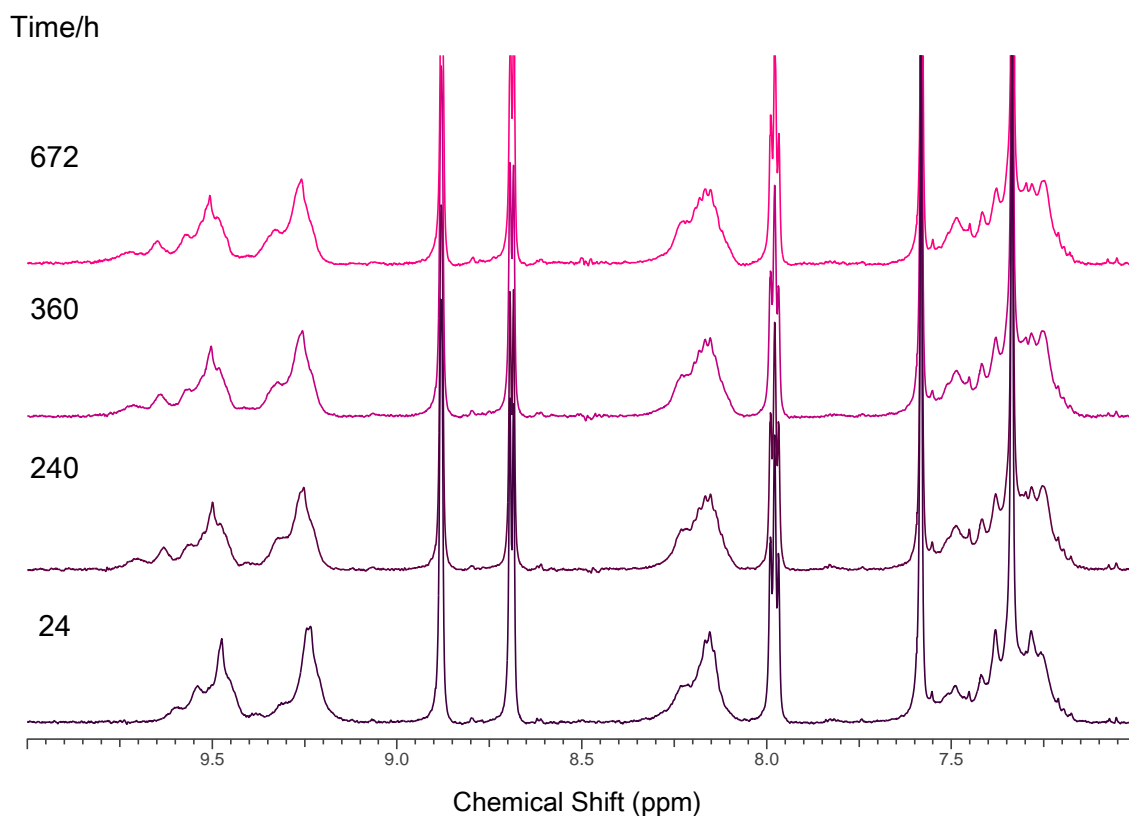


Figure 3.13 ¹H NMR spectra of [Pd₆FL₁₈]·12(BF₄) stella octangula cage over time, 1.0 × Pd. (293 K, 500 MHz, d₆-DMSO)

When the amount of palladium in solution was doubled, the amount of free ligand present in solution was considerably lessened, as illustrated by comparison of Figure 3.13 with Figure 3.14. However, there was still a small amount of free ligand present in the samples that had a higher concentration of palladium and the cage complex peaks were still broad. The amount of free ligand did reduce ever so slightly after 24 hours. For this particular sample, all spectra showed signs of self-sorting, which was especially noticeable on the side-peak of the resonance at 9.5 ppm. The spectra were also more well defined than that of the 1.0 × Pd stella octangula cages.

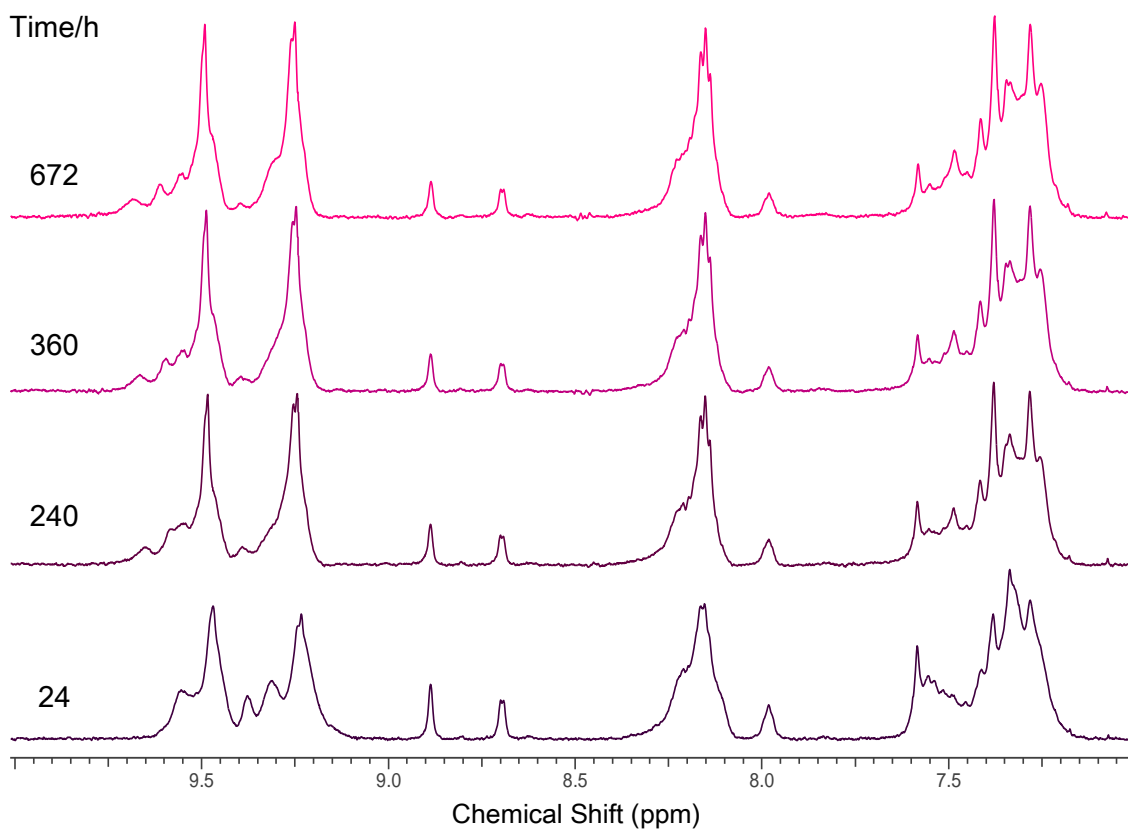


Figure 3.14 ^1H NMR spectra of $[\text{Pd}_6\text{FL}_{18}]\cdot 12(\text{BF}_4)$ stella octangula cage over time, $2.0 \times \text{Pd}$.
(293 K, 500 MHz, d_6 -DMSO)

There appeared to be very little difference between the sample with twice the stoichiometric amount of palladium present and the sample with three times the stoichiometric amount of palladium present (shown in Figure 3.15). The most significant difference was that the $3.0 \times \text{Pd}$ sample had less free ligand present in solution. The $4.0 \times \text{Pd}$ sample (Figure 3.16) was again, very similar to that of $3.0 \times \text{Pd}$.

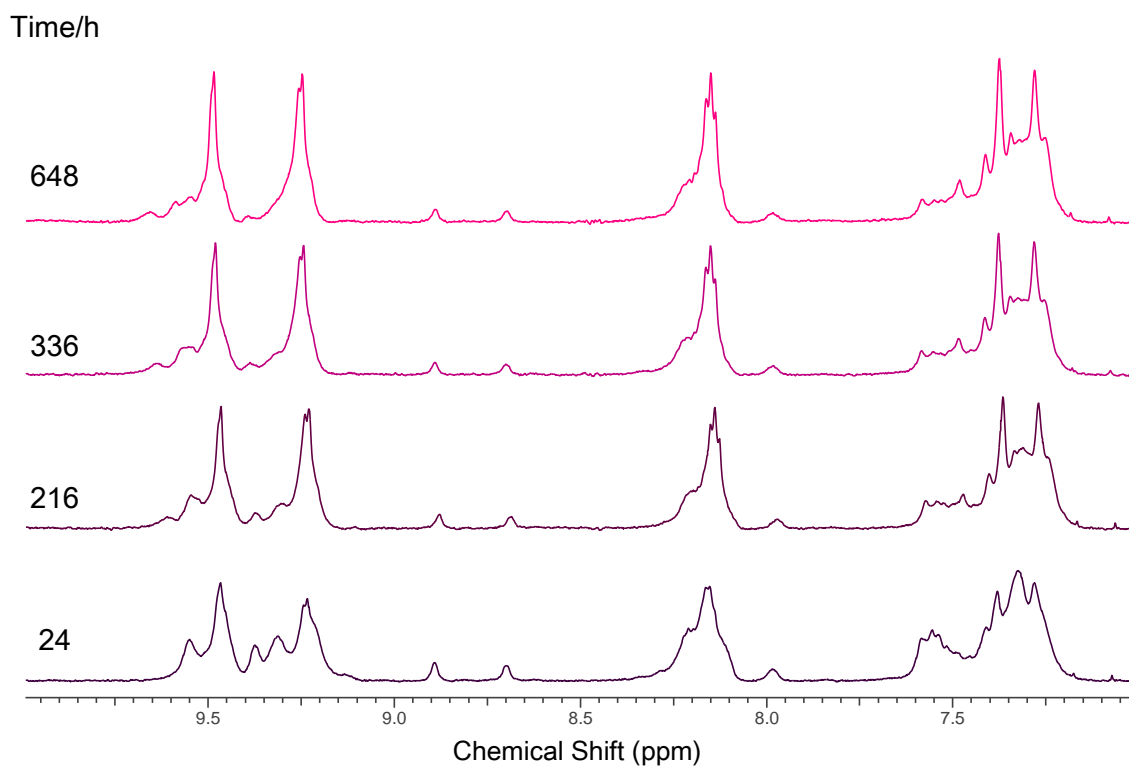


Figure 3.15 ^1H NMR spectra of $[\text{Pd}_6\text{FL}_{18}]\cdot 12(\text{BF}_4)$ stella octangula cage over time, $3.0 \times \text{Pd}$.
(293 K, 500 MHz, d_6 -DMSO)

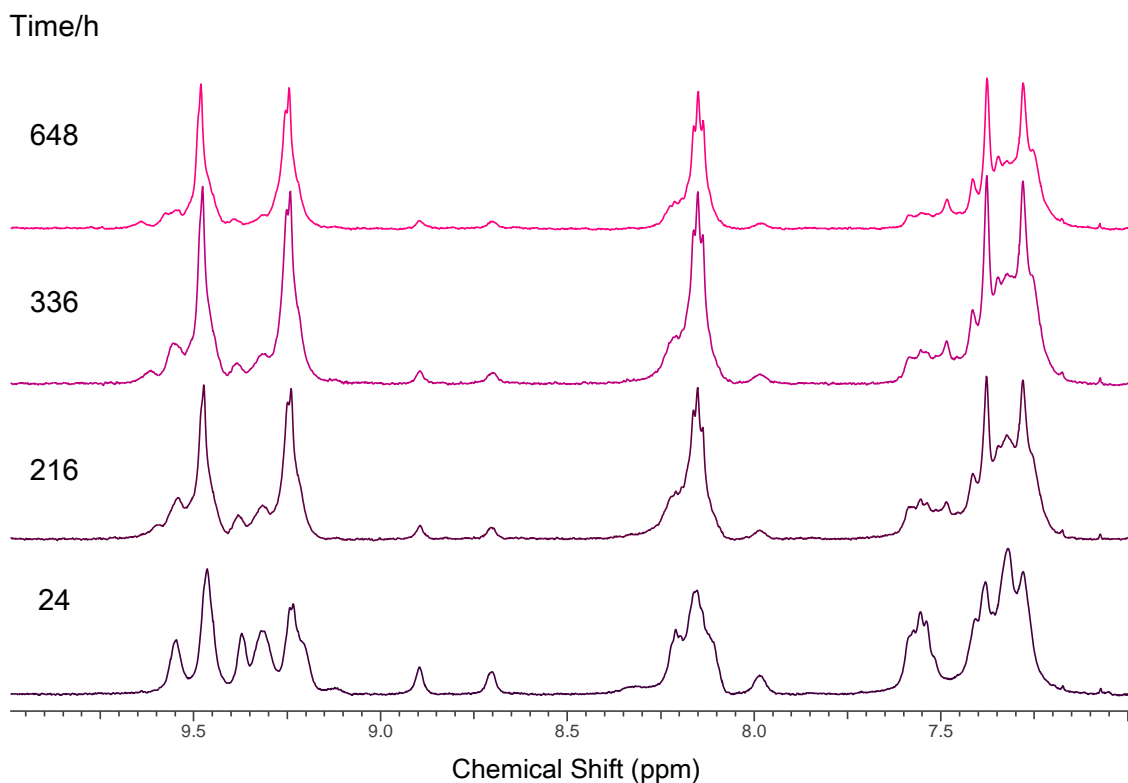


Figure 3.16 ^1H NMR spectra of $[\text{Pd}_6\text{FL}_{18}]\cdot 12(\text{BF}_4)$ stella octangula cage over time, $4.0 \times \text{Pd}$.
(293 K, 500 MHz, d_6 -DMSO)

After one month, no further changes in the spectra were observed. The $1.0 \times \text{Pd}$ sample was the least sorted and still displayed large amounts of free ligand. It was not expected that this sample would undergo any further self-sorting, as indicated by the previous result, where an older sample that was produced in the same way still exhibited a substantial amount of free ligand after five months (Figure 3.11). Although there appeared to be some sort of cage complex present as evidenced by the broadening of peaks and changes in chemical shifts, the broadness of the peaks indicates that the assemblies present were heterochiral cages. The $1.5 \times \text{Pd}$ sample still had a fair quantity of free ligand present, less so than the $1.0 \times \text{Pd}$, but significantly more than the other samples. The 2.0 and $2.5 \times \text{Pd}$ spectra were similar, with the same level of self-sorting and the same amount of free ligand present. The 3.0 , 3.5 and $4.0 \times \text{Pd}$ samples also had very similar spectra to each other. They exhibited smaller

side peaks to the Ha and Hb peaks than those of the 2.0 and 2.5 × Pd spectra and again they had a similar amount of free ligand present.

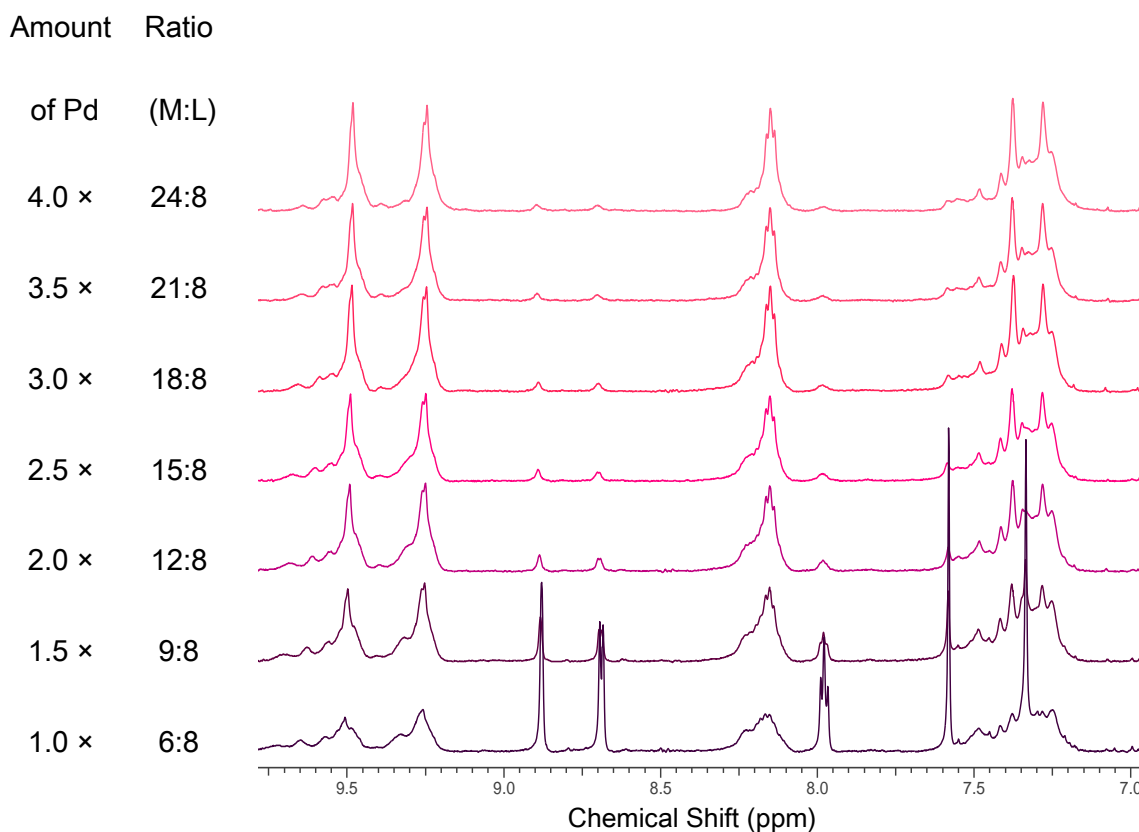


Figure 3.17 ^1H NMR spectra of $[\text{Pd}_6\text{FL}1_8] \cdot 12(\text{BF}_4)$ stella octangula palladium titration after 672 hours for samples 1.0 - 3.0 × Pd and 648 hours for 3.5 and 4.0 × Pd. (293 K, 500 MHz, d_6 -DMSO)

The ^{19}F NMR of this series, shown in Figure 3.18 also showed that the amount of free ligand present was high compared to the amount of cage complex present. The cage peaks were broad in the samples 1.0 – 2.5 × Pd, indicating the possibility of more than one chirality of cage being present in solution. The ligand peak was negligible from 2.5 × Pd upwards.

A large excess of palladium(II) was required for cage formation with the FL1 ligand in d_6 -DMSO. Cage formation required at least three times that required by the M_6L_8 stoichiometry of the stella octangula system.

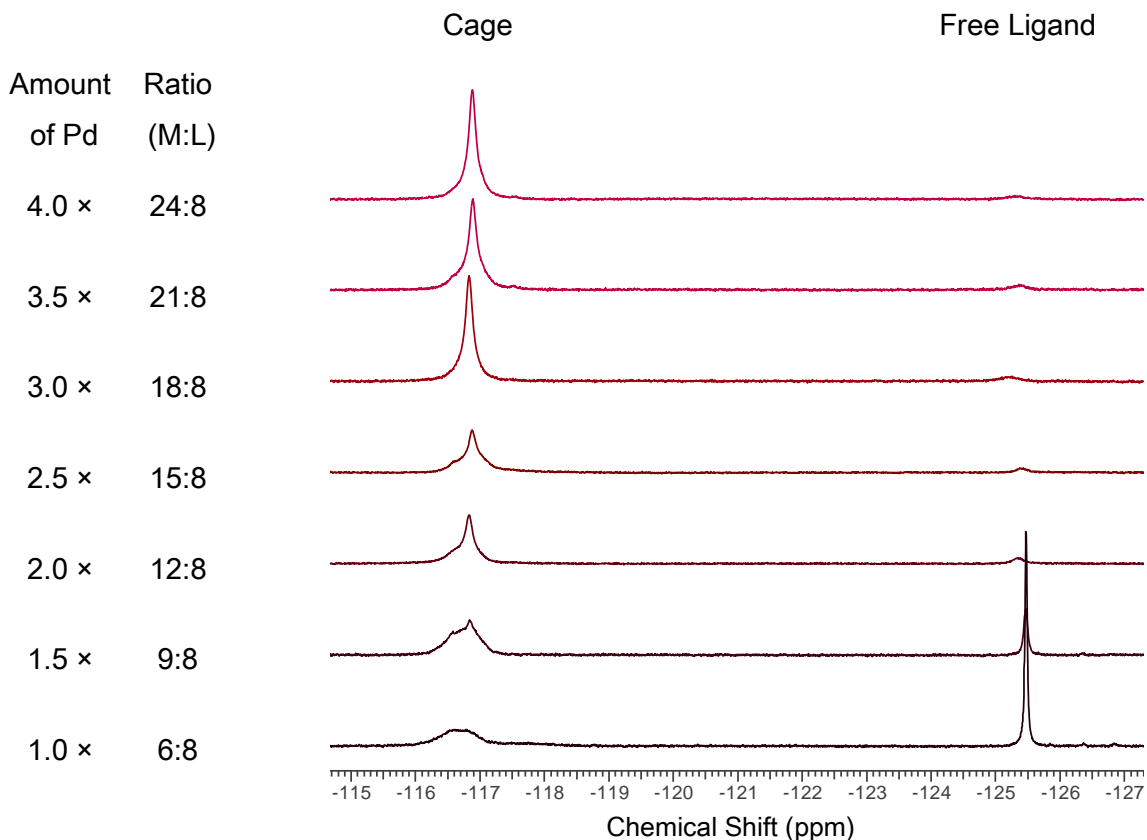


Figure 3.18 ^{19}F NMR spectra of $[\text{Pd}_6\text{FL1}_8]_{12}(\text{BF}_4)_8$ stella octangula palladium. (299 K, 471 MHz, d_6 -DMSO)

3.2.2 Host-Guest Studies with the FL1 Stella Octangula Cage in d_6 -DMSO

As a host-guest interaction between the L1 stella octangula cage and SDS was established in section 2.3. This system was likewise investigated for host-guest interactions, although recognising that the incomplete formation of the cage could be problematic. To accomplish this, a new series of samples was produced. FL1 stella octangula cages with 1.0 and 4.0 × Pd were produced with SDS present at a concentration of 0.0, 1.0 and 10.0 mM. These samples were analysed with ^1H NMR spectroscopy.

This series was produced using a different source of palladium to that in the palladium titration study described in section 3.2.1. That is, a new bottle of tetrakis(acetonitrile)palladium(II)tetrafluoroborate was acquired, this time from Acros

Organics. The variability of the palladium complex was alluded to in section 2.2.1, and more evidence of variability was provided by this series of samples. When the two samples from this series were compared with their counterparts from section 3.2.1, as shown in Figure 3.12, it could be seen that there was considerably less free ligand in the 1.0 × Pd sample in this series than there was in the original sample (Figure 3.12). Also, the two new samples appeared to be at the same phase of self-sorting, as illustrated in Figure 3.19, which was more comparable to the level of self-sorting seen for the 4.0 × Pd sample in the original series. The new 4.0 × Pd sample appeared the same as the original sample.

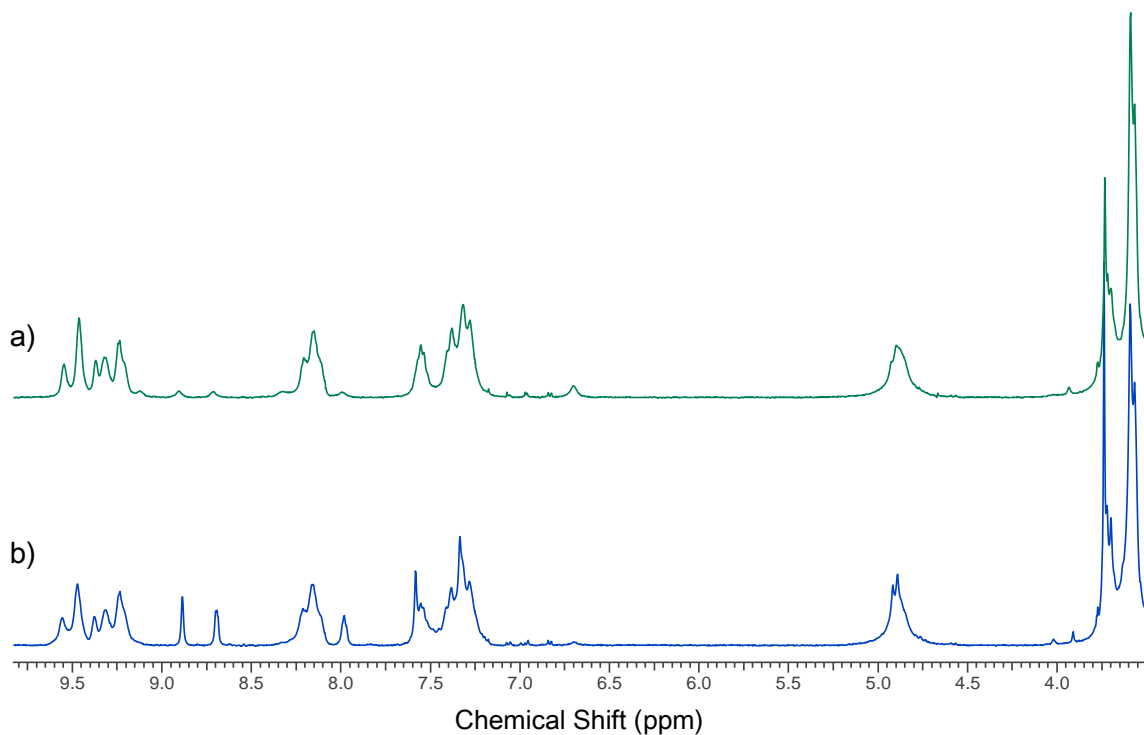


Figure 3.19 ^1H NMR spectra of $[\text{Pd}_6\text{FL}1\text{a}]_{12}(\text{BF}_4)$ stella octangula. a) 4.0 × Pd, b) 1.0 × Pd. (293 K, 500 MHz, d_6 -DMSO)

Figure 3.20 demonstrates that adding SDS to the cage solutions decreased the amount of free ligand present. These samples were prepared directly in NMR tubes, where the ligand, palladium and SDS stock solutions were added together and vortexed to achieve homogeneity. With the addition of the SDS guest, the Ha and Hb peaks showed a downfield shift. This downfield shift was larger for the sample with 10.0 mM of guest present, when compared to the samples with no guest and 1 mM guest present.

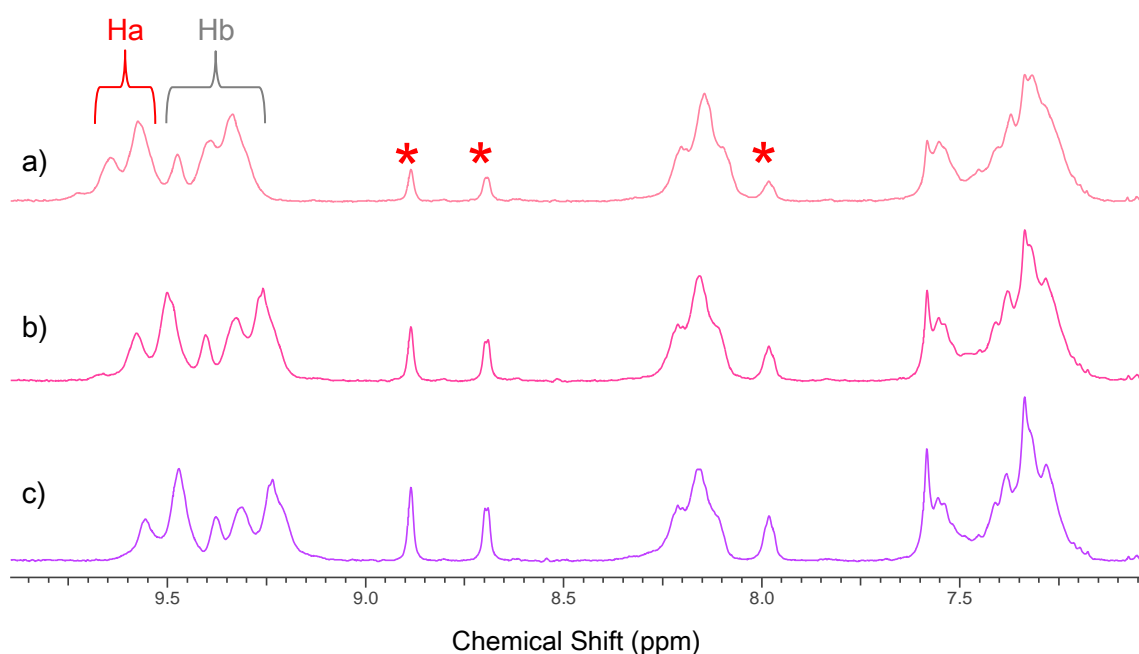


Figure 3.20 ^1H NMR spectra of $1.0 \times \text{Pd} [\text{Pd}_6(\text{FL}1)_6]\text{-}12(\text{BF}_4)$ with *a)* 10.0 mM SDS, *b)* 1.0 mM SDS and *c)* no guest – aromatic region. Free ligand peaks are indicated by *.
(293 K, 500 MHz, d_6 -DMSO)

The other aromatic peaks showed a negligible shift. The SDS peaks, as shown in Figure 3.21 showed a larger shift at 1.0 mM guest concentration than was observed for 10.0 mM guest concentration. This can clearly be seen in the expansions of the H1 and H4 peaks of SDS (refer to section 2.1.3 for SDS assignments), where the 1 mM traces showed a greater downfield/upfield shift respectively. The 10.0 mM traces showed that the SDS peaks had moved closer to their chemical shift when no cage was present.

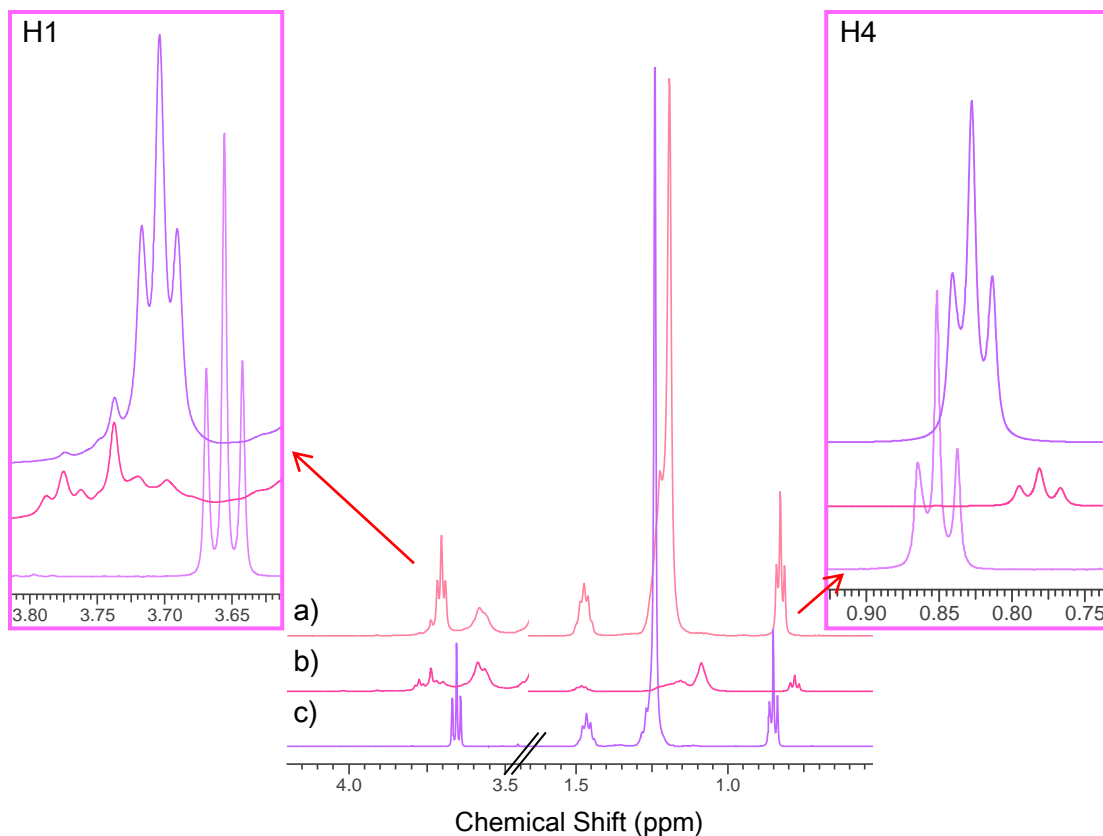


Figure 3.21 ^1H NMR spectra of SDS and $1.0 \times \text{Pd} [\text{Pd}_6(\text{FL}1)_8] \cdot 12(\text{BF}_4)$ with SDS. a) SDS, b) $1.0 \text{ Pd} [\text{Pd}_6(\text{FL}1)_8] \cdot 12(\text{BF}_4)$ with 1.0 mM SDS and c) $1.0 \times \text{Pd} [\text{Pd}_6(\text{FL}1)_8] \cdot 12(\text{BF}_4)$ with 10.0 mM SDS – upfield regions showing SDS peaks. Expansions of the SDS H1 and H4 peaks are shown. (293 K, 500 MHz, d_6 -DMSO)

Similar trends were seen for the $4.0 \times \text{Pd}$ samples. However, they had smaller chemical shift differences when compared to those for the $1.0 \times \text{Pd}$ samples. This is illustrated in Figure 3.22 and Figure 3.23. For both 1.0 and $4.0 \times \text{Pd}$, the chemical shift differences exhibited at 10.0 mM were similar.

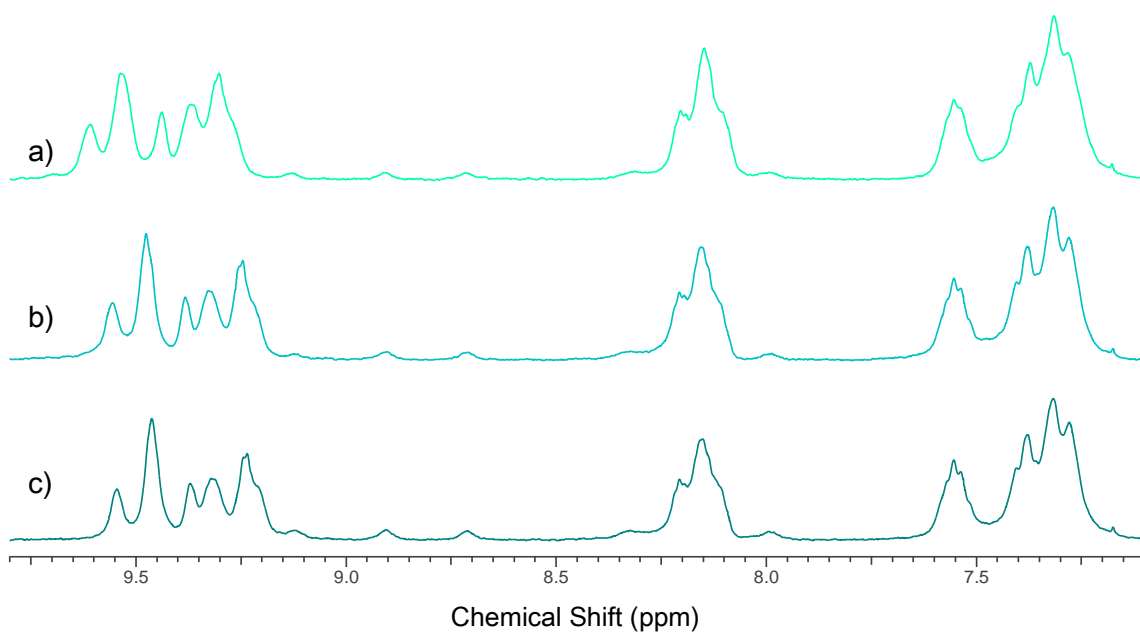


Figure 3.22 ^1H NMR spectra of $4.0 \times \text{Pd} [\text{Pd}_6(\text{FL}1)_8] \cdot 12(\text{BF}_4)$ with a) 10.0 mM SDS, b) 1.0 mM SDS and c) no guest – aromatic region. (293 K, 500 MHz, d_6 -DMSO)

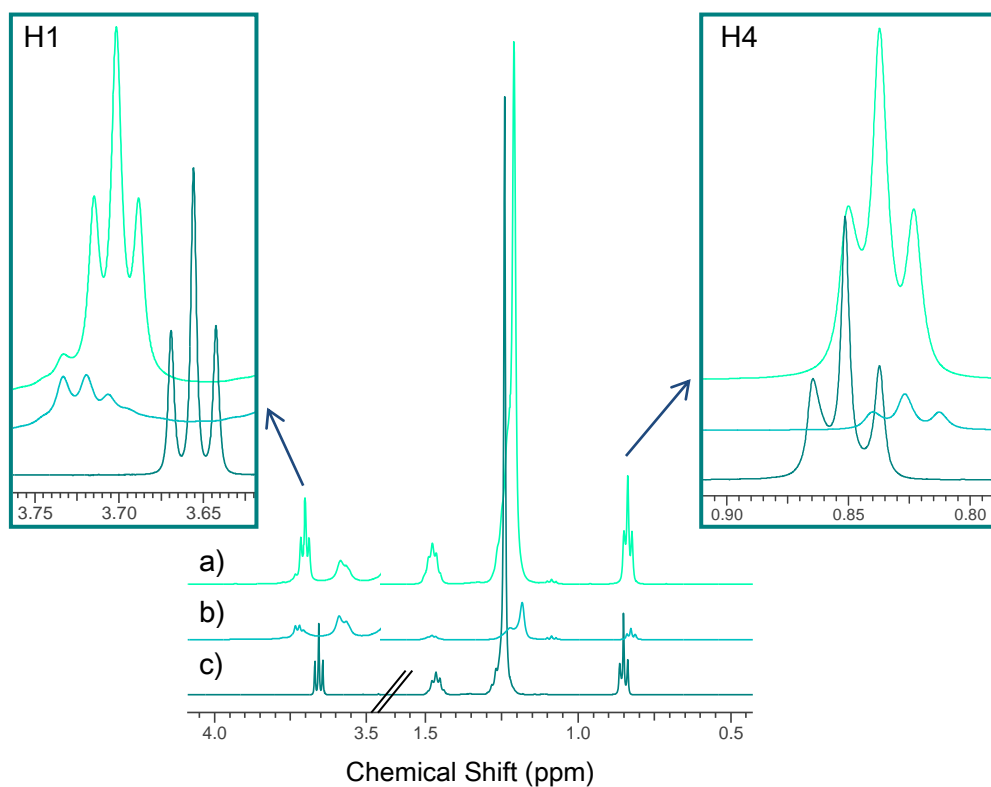


Figure 3.23 ^1H NMR spectra of SDS and $4.0 \times \text{Pd} [\text{Pd}_6(\text{FL}1)_8] \cdot 12(\text{BF}_4)$ with SDS. a) SDS, b) $4.0 \times \text{Pd} [\text{Pd}_6(\text{FL}1)_8] \cdot 12(\text{BF}_4)$ with 1.0 mM SDS and c) $4.0 \times \text{Pd} [\text{Pd}_6(\text{FL}1)_8] \cdot 12(\text{BF}_4)$ with 10.0 mM SDS – upfield regions showing SDS peaks. Expansions of the SDS H1 and H4 peaks are shown. (293 K, 500 MHz, d_6 -DMSO)

^1H NMR titration studies and Job's plots were performed with 1.0 and $4.0 \times \text{Pd}$ $[\text{Pd}_6(\text{FL1})_8] \cdot 12(\text{BF}_4)$ stella octangula cages and SDS to further investigate the host-guest interaction. The titration samples were prepared in sets of eleven, with the concentration of $[\text{Pd}_6(\text{FL1})_8] \cdot 12(\text{BF}_4)$ kept constant at 0.5 mM and the concentration of SDS starting at 0.5 mM as the lowest concentration and then $1.0 - 10.0 \text{ mM}$ in 1.0 mM increments. The data from these analyses were used to attempt the fitting of binding constants for $[\text{Pd}_6(\text{FL1})_8] \cdot 12(\text{BF}_4)$ and SDS host-guest systems. Job's plot samples were prepared at a fixed total concentration of 2.5 mM .

Figure 3.24 shows the ^1H NMR spectra for the $1.0 \times \text{Pd}$ binding experiment. These spectra indicated an interaction between $1.0 \times \text{Pd}$ $[\text{Pd}_6(\text{FL1})_8] \cdot 12(\text{BF}_4)$ and SDS. The SDS chemical shifts showed clear chemical shift changes with decreasing SDS concentration. This is demonstrated in Figure 3.24 b), which shows the resonances of H3 and H4. H3 became increasingly broad as the concentration of SDS was decreased, possibly indicating that the tail sections of SDS could have been experiencing slightly different magnetic environments whilst the NMR data are being collected. The chemical shifts of SDS moved further away from their uncomplexed chemical shift values with decreasing SDS concentration, with H4 shifting upfield by 0.13 ppm . ^{19}F NMR spectra were also collected for this sample set; however, these data gave no indication that the fluorine magnetic environments were affected by the presence of SDS in solution for either the cage or free ligand. Despite the ^1H NMR spectra indicating a host-guest interaction, binding constants could not be determined for $1.0 \times \text{Pd}$ $[\text{Pd}_6(\text{FL1})_8] \cdot 12(\text{BF}_4)$ with SDS.

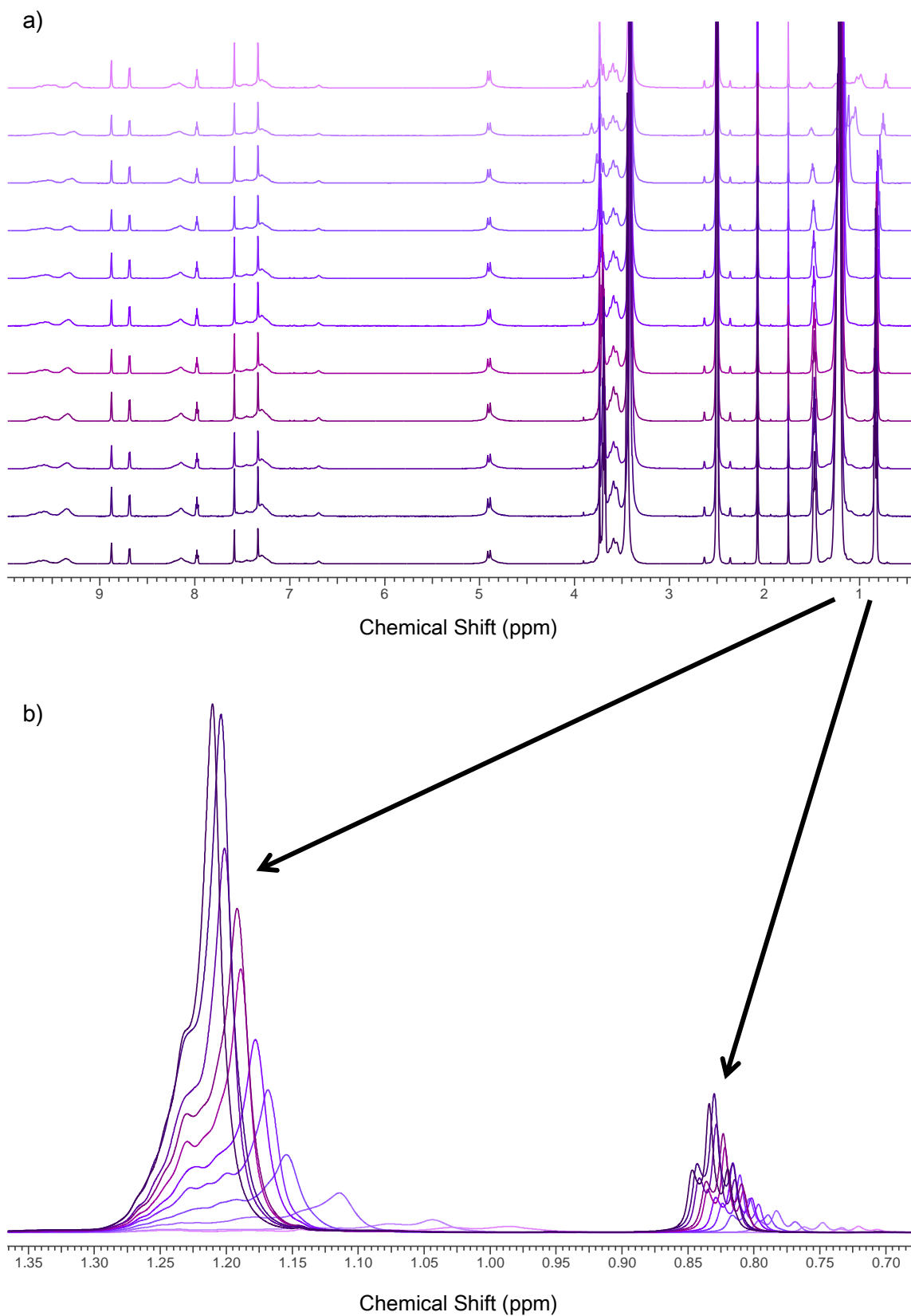


Figure 3.24 ^1H NMR spectra of 0.5 mM $1.0 \times \text{Pd} [\text{Pd}_6(\text{FL}1)_6] \cdot 12(\text{BF}_4)$ SDS with 10.0 mM at the bottom and 0.5 mM at the top, b) superimposed stacked plot of SDS H3 and H4 peaks. (293 K, 500 MHz, d_6 -DMSO)

The spectra for $4.0 \times \text{Pd} [\text{Pd}_6(\text{FL1})_8] \cdot 12(\text{BF}_4)$ and SDS are shown below in Figure 3.25. Whilst the SDS showed the same pattern of chemical shift change seen for $1.0 \times \text{Pd}$, the chemical shift changes were smaller. The H4 protons exhibited their largest change in chemical shift at the lowest SDS concentration, as was seen for $1.0 \times \text{Pd}$. However, Figure 3.25 b) shows that for $4.0 \times \text{Pd}$, that chemical shift difference was only 0.065 ppm, half the chemical shift difference seen for $1.0 \times \text{Pd}$. The same behaviour was also observed for the H3 protons, whose peaks became increasingly broad as the concentration of SDS was decreased, and again, possibly indicative of slightly different chemical environments being sampled during the timeframe of the NMR experiment. ^{19}F NMR data was also recorded for this set of samples, but did not reveal any information regarding the nature of the host-guest interaction.

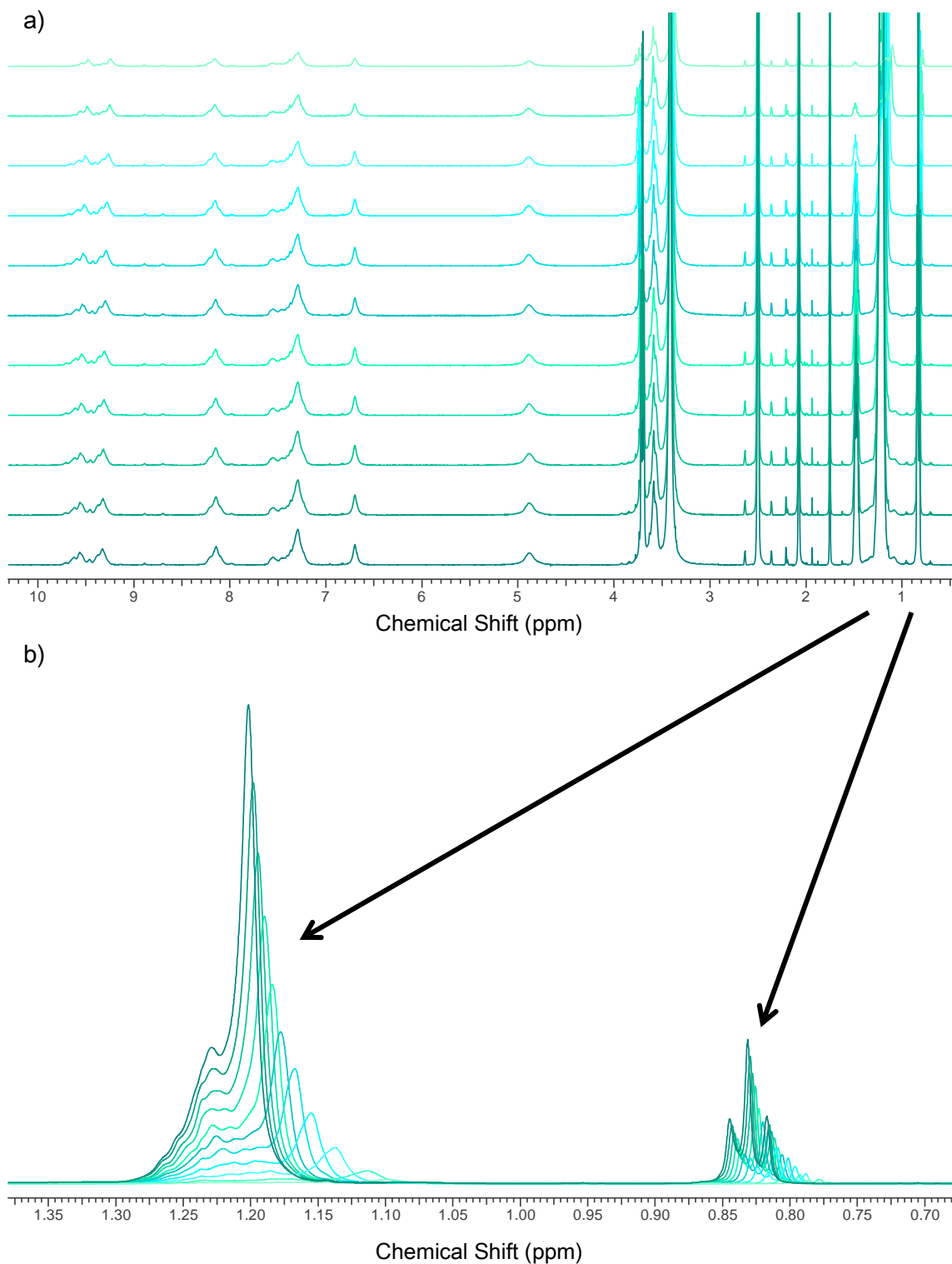


Figure 3.25 ^1H NMR spectra of 0.5 mM $4.0 \times \text{Pd} [\text{Pd}_6(\text{FL1})_8] \cdot 12(\text{BF}_4)$ SDS with 10.0 mM at the bottom and 0.5 mM at the top, b) superimposed stacked plot of SDS H3 and H4 peaks. (293 K, 500 MHz, d_6 -DMSO)

The binding constants of the $4.0 \times \text{Pd} [\text{Pd}_6(\text{FL1})_8] \cdot 12(\text{BF}_4)$ and SDS host-guest system were fitted using the HypNMR 2008¹⁴² programme, as discussed in section 2.3.3.1. The chemical shift data of the titration studies were used for these calculations. The

peaks used for the fitting were the Hb/b of the host molecule and all four peaks of the guest molecules. The fitted cumulative association constants β are listed in Table 3.4. Again, it is important to note that the β_2 is a cumulative association constant, not a stepwise constant. The first association constant ($K_{a1} = \beta_1$) was higher (ca. 10^2 M^{-1}) than that of the second stepwise constant K_{a2} , which can be roughly calculated by dividing β_2/β_1 , this gave a small K_{a2} value of approximately 10^1 M^{-1} . The fitting could only be achieved for a 1:2 host-guest ratio, indicating a 1:2 host-guest interaction for the $4.0 \times \text{Pd} [\text{Pd}_6(\text{FL1})_8] \cdot 12(\text{BF}_4)$ and SDS. Figure 3.26 shows the fitting graphs for this system. These plots indicate that although there were 1:2 host-guest complexes, most of the guest remained free in solution.

Table 3.4 Fitted cumulative association constants for $4.0 \times \text{Pd} [\text{Pd}_6(\text{FL1})_8] \cdot 12(\text{BF}_4)$ and SDS host-guest systems.

Guest	β_1/M^{-1} (H+G \leftrightarrow HG)	β_2/M^{-2} (H+2G \leftrightarrow HG ₂)
SDS	$(4.0 \pm 0.2) \times 10^2$	$(2.7 \pm 0.2) \times 10^4$

The uncertainties are estimates of the standard deviation calculated by HypNMR¹⁴²

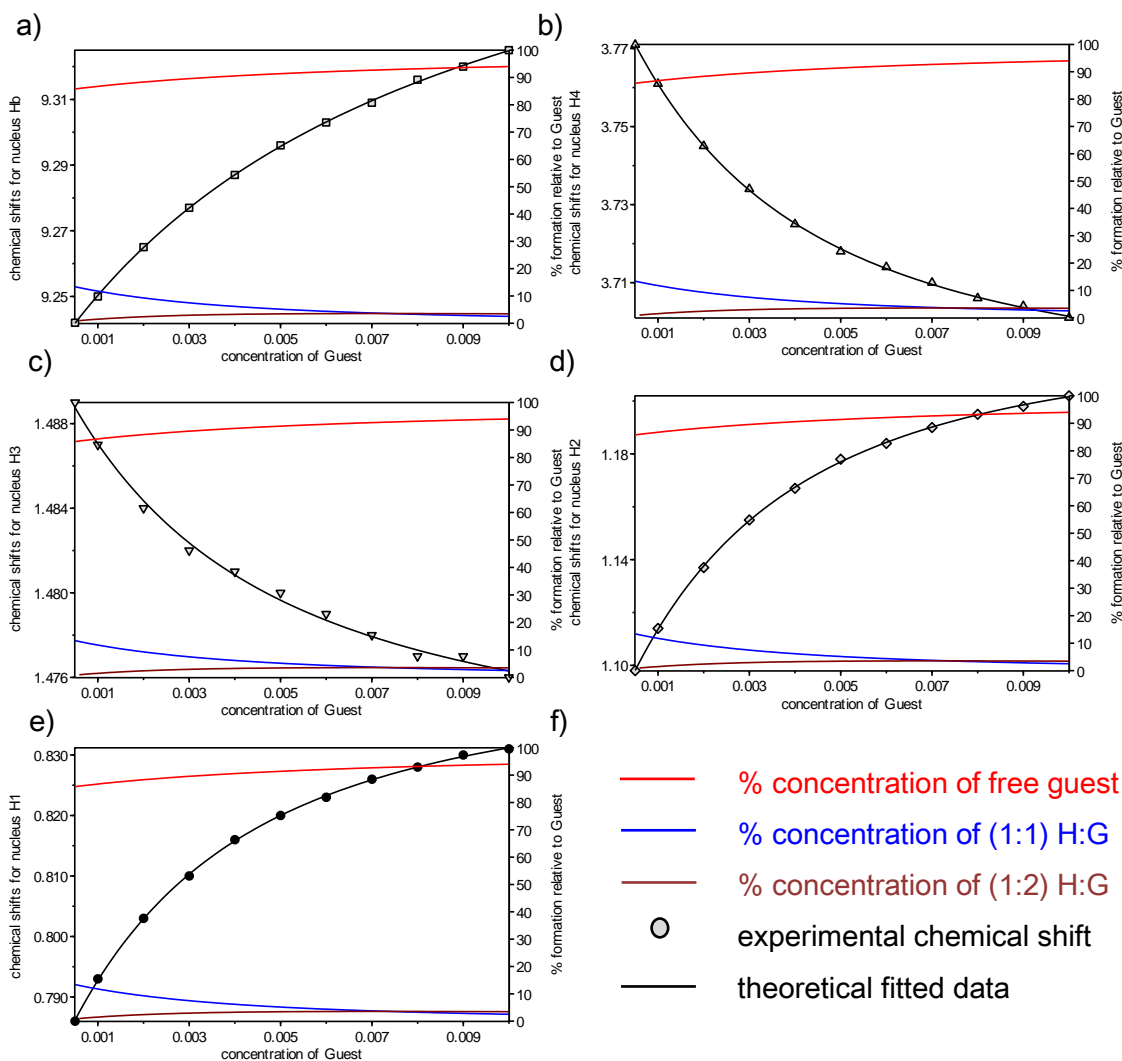


Figure 3.26 Fitting of the ^1H NMR titration data for the $4.0 \times \text{Pd} [\text{Pd}_6(\text{FL}1)_8]^{12+}$ stella octangula cage and SDS, shown for protons: a) Hb, b) H4, c) H3, d) H2, e) H1 and f) legend for plots.

To investigate the stoichiometry of these systems, Job's plot analyses were conducted at a fixed total concentration of 2.5 mM. A brief description of the technique can be found in section 2.3.2. The Job's plots are shown in Figure 3.27. The results for the $1.0 \times \text{Pd} [\text{Pd}_6(\text{FL}1)_8] \cdot 12(\text{BF}_4)$ and SDS system did not show a clear minima or maxima. H1 has a minima of 0.35, H2 was unclear, H3 had a maxima of 0.4 and H4 had a maxima of 0.3. This gave an average $[\text{H}]_0/([\text{H}]_0 + [\text{G}]_0)$ of 0.35, which implies a host-guest stoichiometry of one part host and two parts guest. The Job's plot for $4.0 \times \text{Pd} [\text{Pd}_6(\text{FL}1)_8] \cdot 12(\text{BF}_4)$ has a well-defined $[\text{H}]_0/([\text{H}]_0 + [\text{G}]_0)$ at 0.20. This indicated a five part system with one host to four guests. However it is important to consider that both of

these systems had additional material in solution; that is, free ligand in the $1.0 \times \text{Pd}$ samples and the possibility of excess palladium in the $4.0 \times \text{Pd}$ samples. In addition to that and as mentioned in section 2.3.2, Job's plots, for stoichiometries other than 1:1 are not considered reliable,¹⁴¹ meaning that these results should be treated with caution.

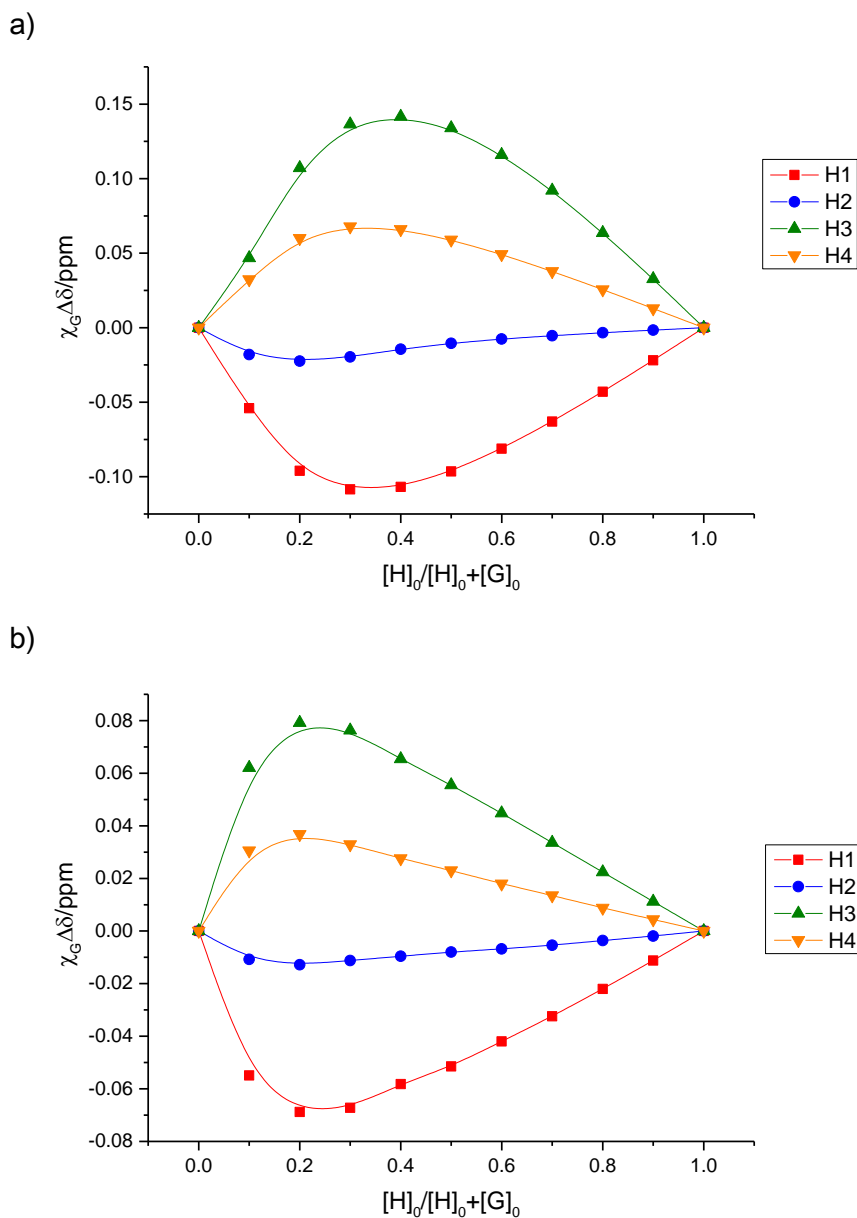
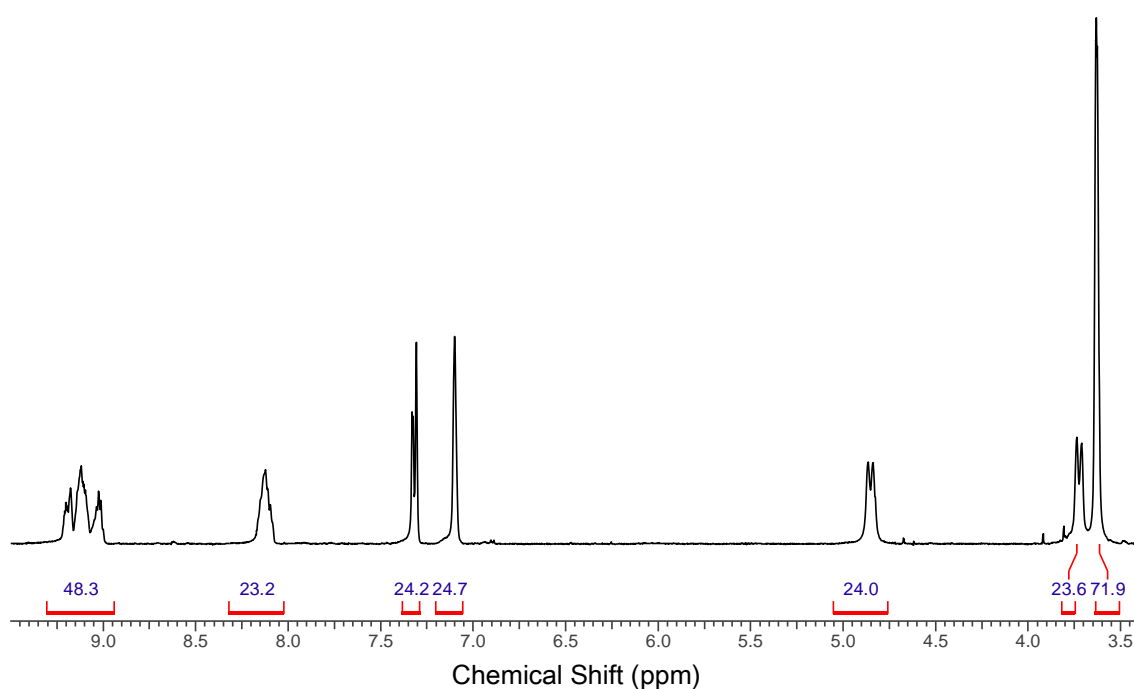


Figure 3.27 Job's plots for $[\text{Pd}_6(\text{FL}1)_6] \cdot 12(\text{BF}_4)$ and SDS. Legends show guest chemical shifts plotted. a) $1.0 \times \text{Pd}$ and b) $4.0 \times \text{Pd}$.

3.2.3 FL1 Stella Octangula Cage in d_3 -Acetonitrile

As discussed in section 3.1.2, it was possible to dissolve both the FL1 ligand and the tetrakis(acetonitrile)palladium(II)tetrafluoroborate in acetonitrile. When these solutions were added together in the correct stoichiometric ratio to form a $[\text{Pd}_6(\text{FL1})_8]^{12+}$ cage system, the following spectrum was seen.



*Figure 3.28 $[\text{Pd}_6(\text{FL1})_8] \cdot 12(\text{BF}_4)$ stella octangula cage with integrations.
(293 K, 500 MHz, d_3 -MeCN)*

There was no free ligand present in this sample, indicating that the self-assembly of the FL1 stella octangula cage had occurred quantitatively. There were no changes observed in the spectrum, which remained unchanged for a period of 4 months. The Ha and Hb protons, (which resonated as multiplets at 9.2 ppm) indicated the complexes formed were heterochiral cages. The ^{19}F NMR spectrum shown in Figure 3.29 exhibited three fluorine environments at an approximate ratio of 1:2:1. This provides further support that the cages were heterochiral, as homochiral cage systems are expected to have only one peak in their ^{19}F NMR spectra.

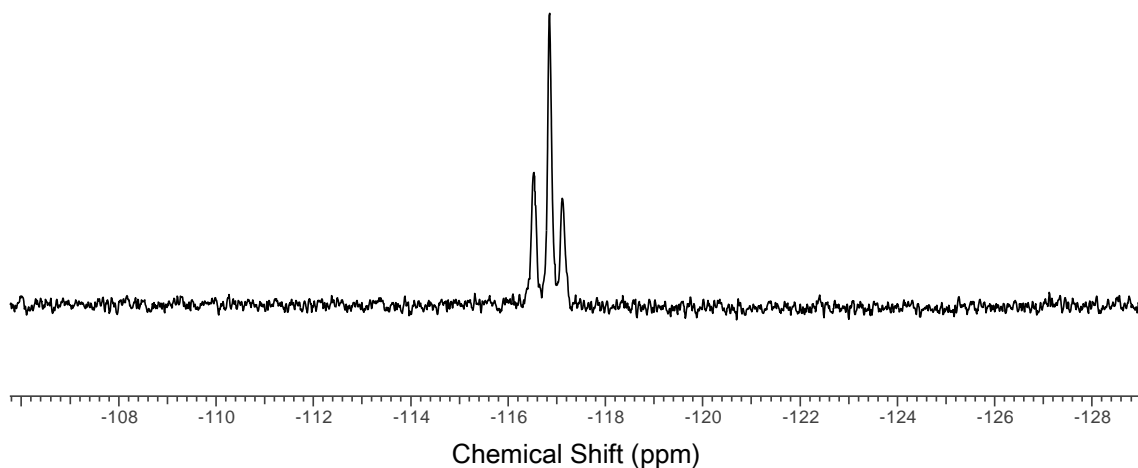


Figure 3.29 ^{19}F NMR spectrum of FL1 ligand. (296 K, 282 MHz, d_3 -MeCN)

The DOSY spectrum shown in Figure 3.30 indicated that there was only one molecular weight of complex in solution, which had a diffusion coefficient of $7.3 \times 10^{-10} \text{ m}^2 \text{ s}^{-1}$.

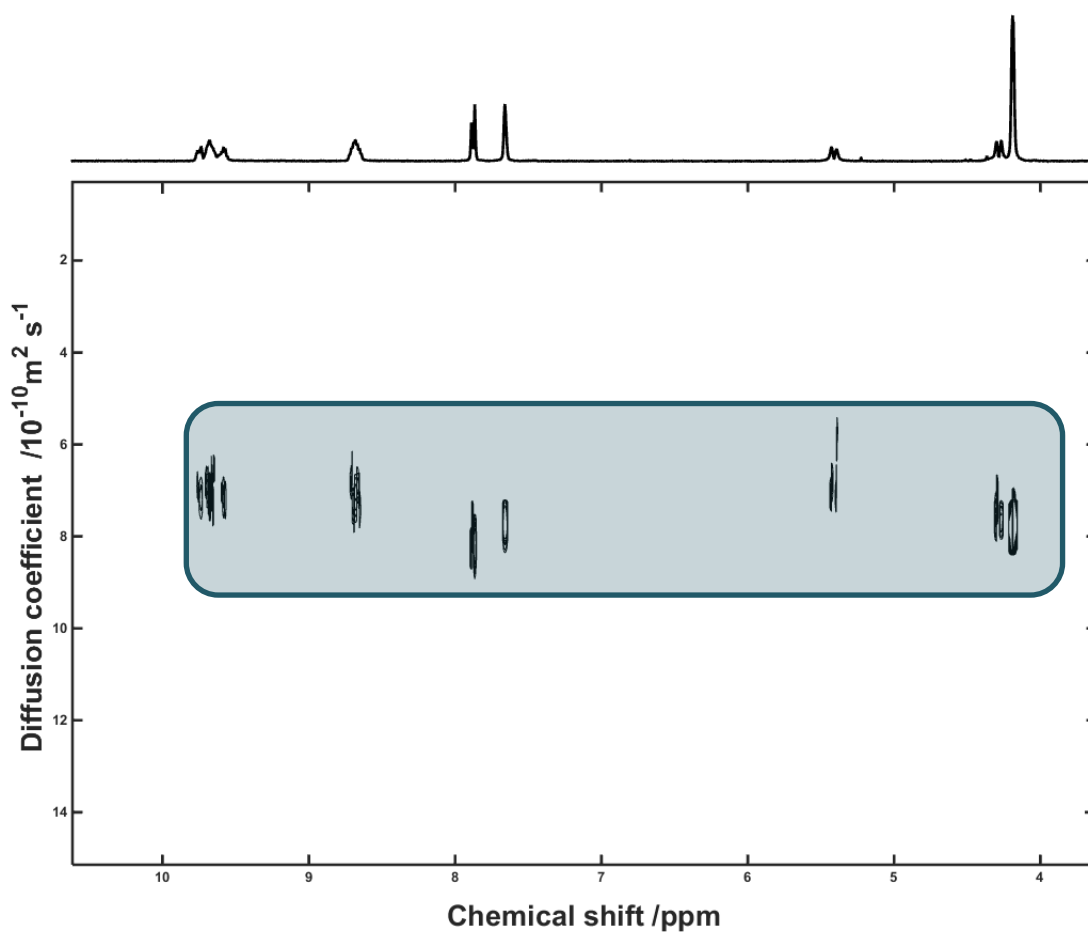


Figure 3.30 ^1H NMR DOSY spectrum of $[\text{Pd}_6(\text{FL1})_8] \cdot 12(\text{BF}_4)$ stella octangula cage. (293 K, 500 MHz, d_3 -MeCN)

Electrospray mass spectroscopic analysis also suggested an M_6L_8 type molecule in solution. The mass spectrum (Figure 3.31) was similar to that seen for the $[Pd_6(L1)_8] \cdot 12(BF_4)$ stella octangula cage shown section 2.3.6. The observed mass peaks corresponded closely to those calculated for this system, as shown in Table 3.5. A series of signals at m/z 2546.3, 1888.2, 1493.4, 1230.1, 1041.8, 900.7 and 791.0 could be assigned to $\{[Pd_6(L1)_8] \cdot (BF_4)_{(12-x)}\}^{x+}$ (where $x = 3, 4, 5, 6, 7, 8, 9$). These signals resulted from the octahedral core of the stella octangula cage, but with different numbers of anions present.

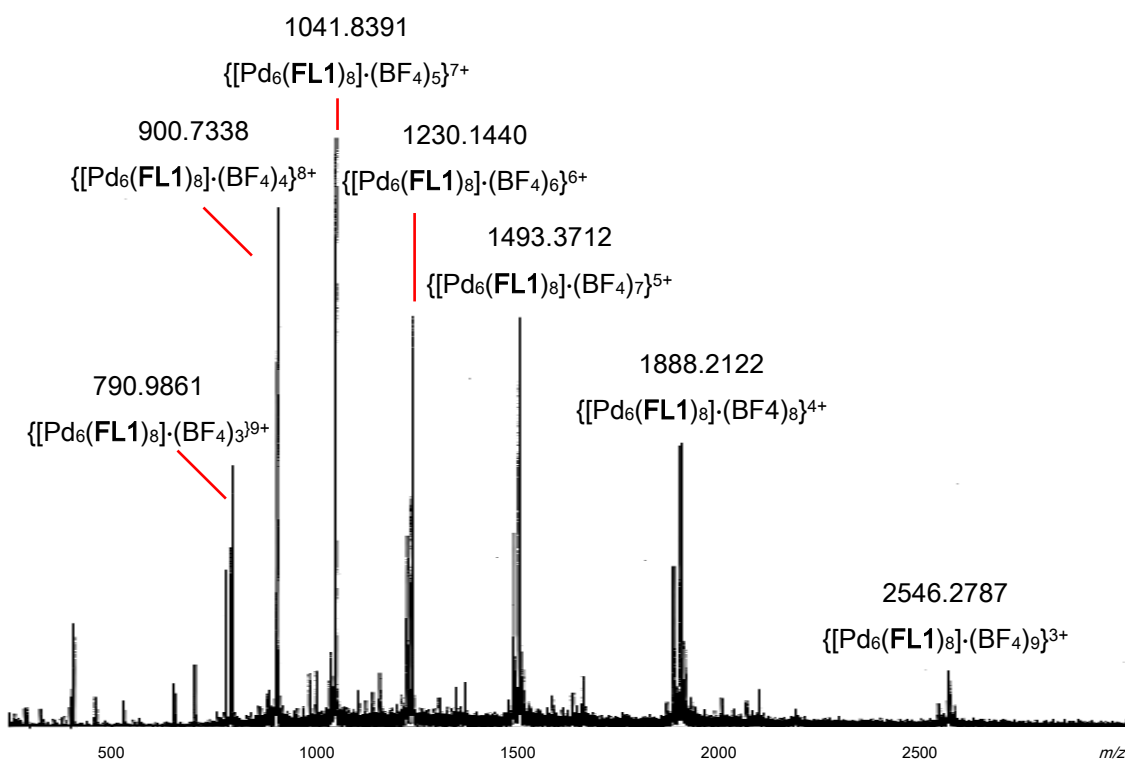


Figure 3.31 ESI-MS of $[Pd_6(FL1)_8] \cdot 12(BF_4)$ stella octangula cage showing various $\{[Pd_6(FL1)_8] \cdot n(BF_4)\}^{12-n+}$ ions.

Table 3.5 Table to show calculated and observed m/z for the $[\text{Pd}_6(\text{FL1})_8] \cdot 12(\text{BF}_4)$ stella octangula cage.

$\{[\text{Pd}_6(\text{FL1})_8] \cdot n(\text{BF}_4)\}^{12-n+}$ ion	Calculated m/z	Observed m/z
$\{[\text{Pd}_6(\text{FL1})_8] \cdot (\text{BF}_4)_3\}^{9+}$	791.1699	790.9861
$\{[\text{Pd}_6(\text{FL1})_8] \cdot (\text{BF}_4)_4\}^{8+}$	900.9165	900.7338
$\{[\text{Pd}_6(\text{FL1})_8] \cdot (\text{BF}_4)_5\}^{7+}$	1042.0193	1041.8391
$\{[\text{Pd}_6(\text{FL1})_8] \cdot (\text{BF}_4)_6\}^{6+}$	1230.1563	1230.1440
$\{[\text{Pd}_6(\text{FL1})_8] \cdot (\text{BF}_4)_7\}^{5+}$	1493.5482	1493.3715
$\{[\text{Pd}_6(\text{FL1})_8] \cdot (\text{BF}_4)_8\}^{4+}$	1888.6360	1888.2122
$\{[\text{Pd}_6(\text{FL1})_8] \cdot (\text{BF}_4)_9\}^{3+}$	2547.1157	2546.2787

The 2-D ROESY spectrum of the $[\text{Pd}_6(\text{FL1})_8] \cdot 12(\text{BF}_4)$ stella octangula cage shown in Figure 3.32 indicated a stable complex that was not in exchange with itself. The rOes observed were the same as those seen in the ROESY spectrum of the FL1 ligand. However, due to the shape of the FL1 stella octangula cage, it would not be expected that any other through-space connections would be observed.

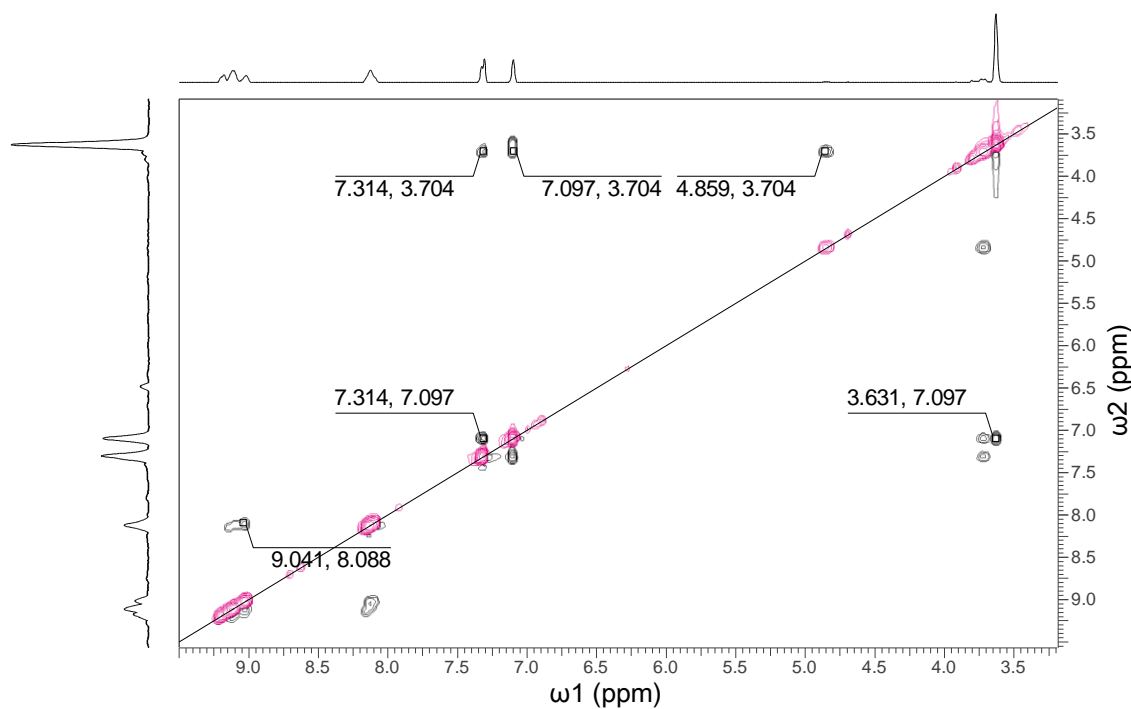


Figure 3.32 Section of 2-D ROESY spectrum for 0.5 mM $[Pd_6(FL1)_8] \cdot 12(BF_4)$ stella octangula cage with through space connections in black and exchange peaks in pink. (293 K, 500 MHz, d_3 -MeCN)

Table 3.6 Table of through-space connections and assignments for $[Pd_6(FL1)_8] \cdot 12(BF_4)$ stella octangula cage.

Through-space Connection/ppm	Assignment
3.631, 7.097	Hd-Hf
4.859, 3.704	H _{endo} -H _{exo}
7.097, 3.704	Hf-H _{exo}
7.314, 3.704	He-H _{exo}
7.314, 7.097	He-Hf
9.041, 8.088	Hb-Hc

Crystals of the FL1 stella octangula cage were initially grown by slow acetone diffusion.

These crystals rapidly decomposed when removed from the mother liquor. A

consequence of this was that X-ray crystallography data could not be collected, despite the samples being studied at the Diamond Light Source. The crystals were highly unstable, disordered and desolvated. It was possible however, to take some images using an optical microscope, prior to the crystal decomposing. The crystals displayed an octangula aspect, as shown in Figure 3.33.

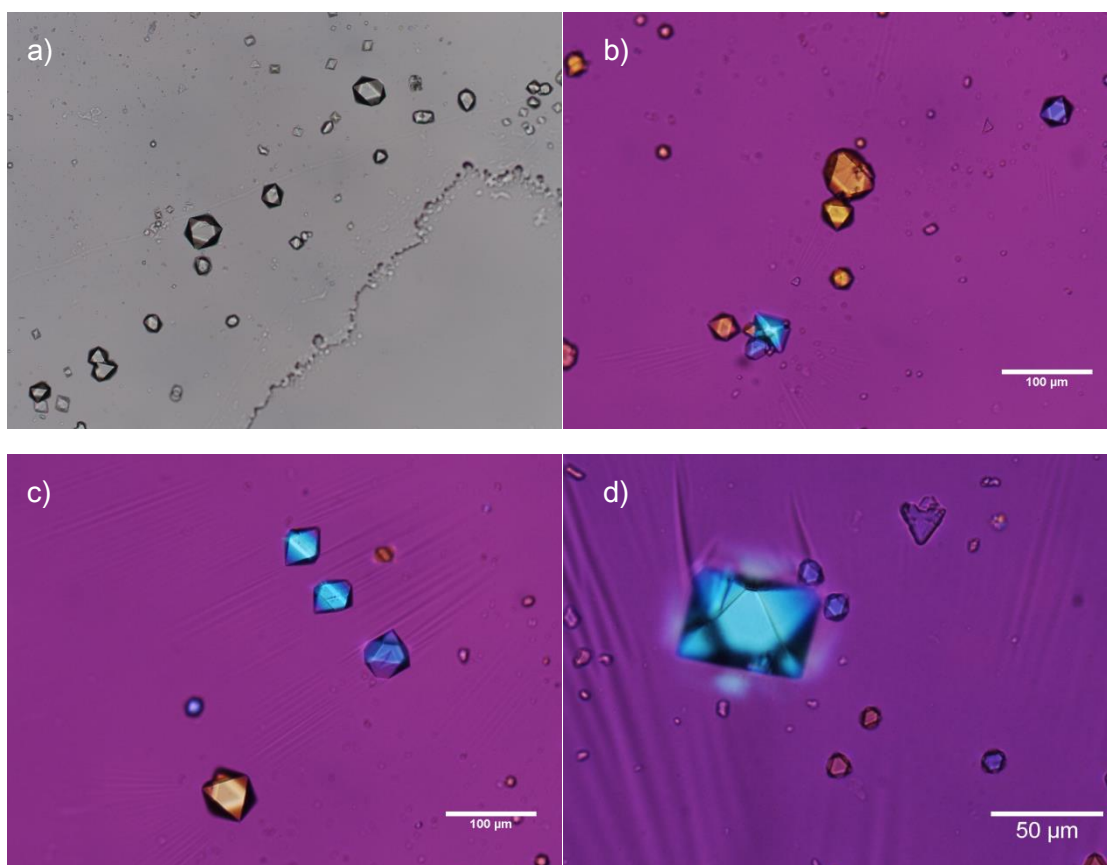


Figure 3.33 Optical microscopy images of $[Pd_6(FL1)_8] \cdot 12(BF_4)$ stella octangula cage, b)-d) are polarised images.

Single crystals were obtained by diffusion of diethyl ether vapours into an d_3 -acetonitrile solution of the FL1 stella octangula cage. This resulted in crystals that diffracted extremely weakly. However, a partially resolved structure could be obtained. The crystals were isostructural with the previously described $[Pd_6(L2_8)] \cdot 12(BF_4)$ stella octangula cage, with both having the tetragonal space group with unit cell dimensions of $a = 30.688(5)$, $c = 45.906(11)$ Å.¹¹³ The data from the published structure was used

as a starting point for the refinement of this data. The structure was found to be highly disordered, with averaged positions showing both ligand enantiomers superimposed on one another. This is shown in Figure 3.34 and Figure 3.35. Only the palladium(II) centres were refined anisotropically. The FL1 cages were not enantiomerically resolved. Instead a statistical mixture of complexes was observed. There was no evidence of chiral self-sorting.

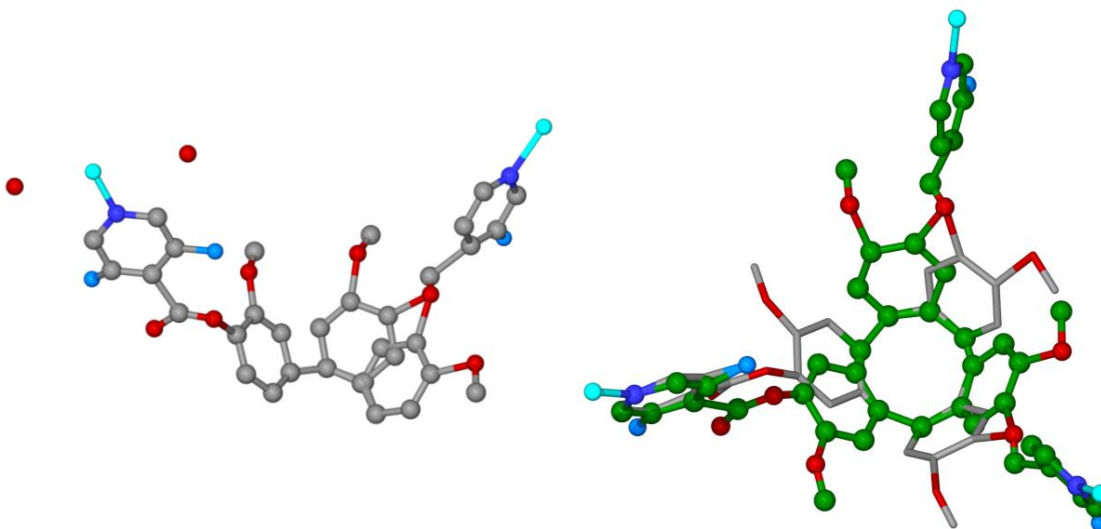


Figure 3.34 a) From the asymmetric unit of $[Pd_6(FL1)_8] \cdot 12(BF_4)$, with carbon atoms in grey, oxygen atoms in red, nitrogen in dark blue, fluorine in blue and palladium in light blue, b) from the crystal structure of $[Pd_6(FL1)_8] \cdot 12(BF_4)$, showing the two disordered enantiomers of the FL1 ligands in each $[Pd_6(FL1)_8] \cdot 12(BF_4)$ cage. Individual ligand enantiomers are distinguished by colour.

The Pd sites had approximate square planar geometry and Pd centres were arranged in an octahedron with respect to one another. The Pd...Pd separations range from 16.1 – 16.6 Å. The cages were approximately 3 nm in diameter. Whilst the gross structural features of the structure were established, exact bond lengths and angles were not reliable due to the low resolution of the data obtained. Figure 3.35 shows images from the crystal structure obtained. It can be seen in Figure 3.35 c) that the positions of the

fluorines of the FL1 ligand were ascertained. The fluorines are pointing in an exo position, away from the cage interior.

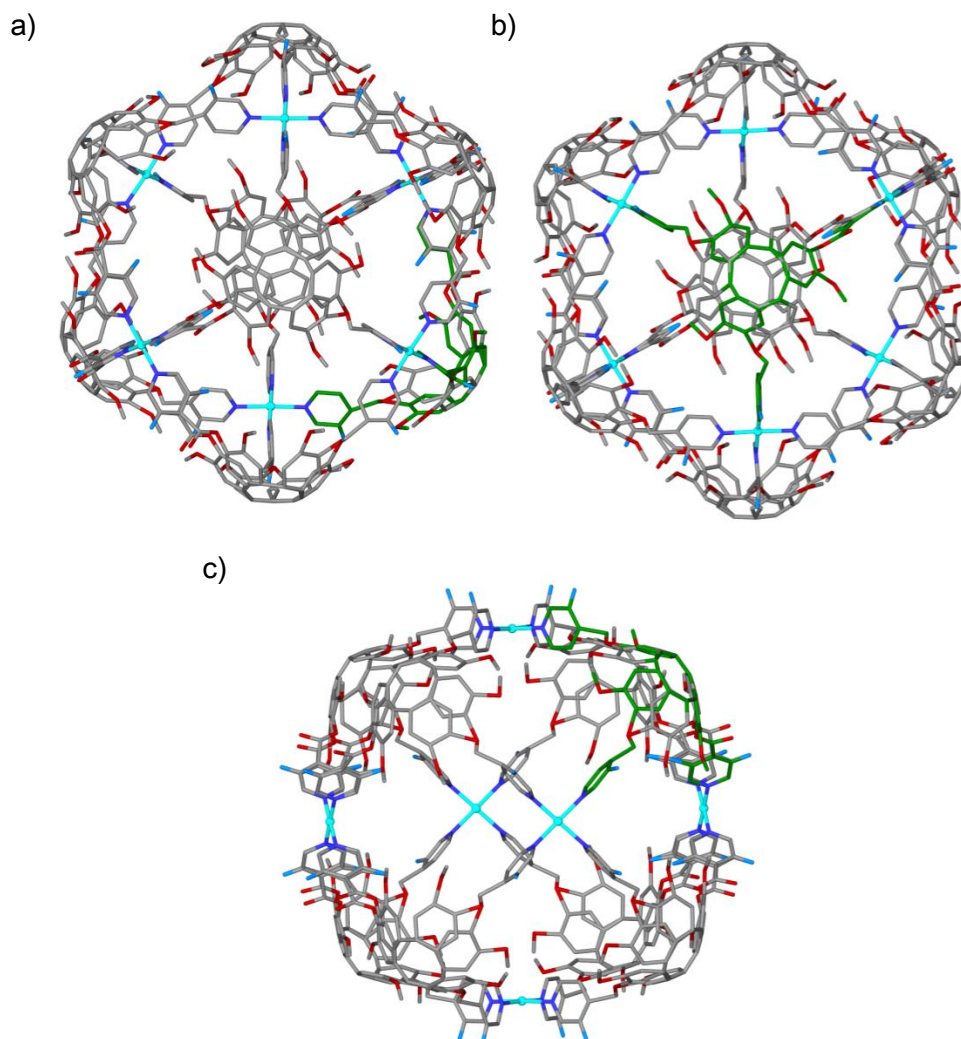


Figure 3.35 From the crystal structure of $[Pd_6(FL1)_8] \cdot 12(BF_4)$ a) and b) from above and c) from the side. One ligand is coloured green.

3.2.4 Host-Guest Studies with the FL1 Stella Octangula Cage in d_3 -Acetonitrile

Host-guest studies with the FL1 stella octangula cage in acetonitrile were conducted with the following guests: adamantane-1-carboxylic acid, 2-bromoadamantane, camphor-*D*, biphenyl, 3-chloro-1-propanol, 1-chlorooctane and 8-chloro-1-octanol. No evidence of any host-guest interaction was seen for these potential guests, with the 1H

NMR merely exhibiting additive spectra. As a result of these ^1H NMR spectra, no further investigations were undertaken with these guests. SDS was not investigated as it was found not to be soluble in α_3 -acetonitrile.

3.3 Discussion

3.3.1 FL1 Ligand

The novel **FL1** ligand has been characterised by ^1H and ^{19}F NMR spectroscopy. It has been shown to be more soluble than **L1**, as illustrated in section 3.1.2. The **FL1** ligand had a more complex ^1H NMR spectrum than **L1**. This is due to the fluorine, which also coupled to the protons on the pyridyl group of the ligand. The **FL1** ligand was devised to investigate the self-assembly of the stella octangula cages, by allowing insight to be gained from ^{19}F NMR spectroscopy. Unfortunately, this has not provided much information with regards to the self-assembly process. It did however, provide information on whether or not a metallo-complex had been formed, as when this process occurred, the characteristic fine structure seen in the **FL1** ligand spectrum (Figure 3.7, Figure 3.9 and Figure 3.10) was lost and the resonance was broadened and shifted downfield by 10 ppm. ^{19}F NMR spectroscopy also revealed no information pertaining to any $[\text{Pd}_6(\mathbf{FL1})_8]\cdot 12(\text{BF}_4)$ host-guest systems studied in this work. This could be due to the orientation of the fluorines of the **FL1** ligand within the $[\text{Pd}_6(\mathbf{FL1})_8]\cdot 12(\text{BF}_4)$ stella octangula cage, which were found to occupy an exo position with regards to the cage interior.

3.3.2 FL1 Stella Octangula Cage in d_6 -DMSO

When **FL1** was used to form a M_6L_8 stella octangula system in d_6 -DMSO, it did not form quantitative homochiral assemblies when the correct stoichiometric ratio of palladium to **FL1** ligand was used, these samples also exhibited a large amount of uncomplexed ligand. When more palladium was added to stella octangula cage samples in d_6 -DMSO, the amount of free ligand in solutions decreased and the samples appeared to self-sort at a faster rate. However, even the sample with 4.0 \times the stoichiometric quantity of Pd, the spectrum is broad. This broadness could be indicative of either ligand exchange within the cages which ceases when the cages become homochiral or a mixture of heterochiral cages in solution. It was shown that having excess palladium present did not encourage the formation of homochiral assemblies, even though it did appear to speed up the rate of self-sorting.

It is possible for **FL1** that the nitrogen of the pyridine is not as readily available as a lone pair when compared to **L1**, due to the electron withdrawing nature of the fluorine. Furthermore, as discussed in section 2.4.1, it is likely that DMSO is in competition with the ligand for the palladium cation.^{138, 144, 145} The addition of fluorine to the pyridyl ring of the ligand also lessens the possibility of a fully homochiral cage, due to the free rotation of the pyridyl ring prior to complexation. Even if the assemblies were to be formed homochirally, in terms of *M* and *P* ligands, that is with either all *M* or all *P* ligands, the ^1H NMR spectra could still be unsymmetrical because of the orientation of the fluorines on the pyridyl arms of each ligand.

3.3.3 Host-Guest Studies with FL1 Stella Octangula Cage in d_6 -DMSO

In section 3.2.2 the host-guest interactions between $1.0 \times \text{Pd}$ and $4.0 \times \text{Pd}$ $[\text{Pd}_6(\text{FL1})_8] \cdot 12(\text{BF}_4)$ cages and SDS were described. The ^1H NMR spectra of the of $1.0 \times \text{Pd}$ and $4.0 \times \text{Pd}$ $[\text{Pd}_6(\text{FL1})_8] \cdot 12(\text{BF}_4)$ cages and SDS appeared to show the same characteristics as those seen between $[\text{Pd}_6(\text{L1})_8] \cdot 12(\text{BF}_4)$ cages and SDS in Chapter 2. That is, a large chemical shift difference was seen for a low concentration of guest, and a smaller difference in chemical shift was observed for the samples with a higher concentration of SDS guest present. This was consistent with what was seen in Chapter 2. That is, the host-guest system was in fast exchange and that at higher guest concentrations, the chemical shifts for the guest were closer to that of free guest in solution as most of the guest will be unbound. It was also observed that having excess palladium present in the samples did have an effect on the chemical shift differences, with smaller chemical shift differences being recorded for the $4.0 \times \text{Pd}$ samples than for the $1.0 \times \text{Pd}$ samples. This was more noticeable at 1.0 mM guest concentration, as both 1.0 and $4.0 \times \text{Pd}$ cages exhibited similar chemical shift differences when there was 10.0 mM of guest present.

This suggests that the fluorine of the **FL1** ligand does not prevent the $[\text{Pd}_6(\text{FL1})_8] \cdot 12(\text{BF}_4)$ stella octangula cage from forming host-guest complexes. The fitting of binding constants for the $4.0 \times \text{Pd}$ $[\text{Pd}_6(\text{FL1})_8] \cdot 12(\text{BF}_4)$ and SDS complex indicated that a 1:2 host:guest stoichiometry was formed, like the analogous $[\text{Pd}_6(\text{L1})_8] \cdot 12(\text{BF}_4)$ and SDS complex. However, the binding constants calculated for the $4.0 \times \text{Pd}$ $[\text{Pd}_6(\text{FL1})_8] \cdot 12(\text{BF}_4)$ and SDS host-guest system indicated that the binding was much weaker than the $[\text{Pd}_6(\text{L1})_8] \cdot 12(\text{BF}_4)$ and SDS system, with all binding constants for $4.0 \times \text{Pd}$ $[\text{Pd}_6(\text{FL1})_8] \cdot 12(\text{BF}_4)$ and SDS being an order of magnitude smaller than those for the

$[\text{Pd}_6(\text{L1})_8] \cdot 12(\text{BF}_4)$ and SDS system. There were also fewer host-guest complexes present in solution, as can be seen from the fitting graphs in Figure 2.24 and Figure 3.26. The titration data for $1.0 \times \text{Pd} [\text{Pd}_6(\text{FL1})_8] \cdot 12(\text{BF}_4)$ and SDS could not be fitted. This could be due to the presence of free ligand in solution, which would lessen the amount of cage present, compounded by the possibility that there was very little host-guest complex present in solution as indicated by the $4.0 \times \text{Pd} [\text{Pd}_6(\text{FL1})_8] \cdot 12(\text{BF}_4)$ and SDS fitting.

The Job's plot analysis indicated that $1.0 \times \text{Pd} [\text{Pd}_6(\text{FL1})_8] \cdot 12(\text{BF}_4)$ and SDS formed a complex with a 1:2 host:guest stoichiometry. However this could not be confirmed by the fitting the titration data. The Job's plot analysis for the $4.0 \times \text{Pd} [\text{Pd}_6(\text{FL1})_8] \cdot 12(\text{BF}_4)$ and SDS system indicated a five-part system with four hosts to one guest. This contradicted the stoichiometry found from the fitting data, which could only be successfully fitted for a 1:2 host to guest stoichiometry. 1:1, 1:3 and 1:4 stoichiometries were also investigated, but fitting could not be achieved for these. Job's analyses are not considered reliable for stoichiometries than 1:1.¹⁴¹ This author found the result from the fitting of the binding constants to be more reliable, considering that the $1.0 \times \text{Pd} [\text{Pd}_6(\text{FL1})_8] \cdot 12(\text{BF}_4)$ and $[\text{Pd}_6(\text{L1})_8] \cdot 12(\text{BF}_4)$ have 1:2 host:guest stoichiometries and that the binding constants were weaker for the $4.0 \times \text{Pd} [\text{Pd}_6(\text{FL1})_8] \cdot 12(\text{BF}_4)$ and SDS complex than for the $[\text{Pd}_6(\text{FL1})_8] \cdot 12(\text{BF}_4)$ and SDS complex as well as the smaller amount of host-guest complexes present in the $4.0 \times \text{Pd} [\text{Pd}_6(\text{FL1})_8] \cdot 12(\text{BF}_4)$ and SDS system.

Although the formation of host-guest complexes was possible with the **FL1** ligand stella octangula cage, it would seem that the addition of fluorine to the ligand reduced the amount of host-guest complexes formed and those host-guest complexes that were

formed were not as tightly bound. This could be a result of the cage portals being less accessible in the **FL1** stella octangula cage compared to the **L1** stella octangula cage, as the fluorine molecule that replaces the proton on the pyridyl ring occupies more of the portal space.

3.3.4 FL1 Stella Octangula Cage in α_3 -Acetonitrile

The characterisation of the **FL1** stella octangula cage in α_3 -acetonitrile is described in section 3.2.3. The ^1H NMR spectrum (Figure 3.28) showed that when **FL1** and Pd were added at a 6:8 stoichiometry, a quantitative complex was immediately formed. This complex was stable at room temperature for at least four months. The formation of the $[\text{Pd}_6(\text{FL1})_8] \cdot 12(\text{BF}_4)$ complex is further evidenced by DOSY and 2-D ROESY NMR spectroscopy, as well as ESI-MS and X-ray crystallography. All of these analyses indicated that a single product was formed. The X-ray crystallography data may be of poor quality, due to the disorder present in the crystals, but it still provides further strong evidence for the formation of $[\text{Pd}_6(\text{FL1})_8] \cdot 12(\text{BF}_4)$ complexes in α_3 -acetonitrile. The disorder in the structure, with each ligand position being a superposition of both *M* and *P* enantiomers of **FL1**, is suggested by Henkelis and co-workers to support the notion that the broadened and unsymmetrical NMR resonances seen in Figure 3.28 can be attributed to a mixture of heterochiral cages.¹¹³ Unfortunately, no host-guest complexes could be produced with the **FL1** stella octangula cage in α_3 -acetonitrile.

3.4 Conclusions

The novel **FL1** ligand has been characterised by ^1H and ^{19}F NMR spectroscopy and it has been found to have better solubility properties than the **L1** ligand. When **FL1** is

applied to stella octangula cage formation it was found to have more self-sorting issues when formed in d_6 -DMSO, requiring four times the amount palladium demanded by the correct M_6L_8 stoichiometry to react with all of the ligand present in solution. The $[Pd_6(\mathbf{FL1})_8] \cdot 12(BF_4)$ in d_6 -DMSO was not as good a host receptacle as the $[Pd_6(\mathbf{L1})_8] \cdot 12(BF_4)$, forming less host-guest complex and exhibiting weaker binding. The $[Pd_6(\mathbf{FL1})_8] \cdot 12(BF_4)$ was found to form immediately and quantitatively in d_3 -acetonitrile, and has been fully characterised, although the crystallography data are of poor quality. In d_3 -acetonitrile, no self-sorting was observed, and in theory, this **FL1** stella octangula cage has many of the attributes desired in a good host. However, no guests investigated in this work could be coerced into its large cavity. Although stella octangula cages were formed with the novel **FL1** ligand, they have transpired to be less suitable for host-guest chemistry than the analogous **L1** stella octangula cage. This research will now move forward to investigate smaller M_3L_2 complexes formed with the **L1** and **FL1** ligands and *cis*-protected palladium(II) complexes and their host-guest properties.

Chapter 4 Cryptophanes

4.1 Introduction

This chapter describes the investigations in producing novel cryptophanes using both the previously described **L1** and **FL1** ligands with commercially available and novel *cis*-protected palladium(II) complexes. The purpose of these investigations was to follow on from work conducted by Henkelis and co-workers⁸⁸, to further study the rearrangement of cryptophanes into stella octangula assemblies and to produce new cryptophane assemblies. Following this, investigations were undertaken to characterise these novel cryptophanes and to explore their host:guest chemistry.

4.2 Initial Investigations

4.2.1 (Ethylenediamine)palladium(II) Dinitrate

(Ethylenediamine)palladium(II) dinitrate, shown in Figure 4.1, is a common source of *cis*-protected palladium in supramolecular chemistry. It is often used when ligands are soluble in water or deuterium oxide.^{89-91, 149}

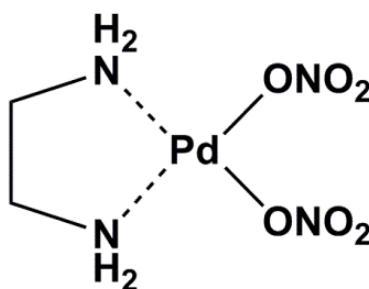


Figure 4.1 (Ethylenediamine)palladium(II) dinitrate.

It has been used by Henkelis and co-workers in DMSO to form a metastable cryptophane with the L2 ligand, the $[\text{Pd}_3(\text{en})(\text{L}2)_2]^{6+}$ complex.⁸⁸ After two weeks at room temperature, the ^1H NMR spectrum of this cryptophane indicated that the cryptophane had degraded and the complex had undergone a rearrangement to a $[\text{Pd}_6(\text{L}2)_8]^{12+}$ stella octangula assembly, as shown in Figure 4.2. It was speculated that the rearrangement was entropically driven due to there being more cationic species present after rearrangement, along with the stella octangula assembly having a higher octahedral symmetry than the cryptophane.¹⁵⁰ Chand *et al.* also saw a similar rearrangement when they used the tripodal ligand 1,3,5-tris(4-pyridylmethyl)benzene to form an $[\text{M}_3\text{L}_2]$ complex with $\text{Pd}(\text{en})(\text{NO}_3)_2$. If this system was heated to 90°C , the $[(\text{Pd}(\text{en})(\text{NO}_3)_2)_3(\text{L}_2)]$ complex rearranged *via* ligand exchange around the Pd(II) centres to give an $[\text{M}_6\text{L}_8]$ and $[\text{Pd}(\text{en})_2](\text{NO}_3)_2$.¹⁵¹

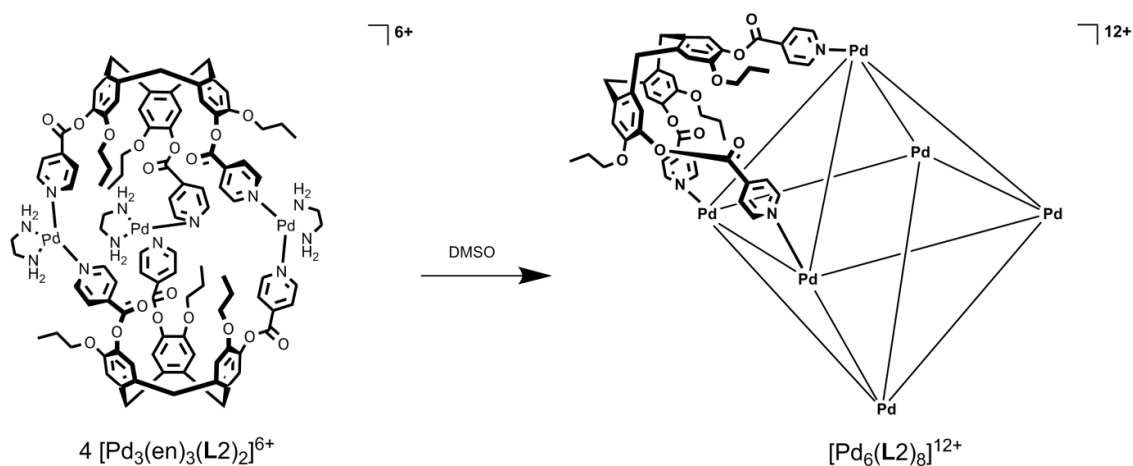


Figure 4.2 Rearrangement of $[\text{Pd}_3(\text{en})_3(\text{L}2)_2]^{6+}$ to $[\text{Pd}_6(\text{L}2)_8]^{12+}$.⁸⁸

The rearrangement of the $[\text{Pd}_3(\text{en})(\text{L}2)_2]^{6+}$ complex was of great interest as it was thought that studying this reaction in more depth could provide information about the stability and stereochemistry of both the cryptophanes and stella octangula assemblies.

Using the methods stipulated by Henkelis and co-workers,⁸⁸ that is, stirring the reaction mixtures in d_6 -DMSO for 16 hours at room temperature, samples were prepared with a

stoichiometric ratio of 3:2 of metal:ligand, using either the L1 or FL1 ligand. No evidence of complexation was seen when the samples were analysed by ^1H & ^{19}F NMR spectroscopy and mass spectroscopy. The ^1H NMR spectra merely showed the superposition of the individual components, as demonstrated by Figure 4.3, showing FL1 ligand and $\text{Pd}(\text{en})(\text{NO}_3)_2$ in d_6 -DMSO. This was confirmed by DOSY analysis, (Figure 4.4) which clearly showed the components diffusing at different rates. The mass spectroscopy also showed no indication of complex formation.

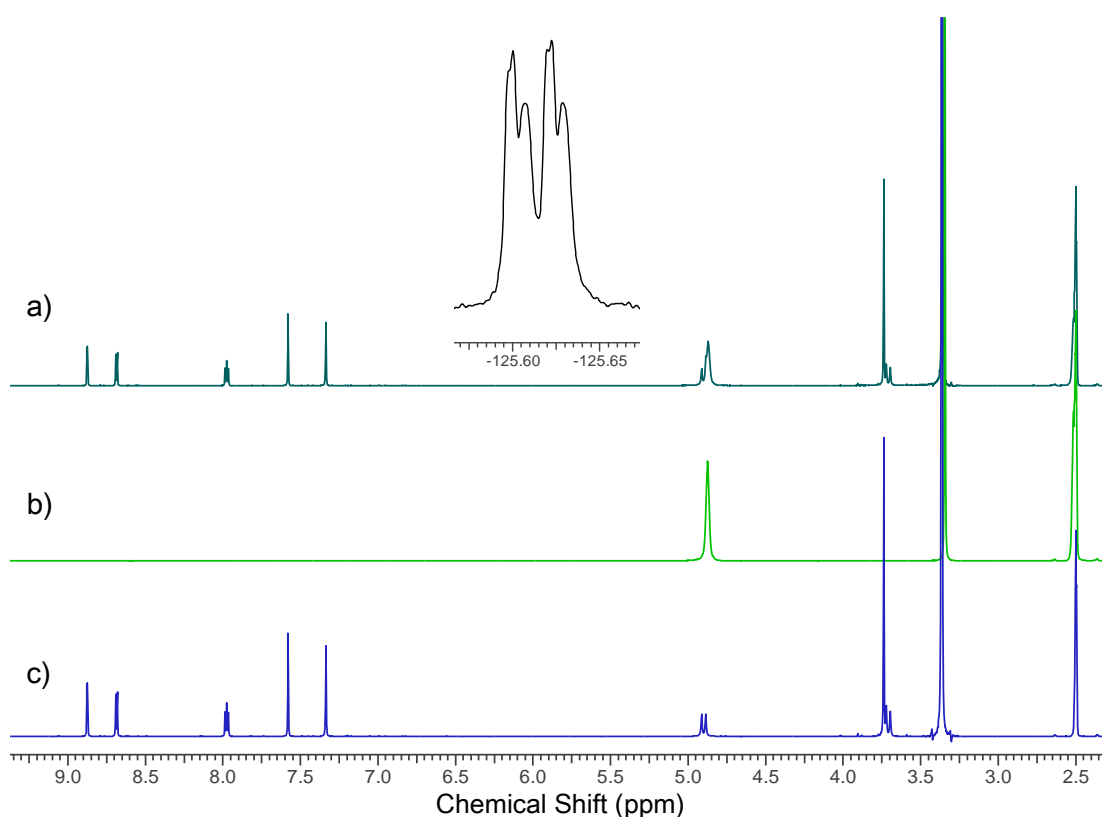


Figure 4.3 ^1H NMR spectra of a) FL1 and $\text{Pd}(\text{en})(\text{NO}_3)_2$ at 2:3 ratio, b) $\text{Pd}(\text{en})(\text{NO}_3)_2$ and c) FL1 (293 K, 500 MHz, d_6 -DMSO) Inset spectrum: ^{19}F NMR spectrum of FL1 + $\text{Pd}(\text{en})(\text{NO}_3)_2$ at 2:3 ratio. (296 K, 282 MHz, d_6 -DMSO)

Attempts were made to produce a $[(\text{Pd}(\text{en}))_3(\text{L1})_2]^{6+}$ system in different deuterated solvents including chloroform, acetonitrile, nitromethane, dichloromethane and a mixture of acetonitrile and water, to no avail. The (ethylenediamine)palladium(II) dinitrate was found to be only sparingly soluble in chloroform, dichloromethane and acetonitrile. It was possible that the vastly improved solubility of the L2 ligand when

compared to L1 and FL1 enabled the formation of the initial cryptophane complex as seen by Henkelis and co-workers.^{88, 113} As this palladium complex proved to be difficult to work with, a different source of palladium was sought to produce novel cryptophanes for host:guest studies and the rearrangement of $M_3(en)L_2 \rightarrow M_6L_8$ assemblies was not investigated any further.

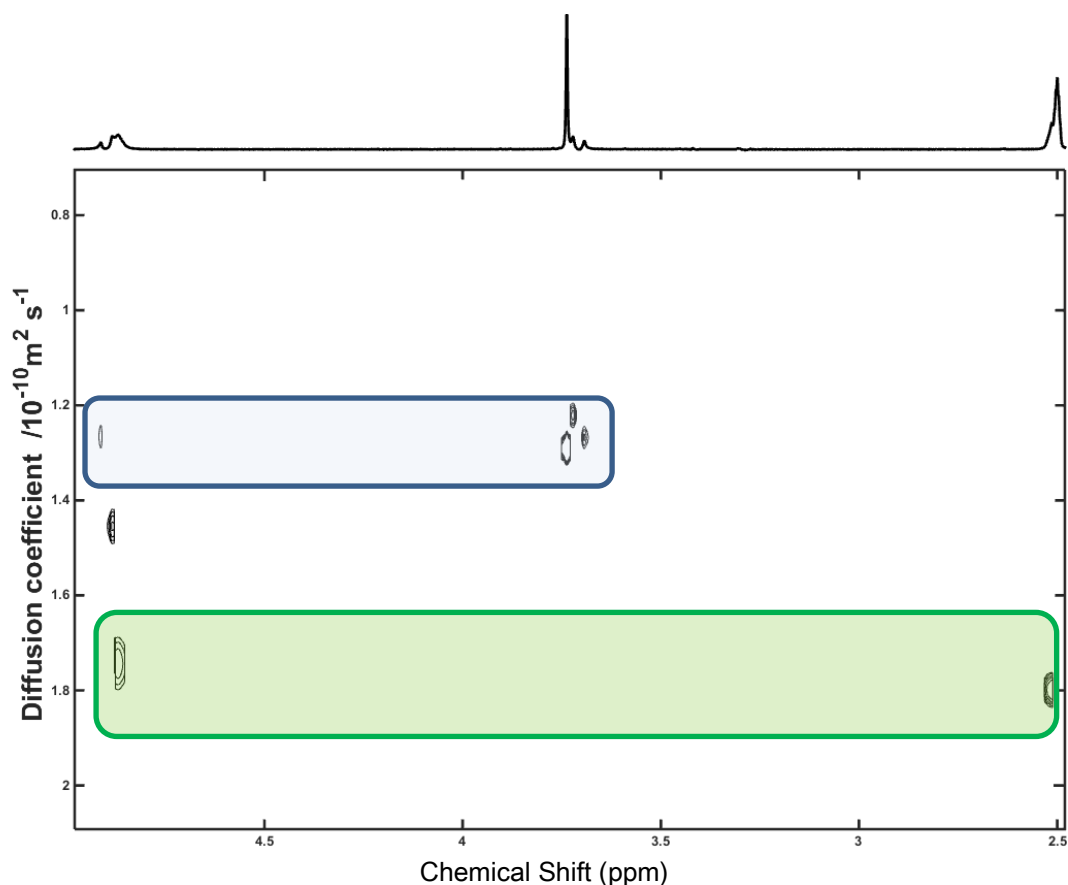


Figure 4.4 1H NMR DOSY spectrum of FL1 and $Pd(en)(NO_3)_2$ at a 2:3 ratio. The FL1 ligand components are highlighted in blue and the $Pd(en)(NO_3)_2$ components are highlighted in green. (293 K, 500 MHz, d_6 -DMSO)

4.2.2 Bis(acetonitrile)-{1,1'-methylenebis(3-benzyl-imidazol-2-ylidene)}palladium

(II) tetrafluoroborate

The novel palladium tecton bis(acetonitrile)-1,1'-methylenebis(3-benzyl-imidazol-2-ylidene)palladium(II)tetrafluoroborate (Figure 4.5), is referred to

using the following notation: $[\text{Pd}(\text{bis-NHC-b})(\text{MeCN})_2]\cdot 2(\text{BF}_4)$ to denote the whole compound and $[\text{Pd}_n(\text{bis-NHC-b})_n]$ will be used to refer to this tecton when it has been complexed. The NHC signifies *N*-heterocyclic carbene and the b denotes that this tecton has benzyl arms. This tecton was specifically designed for the formation of cryptophanes using the propylated **L2** ligand. The synthesis for $[\text{Pd}(\text{bis-NHC-b})(\text{MeCN})_2]\cdot 2(\text{BF}_4)$ is described by Henkelis in unpublished work.¹⁵⁰ As **L2** is analogous to **L1**, and as the combination of **L1** and $[\text{Pd}(\text{bis-NHC-b})(\text{MeCN})_2]\cdot 2(\text{BF}_4)$ to construct cryptophanes had not been attempted, it seemed prudent to investigate this system. The $[\text{Pd}(\text{bis-NHC-b})(\text{MeCN})_2]\cdot 2(\text{BF}_4)$ palladium tecton is a bis-*N*-heterocyclic carbene with benzyl moieties. Bis-*N*-heterocyclic carbene ligands are regarded as strong σ -donor ligands, an advantage in the formation of stable cryptophanes.¹⁵² The electron rich benzyl arms of $[\text{Pd}(\text{bis-NHC-b})(\text{MeCN})_2]\cdot 2(\text{BF}_4)$, which are situated orthogonally to one another, are designed to enable complimentary aromatic interactions with the electron poor pyridyl-ester moiety of the CTG-based ligands. $[\text{Pd}(\text{bis-NHC-b})(\text{MeCN})_2]\cdot 2(\text{BF}_4)$ is similar to the bis-*N*-heterocyclic carbene palladium compound used by Henkelis and co-workers to form cryptophanes with a variety of analogous ligands including **L1**.⁸⁸ That bis-*N*-heterocyclic carbene has naphthyl arms (referred to as bis-NHC-n) in place of the benzyl arms of $[\text{Pd}(\text{bis-NHC-b})(\text{MeCN})_2]\cdot 2(\text{BF}_4)$. They employed it as a *cis*-protecting ligand which enabled stable cryptophane formation. The naphthyl arms resulted in a complex ¹H NMR spectrum, particularly in the aromatic region. It was hoped that $[\text{Pd}(\text{bis-NHC-b})(\text{MeCN})_2]\cdot 2(\text{BF}_4)$, with its benzyl moieties would have a less complex ¹H NMR spectrum, which would be advantageous for host:guest studies, whilst still providing the complimentary aromatic interactions that help to stabilise the cryptophanes.

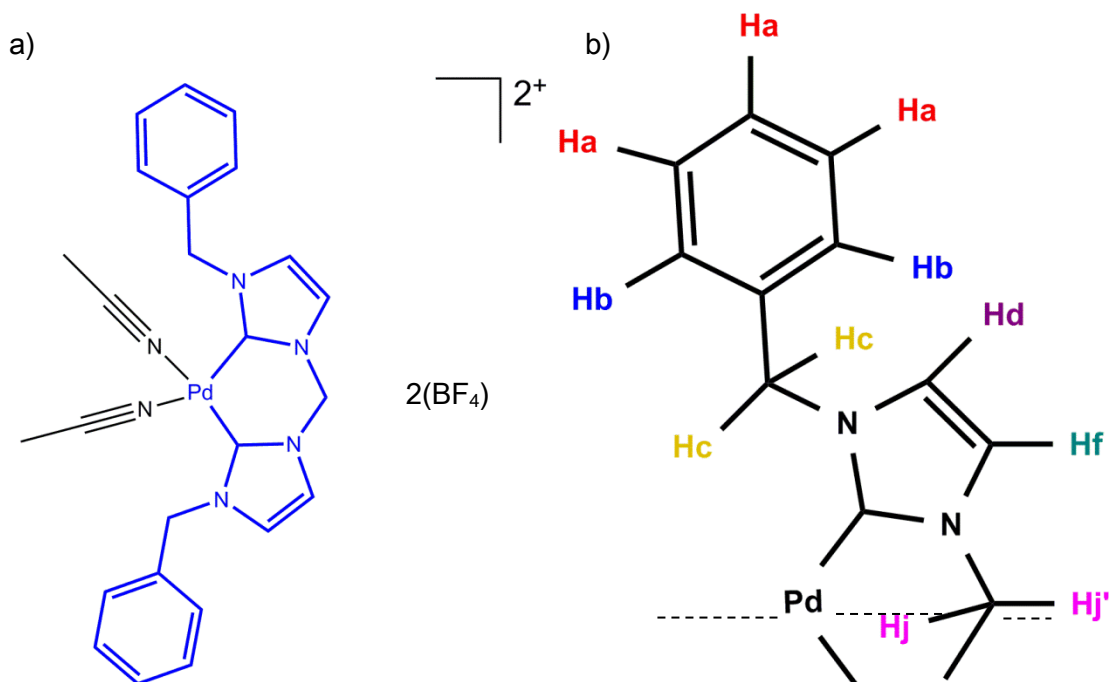


Figure 4.5 a) Tecton

bis(acetonitrile)-{1,1'-methylenebis(3-benzyl-imidazol-2-ylidene)}palladium(II)tetrafluoroborate, b) annotated section of [Pd(bis-NHC-b)] showing unique protons, dashed line indicates a line of 2-fold symmetry.

The [Pd(bis-NHC-b)(MeCN)₂] \cdot 2(BF₄) tecton was soluble in DMSO and nitromethane, but was found to be insoluble in chloroform-*d*₃. The ¹H NMR spectra for [Pd(bis-NHC-b)(MeCN)₂] \cdot 2(BF₄) in *d*₆-DMSO and *d*₃-MeNO₃ are shown below in Figure 4.6 and Figure 4.7. The spectrum was well resolved in *d*₆-DMSO and broad in *d*₃-nitromethane. The protons of the N-CH₂-N bridge of the middle palladium-containing ring resonated as a broad peak and a doublet at 6.40 ppm in *d*₆-DMSO. In *d*₃-nitromethane these protons resonated as two overlapped broad singlets. The protons of the methylene bridges appeared as a well resolved pair of doublets 5.38 ppm in *d*₆-DMSO, in *d*₃-nitromethane the signal for these protons was a broad singlet.

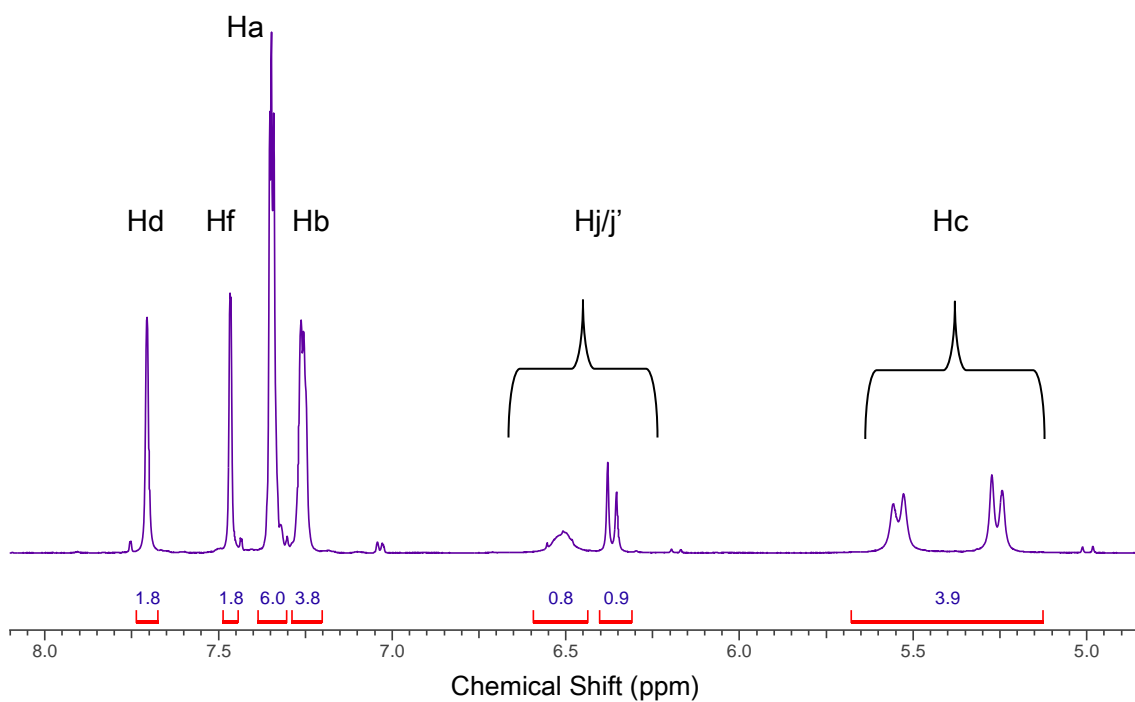


Figure 4.6 ^1H NMR spectrum of $[\text{Pd}(\text{bis-NHC-b})(\text{MeCN})_2] \cdot 2(\text{BF}_4)$ with assignments and integrations. (293 K, 500 MHz, $d_6\text{-DMSO}$)

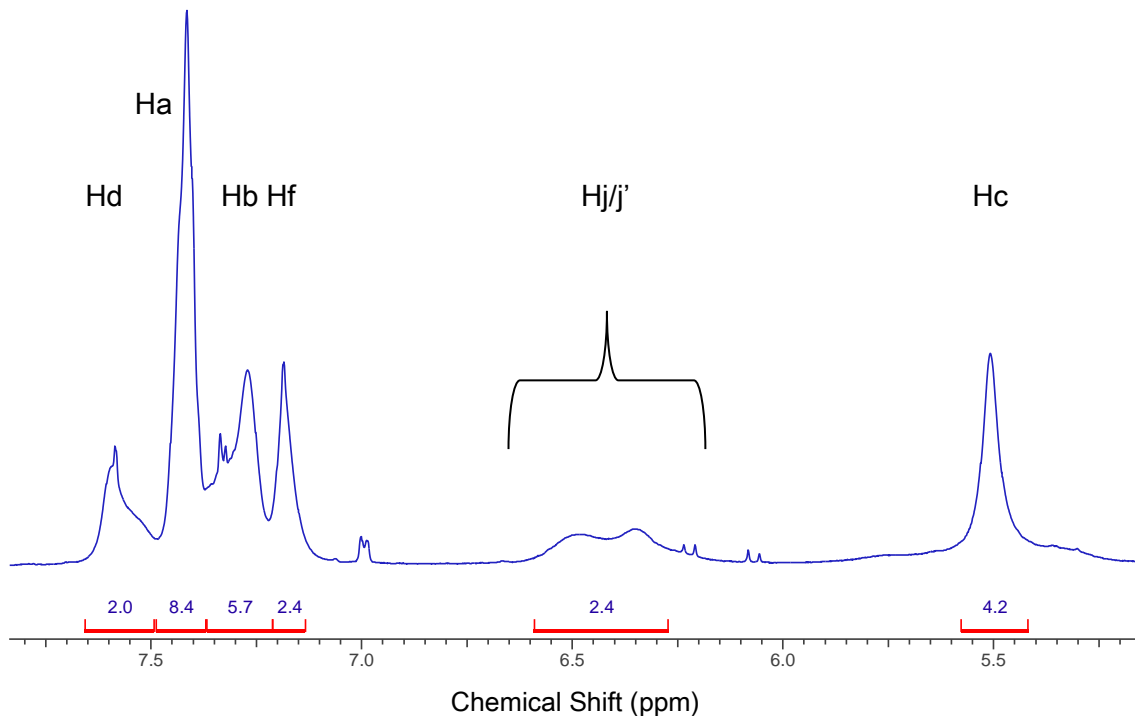


Figure 4.7 ^1H NMR spectrum of $[\text{Pd}(\text{bis-NHC-b})(\text{MeCN})_2] \cdot 2(\text{BF}_4)$ with assignments and integrations. (293 K, 500 MHz, $d_3\text{-MeNO}_2$)

4.2.2.1 L1 and [Pd₃(bis-NHC-b)₃]·2(BF₄) cryptophanes

When L1 and [Pd(bis-NHC-b)(MeCN)₂]₂·2(BF₄) were added together at the stoichiometric ratio of two ligands to three metals in either *d*₆-DMSO or *d*₃-nitromethane, ¹H NMR spectra indicated the formation of metallo-cryptophanes, illustrated below.

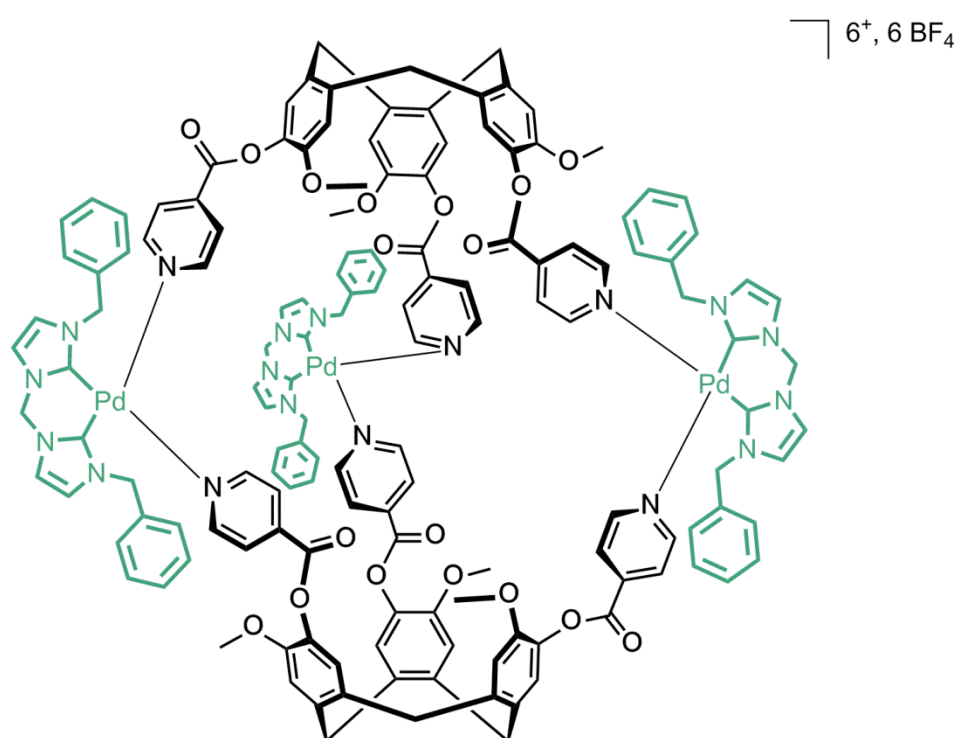


Figure 4.8 [Pd₃(bis-NHC-b)₃(L1)₂]₆(BF₄).

The ¹H NMR spectra were complex in appearance in both of the polar aprotic solvents. In *d*₆-DMSO the L1 ligand peaks were barely shifted, but they no longer displayed the sharpness displayed in the ligand only spectrum [Figure 4.9 c)]. The bis-NHC-b resonances were more noticeably shifted by the complexation, particularly the H_{j/j'} and H_c protons, which had both broadened and shifted downfield. The H_{a/a'} and H_{endo} protons of L1 appeared to be consistent with both *anti*- and *syn*- cryptophane diastereomers being present in solution at a ratio of ~ 35:65, calculated from the

integration of the Ha/a' protons, the signals for which are indicated by the arrows in Figure 4.9. However, the spectra did not allow for unequivocal identification of the *anti* and *syn* cryptophanes. This was consistent with what Henkelis saw with the bis-NHC-n tecton and the L2 ligand,¹⁵⁰ although it would appear that bis-NHC-b gave the opposite conformation to that of bis-NHC-n, as in that case, the larger of the two resonances for the L2 Ha protons was furthest downfield, whereas in this instance with the L1 ligand, the larger Ha/a' proton signal was upfield compared with the lesser Ha/a' component.

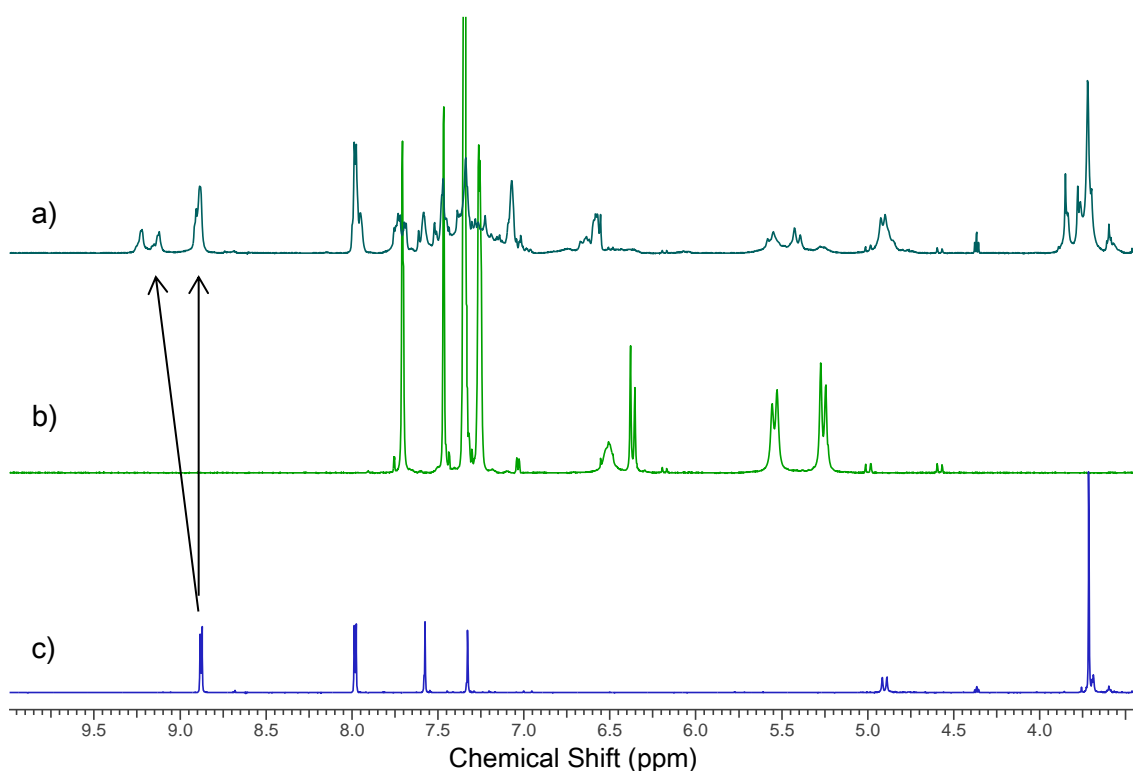


Figure 4.9 ^1H NMR spectra of a) $[\text{Pd}_3(\text{bis-NHC-b})_3(\text{L1})_2]^{6+}$, b) $\text{Pd}(\text{bis-NHC-b})(\text{MeCN})_2 \cdot 2(\text{BF}_4)$ and c) L1. (293 K, 500 MHz, d_6 -DMSO)

The $[\text{Pd}_3(\text{bis-NHC-b})_3(\text{L1})_2]^{6+}$ complex in d_3 -nitromethane showed sharp peaks, in contrast to the broadness seen in the $[\text{Pd}(\text{bis-NHC-b})(\text{MeCN})_2] \cdot 2(\text{BF}_4)$ spectrum [Figure 4.10 b)]. Again the spectrum was indicative of *anti*- and *syn*-cryptophane diastereomers present in solution, however, with a more equal ratio of $\sim 50:50$. The $[\text{Pd}_3(\text{bis-NHC-b})_3(\text{L1})_2]^{6+}$ complexes showed no signs of self-sorting after 144 hours in either solvent.

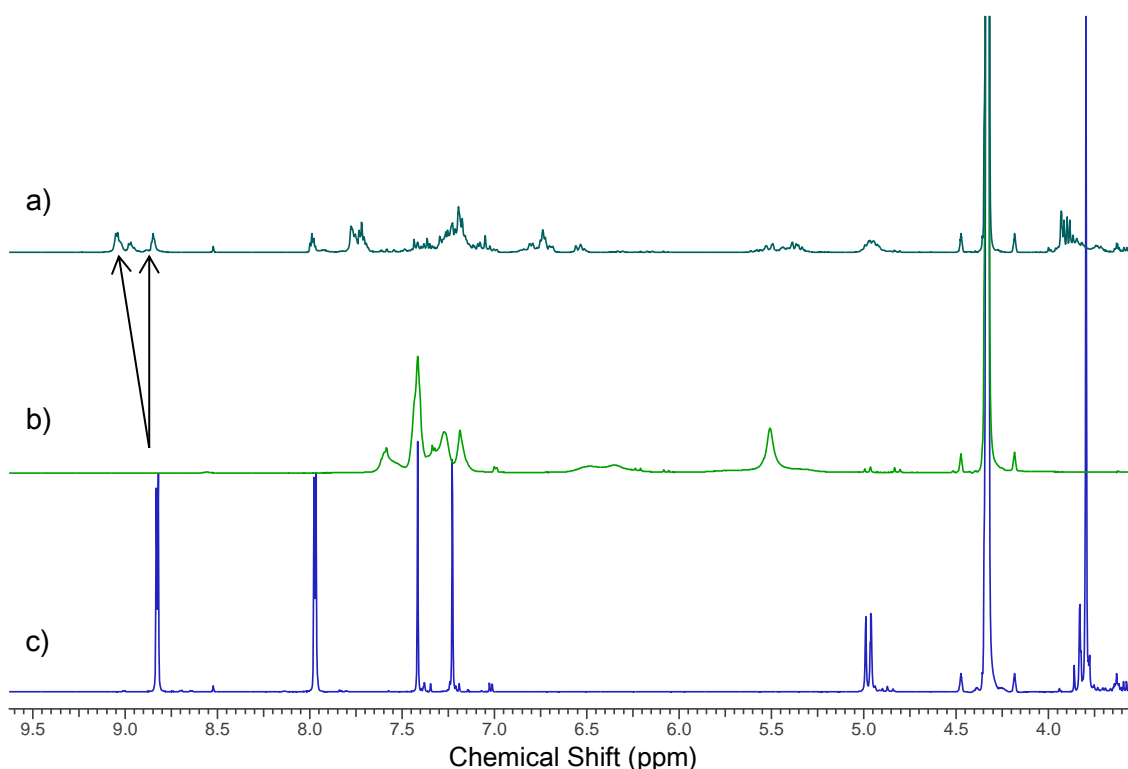


Figure 4.10 ^1H NMR spectra of a) $[\text{Pd}_3(\text{bis-NHC-b})_3(\text{L1})_2]^{6+}$, b) $\text{Pd}(\text{bis-NHC-b})(\text{MeCN})_2 \cdot 2(\text{BF}_4)$ and c) **L1**. (293 K, 500 MHz, $d_3\text{-MeNO}_2$)

The DOSY spectrum of the $[\text{Pd}_3(\text{bis-NHC-b})_3(\text{L1})_2]^{6+}$ complex in $d_6\text{-DMSO}$ (Figure 4.11) indicated the presence of more than one type of species in solution. The diffusion coefficients covered the range of $0.7\text{-}0.9 \times 10^{-10} \text{ m}^2 \text{ s}^{-1}$, which was lower than the diffusion coefficients recorded for **L1** and $[\text{Pd}(\text{bis-NHC-b})(\text{MeCN})_2] \cdot 2(\text{BF}_4)$ which diffused at 1.284 and $1.372 \times 10^{-10} \text{ m}^2 \text{ s}^{-1}$ respectively. This was consistent with a cryptophane-sized complex, with an approximate hydrodynamic radius of 14.4 \AA . For comparison the larger $[\text{Pd}_6(\text{L1})_8]^{12+}$ stella octangula structure has a diffusion coefficient of $0.555 \times 10^{-10} \text{ m}^2 \text{ s}^{-1}$ in $d_6\text{-DMSO}$, which gives a hydrodynamic radius of 19.4 \AA .¹¹⁰

The DOSY spectrum of the $[\text{Pd}_3(\text{bis-NHC-b})_3(\text{L1})_2]^{6+}$ complex in $d_3\text{-MeNO}_2$ (Figure 4.11) indicated only one species in solution, with a diffusion coefficient of $2.650 \times 10^{-10} \text{ m}^2 \text{ s}^{-1}$, which was again smaller than the cryptophane components (Figure 4.12). This gave a hydrodynamic radius of 13.1 \AA , which was again, consistent with a cryptophane-sized complex and was similar to what was reported by Henkelis and co-

workers for the $[\text{Pd}_3(\text{bis-NHC-n})_3(\text{L2})_2]^{6+}$ system, which they measured at 14.4 Å, in nitromethane.⁸⁸ The hydrodynamic radii were derived using the Stokes-Einstein relationship.¹²⁷ The slight difference in hydrodynamic radius was consistent with DMSO being a larger solvent molecule and therefore having a larger solvation sphere.

Table 4.1 Diffusion Coefficients of L1, Pd(bis-NHC-b)(MeCN)₂·2(BF₄) and [Pd₃(bis-NHC-b)₃(L1)₂]⁶⁺.

Solvent	<i>d</i> ₃ -MeNO ₂	<i>d</i> ₆ -DMSO
L1		
Diffusion Coefficient/ 10 ⁻¹⁰ m ² s ⁻¹	6.666	1.284
Pd(bis-NHC-b)(MeCN) ₂ ·2(BF ₄)		
Diffusion Coefficient/ 10 ⁻¹⁰ m ² s ⁻¹	3.529	1.372
Pd ₃ (bis-NHC-b) ₃ (L1) ₂] ⁶⁺		
Diffusion Coefficient/ 10 ⁻¹⁰ m ² s ⁻¹	2.650	0.745
Pd ₃ (bis-NHC-b) ₃ (L1) ₂] ⁶⁺		
Stokes-Einstein Radius/Å	13.1	14.4

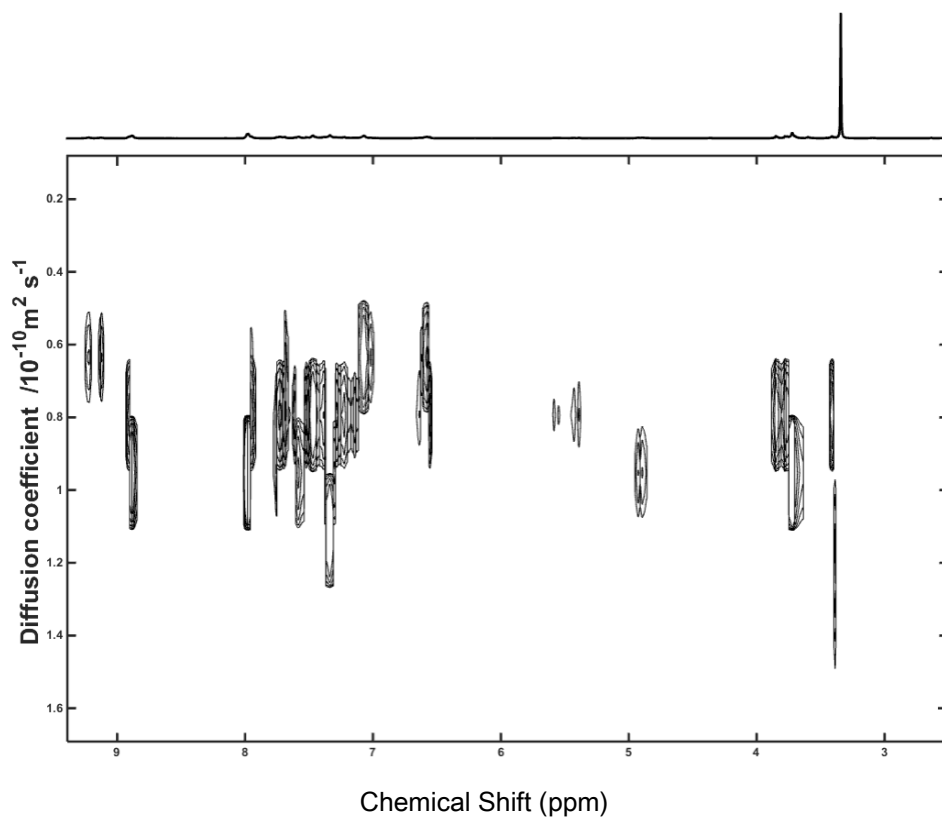


Figure 4.11 ^1H NMR DOSY spectrum of $[\text{Pd}_3(\text{bis-NHC-b})_3(\text{L1})_2]^{6+}$. (293 K, 500 MHz, d_6 -DMSO)

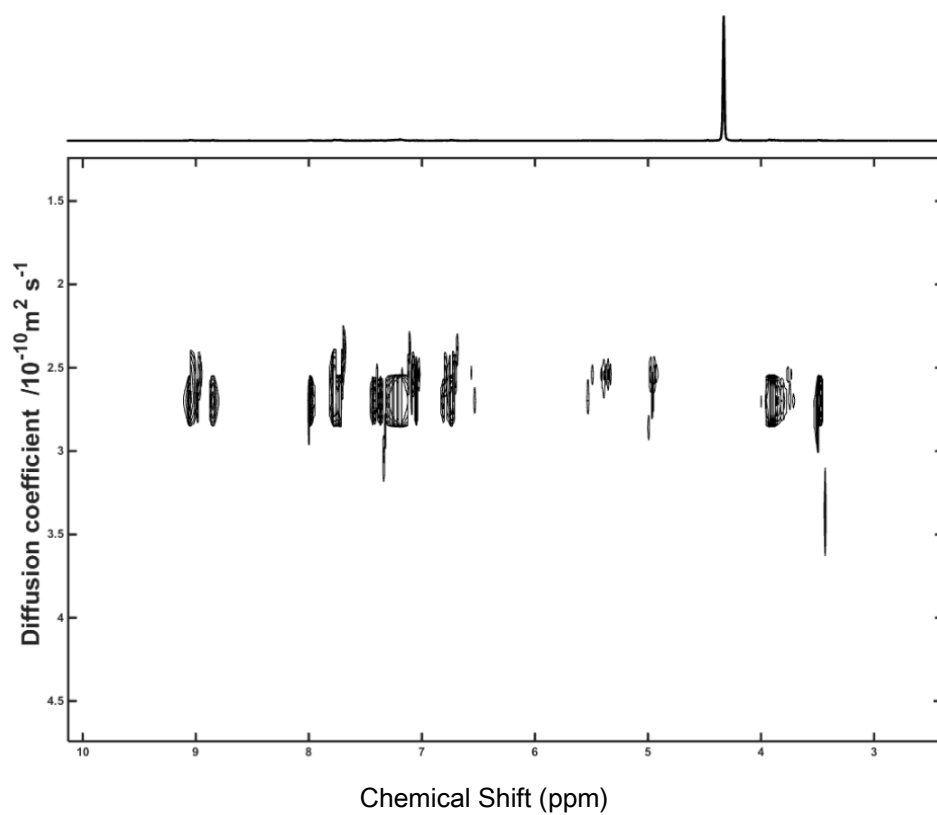


Figure 4.12 ^1H NMR DOSY spectrum of $[\text{Pd}_3(\text{bis-NHC-b})_3(\text{L1})_2]^{6+}$. (293 K, 500 MHz, d_3 -MeNO₂)

To investigate the stability of the $[\text{Pd}_3(\text{bis-NHC-b})_3(\text{L1})_2]^{6+}$ cryptophane systems, VT ^1H NMR experiments were conducted. $[\text{Pd}(\text{bis-NHC-b})(\text{MeCN})_2]\cdot 2(\text{BF}_4)$ was found to be stable up to 60°C . The $[\text{Pd}_3(\text{bis-NHC-b})_3(\text{L1})_2]^{6+}$ complex in d_6 -DMSO exhibited peak-broadening, with the spectra becoming simplified as the temperature was increased. It appeared that the preferred diastereomer at room temperature was favoured with increasing temperature, as the minor components of the spectrum are seen to diminish as the temperature was increased. Although the spectrum recorded at 60°C appeared very similar to what would be expected if the cryptophane had disintegrated [that is, like a superposition of **L1** and $[\text{Pd}(\text{bis-NHC-b})(\text{MeCN})_2]\cdot 2(\text{BF}_4)$], the Hj/j' and Hc resonances of the (bis-NHC-b) component remained broadened, and were different in appearance to $[\text{Pd}(\text{bis-NHC-b})(\text{MeCN})_2]\cdot 2(\text{BF}_4)$ at 60°C , inferring that the components were still complexed. The top spectrum of Figure 4.13 is the complex at 20°C , recorded after the heating experiment; it had the same appearance of the initial spectrum recorded prior to heating, implying that the process is reversible.

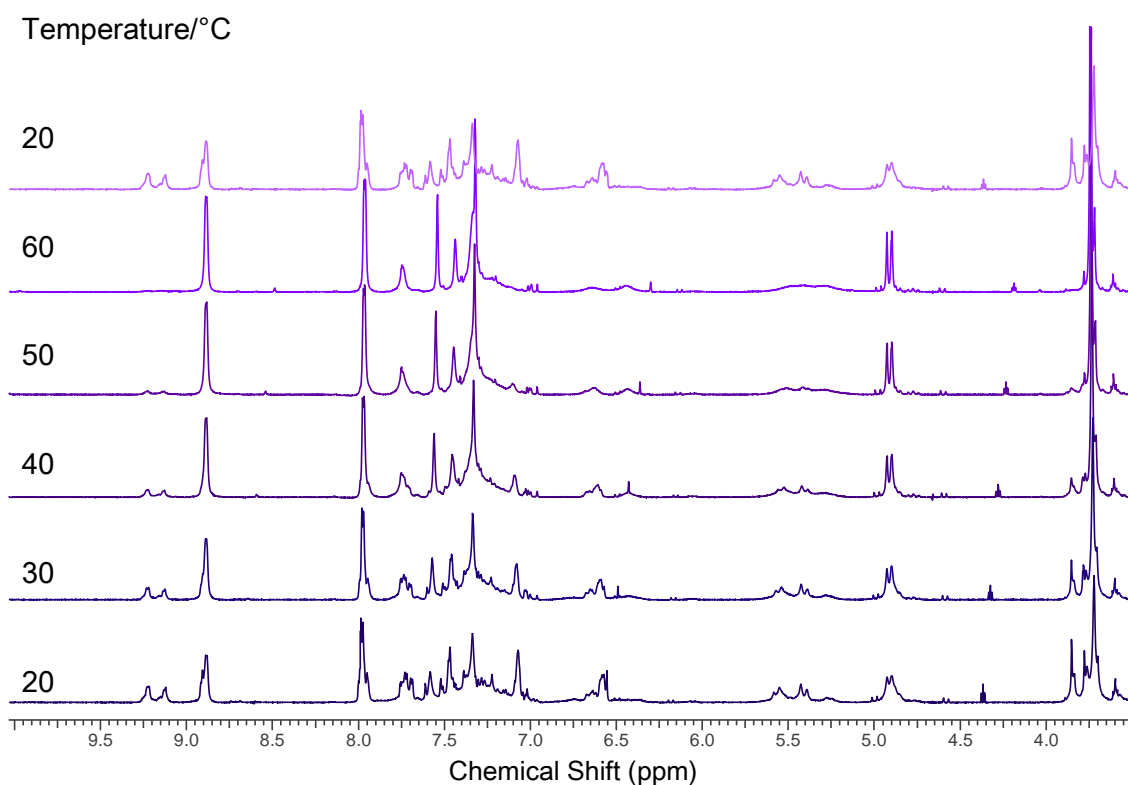


Figure 4.13 ^1H NMR spectrum of $[\text{Pd}_3(\text{bis-NHC-b})_3(\text{L1})_2]^{6+}$ at 293 - 333 K. The top spectrum was recorded after the sample had cooled to 20°C after heating. (500 MHz, d_6 -DMSO)

The $[\text{Pd}_3(\text{bis-NHC-b})_3(\text{L1})_2]^{6+}$ complex in d_3 -nitromethane (Figure 4.14) exhibited little change with increasing temperature up to 60°C. The complex was stable up to these temperatures, showing no signs of disintegration into its constituent parts and no preference for one diastereomer over the other. Again, the spectrum recorded at 20°C after the heat cycle was identical to the initial spectrum recorded at 20°C.

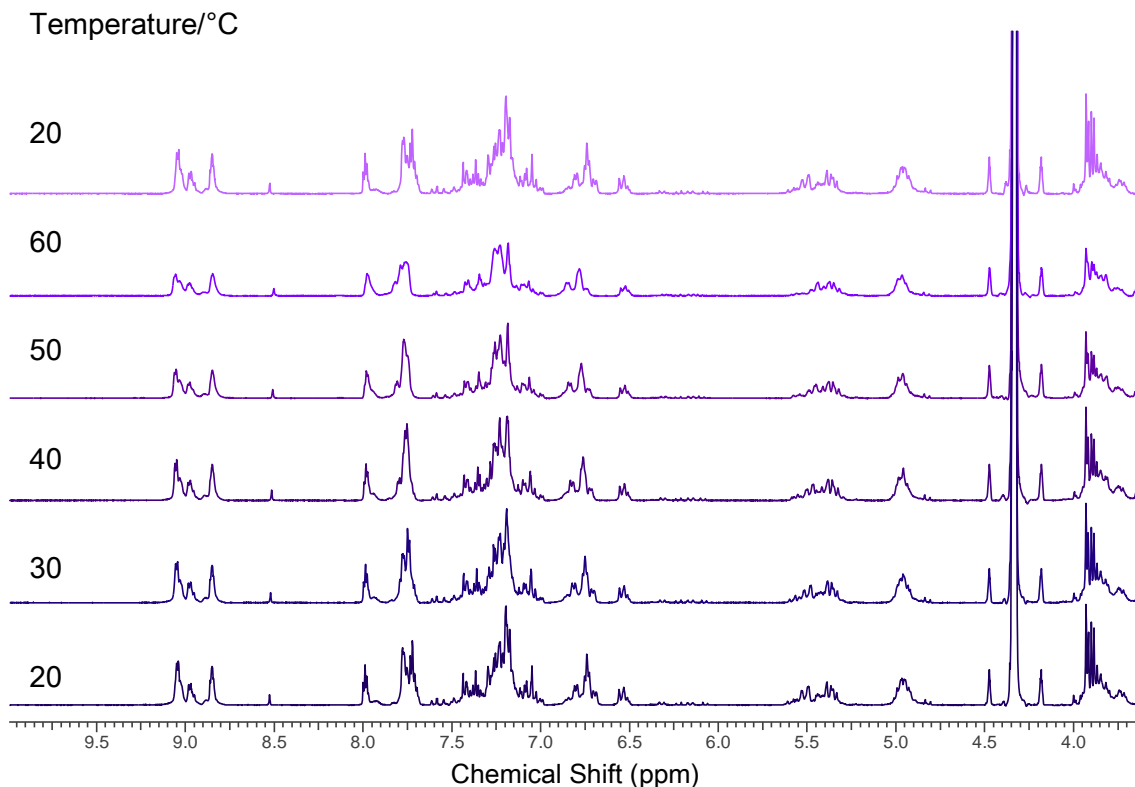


Figure 4.14 ^1H NMR spectrum of $[\text{Pd}_3(\text{bis-NHC-b})_3(\text{L1})_2]^{6+}$ at 293 - 333 K. The top spectrum was recorded after the sample had cooled to 20°C after heating. (500 MHz, $d_3\text{-MeNO}_2$)

To further characterise these complexes and to assess their suitability as hosts for host:guest investigations, 2-D NMR analyses were undertaken. COSY spectra of the $[\text{Pd}_3(\text{bis-NHC-b})_3(\text{L1})_2]^{6+}$ complexes (Figure 4.15 and Figure 4.16) were similar in appearance to the COSY spectra of the **L1** ligand alone, with clear cross-peaks between $\text{H}_{\text{a}}/\text{a}'$ and $\text{H}_{\text{b}}/\text{b}'$ protons of the pyridyl arm and between the H_{endo} and H_{exo} protons of the CTG-bowl. However, the spectra of the $[\text{Pd}_3(\text{bis-NHC-b})_3(\text{L1})_2]^{6+}$ complexes were complicated by the presence of the *anti*- and *syn*-cryptophane diastereomers. This was particularly noticeable with the coupling between the pyridyl protons (in the red boxes) and the CTG-bowl methylene protons (blue boxes). For the pyridyl protons, there were cross-peaks seen for all three of the $\text{H}_{\text{a}}/\text{a}'$ environments, this was useful in determining some assignments and it could be seen that there were $\text{H}_{\text{a}}/\text{a}'$ - $\text{H}_{\text{b}}/\text{b}'$ cross-peaks for both diastereomers of the cryptophane. However the

spectra were still too complicated to unambiguously assign in the aromatic region, particularly in the region of 6.5 - 7.5 ppm.

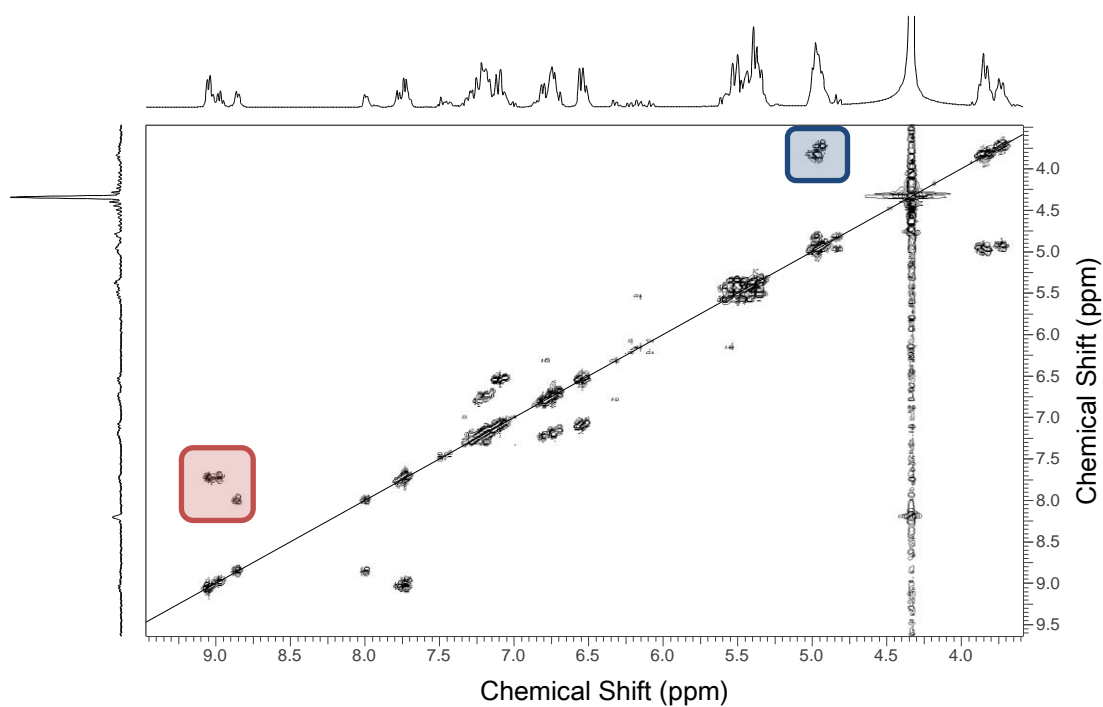


Figure 4.15 ^1H NMR DQF-COSY spectrum of $[\text{Pd}_3(\text{bis-NHC-b})_3(\text{L1})_2]^{3+}$. The blue box indicates intramolecular coupling between the CTG-bowl methylene protons. The red box indicates intramolecular coupling of the Ha/a' protons of the L1 ligand. (293 K, 500 MHz, d_6 -DMSO)

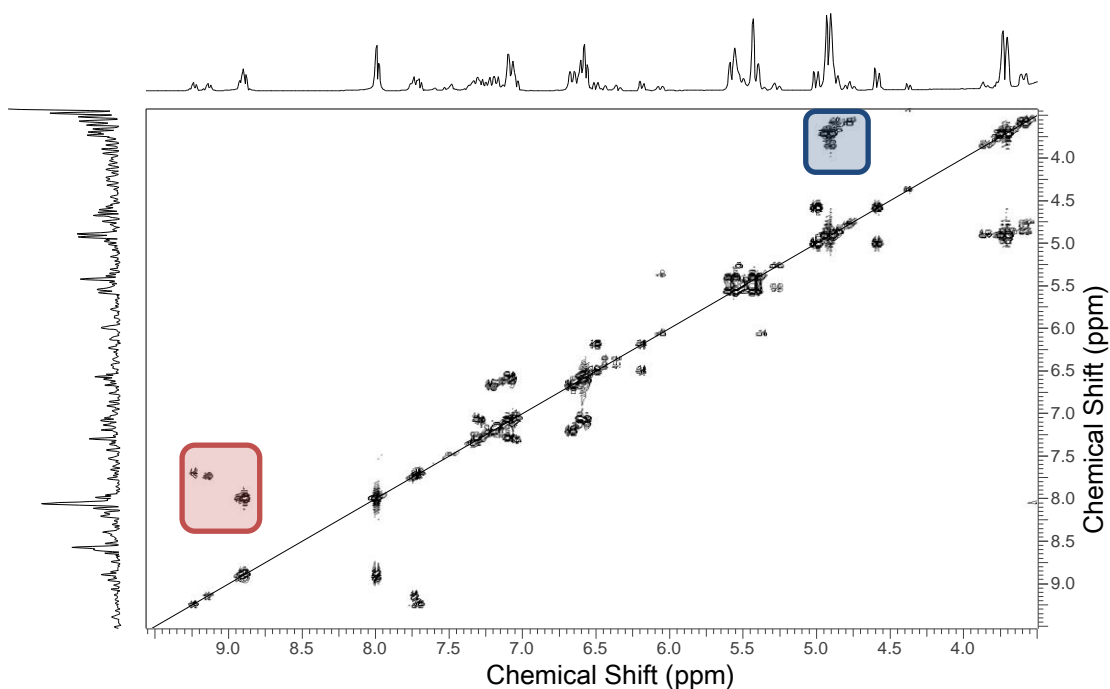


Figure 4.16 ^1H NMR DQF-COSY spectrum of $[\text{Pd}_3(\text{bis-NHC-b})_3(\text{L1})_2]^{6+}$. The blue box indicates intramolecular coupling between the CTG-bowl methylene protons. The red box indicates intramolecular coupling of the $\text{Ha/a}'$ protons of the L1 ligand. (293 K, 500 MHz, $d_3\text{-MeNO}_2$)

Figure 4.17 shows the 2-D ROESY NMR spectrum of $[\text{Pd}_3(\text{bis-NHC-b})_3(\text{L1})_2]^{6+}$ in $d_6\text{-DMSO}$. The aromatic region showed intramolecular exchange within the $[\text{Pd}_3(\text{bis-NHC-b})_3(\text{L1})_2]^{6+}$ complex. This was manifested by the pyridyl $\text{Ha/a}'$ protons of L1, which showed exchange with $\text{Ha/a}'$ of the other diastereomer, as well as rOes to $\text{Hb/b}'$ of L1 and possibly to Hb of (bis-NHC-b). This exchange was less prevalent in nitromethane (Figure 4.18) and more rOes were present. However, due to the second-order nature of the aromatic peaks in the region of 6.5 - 8 ppm, peak assignment was difficult. Because of the intramolecular exchange and difficulty in correctly assigning the spectra of the $[\text{Pd}_3(\text{bis-NHC-b})_3(\text{L1})_2]^{6+}$ complexes, it was decided that although new cryptophanes had been developed, that they were not suitable for host:guest studies of the type reported in Chapter 2.

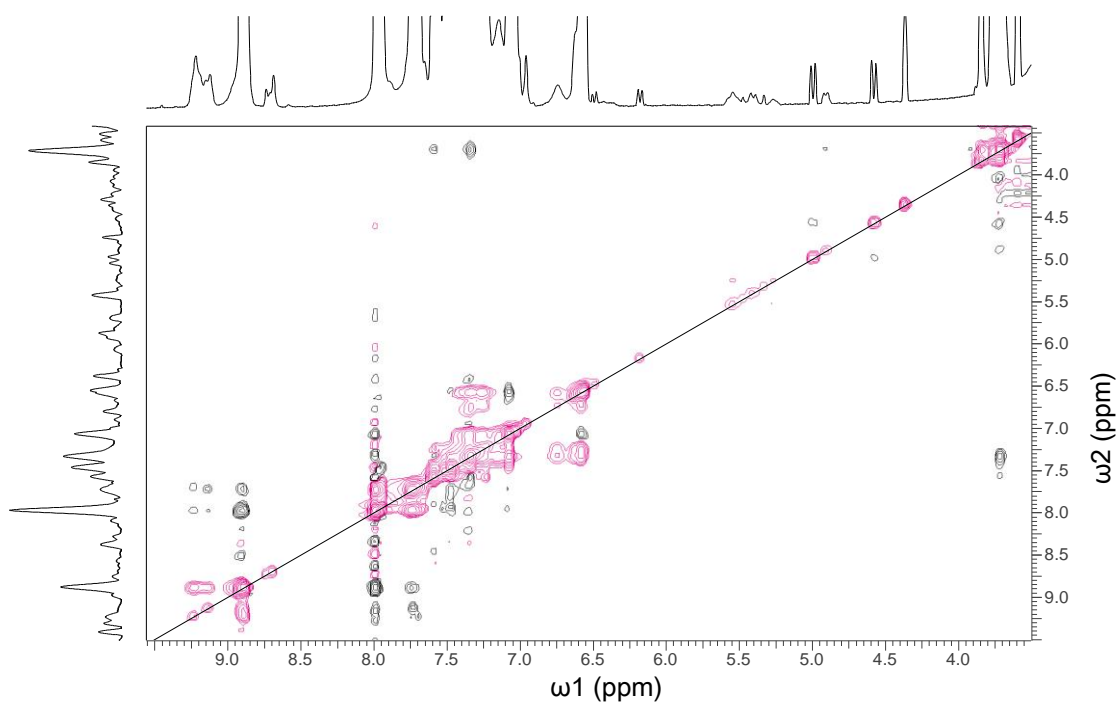


Figure 4.17 ¹H NMR ROESY spectrum of $[Pd_3(\text{bis-NHC-b})_3(L1)_2]^{6+}$ exchange peaks in pink and through-space connections in black. (293 K, 500 MHz, d_6 -DMSO)

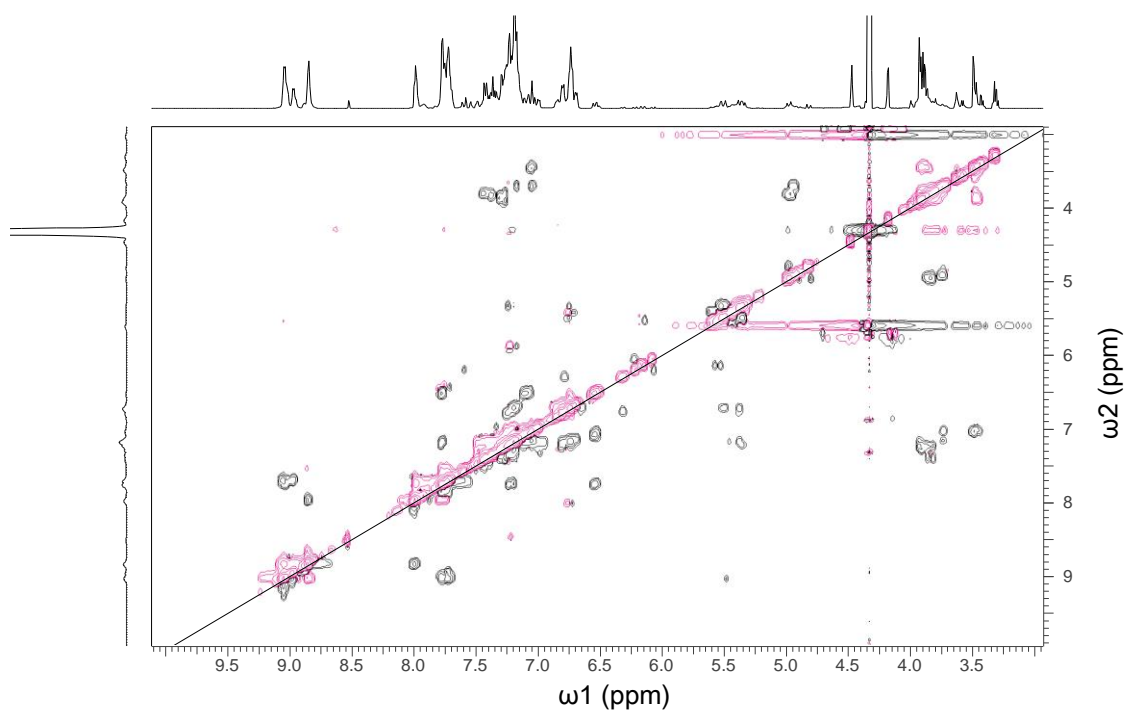


Figure 4.18 ¹H NMR ROESY spectrum of $[Pd_3(\text{bis-NHC-b})_3(L1)_2]^{6+}$ exchange peaks in pink and through-space connections in black. (293 K, 500 MHz, d_3 -MeNO₂)

4.2.3 [1,3-Bis(diphenylphosphino)propane]palladium(II)triflate

In an attempt to emulate the work by Shinkai and co-workers, who used a pyridyl cyclotrimeratrylene derivative (which is similar to the L1 ligand) with commercially available [1,3-bis(diphenylphosphino)ethane] (dppe) and [1,3-bis(diphenylphosphino)propane] (dppp) to produce the first metallo-cryptophanes,⁷¹ [1,3-bis(diphenylphosphino)propane]palladium(II)triflate $[\text{Pd}(\text{dppp})]^{2+}$ was used (Figure 4.19). The propane bridged compound was used due to the lack of commercially available dppe with a triflate anion or other suitably labile anion.

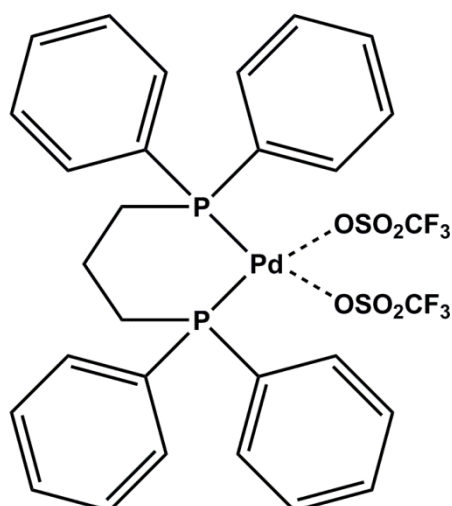


Figure 4.19 [1,3-Bis(diphenylphosphino)propane]palladium(II)triflate.

This palladium(II) complex was found to be easy to work with and dissolved well in the polar aprotic solvents used throughout this work. This compound has been characterised to enable comparison with cryptophanes formed with $[\text{Pd}(\text{dppp})]^{2+}$. This is discussed in section 4.3.1. Using $[\text{Pd}(\text{dppp})]^{2+}$, as per Shinkai and co-workers, L1 was used to attempt cryptophane formation.⁷¹ This was first tried in *d*₂-tetrachloroethane (TCE), as described in the Shinkai paper. This yielded a complex which had a poorly resolved ¹H NMR spectrum and which showed no signs of self-

sorting. TCE is an expensive, toxic solvent that evaporates quickly. As $[\text{Pd}(\text{dppp})]^{2+}$ was found to dissolve well in polar aprotic solvents, cryptophanes were formed in d_6 -DMSO, d_3 -MeNO₂ and d_3 -MeCN. The cryptophanes developed with $[\text{Pd}(\text{dppp})]^{2+}$ are described in the next section, 4.3.

4.3 Results

4.3.1 ¹H NMR Analysis of $[\text{Pd}(\text{dppp})]^{2+}$

As described in section 4.2.3, $[\text{Pd}(\text{dppp})]^{2+}$ was very soluble in the polar aprotic solvents d_6 -DMSO, d_3 -MeCN and d_3 -MeNO₂. As such, it has been characterised by ¹H and ³¹P NMR spectroscopy. The ³¹P NMR spectroscopy of cryptophanes formed with $[\text{Pd}(\text{dppp})]^{2+}$ aided in the determination of whether *anti* and/or *syn* cryptophanes were present; with *anti* cryptophanes, the two phosphorous atoms experience a similar magnetic environment and gave a single peak in their ³¹P NMR spectrum; whereas in the *syn* conformation, they were diastereotopic, resulting in two peaks.⁸³ The ¹H NMR spectra of $[\text{Pd}(\text{dppp})]^{2+}$ in d_6 -DMSO and d_3 -MeNO₂ were similar, both revealing 5 proton environments. These proton environments are displayed in Figure 4.20 and the ¹H NMR spectra are shown for $[\text{Pd}(\text{dppp})]^{2+}$ in d_6 -DMSO and d_3 -MeNO₂ in Figure 4.21 and Figure 4.22, respectively. The resonances for the propylene bridge peaks showed second order effects due to coupling to the phosphorus atoms, as well as coupling between protons labelled Hd and He.

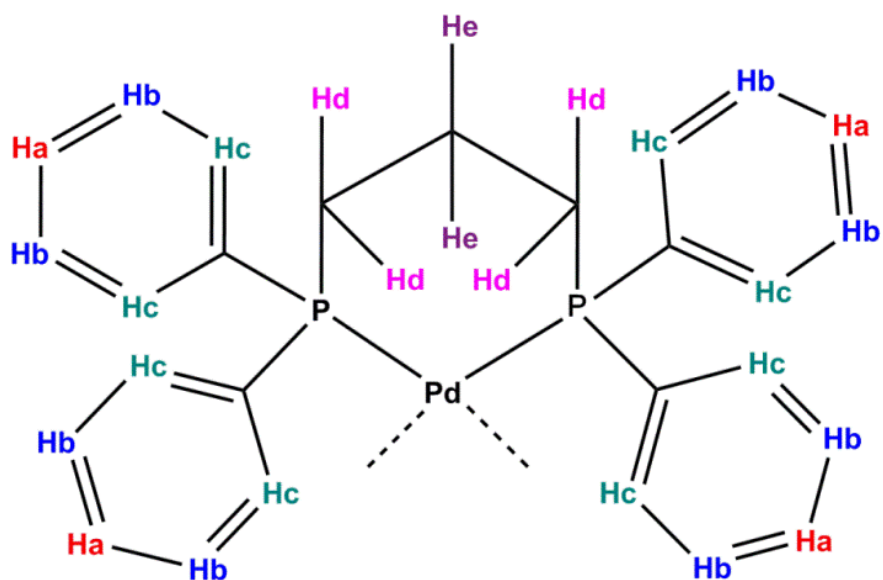


Figure 4.20 [1,3-Bis(diphenylphosphino)propane]palladium(II), annotated to show unique protons, 5 proton environments.

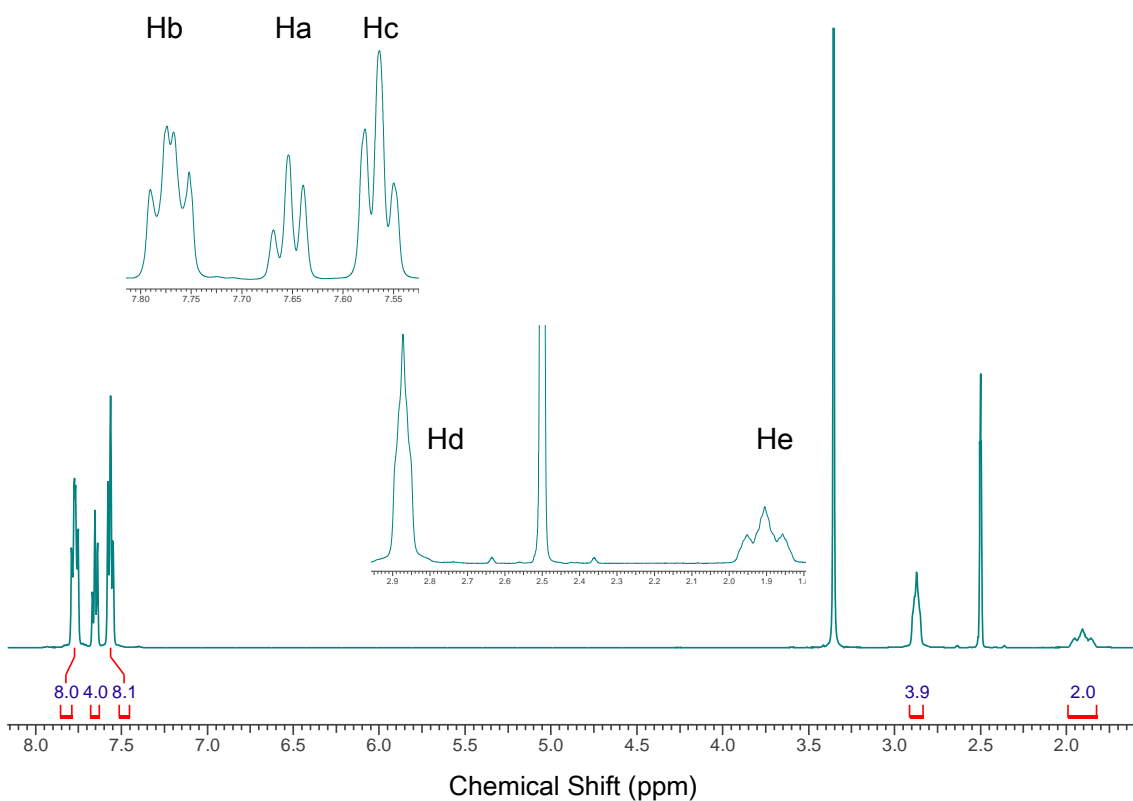


Figure 4.21 ^1H NMR spectrum of [1,3-bis(diphenylphosphino)propane]palladium(II)triflate with integrations. Inset spectra show the aromatic peaks and the propyl bridge peaks at 2.9 and 1.9 ppm. (293 K, 500 MHz, d_6 -DMSO)

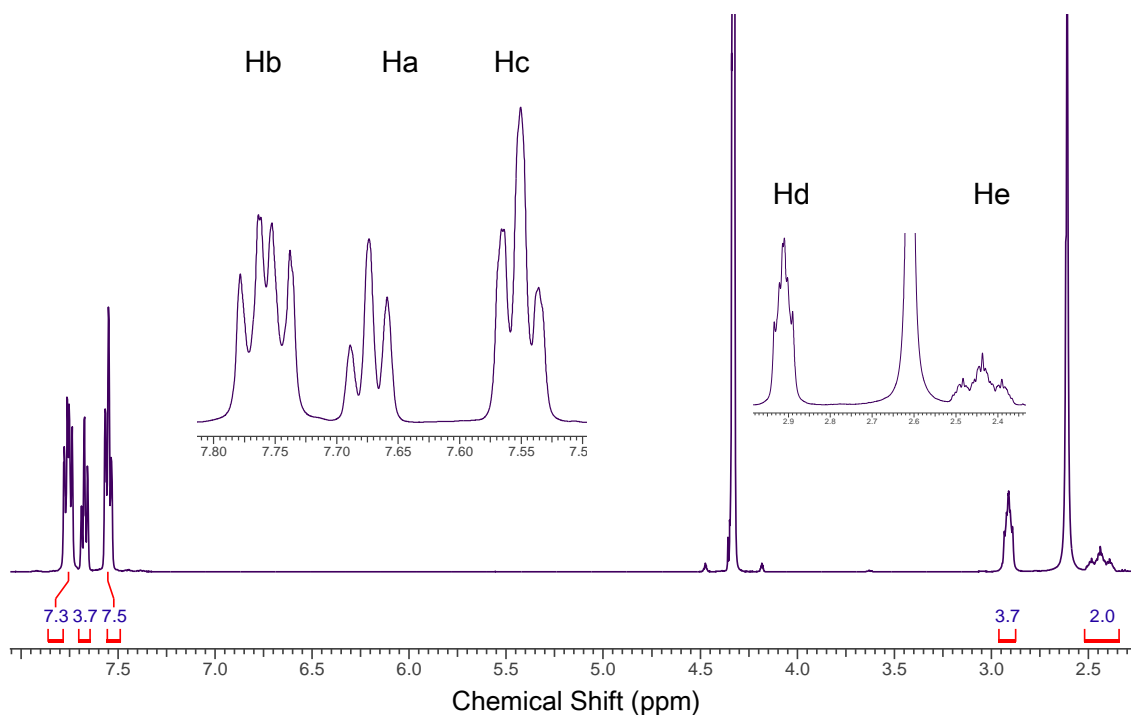


Figure 4.22 ^1H NMR spectrum of [1,3-bis(diphenylphosphino)propane]palladium(II)triflate with integrations. Inset spectra showing the aromatic peaks and the propyl bridge peaks at 2.9 and 2.4 ppm. (293 K, 500 MHz, d_3 -MeNO $_2$)

The ^1H NMR spectrum of $[\text{Pd}(\text{dppp})]^{2+}$ in d_3 -MeCN, shown in Figure 4.23 was noticeably different in the aromatic region, where only two proton environments were seen, as the peaks for Ha and Hb overlapped and a second order spectrum was seen for these protons. The propylene bridge peaks were well resolved, particularly in comparison to the ^1H NMR spectrum of $[\text{Pd}(\text{dppp})]^{2+}$ in d_6 -DMSO (Figure 4.21).

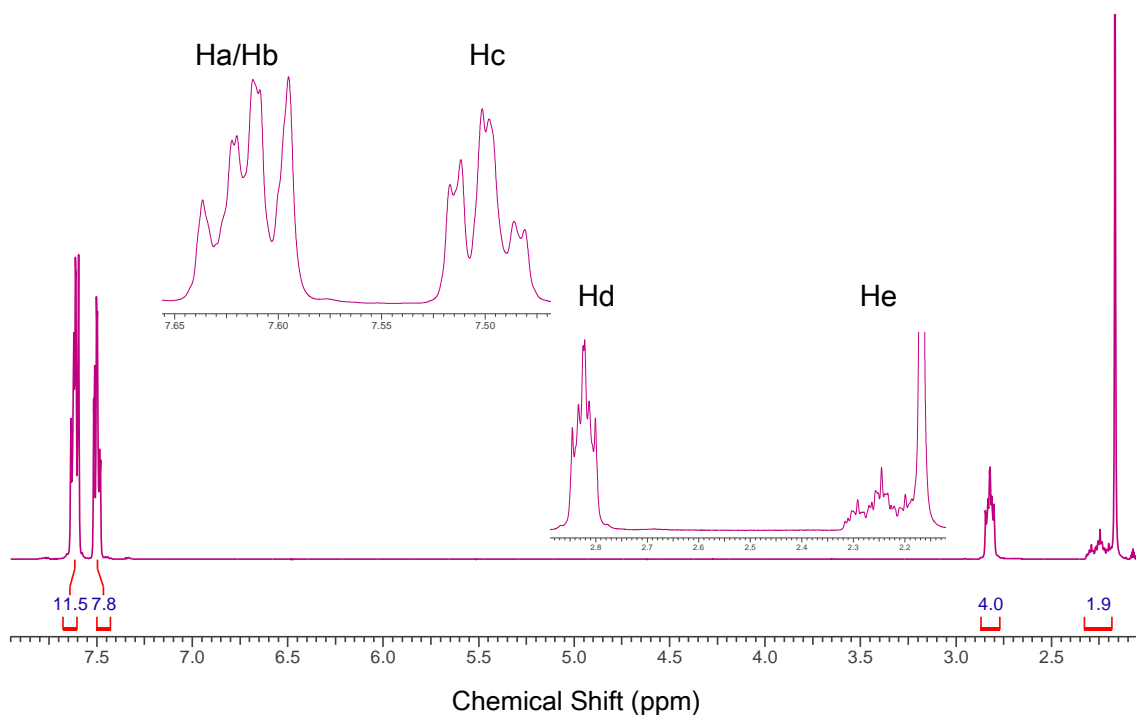


Figure 4.23 ^1H NMR spectra of [1,3-bis(diphenylphosphino)propane]palladium(II)triflate with integrations. Inset spectra showing the aromatic peaks and the propyl bridge peaks at 2.9 and 2.2 ppm. (293 K, 500 MHz, d_3 -MeCN)

During the preparation of cryptophanes with $[\text{Pd}(\text{dppp})]^{2+}$, it was noticed that the ^1H NMR spectra for these complexes had different appearances at different concentrations. To further investigate this, NMR samples of $[\text{Pd}(\text{dppp})]^{2+}$ were prepared in the range of 0.5 - 5.0 mM and analysed by ^1H and ^{31}P NMR spectroscopy in d_6 -DMSO, d_3 -MeCN and d_3 -MeNO₂. Both the ^1H and ^{31}P NMR spectra of $[\text{Pd}(\text{dppp})]^{2+}$ in d_3 -MeNO₂ showed no change in either proton or phosphorous environments in this concentration range. In d_3 -MeCN the ^{31}P spectra displayed only one peak, indicative of only one phosphorous environment in this concentration range. The ^1H NMR spectra was more interesting and is shown in Figure 4.24. The Ha/Hb resonances did change in appearance throughout the concentration range of 0.5 - 5.0 mM, however, they retained their second order appearance and no evidence was seen of the in the presence of different conformations of $[\text{Pd}(\text{dppp})]^{2+}$ in d_3 -MeCN solution.

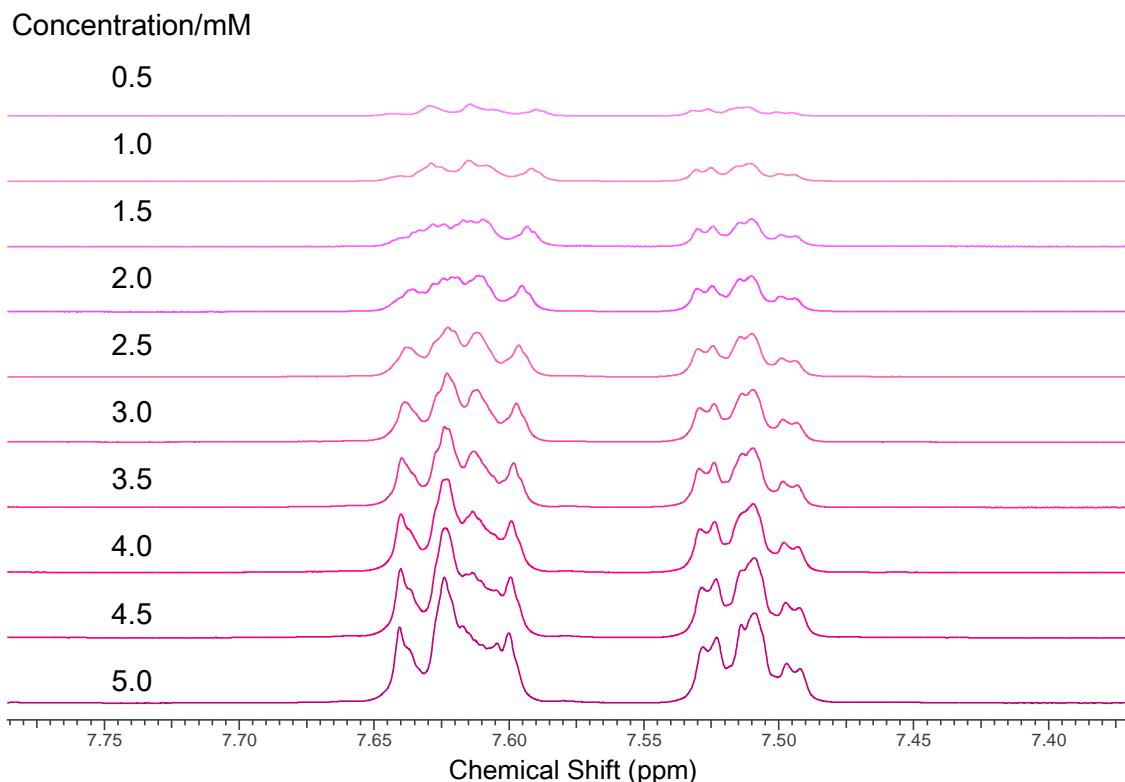


Figure 4.24 ^1H NMR spectra of [1,3-bis(diphenylphosphino)propane]palladium(II)triflate in acetonitrile at 0.5 – 5.0 mM, showing the aromatic peaks. (293 K, 500 MHz, d_3 -MeCN)

The ^1H NMR spectra of $[\text{Pd}(\text{dppp})]^{2+}$ in d_6 -DMSO in the range 0.5 – 5.0 mM revealed additional peaks in d_6 -DMSO solution. In the spectra shown in Figure 4.25, an additional small broad triplet at 7.51 ppm was seen in the aromatic region. This small triplet had the same couplings as observed for the Ha resonance and Hc resonances of $J = 7.3$ Hz. The Hd peak at 2.85 ppm had a side peak downfield at 2.95 ppm. These additional resonances were caused by the diphosphine six-membered ring interconverting between chair forms, as illustrated in Figure 4.26. This process was slow enough on the NMR timescale in d_6 -DMSO to be observed. It could be seen from the spectra that one of the chair conformations was the preferred orientation.

Concentration/mM

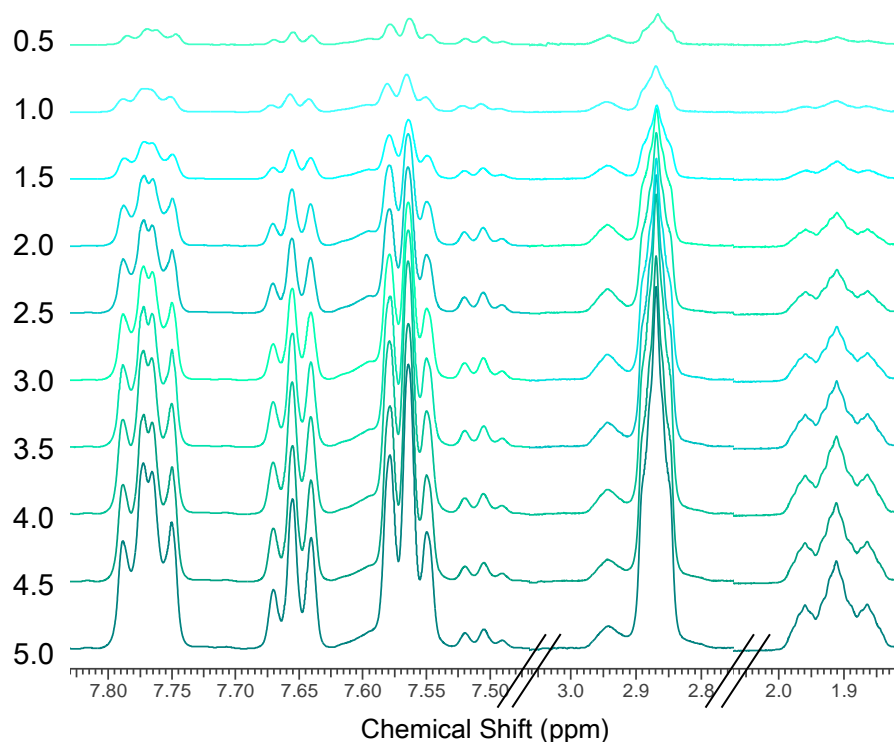


Figure 4.25 ^1H NMR spectra of [1,3-Bis(diphenylphosphino)propane]palladium(II)triflate 0.5 – 5.0 mM. (293 K, 500 MHz, d_6 -DMSO)

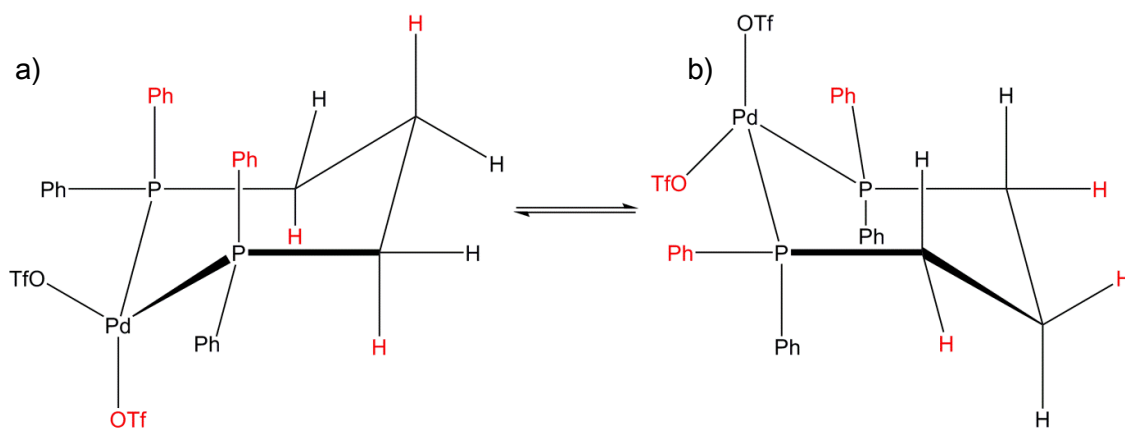


Figure 4.26 Chair conformations of [1,3-Bis(diphenylphosphino)propane]palladium(II)triflate, a) axial moieties in red, b) after interconversion the red moieties are now in the equatorial position.

The ^{31}P NMR spectra showed two phosphorous environments in d_6 -DMSO solution, as illustrated in Figure 4.27. The broad peak at 17.21 ppm was the peak of both phosphorus atoms in $[\text{Pd}(\text{dppp})]^{2+}$. The small peak at 10.10 ppm did not change in intensity, and was most likely a contaminant in the d_6 -DMSO, as this peak was not

observed in d_3 -MeCN and d_3 -MeNO₂. If it was a contaminant in the [Pd(dppp)]²⁺, it would be affected by the change in [Pd(dppp)]²⁺ concentration.

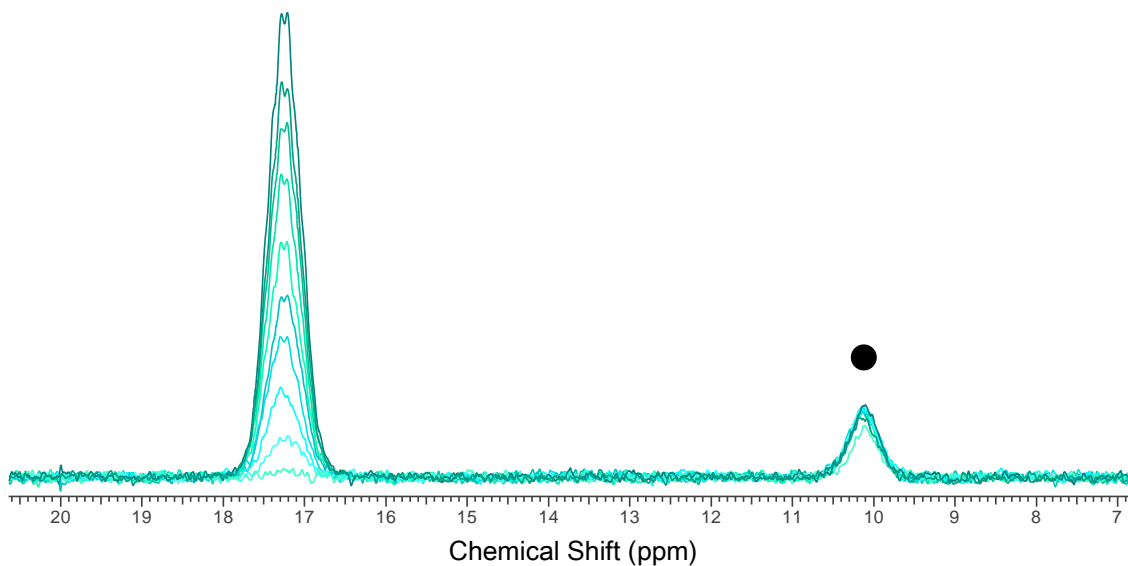


Figure 4.27 ³¹P NMR spectra of [1,3-Bis(diphenylphosphino)propane]palladium(II)triflate 0.5 – 5.0 mM, shown as a superimposed stacked plot, solvent contaminant marked with a black dot (•). (300 K, 121 MHz, *d*₆-DMSO)

To further investigate the slow exchange regime between the different chair conformations of the six-membered diphosphine ring of [Pd(dppp)]²⁺ in *d*₆-DMSO solutions, the 0.5 and 5 mM samples were subjected to VT ¹H NMR experiments. The samples were heated in 10°C increments from 25 - 75°C and a further spectrum was recorded after the sample had cooled back down to 25°C. The spectra for 5.0 mM [Pd(dppp)]²⁺ are shown in Figure 4.28. No changes in the spectra were observed.

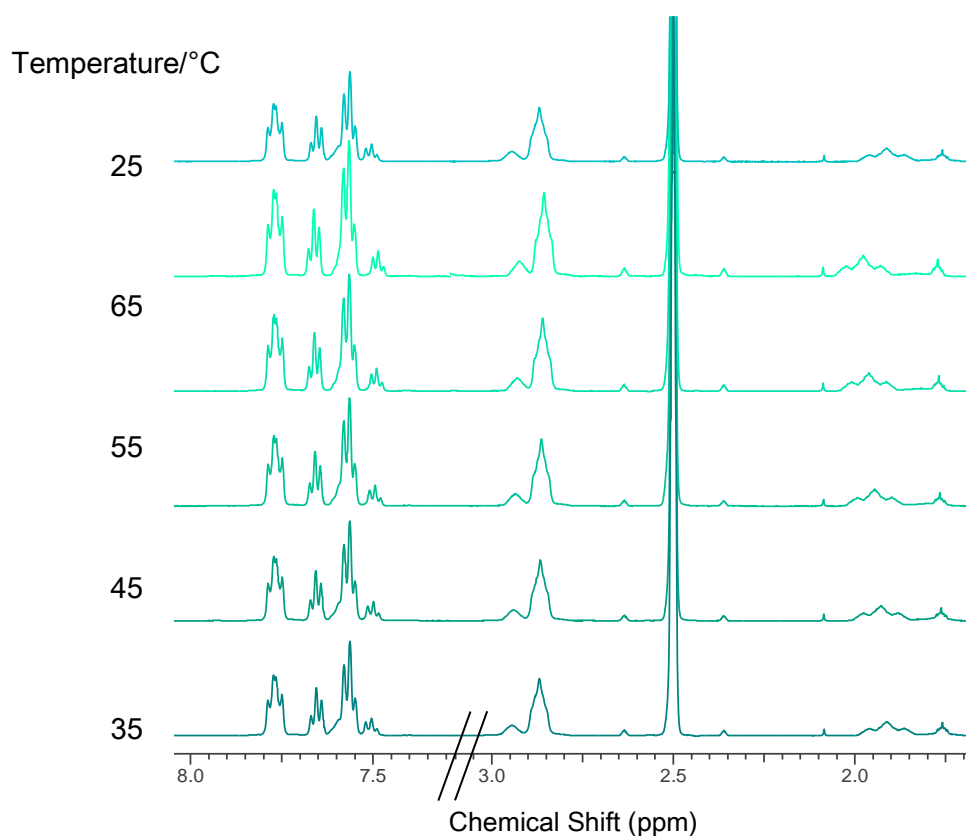


Figure 4.28 ^1H NMR spectra of 5.0 mM [1,3-Bis(diphenylphosphino)propane]palladium(II)triflate at 298 - 348 K. The top spectrum was recorded after the sample had cooled to 25°C after heating. (293 K, 500 MHz, d_6 -DMSO)

The spectra for 0.5 mM $[\text{Pd}(\text{dppp})]^{2+}$ are shown in Figure 4.29. Contrary to what was observed for 5.0 mM $[\text{Pd}(\text{dppp})]^{2+}$, the 0.5 mM $[\text{Pd}(\text{dppp})]^{2+}$ sample had changed considerably during and after the VT experiment. As the temperature was increased, an additional He peak was observed. At 55°C, the Hd and He protons indicated that the populations of the two chair conformations were now equal. As the temperature was further increased, the populations of the two conformations did not remain equal, with the previously preferred conformation no longer the preferred conformation at elevated temperatures. There were also dramatic changes in the aromatic region, with the small triplet at 7.51 ppm becoming more prominent as the temperature was increased and appearing to be in exchange with the Ha triplet at 7.66 ppm. As previously noted, these triplets were coupled to each other, as well as to Hc. The Hb at 7.77 ppm peak also diminished as the temperature was increased. The multiplet at 7.58 ppm became a

second-order multiplet after heating, with an integral of 12 protons. This multiplet was now assigned to Ha and Hb of $[\text{Pd}(\text{dppp})]^{2+}$, with the triplet at 7.50 ppm assigned to Hc. All of the aromatic peaks and the He peak had shifted upfield, meaning that they were experiencing more shielding than in the original conformation. Conversely, the new Hd peak was slightly less shielded than in the original conformation. The sample recorded after the VT experiment (Figure 4.29, top trace) showed that this population change between the different chair conformations was retained.

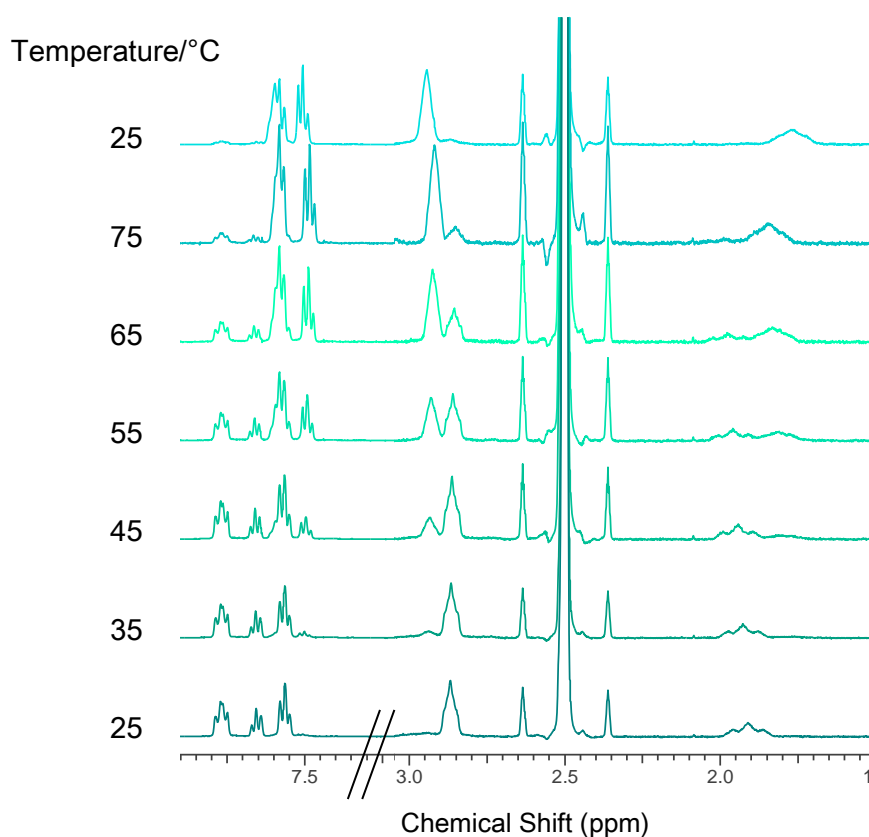


Figure 4.29 ^1H NMR spectra of 0.5 mM [1,3-Bis(diphenylphosphino)propane]palladium(II)triflate at 298 - 348 K. The top spectrum was recorded after the sample had cooled to 25°C after heating. (293 K, 500 MHz, d_6 -DMSO)

4.3.2 L1 + [Pd(dppp)]²⁺ Cryptophanes

When [1,3-bis(diphenylphosphino)propane]palladium(II)triflate and **L1** were combined in a 3:2 ratio in polar aprotic solvents, the ¹H NMR spectra indicated the formation of stable metallo-cryptophanes, illustrated in Figure 4.30. As the **L1** ligand is a racemate of *M* and *P* enantiomers, a mixture of diastereomers would be anticipated from the self-assembly process, as described in section 1.3.2. These diastereomers consisted of the achiral *M,P syn (meso)* conformations and the two chiral *M,M* and *P,P anti* conformations. These diastereomers can be identified using ¹H NMR spectroscopy. The *anti* diastereomer has homotopic [Pd(dppp)]²⁺ Hd protons and homotopic He protons, which means that each set of protons experience a very similar magnetic environment and resonate as one peak. One peak is observed for Hd and one peak is observed for He. For the *syn* diastereomer, the [Pd(dppp)]²⁺ Hd and He protons are diastereotopic, that is they both experience on average a different magnetic environment, which results both sets of protons resonating as two peaks.^{71, 83} This could also be seen in the ³¹P NMR spectroscopy of cryptophanes, as described in section 4.3.1 for [Pd(dppp)]²⁺. These cryptophanes showed no changes in their NMR spectra after the initial self-assembly process. ¹H NMR spectra indicated these complexes were stable when stored at room temperature for over one month. As these complexes looked quite different in *d*₆-DMSO, *d*₃-MeCN and *d*₃-MeNO₂, they will be described separately for each solvent in the following sections. The [Pd₃(dppp)₃(**L1**)₂·6(OTf) cryptophanes have been characterised using a variety of NMR methods including 1-D ¹H and ³¹P and 2-D ROESY techniques.

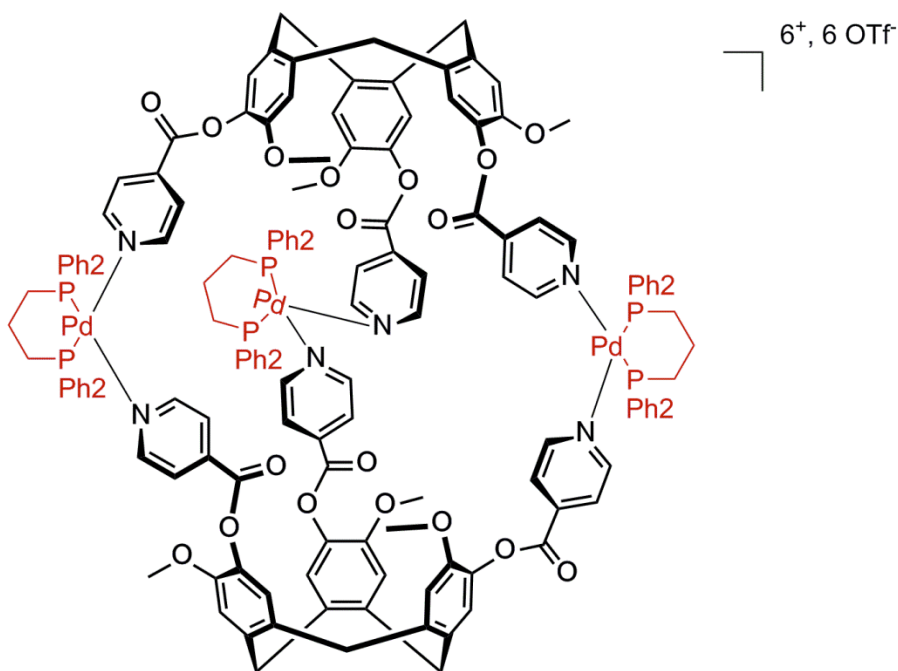


Figure 4.30 $[Pd_3(dppp)_3(L1)_2] \cdot 6(OTf)$ cryptophane.

4.3.2.1 L1 + $[Pd(dppp)]^{2+}$ Cryptophanes in d_6 -DMSO

The 1H NMR spectrum of $[Pd_3(dppp)_3(L1)_2]^{6+}$ in d_6 -DMSO is shown below in Figure 4.31, alongside uncomplexed L1 ligand and $[Pd(dppp)]^{2+}$ 1H NMR spectra in d_6 -DMSO for comparison. The 1H NMR spectrum of $[Pd_3(dppp)_3(L1)_2]^{6+}$ displayed broad resonances indicative of complexation. This was evident for both the L1 and $[Pd(dppp)]^{2+}$ peaks. The chemical shift changes as a result of complexation were small. The complex was shown to be stable at room temperature for up to 36 days. This $[Pd_3(dppp)_3(L1)_2]^{6+}$ cryptophane was investigated at concentrations ranging from 0.5 - 5.0 mM. The initial spectrum appeared to indicate only one cryptophane conformation as there was only one resonance each for both the Hd and the He protons of $[Pd(dppp)]^{2+}$, which was indicative of the *anti* cryptophane conformation. However, the peaks of the complex were very broad, so it was not possible to state with certainty that this was the case from this spectrum alone.

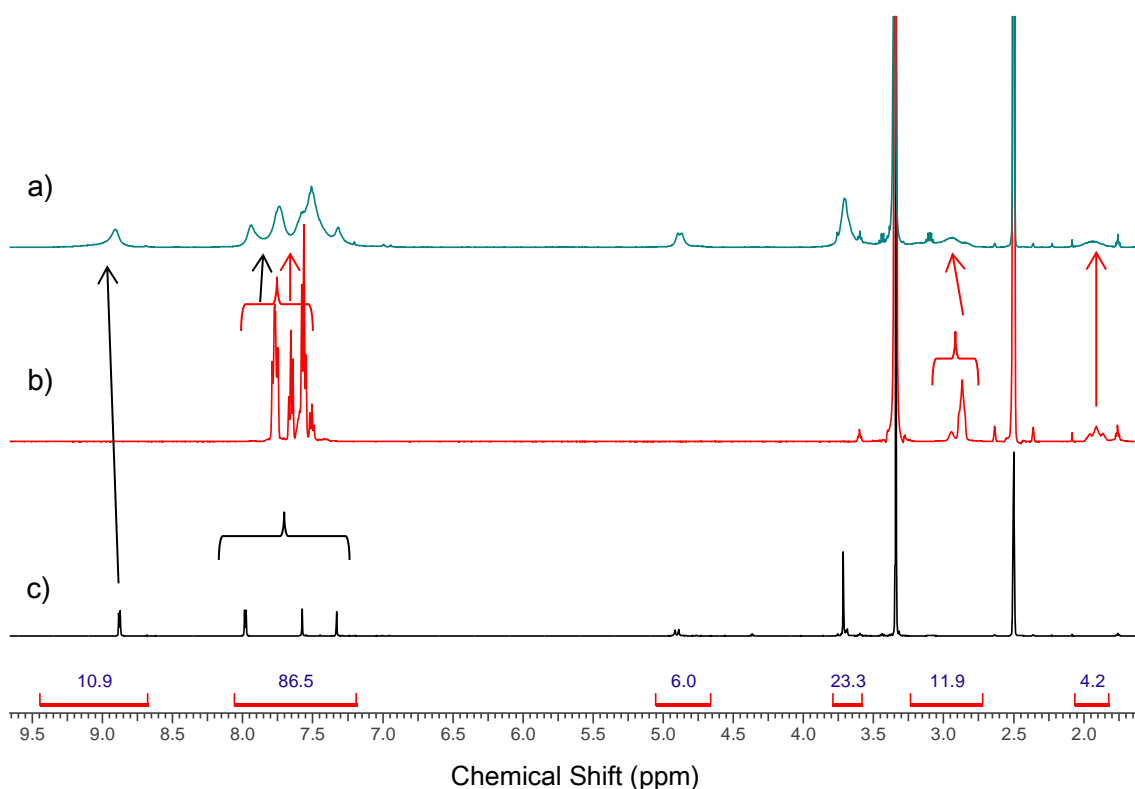


Figure 4.31 ¹H NMR spectra of a) green trace, [Pd₃(dppp)₃(L1)₂]⁶⁺, b) red trace, [1,3-bis(diphenylphosphino)propane]palladium(II)triflate, c) black trace, L1. Integrations are shown for [Pd₃(dppp)₃(L1)₂]⁶⁺. (293 K, 500 MHz, d₆-DMSO)

Further evidence of metallo-cryptophane formation came from the 2-D ROESY analysis of the [Pd₃(dppp)₃(L1)₂]⁶⁺ complex. The intramolecular through space connections seen in the L1 ligand were seen the ROESY spectrum of the [Pd₃(dppp)₃(L1)₂]⁶⁺ cryptophane, that is Ha/a'-Hb/b' and Hd-Hc and He-Hc. One weak through-space connection was seen between a [Pd(dppp)]²⁺ phenyl proton and an L1 pyridyl proton. This is shown in Figure 4.32. To help assign this broad spectrum, ¹H COSY data was used, (appendix A.1) which allowed for the unambiguous determination of the Hb proton of the [Pd(dppp)]²⁺.

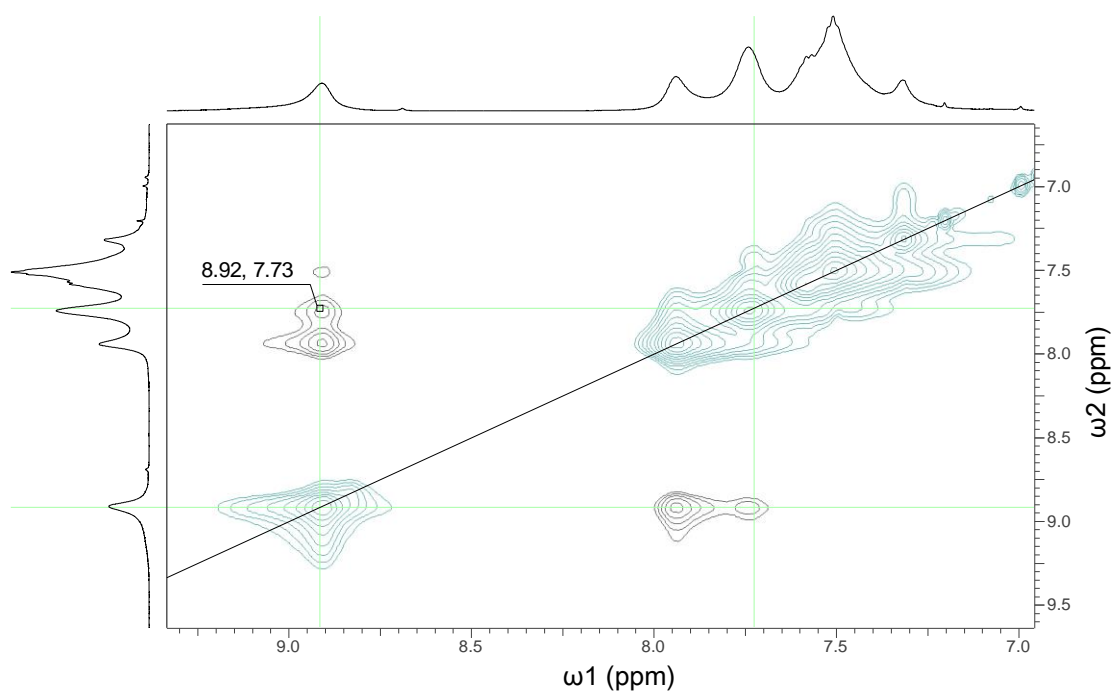


Figure 4.32 Section of ^1H NMR ROESY spectrum of $[\text{Pd}_3(\text{dppp})_3(\text{L}1)_2]^{2+}$, aromatic region showing weak through-space connections between the H_a/a' proton of the L1 pyridyl group and H_b protons of the phenyl arms of $[\text{Pd}(\text{dppp})]^{2+}$. Exchange peaks are in blue and rOes are in black.

(293 K, 500 MHz, d_6 -DMSO)

Due to the shape of the L1 ligand and $[\text{Pd}(\text{dppp})]^{2+}$ respectively, Figure 4.33 illustrates that other through-space connections between L1 and $[\text{Pd}(\text{dppp})]^{2+}$ were unlikely to be observed, as only the pyridyl arms of L1 and the phenyl arms of $[\text{Pd}(\text{dppp})]^{2+}$ were in close proximity to each other in this complex and this was borne out by the experimental data.

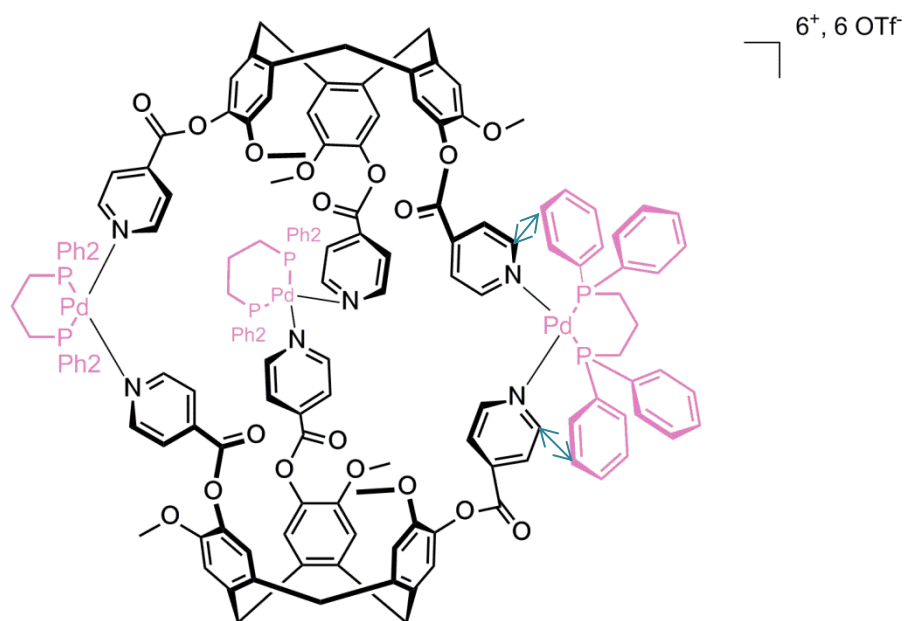


Figure 4.33 $[Pd_3(dppp)_3(L1)_2] \cdot 6(OTf)$ cryptophane in DMSO, with one $[Pd(dppp)]^{2+}$ group drawn fully to show the through-space connections between $H_{a/a'}$ of the L1 ligand and H_b of $[Pd(dppp)]^{2+}$, which are indicated by the blue arrows.

It can be seen in Figure 4.34 that the 1H NMR spectra of $[Pd_3(dppp)_3(L1)_2]^{6+}$ in d_6 -DMSO varied with decreasing concentration. Initially, two sets of identical samples were prepared by different methods. The first set was prepared from stocks of L1 and stocks of $[Pd(dppp)]^{2+}$. The second set was prepared from a stock of pre-combined $[Pd_3(dppp)_3(L1)_2]^{6+}$ to see if this had any effect on the self-assembly of the cryptophanes. It did not and the resulting sets of spectra were identical.

It can be seen in Figure 4.34, that as the concentration of $[Pd_3(dppp)_3(L1)_2]^{6+}$ complex was increased, the peaks became broader. This is because both *syn* and *anti* cryptophanes were formed in d_6 -DMSO, but not in equal proportions, with the majority of cryptophanes having the *anti* conformation. As the concentration of $[Pd_3(dppp)_3(L1)_2]^{6+}$ was increased, the amounts of both of the conformations present were increased in proportion. This was most clearly shown by the resonances of H_d protons the $[Pd(dppp)]^{2+}$ propylene bridge protons, which are shown in more detail in Figure 4.35.

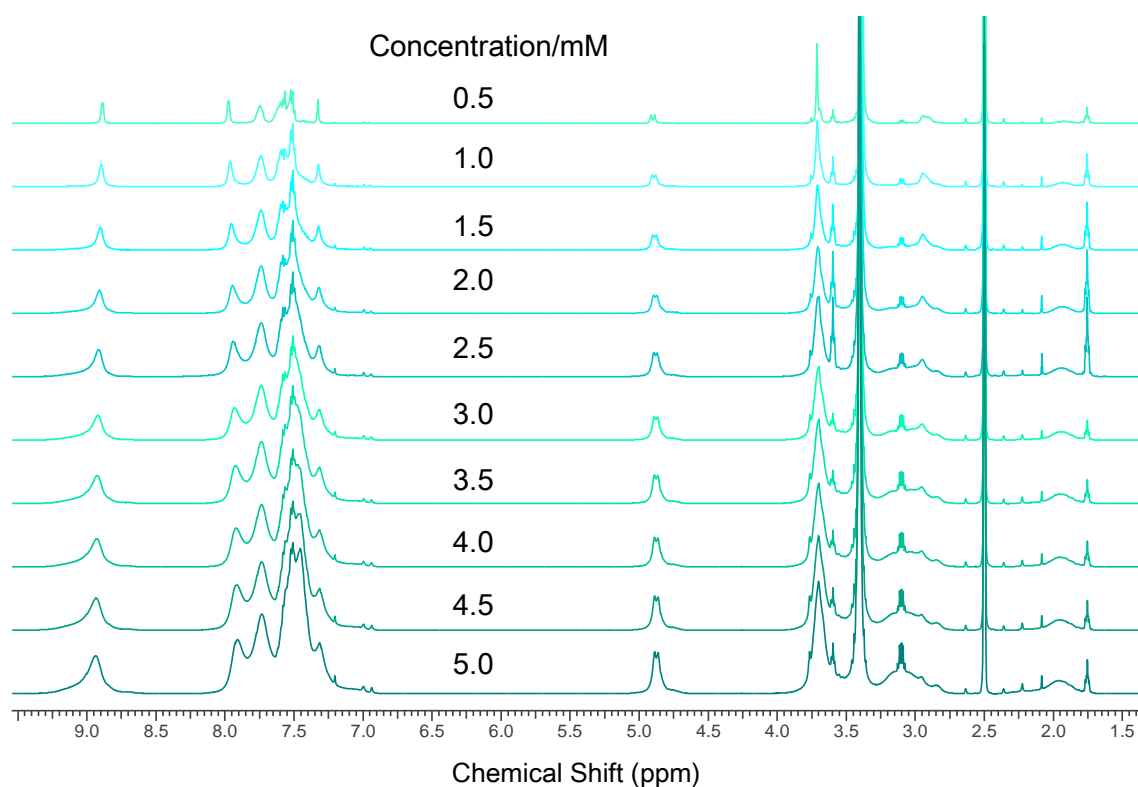


Figure 4.34 ^1H NMR spectra of $[\text{Pd}_3(\text{dppp})_3(\text{L1})_2]^{6+}$ at 0.5 – 5.0 mM. (293 K, 500 MHz, d_6 -DMSO)

At 0.5 mM, only the resonance for the *anti* cryptophane could be clearly discerned, this peak is marked with a blue asterisk in Figure 4.35 b). A small shoulder can just be made out that is indicative of the *syn* cryptophane conformation. As the samples became more concentrated, the *syn* resonance grew in intensity (marked by the red diamond in Figure 4.35). Only one *syn* Hd peak was observed. It was possible that the other peak was overlapped by the *anti* resonance. Evidence of the exchange between the chair conformations of $[\text{Pd}(\text{dppp})]^{2+}$ can be seen in the Hd *anti* resonance. At 0.5 mM the two chair conformation populations were almost equal, but as the concentration of $[\text{Pd}_3(\text{dppp})_3(\text{L1})_2]^{6+}$ was increased, the rate of exchange between the conformations increased, shown by the broad resonance that has coalesced. The well-resolved multiplet at 3.1 ppm, which falls in the middle of what appears to be a rather broad resonance of the Hd protons and is identified by the black dot, is a contaminant in the L1 ligand.

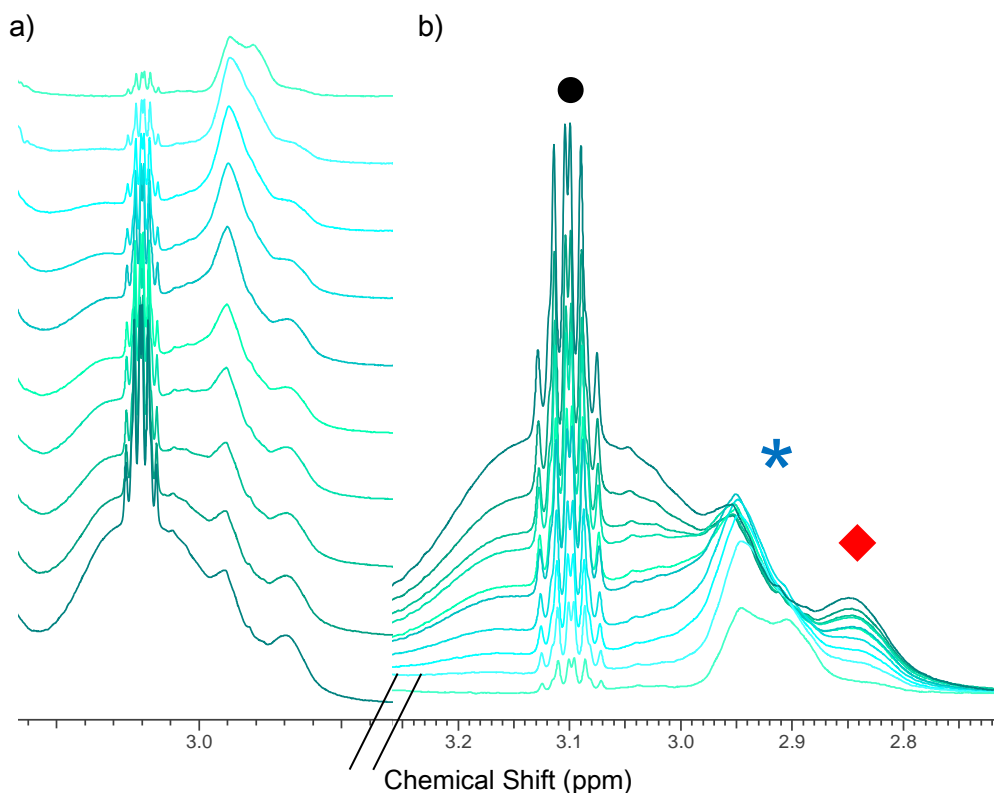


Figure 4.35 ^1H NMR spectra of $[\text{Pd}_3(\text{dppp})_3(\text{L1})_2]^{6+}$ Hd $[\text{Pd}(\text{dppp})]^{2+}$ resonance with 5.0 mM at the bottom and 0.5 mM at the top. a) stacked plot, b) superimposed stacked plot, (●) black dot indicates contaminant in L1 ligand, (*) blue asterisk indicates Hd anti resonance, (◆) red diamond indicates Hd syn resonance. (293 K, 500 MHz, d_6 -DMSO)

The ^{31}P NMR spectra of $[\text{Pd}_3(\text{dppp})_3(\text{L1})_2]^{6+}$ in the same concentration range (0.5 - 5.0 mM) are shown in Figure 4.36. At high concentrations, 3 different phosphorus environments were seen, a broad peak at 15.1 ppm, a singlet at 10.0 ppm and another broad peak at 7.0 ppm. The singlet at 10.0 ppm was indicative of a contaminant in the d_6 -DMSO as described in section 4.3.1. As the concentration of $[\text{Pd}_3(\text{dppp})_3(\text{L1})_2]^{6+}$ in d_6 -DMSO was reduced, the broad peak at 15.1 ppm reduced in intensity and narrowed. The broad peak at 7.0 ppm also reduced in intensity and at 0.5 mM (top trace in Figure 4.36) was not seen. This is in contrast to uncomplexed $[\text{Pd}(\text{dppp})]^{2+}$, which had only one $[\text{Pd}(\text{dppp})]^{2+}$ phosphorus environment (Figure 4.27). This implies that both *syn* and *anti* cryptophanes are present, however one of the *syn* peaks was masked by the other resonances present in the spectrum, most probably that of the *anti* cryptophane at 15.1

ppm, which displayed a broad shoulder. At 0.5 mM, only the resonance for the *anti* cryptophane was observed.

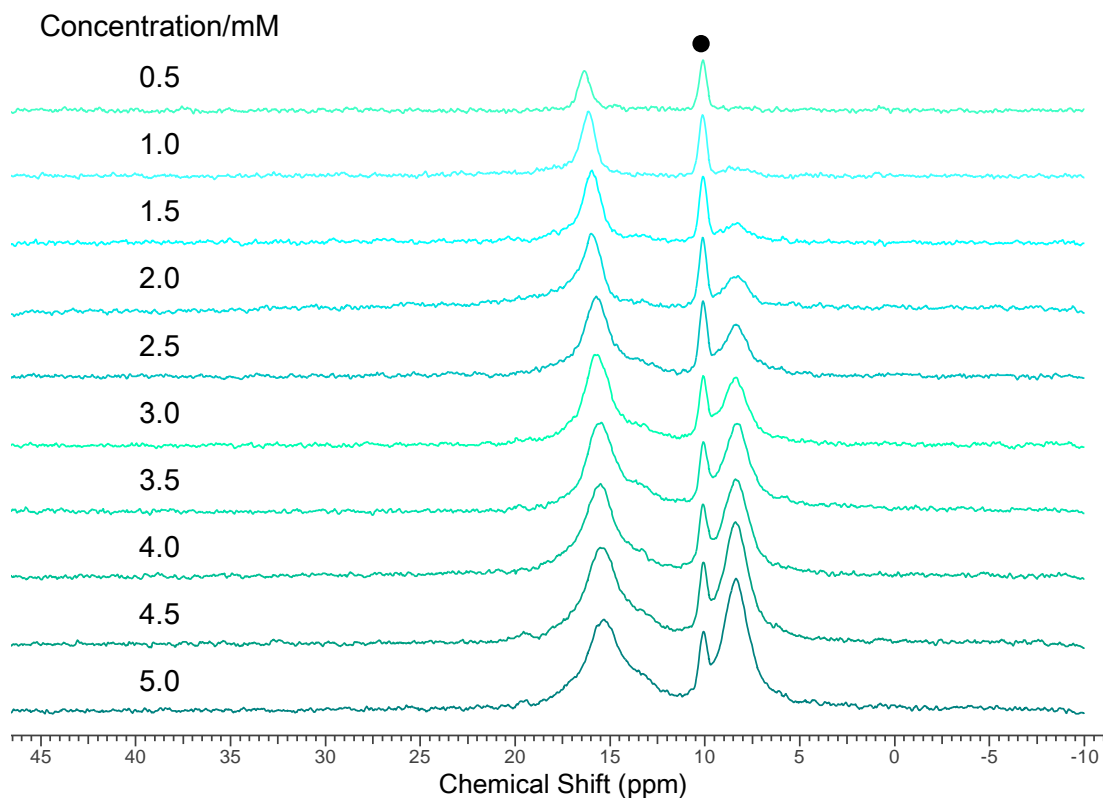


Figure 4.36 ³¹P NMR spectra of [Pd₃(dppp)₃(L1)₂]⁶⁺ at 0.5 – 5.0 mM. (•) black dot indicates contaminant in *d*₆-DMSO. (300 K, 121 MHz, *d*₆-DMSO)

The sample of 0.5 mM [Pd₃(dppp)₃(L1)₂]⁶⁺ in *d*₆-DMSO was subjected to a VT ¹H NMR investigation to further investigate the dynamic equilibria. The sample was heated in 10°C increments from 25 - 75°C. The spectra from the experiment are shown in Figure 4.37. The top trace is the spectrum recorded after the sample had cooled back down to 25°C. It can be seen that this spectrum is identical to the initial spectrum recorded at 25°C. A change observed is in the exchanging [Pd(dppp)]²⁺ Hd peaks, which as the temperature was raised to 45°C shows that the two chair conformations now have equal populations. This change in chair conformation populations continued up to 75°C. After the VT experiment, the chair conformation resumed the population levels

seen initially at room temperature. This was also reflected in the $[\text{Pd}(\text{dppp})]^{2+}$ aromatic peaks. This was quite different to what was observed when uncomplexed $[\text{Pd}(\text{dppp})]^{2+}$ was subjected to a VT experiment (Figure 4.29), where the conformation changed during the heating process and did not return to its original conformation. This indicated that the cryptophane was stable in the *anti* conformation up to 75°C

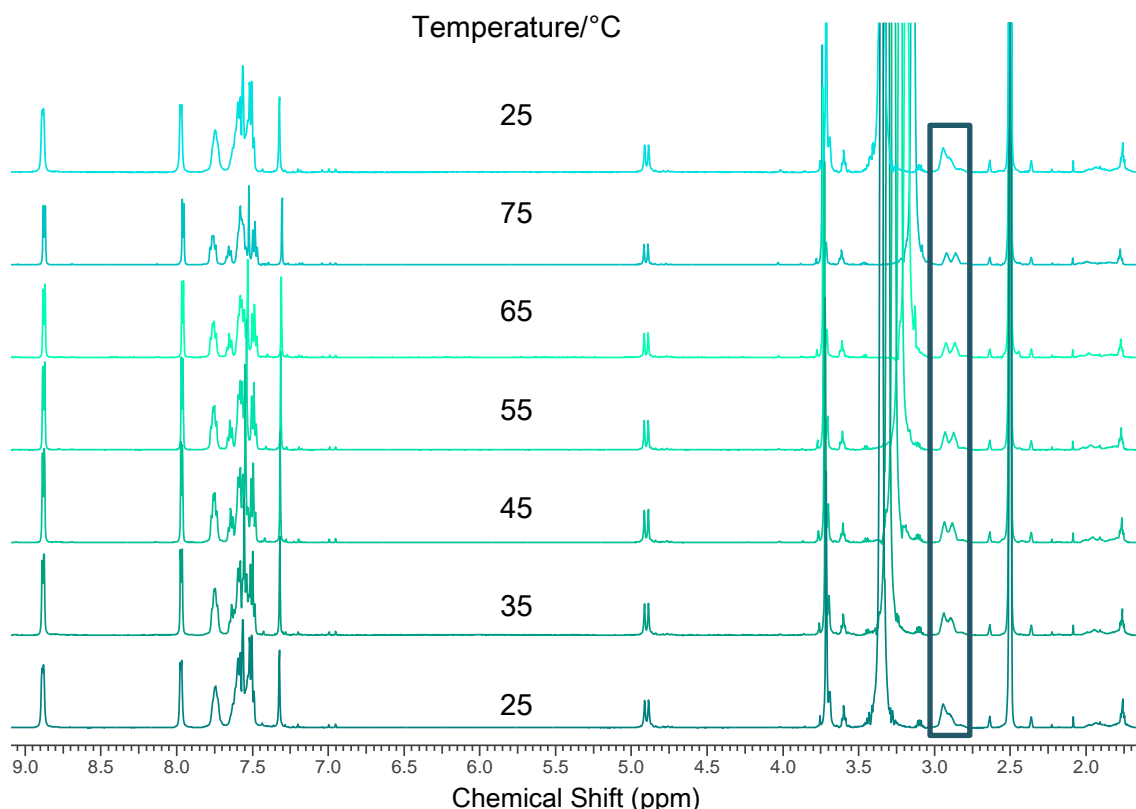


Figure 4.37 ^1H NMR spectra of 0.5 mM $[\text{Pd}_3(\text{dppp})_3(\text{L}1)_2]^{6+}$ at 298 - 348 K. The top spectrum was recorded after the sample had cooled to 25°C after heating. The box highlights the $[\text{Pd}(\text{dppp})]^{2+}$ Hd peaks. (500 MHz, d_6 -DMSO)

The 5 mM $[\text{Pd}_3(\text{dppp})_3(\text{L}1)_2]^{6+}$ sample was also subjected to a VT NMR experiment. The sample was heated from 25°C to 75°C; the spectra from this experiment are shown Figure 4.38. As the temperature was increased, the spectra started to sharpen, and the Hd resonances coalesced into a broad peak, although there is a small *syn* peak present. This was indicative of the *anti* cryptophane conformation being the preferred isomer at slightly elevated temperatures. As there was only one Hd *anti* peak, this also indicated an increased rate of exchange between the two chair conformations

of $[\text{Pd}(\text{dppp})]^{2+}$. The peaks in the aromatic region also sharpened considerably with the increase in temperature. The spectra at slightly elevated temperatures implied that there was a highly symmetrical complex in solution. However, the spectrum recorded after the sample had cooled was identical to the original spectrum recorded at 25°C, indicating that at room temperature neither the *anti* or *syn* isomers were thermodynamically preferred.

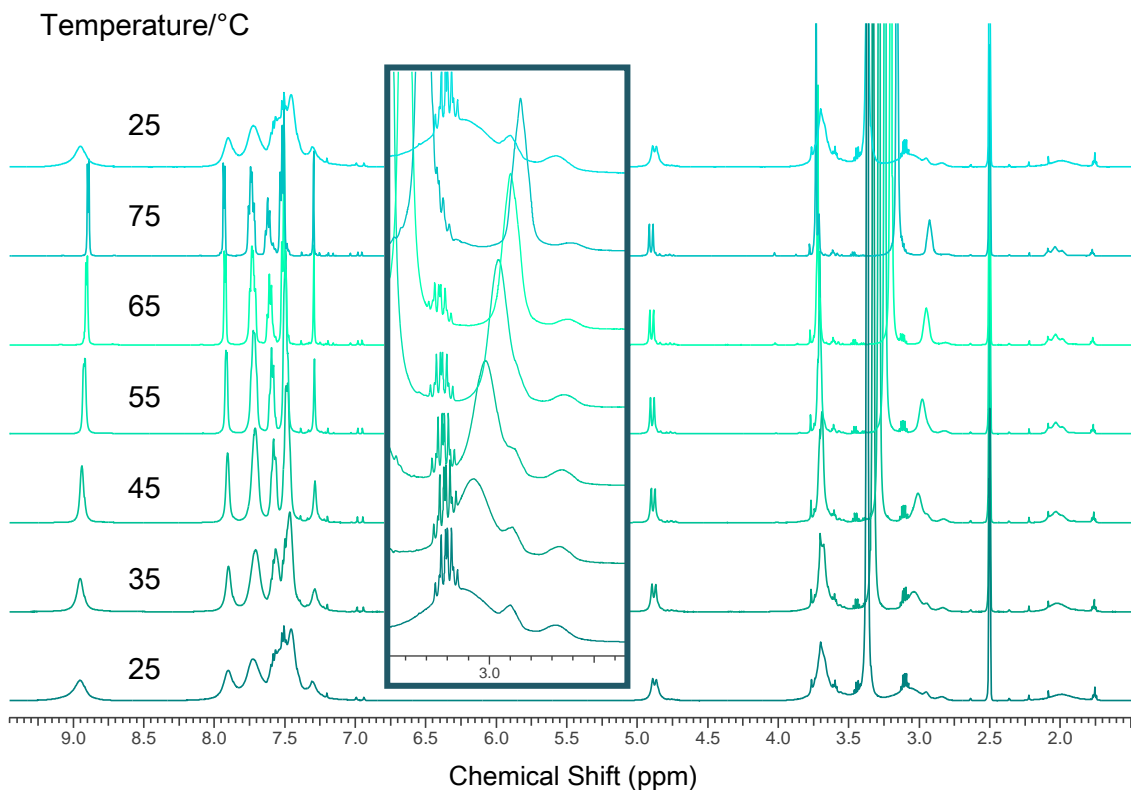


Figure 4.38 ^1H NMR spectra of 5.0 mM $[\text{Pd}_3(\text{dppp})_3(\text{L1})_2]^{6+}$ at 298 - 348 K. The top spectrum was recorded after the sample had cooled to 25°C after heating. The box shows an expansion of the Hd peaks of $[\text{Pd}(\text{dppp})]^{2+}$. (500 MHz, d_6 -DMSO)

4.3.2.2 L1 + $[\text{Pd}(\text{dppp})]^{2+}$ Cryptophanes in d_3 -MeCN

The addition of L1 and $[\text{Pd}(\text{dppp})]^{2+}$ at a 2:3 ratio in d_3 -acetonitrile resulted in a sharp, well-resolved ^1H NMR spectrum, shown in Figure 4.39 a), with the spectra of L1 and $[\text{Pd}(\text{dppp})]^{2+}$, also in d_3 -MeCN for comparison. The spectrum was highly symmetrical, indicating that a highly symmetrical complex had been formed. The peaks of $[\text{Pd}_3(\text{dppp})_3(\text{L1})_2]^{6+}$ in d_3 -MeCN were slightly broadened, indicative of complexation. The L1 peaks showed little change in chemical shift, with the exception of the Hb/b' peak, which shifted upfield by 0.21 ppm. The aromatic peaks of $[\text{Pd}(\text{dppp})]^{2+}$ in the $[\text{Pd}_3(\text{dppp})_3(\text{L1})_2]^{6+}$ complex were now resolved into three peaks, indicating that the magnetic environment of the phenyl arms of $[\text{Pd}(\text{dppp})]^{2+}$ had changed. The propylene

bridge Hd peaks shifted downfield by 0.26 ppm. The propylene peaks Hd and He indicated that only the *anti* cryptophane was present in solution.

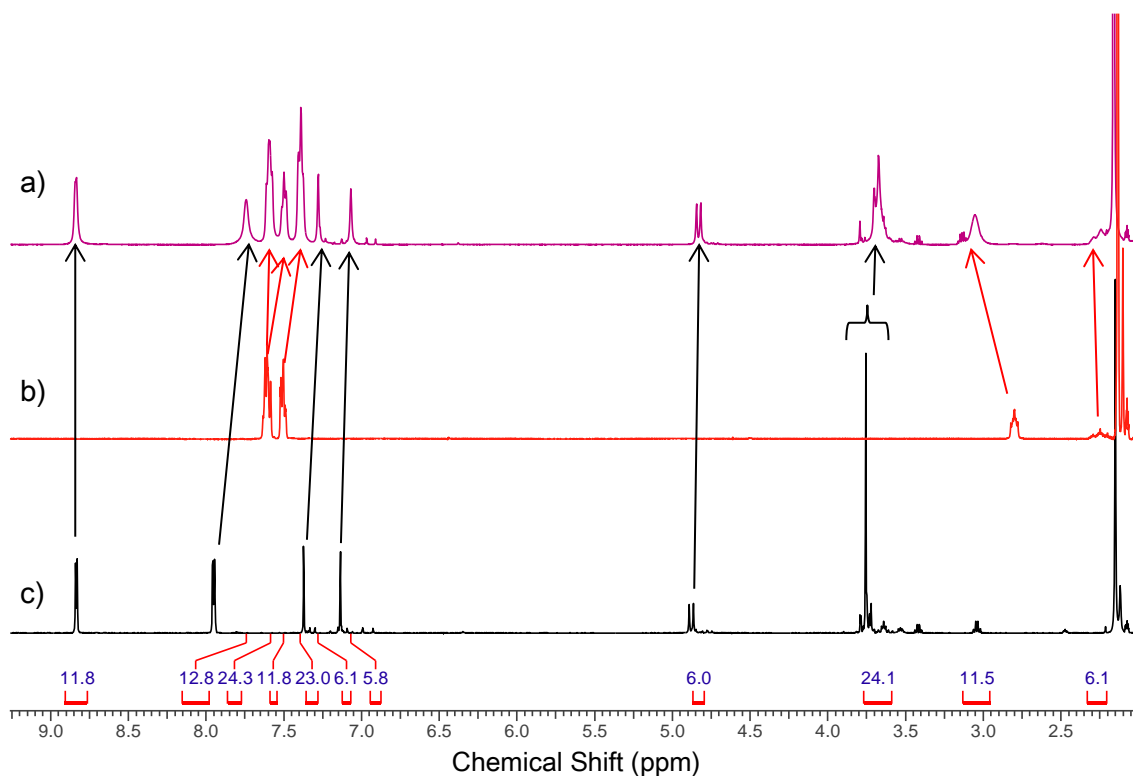


Figure 4.39 ¹H NMR spectra of a) pink trace, $[\text{Pd}_3(\text{dppp})_3(\text{L}1)_2]^{6+}$, b) red trace, $[1,3\text{-bis}(\text{diphenylphosphino})\text{propane}]\text{palladium}(\text{II})\text{triflate}$, c) black trace, L1. Integrations are shown for $[\text{Pd}_3(\text{dppp})_3(\text{L}1)_2]^{6+}$. (293 K, 500 MHz, $d_3\text{-MeCN}$)

The 2-D ROESY NMR spectrum of $[\text{Pd}_3(\text{dppp})_3(\text{L}1)_2]^{6+}$ in d_3 -acetonitrile, shown in Figure 4.40, provided further evidence of cryptophane formation. The through-space connections observed are listed and assigned in Table 4.2. Through-space connections were seen between Ha/a' protons of the L1 pyridyl arms and Hc and Hb of the $[\text{Pd}(\text{dppp})]^{2+}$ arms, showing that these protons were in close proximity to each other. This is shown in the expanded region of the ROESY spectrum in Figure 4.41 and illustrated in Figure 4.42.

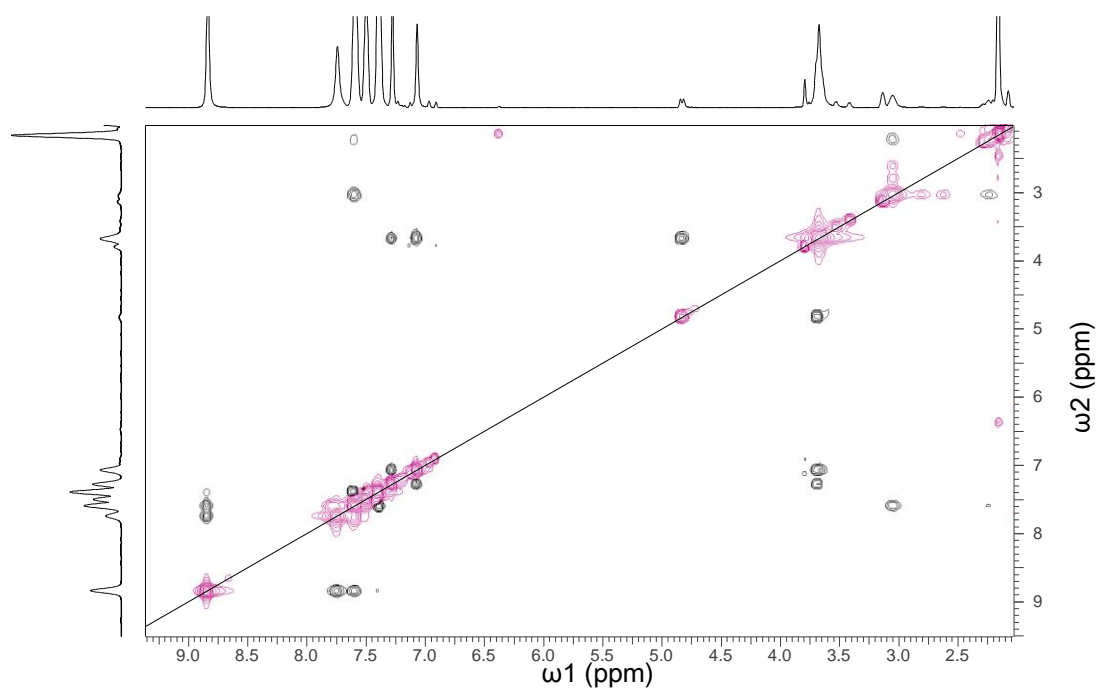


Figure 4.40 ^1H NMR ROESY spectrum of $[\text{Pd}_3(\text{dppp})_3(\text{L}1)_2]^{3+}$, Exchange peaks are in pink and rOes are in black. (293 K, 500 MHz, d_3 -MeCN)

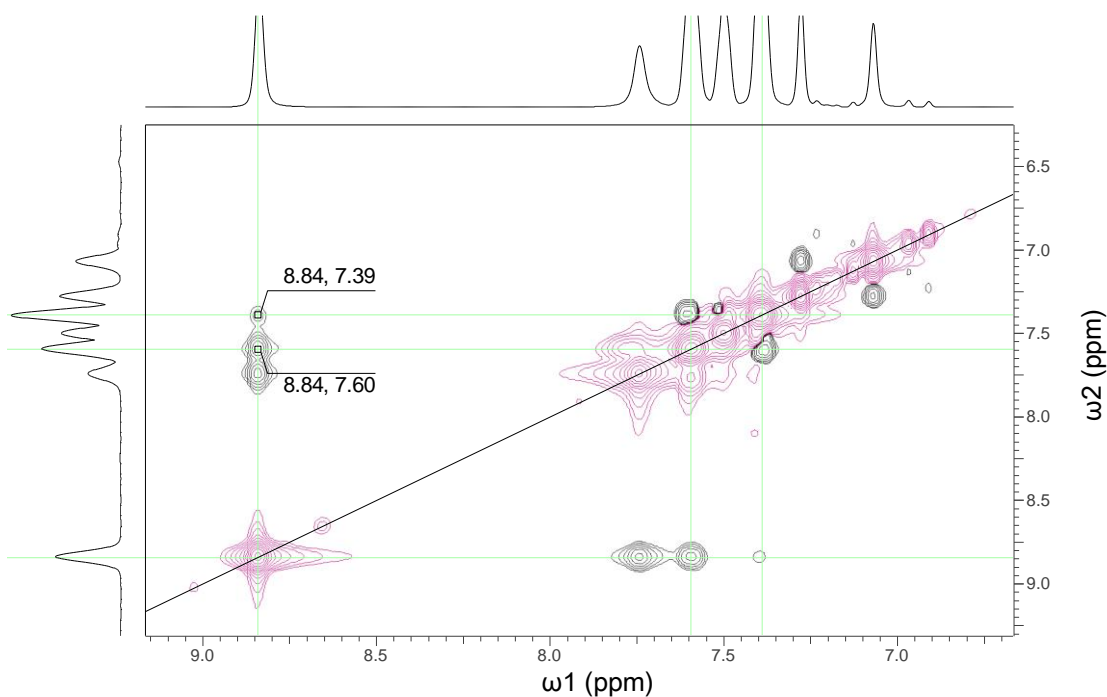


Figure 4.41 Section of ^1H NMR ROESY spectrum of $[\text{Pd}_3(\text{dppp})_3(\text{L}1)_2]^{3+}$, aromatic region showing through-space connections between the H_a/a' proton of the L1 pyridyl group and H_b and H_c protons of the phenyl arms of $[\text{Pd}(\text{dppp})]^{3+}$. Exchange peaks are in pink and rOes are in black. (293 K, 500 MHz, d_3 -MeCN)

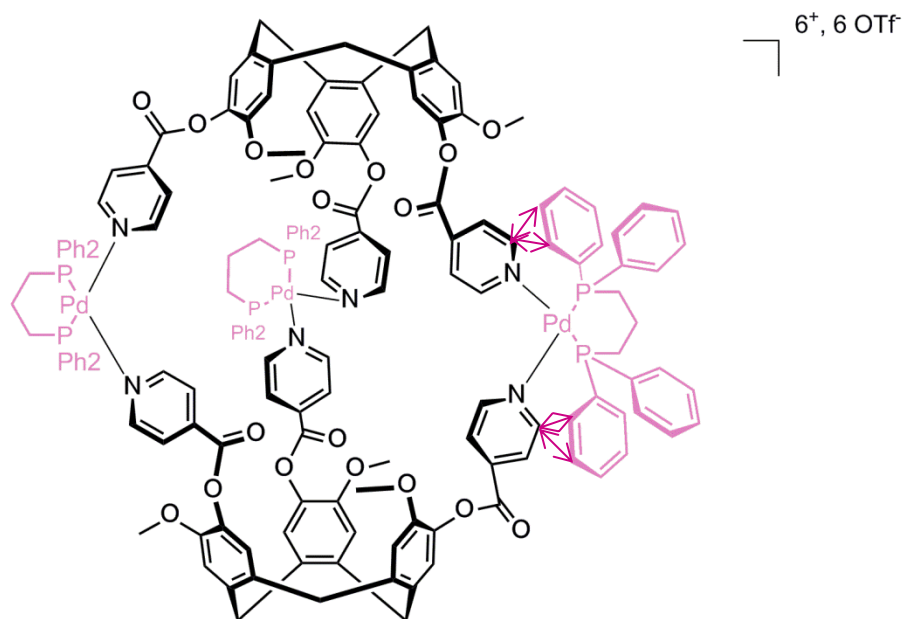


Figure 4.42 $[Pd_3(dppp)_3(L1)_2] \cdot 6(OTf)$ cryptophane in MeCN, with one $[Pd(dppp)]^{2+}$ group drawn fully to show the through-space connections between Ha/a' of the L1 ligand and Hb and Hc of $[Pd(dppp)]^{2+}$, which are indicated by the pink arrows.

Table 4.2 Table of through-space connections and assignments for [Pd₃(dppp)₃(L1)₂]⁶⁺(OTf)₆ cryptophane in d₃-MeCN. L1 listed in black and [Pd(dppp)]²⁺ listed in red.

Through-space Connection/ppm	Assignment
2.20, 3.05	Hd-He
2.20, 7.60	He-Hb
3.05, 7.60	Hd-Hb
3.70, 4.83	H _{endo} -H _{exo}
3.70, 7.07	Hc-He
3.70, 7.27	Hc-Hd
7.07, 7.27	He-Hd
7.39, 7.60	Hc-Hb
7.39, 8.84	Hc-Ha
7.60, 8.84	Hb-Ha
7.75, 8.84	Hb-Ha

The [Pd₃(dppp)₃(L1)₂]⁶⁺ complex in d₃-acetonitrile was studied in the range 0.5 - 5.0 mM by ¹H and ³¹P NMR spectroscopy, to investigate if the concentration of the complex had an effect on the conformation of cryptophanes formed. The ¹H NMR spectra are shown in Figure 4.43. There appeared to be no change in the proton environments in this concentration range, indicating that only the *anti* cryptophane was present in solution. The ³¹P NMR spectra however, (Figure 4.44) showed that a small amount of the phosphorus present was experiencing a different phosphorus environment at high concentrations (4.0 - 5.0 mM). A low intensity, broad resonance was seen downfield 10.0 ppm. A closer inspection of the ¹H NMR spectra revealed the

presence of a small amount of *syn* cryptophane isomers. This was seen most clearly in the $H_{a/a'}$ and the H_{endo} peaks of **L1**, and additional $[Pd(dppp)]^{2+}$ Hd peaks, as shown in Figure 4.45 a), b) and c) respectively. The *syn* isomer peaks were very low in intensity, with a very low signal-to-noise ratio. As the concentration of the $[Pd_3(dppp)_3(L1)_2]^{6+}$ complex was increased, the amount of *syn* isomer present in solution increased relatively. The *syn* isomer peaks could be identified by 1H NMR spectroscopy throughout the concentration range. This was not observed in the ^{31}P NMR spectroscopy analysis, as this technique is less sensitive than 1H NMR spectroscopy.¹³⁶ The 5.0 mM $[Pd_3(dppp)_3(L1)_2]^{6+}$ was subjected to a 1H NMR VT experiment. The complex was found to be stable up to 65°C and no change in conformation of the cryptophane was detected.

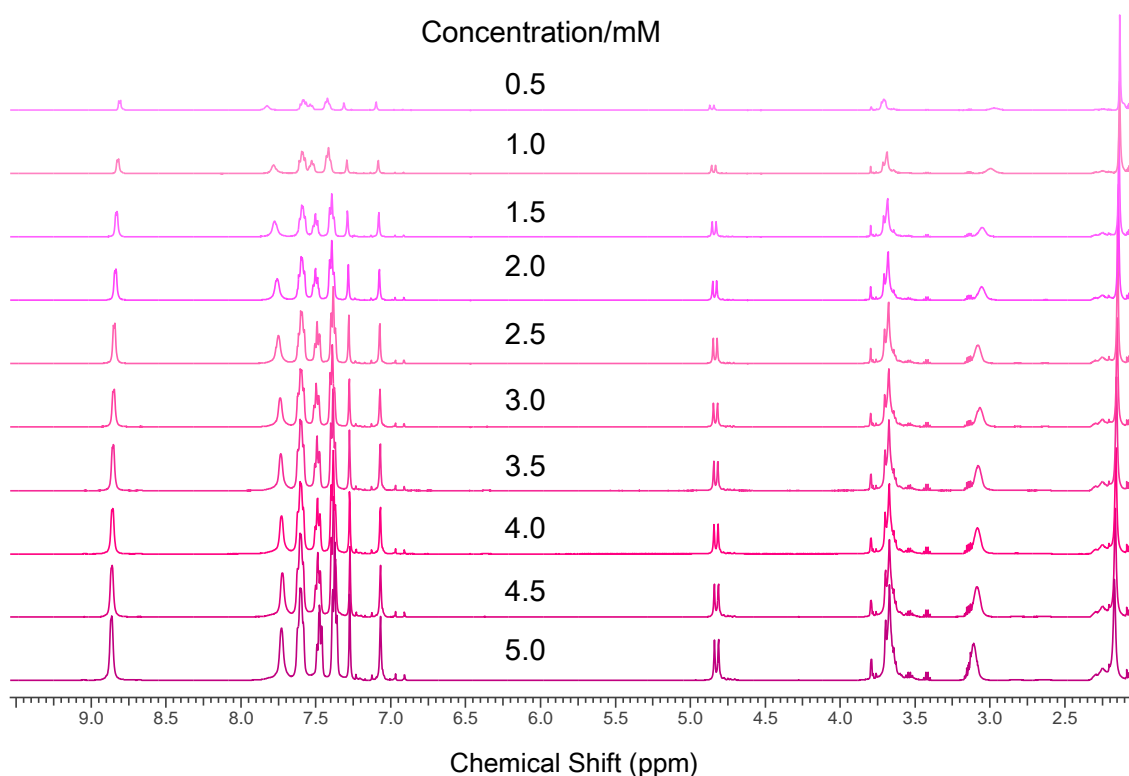


Figure 4.43 1H NMR spectra of $[Pd_3(dppp)_3(L1)_2]^{6+}$ at 0.5 – 5.0 mM.
(293 K, 500 MHz, d_3 -MeCN)

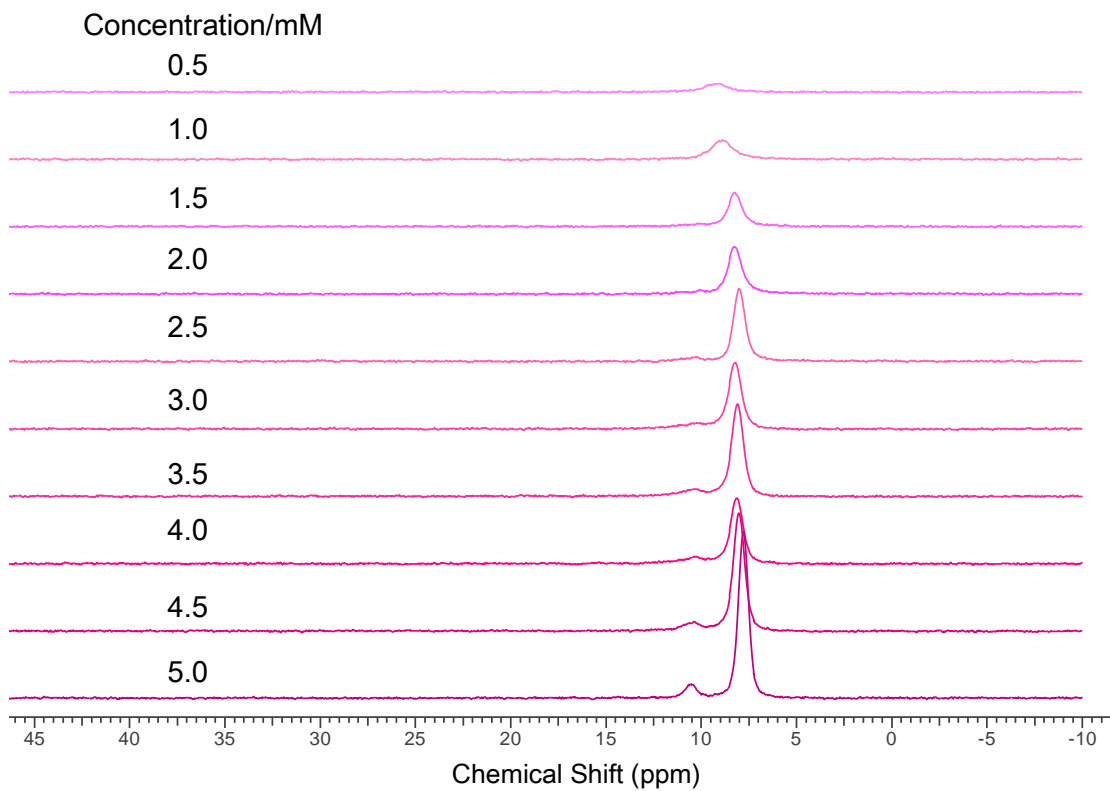


Figure 4.44 ^{31}P NMR spectra of $[\text{Pd}_3(\text{dppp})_3(\text{L}1)_2]^{3+}$ at 0.5 – 5.0 mM.
(300 K, 121 MHz, d_3 -MeCN)

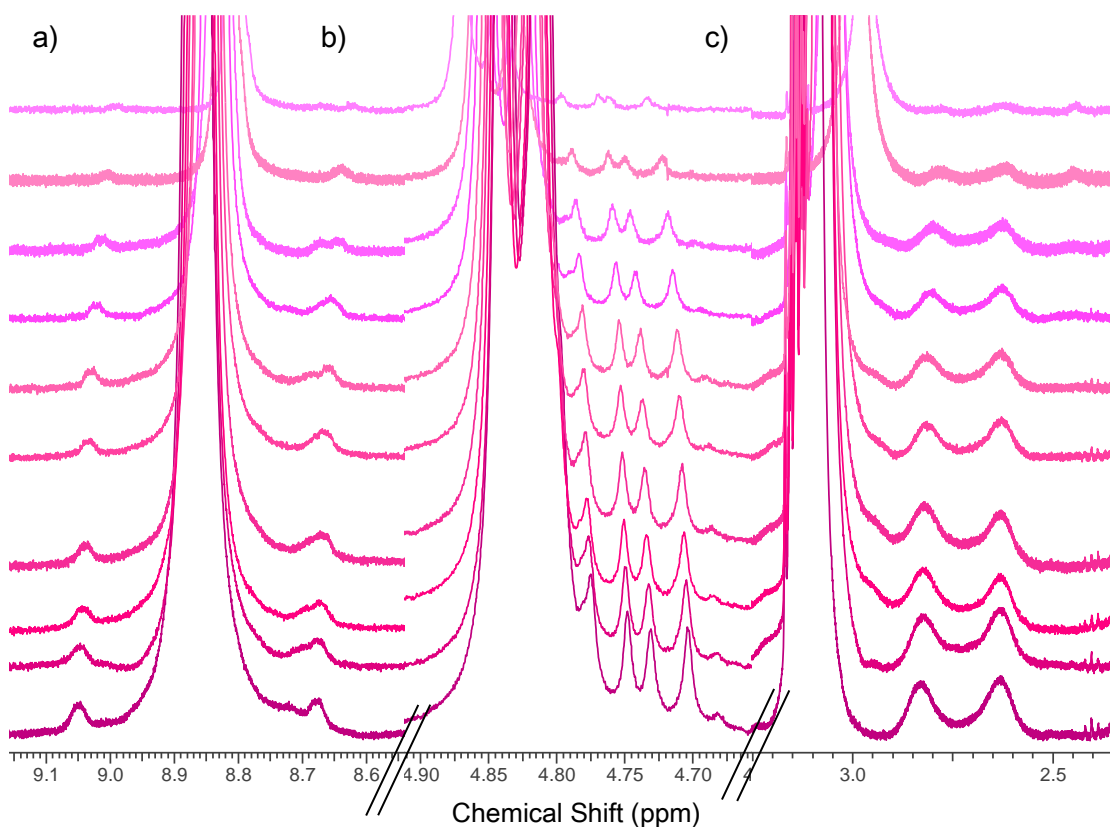


Figure 4.45 ^1H NMR spectra of $[\text{Pd}_3(\text{dppp})_3(\text{L}1)_2]^{3+}$ with 5.0 mM at the bottom and 0.5 mM at the top a) H_a/a' peaks, b) H_{endo} peaks and c) H_d syn peaks.
(293 K, 500 MHz, d_3 -MeCN)

4.3.2.3 L1 + [Pd(dppp)]²⁺ Cryptophanes in *d*₃-MeNO₂

When the [Pd₃(dppp)₃(L1)₂]⁶⁺ complex was formed in *d*₃-nitromethane, a complex proton spectrum was observed (Figure 4.46). The peaks of the complex were broad, and did not indicate the formation of a highly symmetrical complex. This was highlighted by the Ha/a' resonances of L1 in the [Pd₃(dppp)₃(L1)₂]⁶⁺ complex, which were shifted downfield compared to uncomplexed L1, and exhibited a broad shoulder indicating that the Ha/a' protons were experiencing different magnetic environments. The ¹H NMR spectrum also appeared to indicate that both *anti* and *syn* cryptophanes were present, as there are three [Pd(dppp)]²⁺ He resonances present (shown by the inset spectrum in Figure 4.46). There was only a small amount of the *syn* isomer present, with a ratio of 1:10 *syn:anti* observed for the He protons.

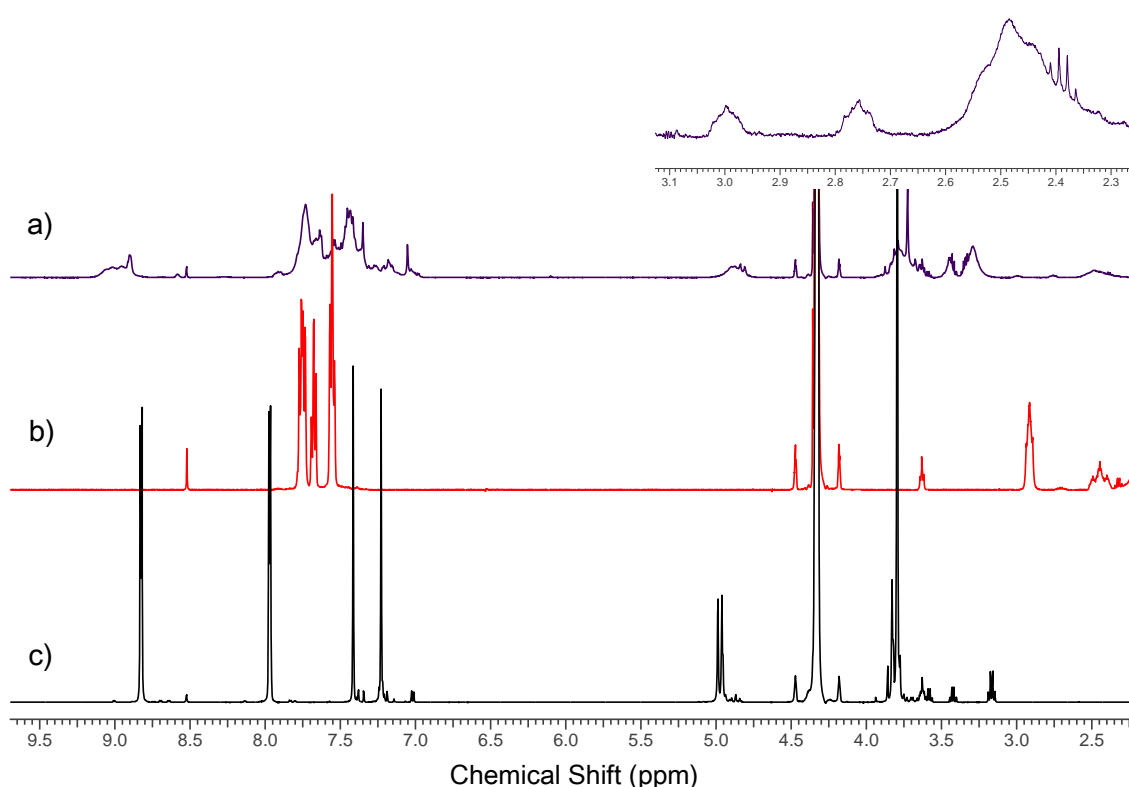


Figure 4.46 ¹H NMR spectra of a) purple trace, [Pd₃(dppp)₃(L1)₂]⁶⁺, b) red trace, [1,3-bis(diphenylphosphino)propane]palladium(II)triflate, c) black trace, L1. Inset spectrum shows expansion of [Pd(dppp)₃(L1)₂]⁶⁺ He peaks. (293 K, 500 MHz, *d*₃-MeNO₂)

The 2-D ROESY spectrum of $[\text{Pd}_3(\text{dppp})_3(\text{L1})_2]^{6+}$ in d_3 -nitromethane is shown in Figure 4.47. Although the spectrum was complex in the aromatic region, with peaks overlapping, it was possible to assign the rOe seen between the Ha/a' peaks at 8.90 ppm to a peak at 7.74 ppm using the HMQC spectra of $[\text{Pd}_3(\text{dppp})_3(\text{L1})_2]^{6+}$ and uncomplexed L1 and $[\text{Pd}(\text{dppp})]^{2+}$ in d_3 -MeNO₂ (appendix A.2). The peak at 7.74 ppm was assigned to the Hb resonance of $[\text{Pd}(\text{dppp})]^{2+}$. This through-space connection is seen in Figure 4.48.

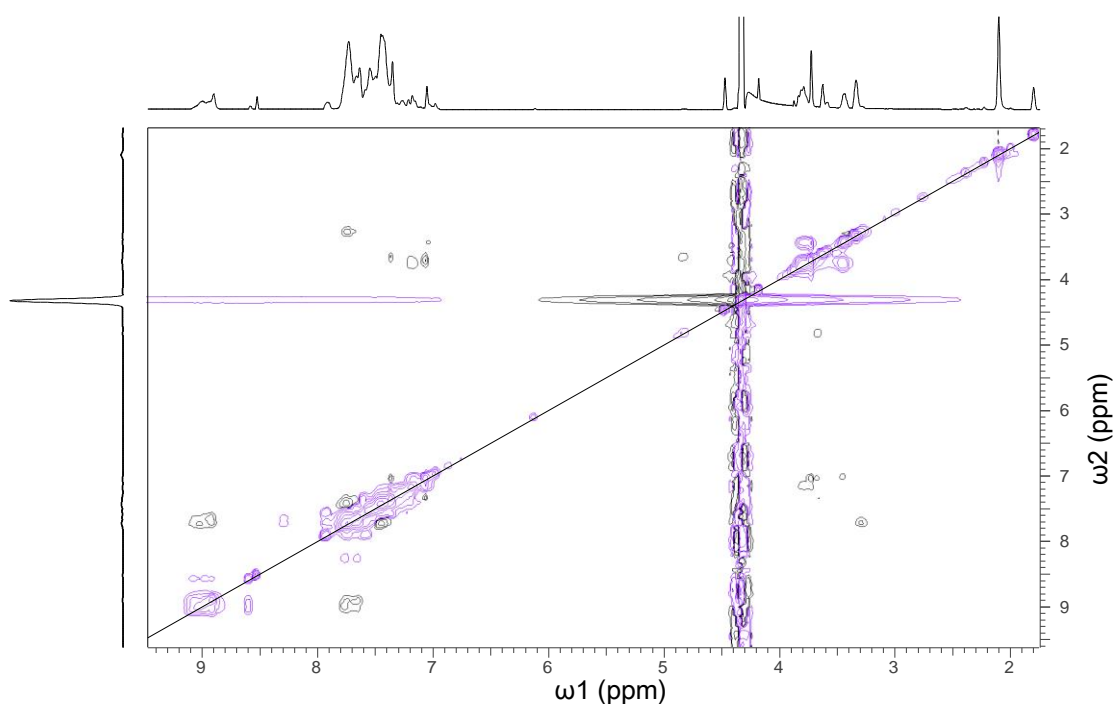


Figure 4.47 ^1H NMR ROESY spectrum of $[\text{Pd}_3(\text{dppp})_3(\text{L1})_2]^{6+}$. Exchange peaks are in purple and rOes are in black. (293 K, 500 MHz, d_3 -MeNO₂)

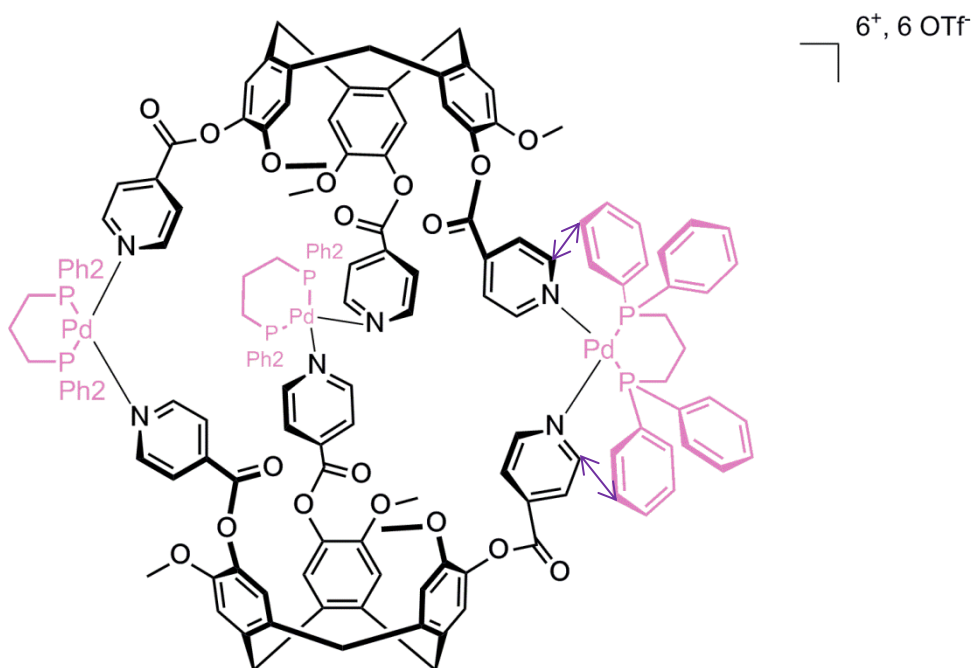


Figure 4.48 $\text{Pd}_3(\text{dppp})_3(\text{L1})_2 \cdot 6(\text{OTf})$ cryptophane in MeNO_2 , with one $[\text{Pd}(\text{dppp})]^{2+}$ group drawn fully to show the through-space connections between $\text{Ha/a}'$ of the L1 ligand and Hb of $[\text{Pd}(\text{dppp})]^{2+}$, which are indicated by the purple arrows.

When the $[\text{Pd}_3(\text{dppp})_3(\text{L1})_2]^{6+}$ in d_3 -nitromethane was studied in the range 0.5 – 5.0 mM (Figure 4.49), ^1H NMR spectroscopy revealed that both conformers of cryptophane were present throughout this concentration range, as indicated by the three $[\text{Pd}(\text{dppp})]^{2+}$ He resonances. The ratio of *syn:anti* (1:10) cryptophanes remained constant throughout the experiment. The $\text{Ha/a}'$ resonance at 9.0 ppm underwent the most dramatic change; at 5.0 mM (bottom trace of Figure 4.49) a broad multiplet resembling a doublet of doublets was seen, whereas at 0.5 mM what appeared to be a single broad doublet was observed. The L1 H_{endo} peak was also indicative of the presence of both cryptophane enantiomers. At high concentrations, a broad multiplet was observed, but as the concentration of $[\text{Pd}_3(\text{dppp})_3(\text{L1})_2]^{6+}$ was decreased, a doublet overlapping with the a broad peak was seen.

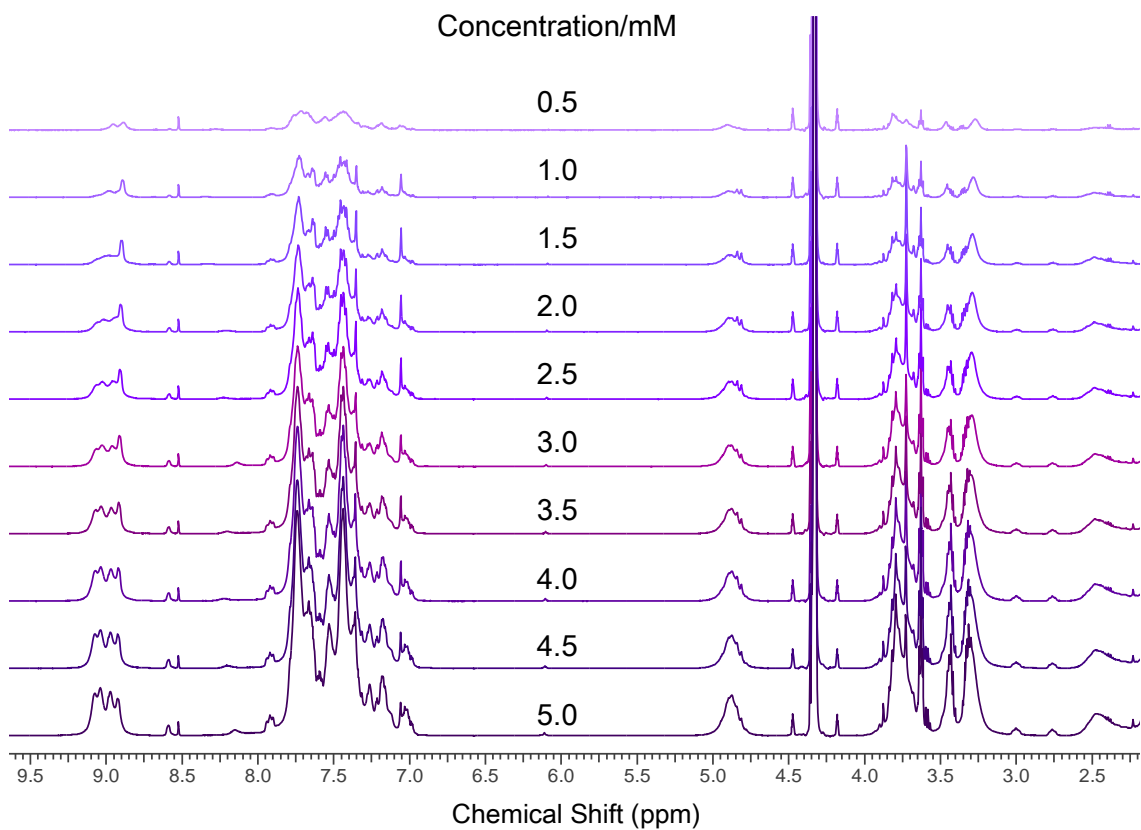


Figure 4.49 ¹H NMR spectra of $[Pd_3(dppp)_3(L1)_2]^{6+}$ at 0.5 – 5.0 mM.
(293 K, 500 MHz, *d*₃-MeNO₂)

In the ³¹P NMR spectra (Figure 4.50), three phosphorus environments were observed. This indicated the presence of both *anti* and *syn* cryptophanes. The *anti* resonance at 7.3 ppm is the main component, with a ratio of *syn:anti* approximated at 1:13, at low concentrations, the *syn* peaks were barely discernible.

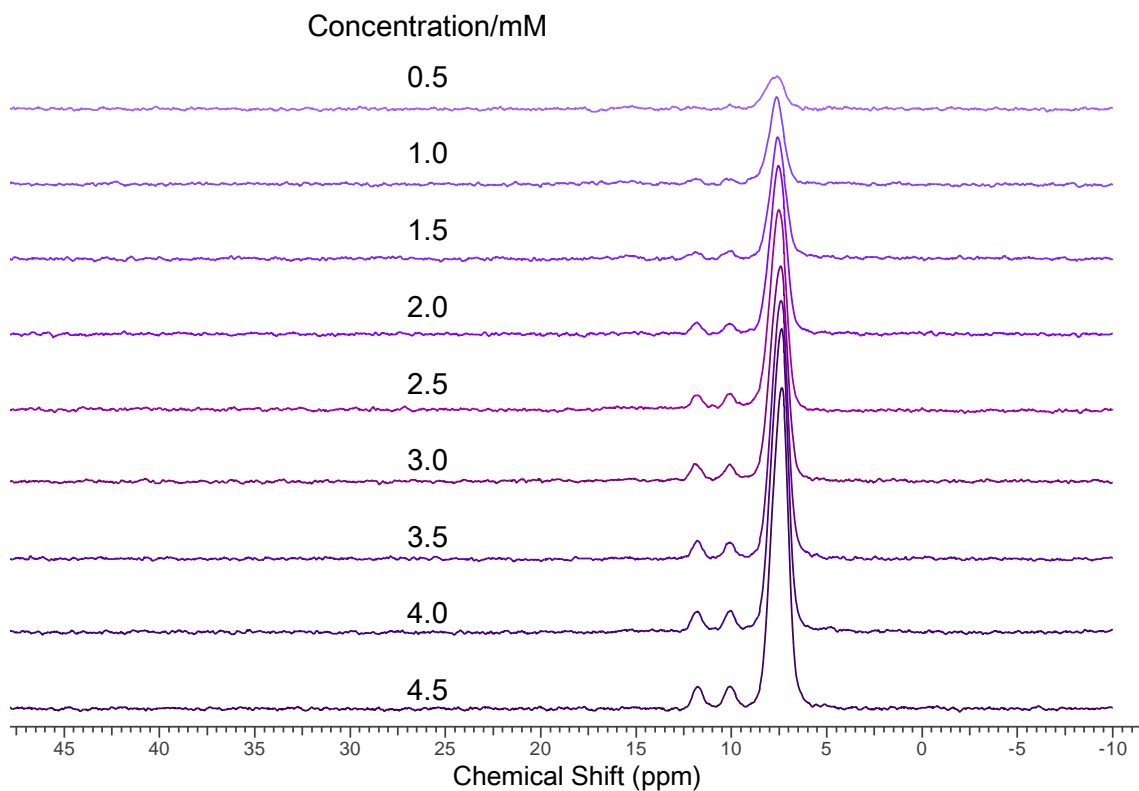


Figure 4.50 ^{31}P NMR spectra of $[\text{Pd}_3(\text{dppp})_3(\text{L}1)_2]^{6+}$ at 0.5 – 4.5 mM.
(300 K, 121 MHz, $d_3\text{-MeNO}_2$)

4.3.3 FL1 + $[\text{Pd}(\text{dppp})]^{2+}$

When [1,3-bis(diphenylphosphino)propane]palladium(II)triflate and **FL1** were combined in a 3:2 ratio in $d_6\text{-DMSO}$, $d_3\text{-MeCN}$ and $d_3\text{-MeNO}_2$, the ^1H NMR spectra indicated the formation of stable metallo-cryptophanes. These cryptophanes showed no changes in their NMR spectra after the initial self-assembly process and like the $[\text{Pd}_3(\text{dppp})_3(\text{L}1)_2]^{6+}$ cryptophanes, the ^1H NMR spectra indicated these complexes were stable when stored at room temperature for over one month. As these complexes looked quite different in $d_6\text{-DMSO}$, $d_3\text{-MeCN}$ and $d_3\text{-MeNO}_2$, they will be described separately for each solvent in the following sections.

4.3.3.1 FL1 + [Pd(dppp)]²⁺ Cryptophanes in d₆-DMSO

When FL1 and [Pd(dppp)]²⁺ were combined in a 2:3 ligand:metal ratio in d₆-DMSO, a sharp, well-resolved ¹H NMR spectrum was observed, as shown in the green trace in Figure 4.51. At first inspection, it appeared to merely be the additive spectra of the cryptophane components. However, all of the peaks showed small chemical shift changes. Only one peak was seen for each of the [Pd(dppp)]²⁺ propylene bridge resonances, signifying that only the *anti* cryptophane was present. This indicates that a highly symmetrical complex had been generated.

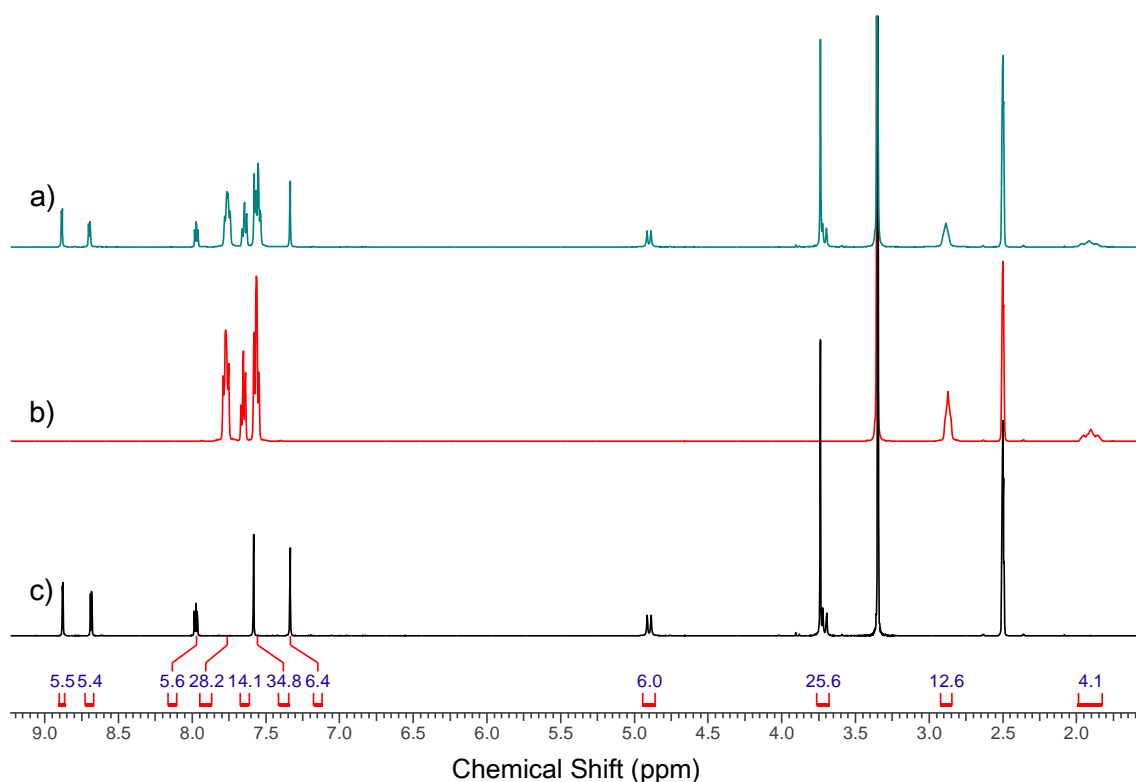


Figure 4.51 ¹H NMR spectra of a) green trace, [Pd₃(dppp)₃(FL1)₂]⁶⁺, b) red trace, [1,3-bis(diphenylphosphino)propane]palladium(II)triflate, c) black trace, FL1. Integrations are shown for [Pd₃(dppp)₃(FL1)₂]⁶⁺. (293 K, 500 MHz, d₆-DMSO)

A section of the aromatic region of the 2-D ROESY spectrum of [Pd₃(dppp)₃(FL1)₂]⁶⁺ is shown in Figure 4.52. As the FL1 ligand is fluorine labelled, it is easier to assign the aromatic region of its complexes when compared with L1. This is also helped by the ¹H

NMR spectrum of $[\text{Pd}_3(\text{dppp})_3(\text{FL1})_2]^{6+}$ being much sharper than that seen for its **L1** analogue (section 4.3.2.1). Clear through-space connections could be seen between H_a and H_b of the **FL1** ligand and H_b of $[\text{Pd}(\text{dppp})]^{2+}$. These connections are illustrated in Figure 4.53, and like the **L1** cryptophanes, no other rOes would be expected.

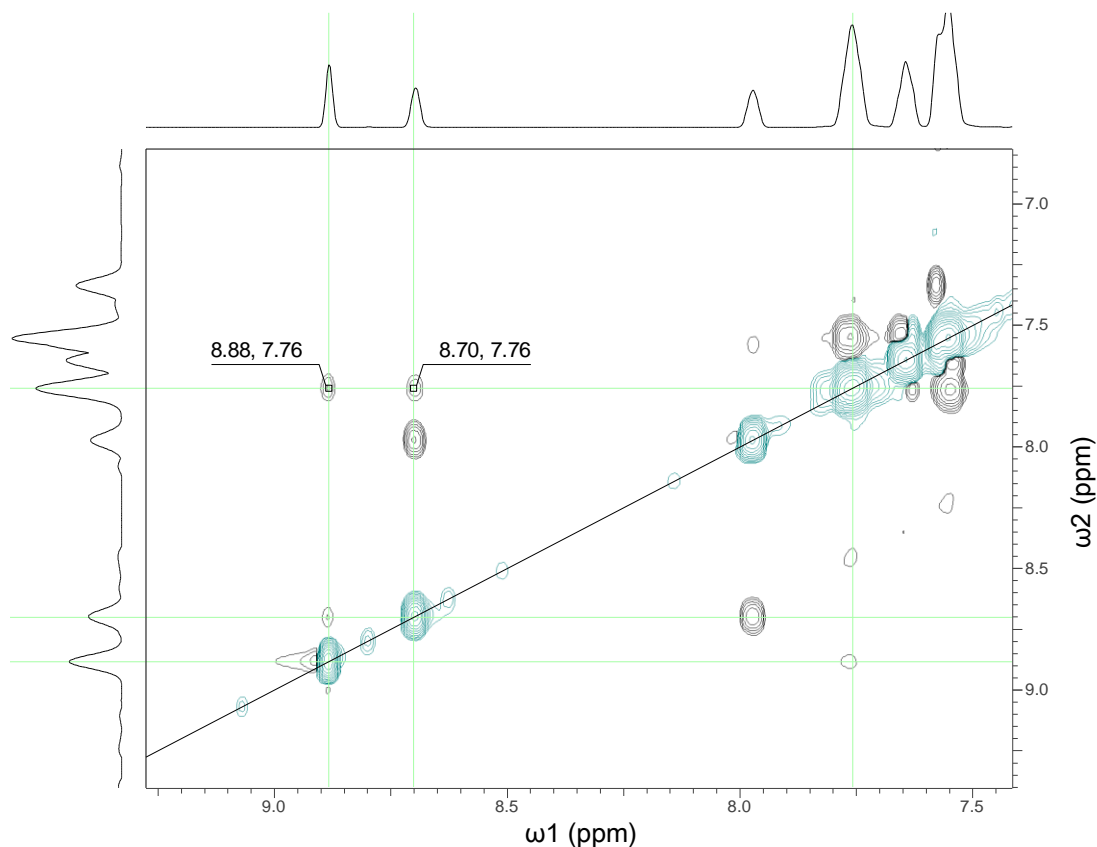


Figure 4.52 Section of ^1H NMR ROESY spectrum of $[\text{Pd}_3(\text{dppp})_3(\text{FL1})_2]^{6+}$, aromatic region showing a weak through-space connections between the H_a and H_b protons of the **FL1** pyridyl group and H_b protons of the phenyl arms of $[\text{Pd}(\text{dppp})]^{2+}$. Exchange peaks are in blue and rOes are in black. (293 K, 500 MHz, d_6 -DMSO)

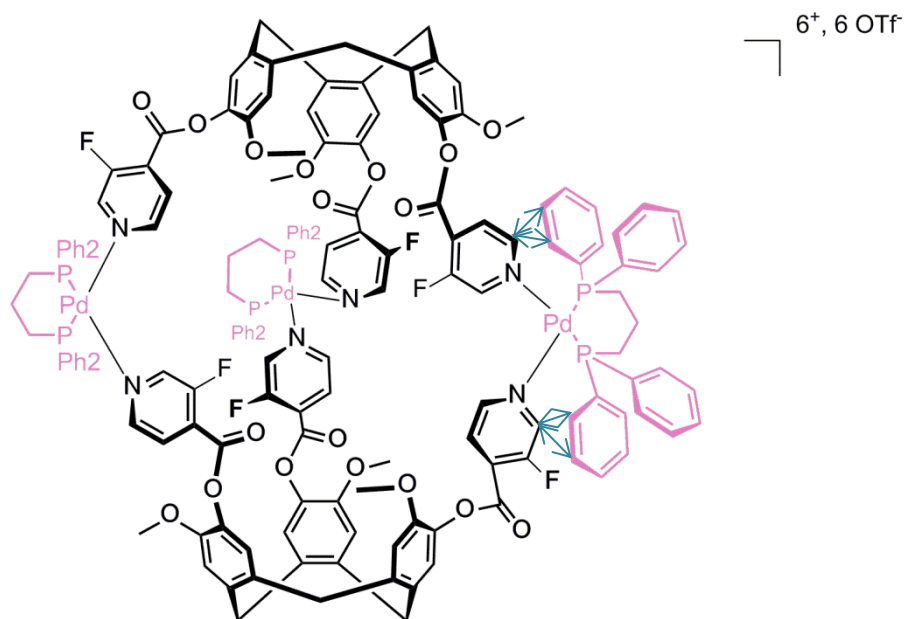


Figure 4.53 $Pd_3(dppp)_3(FL1)_2-6(OTf)$ cryptophane in DMSO, with one $[Pd(dppp)]^{2+}$ group drawn fully to show the through-space connections between Ha/Hb of the FL1 ligand and Hb of $[Pd(dppp)]^{2+}$, which are indicated by the blue arrows.

Electrospray mass spectroscopic analysis of the $[Pd_3(dppp)_3(FL1)_2]^{6+}$ system in d_6 -DMSO showed that it is highly dynamic in the gas phase (Figure 4.54). It was noted that the [1,3-bis(diphenylphosphino)propane]palladium(II)triflate ($[Pd(dppp)]^{2+}$) did not break up in these conditions. A variety of different adducts were observed, with the fragmentation pattern indicating a situation where a $[Pd_3(dppp)_3(FL1)_2]^{6+}$ fragment gained a metal and lost a ligand. For example, the first three entries of Table 4.3, which correspond to the first three peaks in Figure 4.54 were calculated to represent M_2L_5 , M_3L_4 and M_4L_5 fragments. The next three peaks were calculated to represent M_1L_4 , M_2L_3 and M_3L_2 fragments and the last four peaks were calculated to represent M_2L_6 , M_3L_5 , M_4L_4 and M_5L_3 fragments. These last two groups of fragments gained two triflate ions for each ligand gained, but this was not seen for the first group.

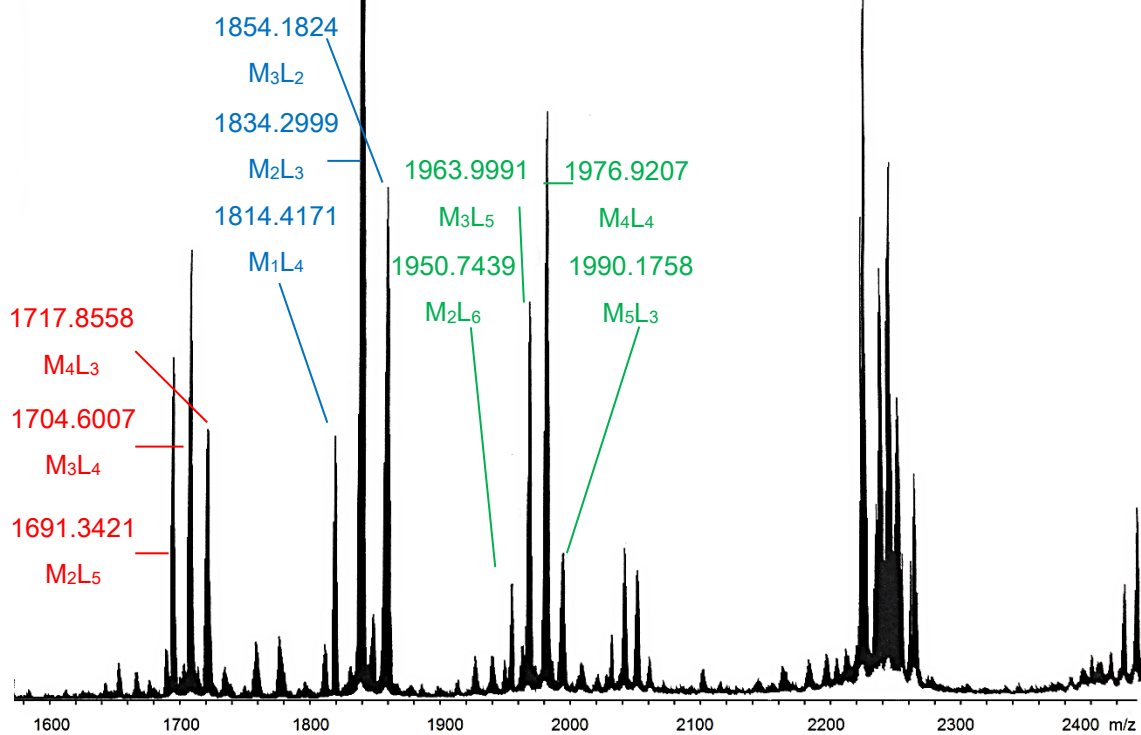


Figure 4.54 ESI-MS of Pd₃(dppp)₃(FL1)₂]·6(CF₃SO₃) cryptophane.

Table 4.3 Table to show calculated and observed m/z for the [Pd₃(dppp)₃(FL1)₂]-6(CF₃SO₃) cryptophane in DMSO.

$\{[(dppp)_3(FL1)_2] \cdot n(CF_3SO_3)\}^{6-n+}$ ion	Calculated <i>m/z</i>	Observed <i>m/z</i>
$\{[Pd_2(dppp)_2(FL1)_5] \cdot (CF_3SO_3)_1\}^{3+}$	1690.3421	1691.6791
$\{[Pd_3(dppp)_3(FL1)_4] \cdot (CF_3SO_3)_5\}^{3+}$	1703.2638	1704.6007
$\{[Pd_4(dppp)_4(FL1)_3] \cdot (CF_3SO_3)_5\}^{3+}$	1716.1855	1717.8558
$\{[Pd_1(dppp)_1(FL1)_4] \cdot (CF_3SO_3)_0\}^{2+}$	1813.4135	1814.4171
$\{[Pd_2(dppp)_2(FL1)_3] \cdot (CF_3SO_3)_2\}^{2+}$	1832.7961	1834.2999
$\{[Pd_3(dppp)_3(FL1)_2] \cdot (CF_3SO_3)_4\}^{2+}$	1852.1786	1854.1824
$\{[Pd_2(dppp)_2(FL1)_6] \cdot (CF_3SO_3)_1\}^{3+}$	1949.4066	1950.7439
$\{[Pd_3(dppp)_3(FL1)_5] \cdot (CF_3SO_3)_3\}^{3+}$	1962.3283	1963.9991
$\{[Pd_4(dppp)_4(FL1)_4] \cdot (CF_3SO_3)_5\}^{3+}$	1975.2500	1976.9207
$\{[Pd_6(dppp)_5(FL1)_3] \cdot (CF_3SO_3)_7\}^{3+}$	1988.1717	1990.1758

When [Pd₃(dppp)₃(FL1)₂]⁶⁺ in *d*₆-DMSO was studied in the range 0.5 – 5.0 mM (Figure 4.55), the complex appeared unchanged. However, on closer inspection, the chemical shifts of the [Pd₃(dppp)₃(FL1)₂]⁶⁺ complex shifted further away from the chemical shifts of uncomplexed FL1 and [Pd(dppp)]²⁺ as the concentration of [Pd₃(dppp)₃(FL1)₂]⁶⁺ was increased. At 0.5 mM, the [Pd₃(dppp)₃(FL1)₂]⁶⁺ complex chemical shifts were similar to that of the uncomplexed components. At low concentrations, the [Pd(dppp)]²⁺ propylene bridge protons, Hd [Figure 4.55 b)], resonated as two multiplets, indicative of the slow exchange dynamics of the [Pd(dppp)]²⁺ diphosphine six-membered ring. As the concentration increased, the peaks broadened and coalesced into a broad singlet.

This showed that the exchange regime increased in rate as the concentration of $[\text{Pd}_3(\text{dppp})_3(\text{FL1})_2]^{6+}$ was increased.

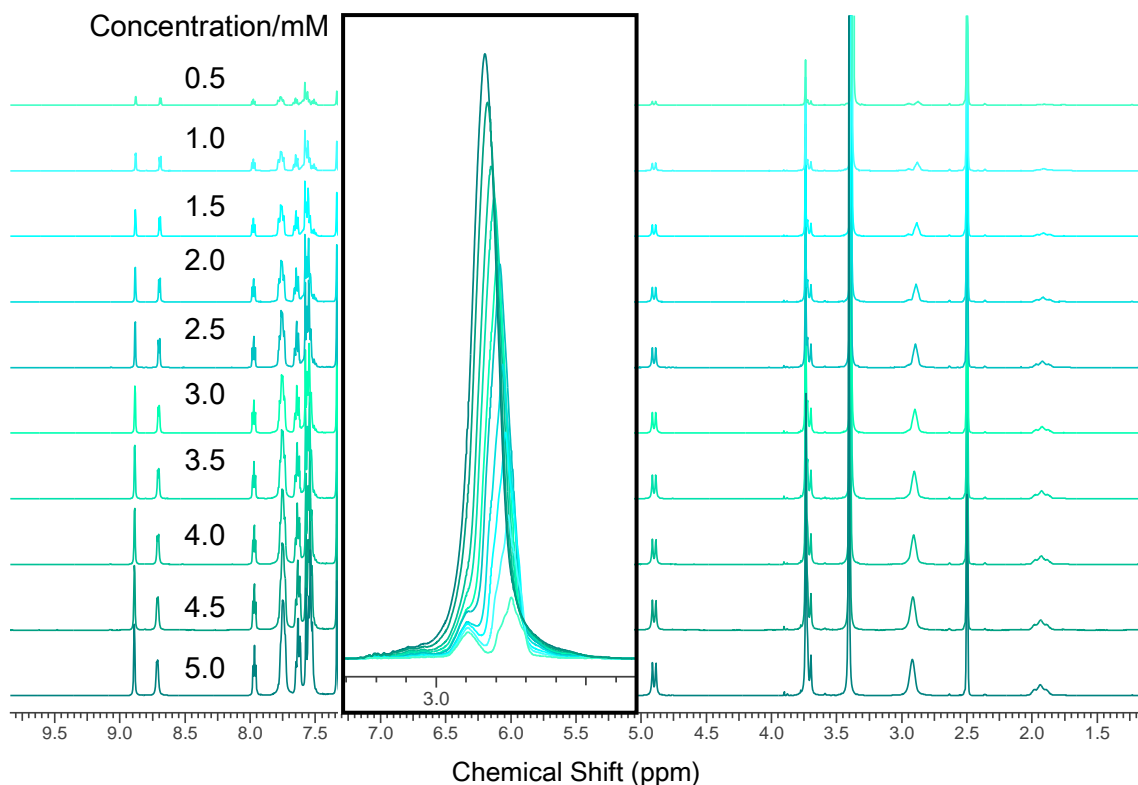


Figure 4.55 ^1H NMR spectra of $[\text{Pd}_3(\text{dppp})_3(\text{FL1})_2]^{6+}$ at 0.5 – 5.0 mM. Inset spectra show the superimposed stacked plot of the Hd peaks. (293 K, 500 MHz, d_6 -DMSO)

The ^{19}F NMR spectra of $[\text{Pd}_3(\text{dppp})_3(\text{FL1})_2]^{6+}$ in d_6 -DMSO from 0.5 – 5.0 mM is shown in Figure 4.56. Just one fluorine peak was seen. As the concentration was increased, the peak shifted slightly downfield and broadened significantly.

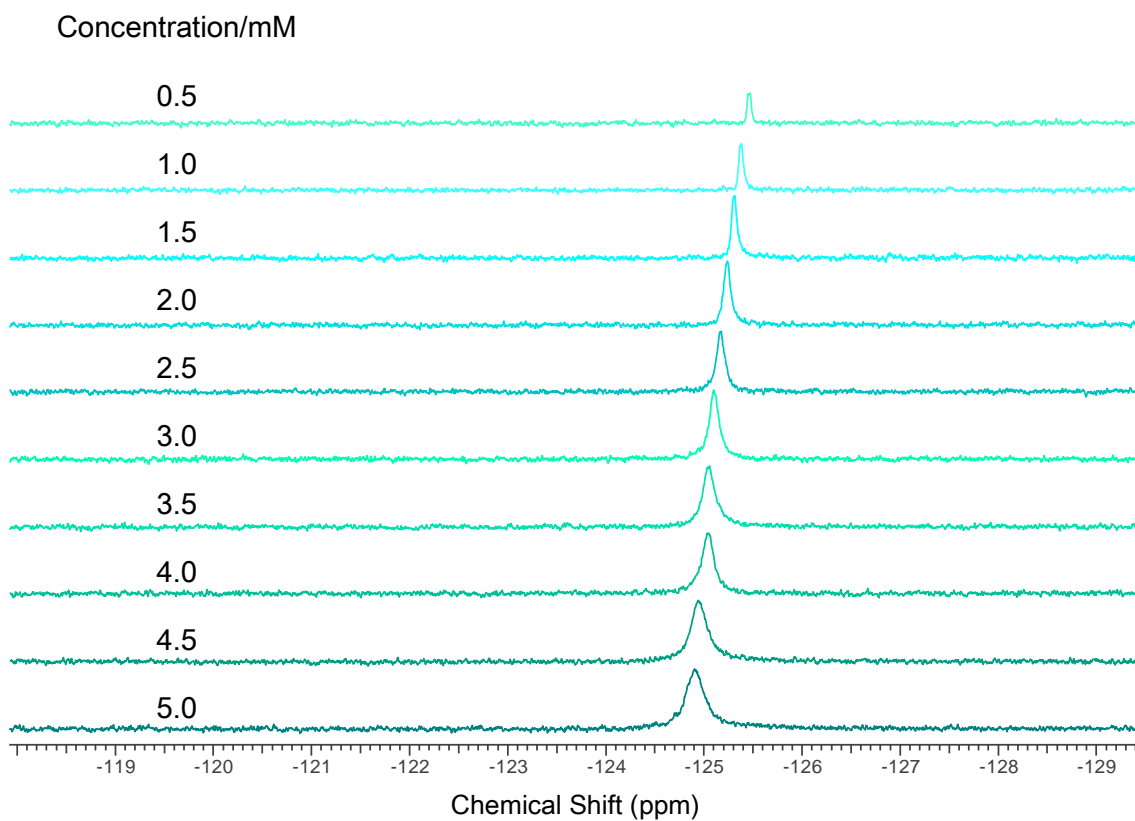


Figure 4.56 ^{19}F NMR spectra of $[\text{Pd}_3(\text{dppp})_3(\text{FL1})_2]^{6+}$ at 0.5 – 5.0 mM.
(299 K, 282 MHz, d_6 -DMSO)

The ^{31}P NMR spectra of the concentration study of $[\text{Pd}_3(\text{dppp})_3(\text{FL1})_2]^{6+}$ are shown in Figure 4.57. There was one $[\text{Pd}(\text{dppp})]^{2+}$ peak at 15.6 ppm and the contaminant peak at 10.0 ppm, as discussed in section 4.3.1. This is indicated that of only one phosphorous environment, indicative of the *anti* cryptophane enantiomer present in solution.

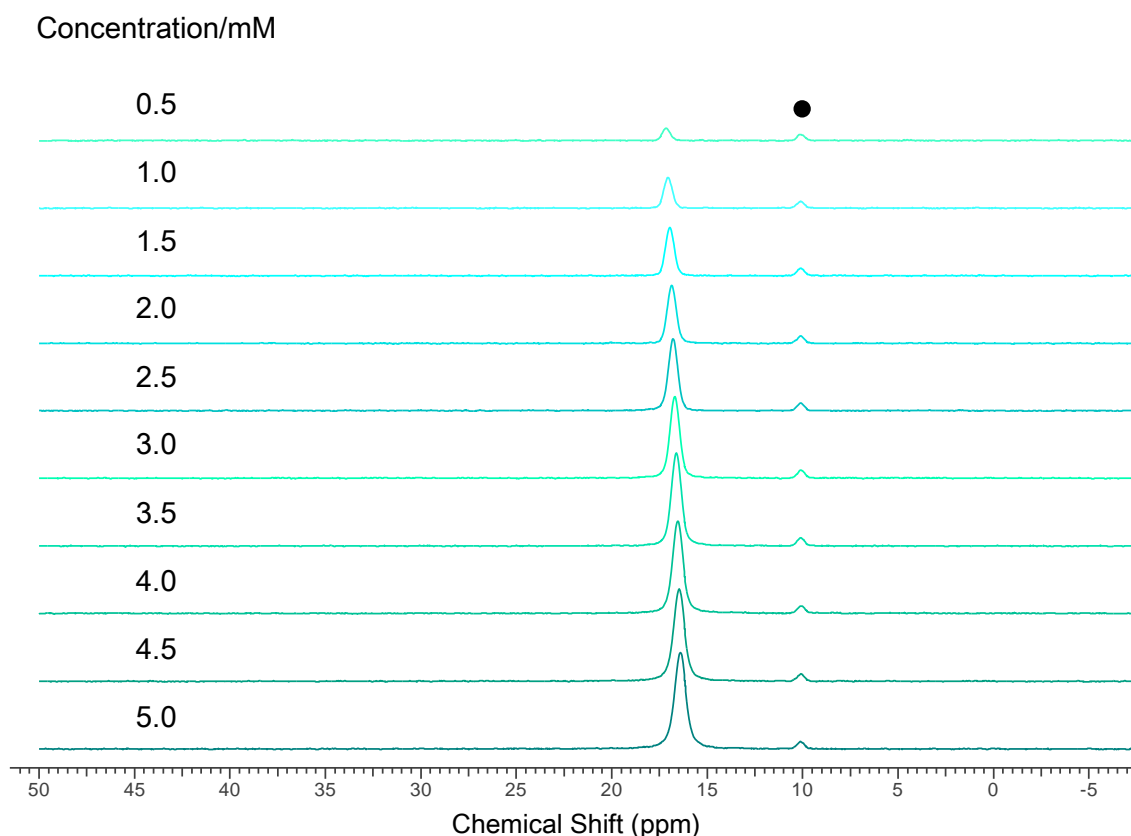


Figure 4.57 ^{31}P NMR spectra of $[\text{Pd}_3(\text{dppp})_3(\text{FL1})_2]^{6+}$ at 0.5 – 5.0 mM. (•) black dot indicates contaminant in d_6 -DMSO. (300 K, 121 MHz, d_6 -DMSO)

The 0.5 mM $[\text{Pd}_3(\text{dppp})_3(\text{FL1})_2]^{6+}$ sample was subjected to a VT experiment. The resultant spectra are shown in Figure 4.58. At 25° two peaks for both Hd and He of $[\text{Pd}(\text{dppp})]^{2+}$ were observed. As the sample was heated to 75°C, no change was observed in these peaks. The only change seen was that of the FL1 He peak, which is one of the protons on the aromatic ring of the FL1. The peak shifted considerably upfield as the temperature was increased. However when the sample is cooled back down to 25°C, the spectrum recorded is the same as the original spectrum at 25°C (top and bottom traces of Figure 4.58).

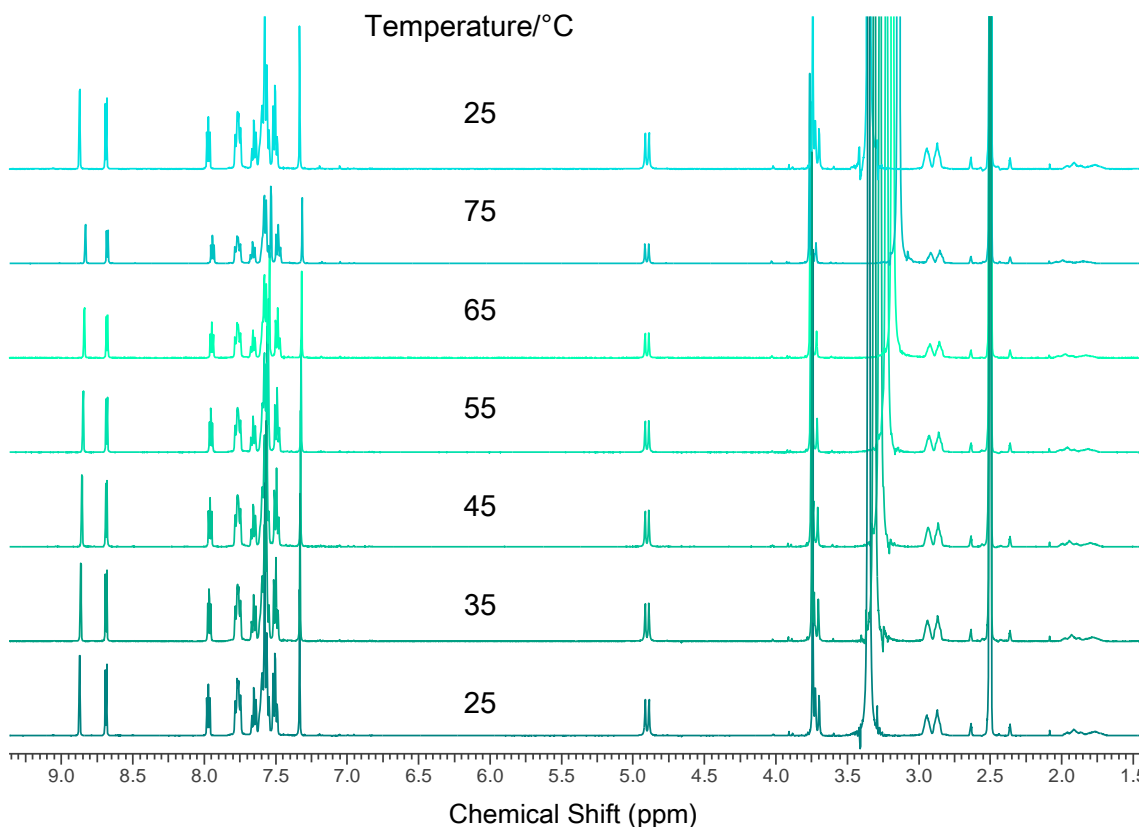


Figure 4.58 ^1H NMR spectra of 0.5 mM $[\text{Pd}_3(\text{dppp})_3(\text{FL1})_2]^{6+}$ at 298 - 348 K. The top spectrum was recorded after the sample had cooled to 25°C after heating. (500 MHz, d_6 -DMSO)

4.3.3.2 FL1 + $[\text{Pd}(\text{dppp})]^{2+}$ Cryptophanes in d_3 -MeCN

When FL1 and $[\text{Pd}(\text{dppp})]^{2+}$ were added in a 2:3 ligand to metal ratio in d_3 -acetonitrile, a sharp, well resolved ^1H NMR spectrum was observed, as seen in the pink trace of Figure 4.59. At first inspection the spectrum appeared to be the superposition of the FL1 and $[\text{Pd}(\text{dppp})]^{2+}$ components. Unlike the analogous L1 cryptophane in acetonitrile (section 4.3.2.2), in which the $[\text{Pd}(\text{dppp})]^{2+}$ aromatic peaks were split into three peaks, (Figure 4.39), in the $[\text{Pd}_3(\text{dppp})_3(\text{FL1})_2]^{6+}$ complex, this did not happen.

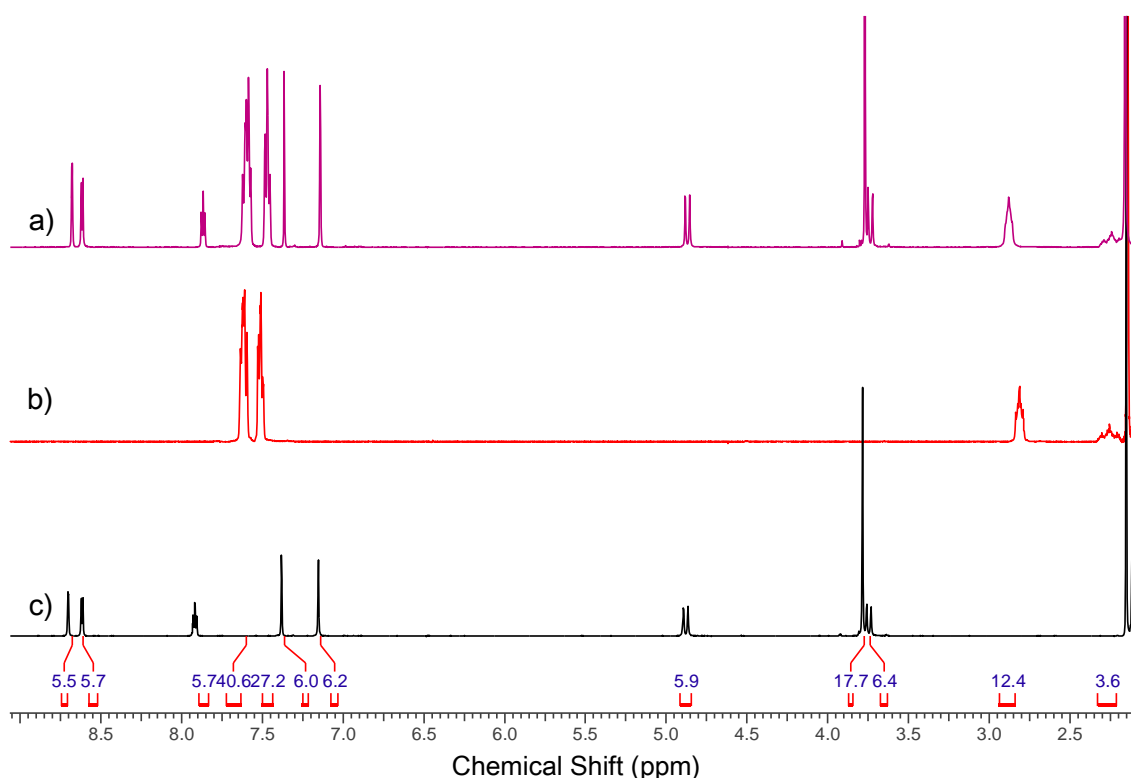


Figure 4.59 ^1H NMR spectra of a) pink trace, $[\text{Pd}_3(\text{dppp})_3(\text{FL}1)_2]^{6+}$, b) red trace, $[1,3\text{-bis(diphenylphosphino)propane}]\text{palladium(II)triflate}$, c) black trace, FL1. Integrations are shown for $[\text{Pd}_3(\text{dppp})_3(\text{FL}1)_2]^{6+}$. (293 K, 500 MHz, $d_3\text{-MeCN}$)

A 2-D ROESY was recorded for $[\text{Pd}_3(\text{dppp})_3(\text{FL}1)_2]^{6+}$ complex in $d_3\text{-acetonitrile}$. No through-space connections between FL1 and $[\text{Pd}(\text{dppp})]^{2+}$ were observed. The only rOes seen were intermolecular connections within the FL1 ligand and intermolecular connections between $[\text{Pd}(\text{dppp})]^{2+}$.

The $[\text{Pd}_3(\text{dppp})_3(\text{FL}1)_2]^{6+}$ complex in $d_3\text{-acetonitrile}$ was investigated in the range 0.5 - 5.0 mM. The spectra for this experiment are shown in Figure 4.60. At low concentrations, the spectra resembled the superposition of FL1 and $[\text{Pd}(\text{dppp})]^{2+}$. As the concentration of $[\text{Pd}_3(\text{dppp})_3(\text{FL}1)_2]^{6+}$ was increased, some slight peak broadening was observed, as well as changes to the chemical shifts. The most noticeable change in the spectra were seen for the $[\text{Pd}(\text{dppp})]^{2+}$ aromatic peaks: as the concentration was increased, the multiplet that represents the Hb and Ha protons started to split into two separate resonances.

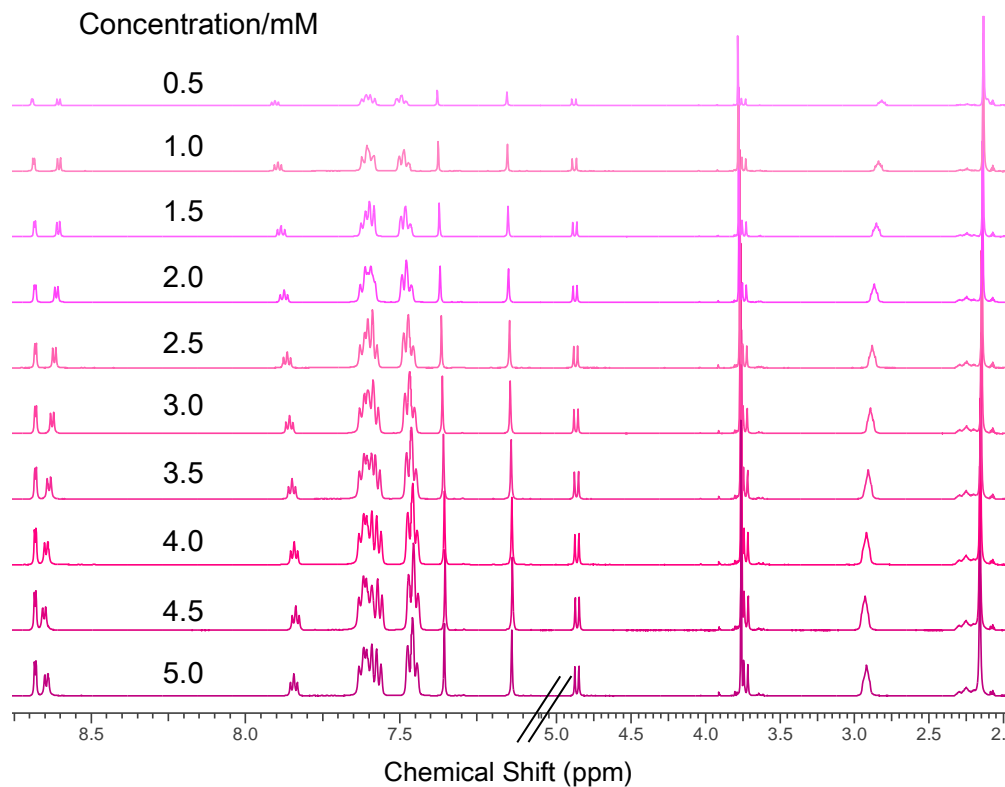


Figure 4.60 ^1H NMR spectra of $[\text{Pd}_3(\text{dppp})_3(\text{FL1})_2]^{6+}$ at 0.5 – 5.0 mM.
(293 K, 500 MHz, d_3 -MeCN)

The ^{19}F NMR spectra for the $[\text{Pd}_3(\text{dppp})_3(\text{FL1})_2]^{6+}$ complex in d_3 -acetonitrile in the concentration range 0.5 – 5.0 mM is shown in Figure 4.61. These data were collected using broadband decoupling, so that just information regarding the fluorine environments was acquired. At 0.5 mM a sharp singlet was observed. As the concentration was increased, this peak shifted downfield and broadened considerably.

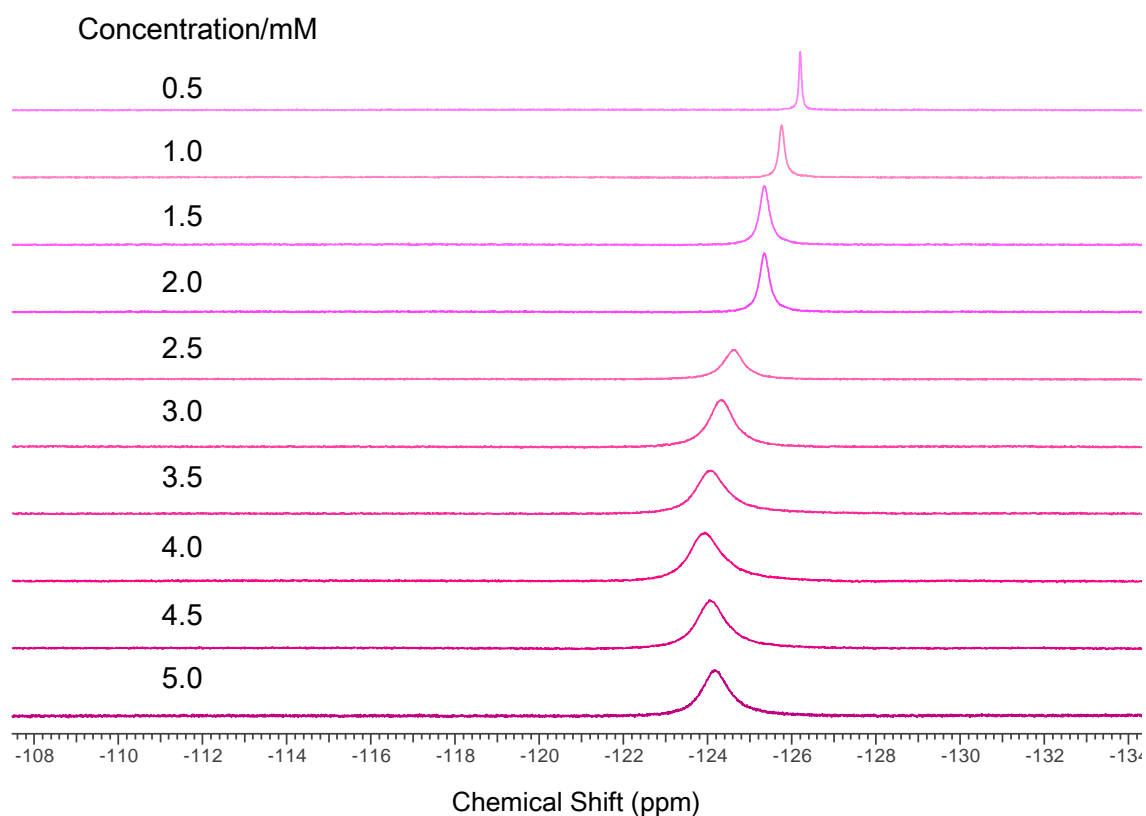


Figure 4.61 ^{19}F – $\{^1\text{H}\}$ NMR spectra of $[\text{Pd}_3(\text{dppp})_3(\text{FL1})_2]^{6+}$ at 0.5 – 5.0 mM.
(299 K, 282 MHz, d_3 -MeCN)

The ^{31}P NMR spectra for the $[\text{Pd}_3(\text{dppp})_3(\text{FL1})_2]^{6+}$ complex in d_3 -acetonitrile in the concentration range 0.5 – 5.0 mM are shown in Figure 4.62. Only one phosphorus environment was observed, indicative of only *anti* cryptophanes being present in solution.

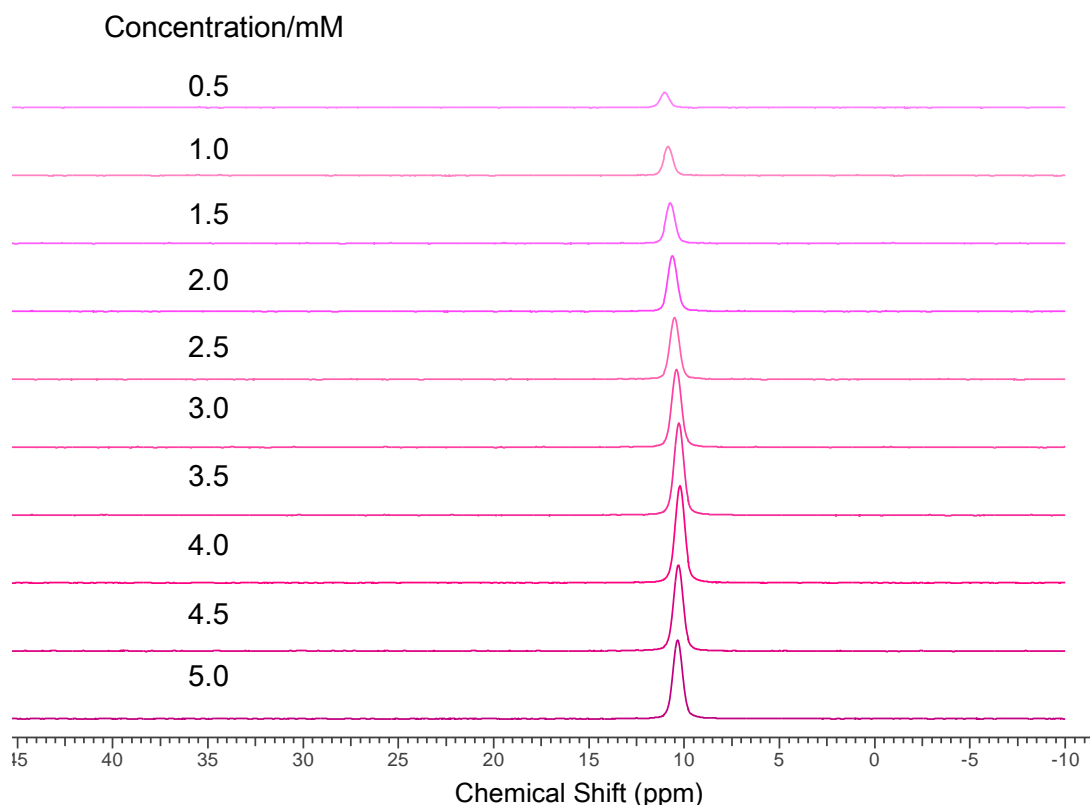


Figure 4.62 ^{31}P NMR spectra of $[\text{Pd}_3(\text{dppp})_3(\text{FL1})_2]^{3+}$ at 0.5 – 5.0 mM.
(300 K, 121 MHz, d_3 -MeCN)

Single crystals of $[\text{Pd}_3(\text{dppp})_3(\text{FL1})_2] \cdot 6(\text{OTf})$ in acetonitrile were grown by diffusion of diethyl ether vapours. The crystals were of poor quality, with poor internal consistency and only exhibited weak diffraction, with no diffraction observed at high angles. Despite multiple attempts, higher quality crystals could not be grown. The structure was solved in the triclinic space group $P\bar{1}$. The crystals have approximate C_3 symmetry, but crystallographic symmetry was not observed, as the carbonyl groups of the **FL1** ligands were facing in different directions, as seen in Figure 4.63. The fluorines were ordered and all pointed in the same direction, illustrated in Figure 4.63 a) and b). The palladium had the expected square planar geometry, with inter-metallic Pd \cdots Pd distances of 18 Å. The diphosphine ligands formed a six-membered ring with the palladium, which displayed the chair conformation, illustrated in Figure 4.63. The distance measured between the basal hydrogens of the two **FL1** ligands was 15.6 Å. The equatorial radius

was measured at 14.9 Å, which gave the static cage dimensions of 15.6 × 29.8 Å and an oblate spheroid shape. The crystals showed the achiral *meso* conformation, which were comprised of both *M* and *P* FL1 ligand enantiomers.

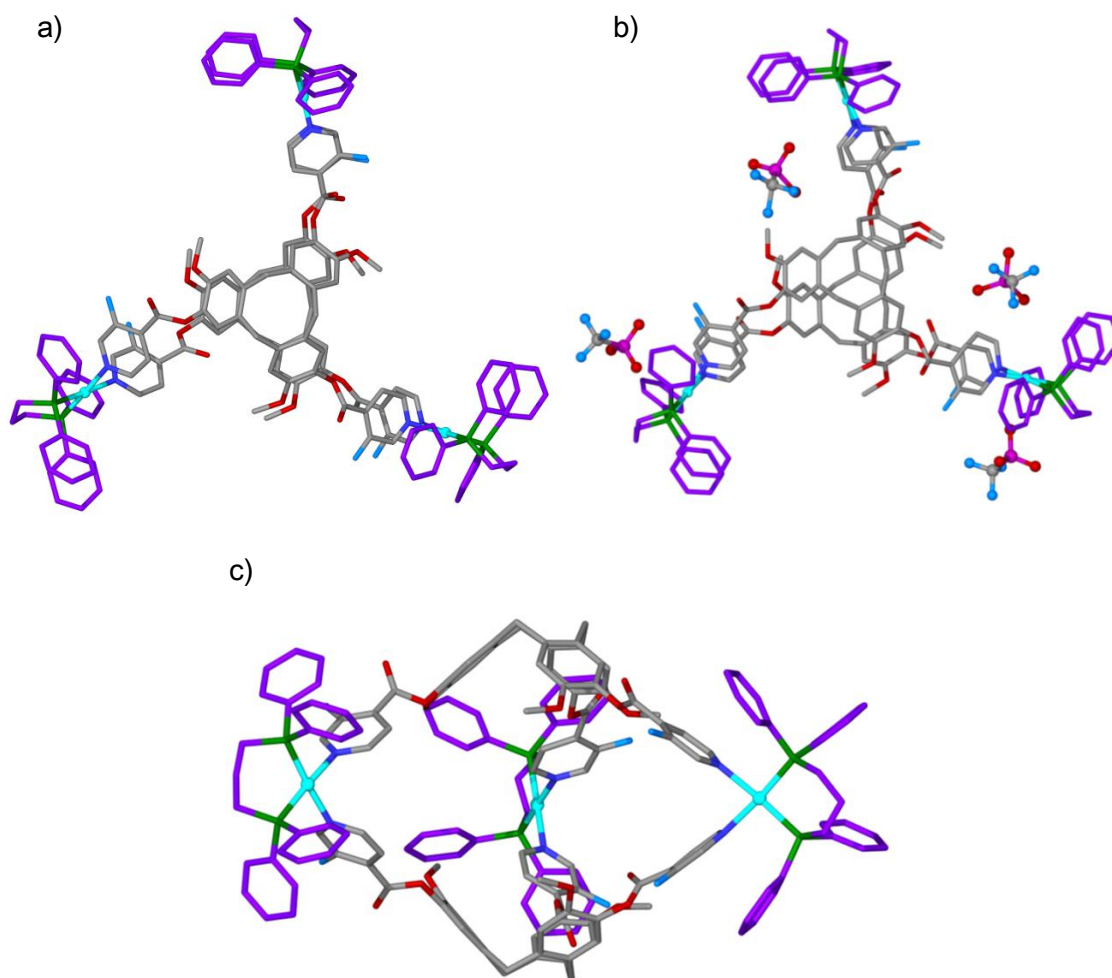


Figure 4.63 From the crystal structure of complex $[Pd_3(dppp)_3(FL1)_2] \cdot 6(OTf)$, FL1 ligands in grey and $[Pd(dppp)]^{2+}$ shown in purple, a) as viewed from the top, b) as viewed from the top with the four triflate anions that have been located, c) as viewed from the side.

Through second-sphere interactions, the triflate anions formed electrostatic associations with the palladium(II) centres, with separations of 2.9, 3.5, 4.0 and 4.2 Å. This is illustrated in Figure 4.64. Only four of the six triflate counter-ions could be located within the structure.

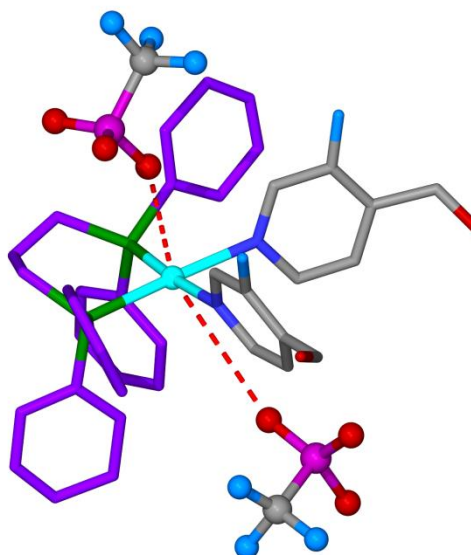


Figure 4.64 From the crystal structure of complex $[Pd_3(dppp)_3(FL1)_2] \cdot 6(OTf)$. One $[Pd(dppp)]^{2+}$ arm showing the second-sphere coordination between the triflate anion and palladium(II) centres.

One of the FL1 ligands experienced π - π stacking between its pyridyl groups and one phenyl arm of each $[Pd(dppp)]^{2+}$, with centroid separations measured at 3.4, 3.6 and 3.7 Å. Due to the size of the six-membered diphosphine rings, $[Pd(dppp)]^{2+}$ was not large enough to experience this interaction with both FL1 ligands. This can be seen in the space-filling model of Figure 4.65 a): on the $[Pd(dppp)]^{2+}$ displayed on the left-hand side, in which the lower phenyl arm can be seen in close proximity to the nearby pyridyl of the FL1 ligand, the torsion of the six-membered ring causes the upper phenyl arm to be held away from the pyridyl group closest to it. The space-filling model also displays the large cavity present in the cryptophane. The packing diagram shown in Figure 4.65 b), shows the cryptophanes packed into a large open framework.

a)

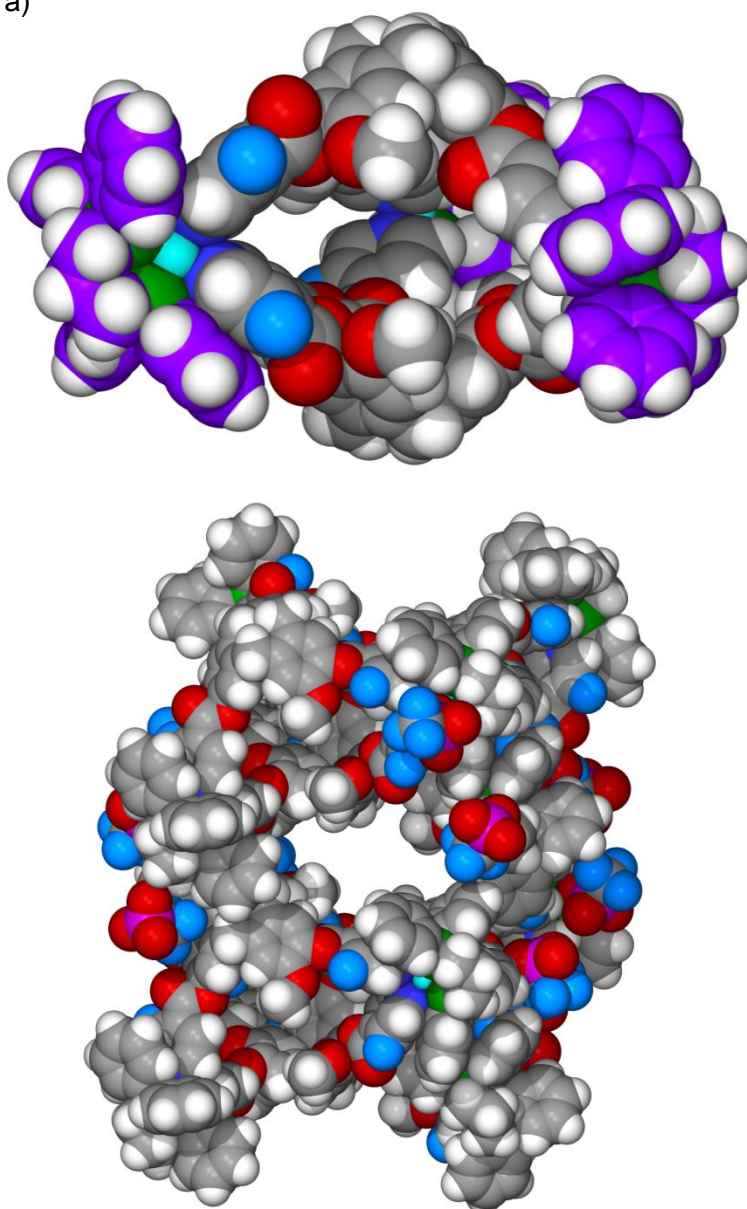


Figure 4.65 a) From the crystal structure of $[Pd_3(dppp)_3(FL1)_2] \cdot 6(OTf)$, a) side view displaying the large cavity. The FL1 ligand is shown in grey and $[Pd(dppp)]^{2+}$ in purple, b) packing diagram of $[Pd_3(dppp)_3(FL1)_2] \cdot 6(OTf)$. The cryptophane is displayed in space-filling mode, with solvent and OTf anions omitted for clarity.

4.3.3.3 FL1 + $[Pd(dppp)]^{2+}$ Cryptophanes in d_3 -MeNO₂

When FL1 and $[Pd(dppp)]^{2+}$ were combined in a 2:3 ligand:metal ratio in d_3 -MeNO₂, a well-resolved ¹H NMR spectrum was observed (Figure 4.66). The FL1 pyridyl Ha and Hb peaks shifted downfield and broadened, indicative of complexation. The

$[\text{Pd}(\text{dppp})]^{2+}$ resonances of the propylene bridge also broadened and shifted considerably downfield, by 0.42 ppm. The spectrum was indicative of only the *anti* conformation being present in d_3 -nitromethane solution, as there was only one resonance for each of the $[\text{Pd}(\text{dppp})]^{2+}$ propylene bridge protons Hd and He.

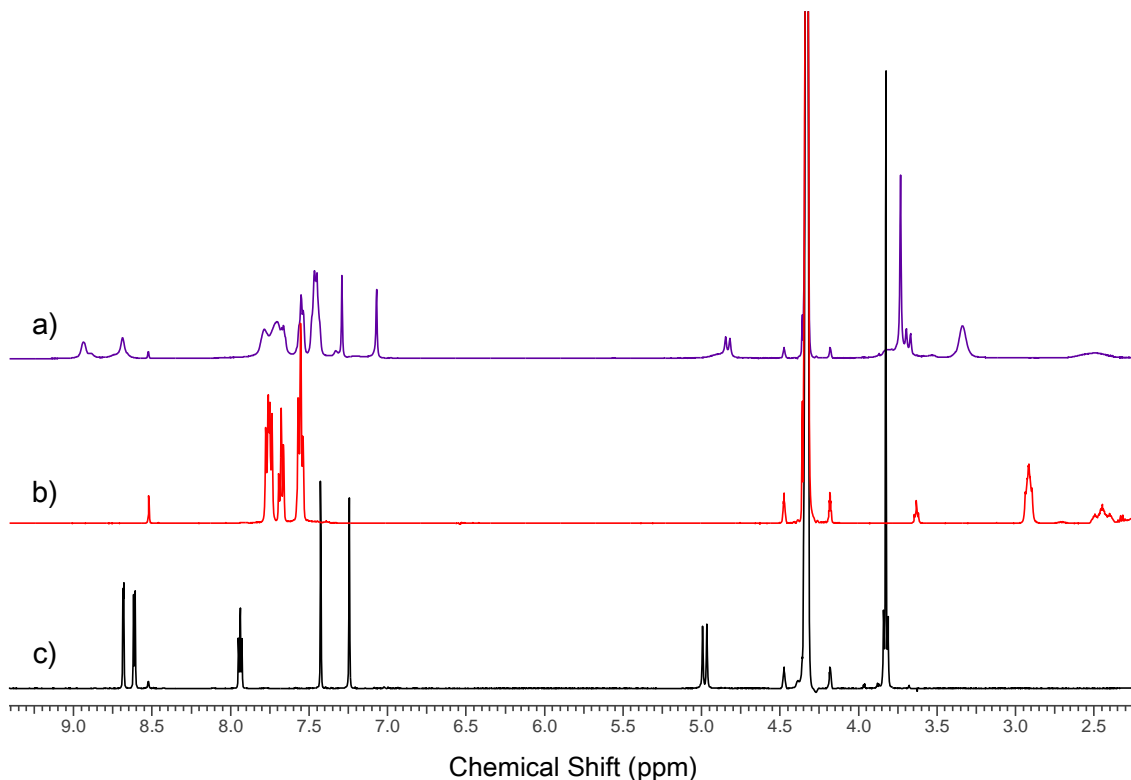


Figure 4.66 ^1H NMR spectra of a) purple trace, $[\text{Pd}_3(\text{dppp})_3(\text{FL1})_2]^{2+}$, b) red trace, $[\text{1,3-bis(diphenylphosphino)propane}]\text{palladium(II)triflate}$, c) black trace, FL1. (293 K, 500 MHz, $d_3\text{-MeNO}_2$)

2-D ROESY NMR analysis of $[\text{Pd}_3(\text{dppp})_3(\text{FL1})_2]\cdot 6(\text{OTf})$ in d_3 -nitromethane provided further evidence of complex formation (Figure 4.67), with through-space connections observed between Hb of the $[\text{Pd}(\text{dppp})]^{2+}$ and Hb of the FL1 pyridyl groups. The through-space connections observed are listed and assigned in Table 4.4. It was noted that the resonance for the Hb protons of $[\text{Pd}(\text{dppp})]^{2+}$ appeared to be split into two resonances in the region of 7.7 ppm. This was confirmed by 2-D HMQC analysis (appendix A.3). The through-space connections are illustrated in Figure 4.68.

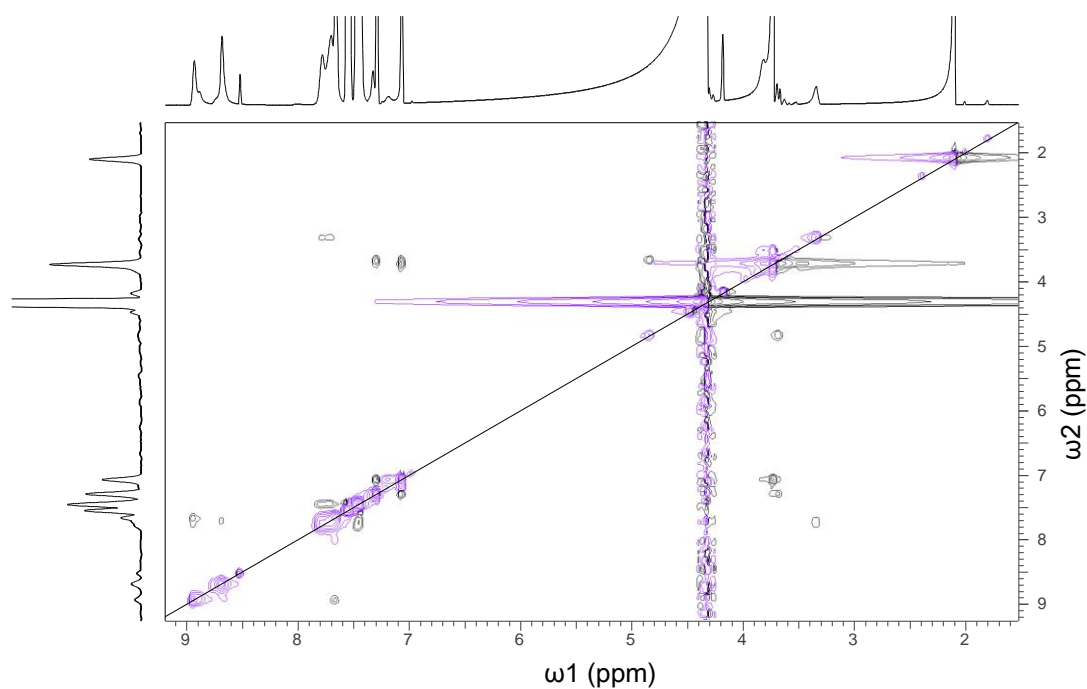


Figure 4.67 ^1H NMR ROESY spectrum of $[\text{Pd}_3(\text{dppp})_3(\text{FL}1)_2]\text{P}^+$. Exchange peaks are in purple and rOes are in black. (293 K, 500 MHz, $d_3\text{-MeNO}_2$)

Table 4.4 Table of through-space connections and assignments for $[\text{Pd}_3(\text{dppp})_3(\text{FL}1)_2](\text{OTf})_6$ cryptophane in $d_3\text{-MeNO}_2$. L1 listed on black and $[\text{Pd}(\text{dppp})]\text{P}^+$ listed in red.

Through-space Connection/ppm	Assignment
3.68, 4.85	H _{exo} -H _{endo}
3.68, 7.07	H _{exo} -He
3.68, 7.29	H _{exo} -Hd
7.45, 7.71	Hc-Hb
7.45, 7.80	Hc-Hb
7.66, 8.94	Hc-Ha
8.67, 7.71	Hb-Hb

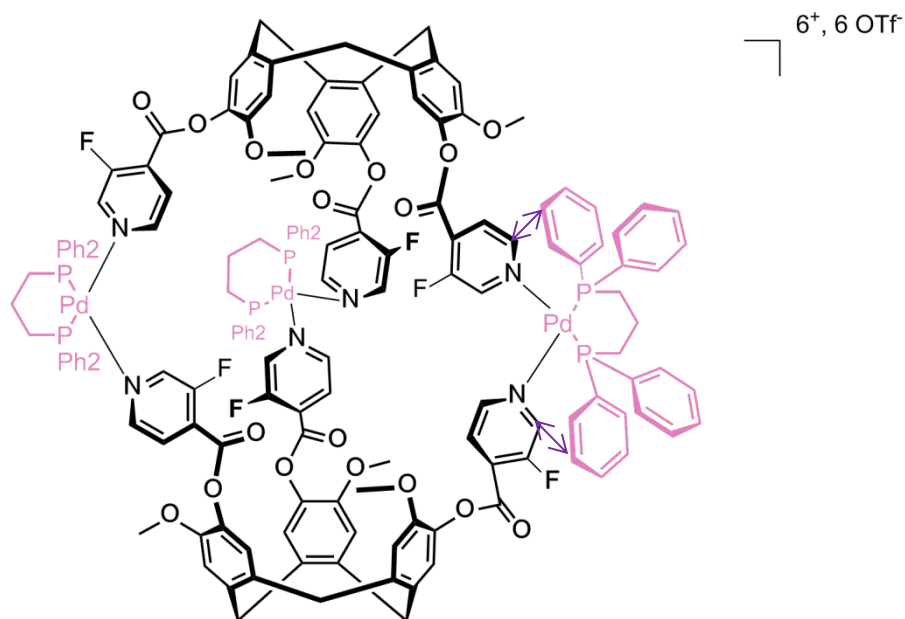


Figure 4.68 $\text{Pd}_3(\text{dppp})_3(\text{FL1})_2 \cdot 6(\text{OTf})$ cryptophane in MeNO_2 , with one $[\text{Pd}(\text{dppp})]^{2+}$ group drawn fully to show the through-space connections between Hb of the FL1 ligand and Hb of $[\text{Pd}(\text{dppp})]^{2+}$, which are indicated by the purple arrows.

When the $[\text{Pd}_3(\text{dppp})_3(\text{FL1})_2] \cdot 6(\text{OTf})$ cryptophane in α_3 -nitromethane was studied in the range 0.5 – 5.0 mM (Figure 4.69), no change in the conformation of the cryptophane was seen. The only change observed was that of the overlapping $[\text{Pd}(\text{dppp})]^{2+}$ Hb and FL1 Hc peaks at 7.7 ppm, which appeared to move apart as the concentration of $[\text{Pd}_3(\text{dppp})_3(\text{FL1})_2]^{6+}$ was increased. The ^{31}P NMR spectra (Figure 4.70) also indicate that the only conformation seen for $[\text{Pd}_3(\text{dppp})_3(\text{FL1})_2] \cdot 6(\text{OTf})$ in α_3 -nitromethane was the *anti* isomer, with only one peak being observed throughout this concentration range.

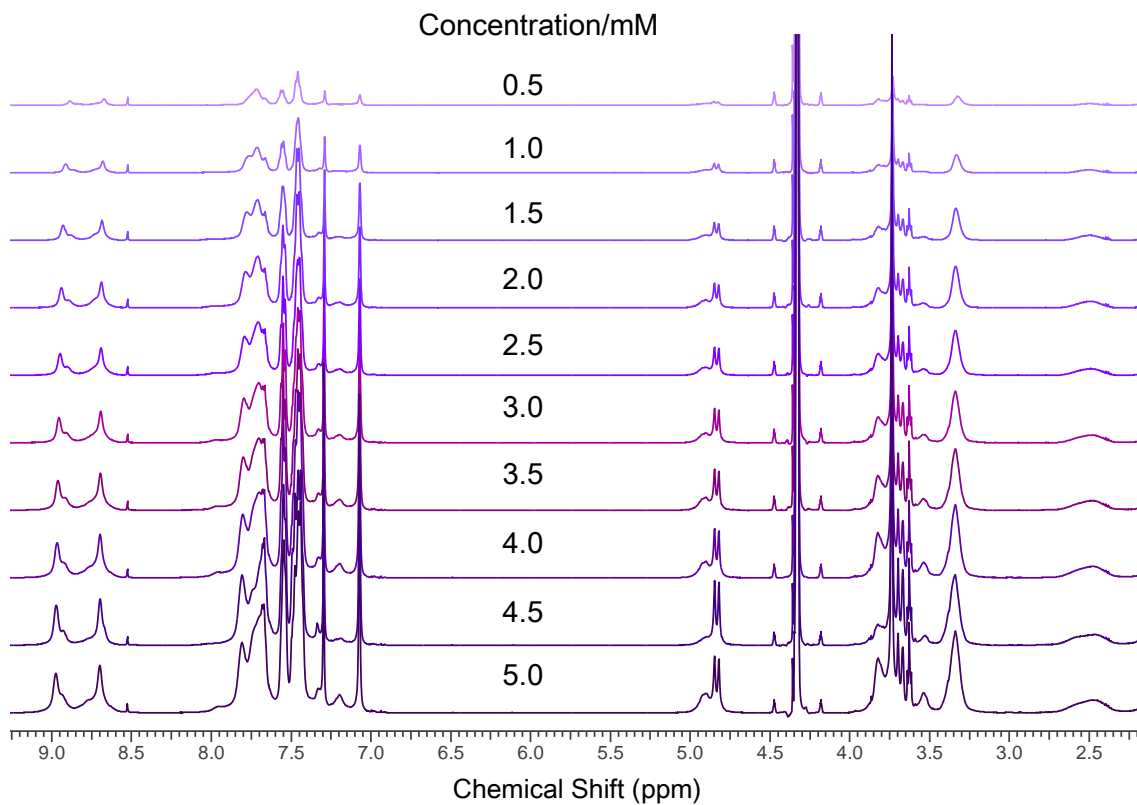


Figure 4.69 ^1H NMR spectra of $[\text{Pd}_3(\text{dppp})_3(\text{FL}1)_2]^{6+}$ at 0.5 – 5.0 mM.
(293 K, 500 MHz, $d_3\text{-MeNO}_2$)

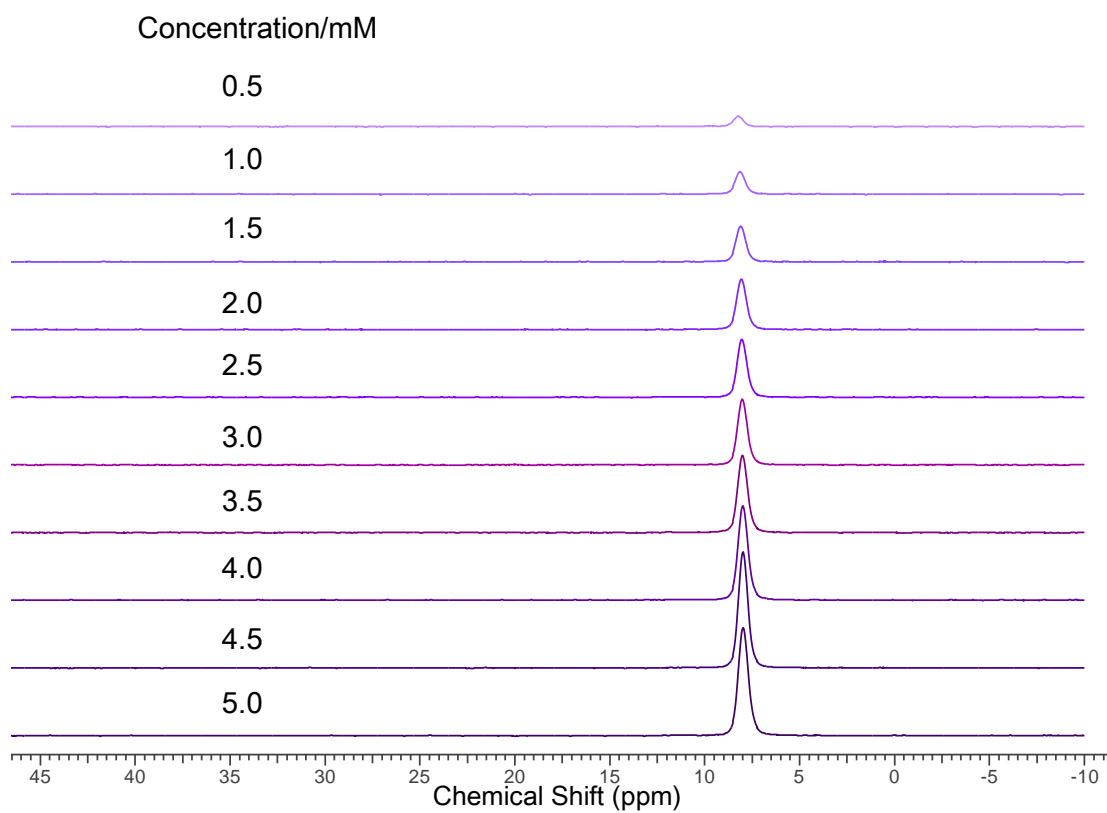


Figure 4.70 ^{31}P NMR spectra of $[\text{Pd}_3(\text{dppp})_3(\text{FL}1)_2]^{6+}$ at 0.5 – 5.0 mM.
(300 K, 121 MHz, $d_3\text{-MeNO}_2$)

The broadband decoupled ^{19}F NMR spectra of $[\text{Pd}_3(\text{dppp})_3(\text{FL1})_2]^{6+}$ in the concentration range 0.5 – 5 mM, shown in Figure 4.71 revealed that at least 5 different fluorine environments were found in d_3 -nitromethane, with the most intense and sharpest peak at -120.2 ppm. This indicated that the fluorines were not orientated in the same way as each other. These environments did not change as the concentration was varied, indicating that the same cryptophane conformation was held throughout.

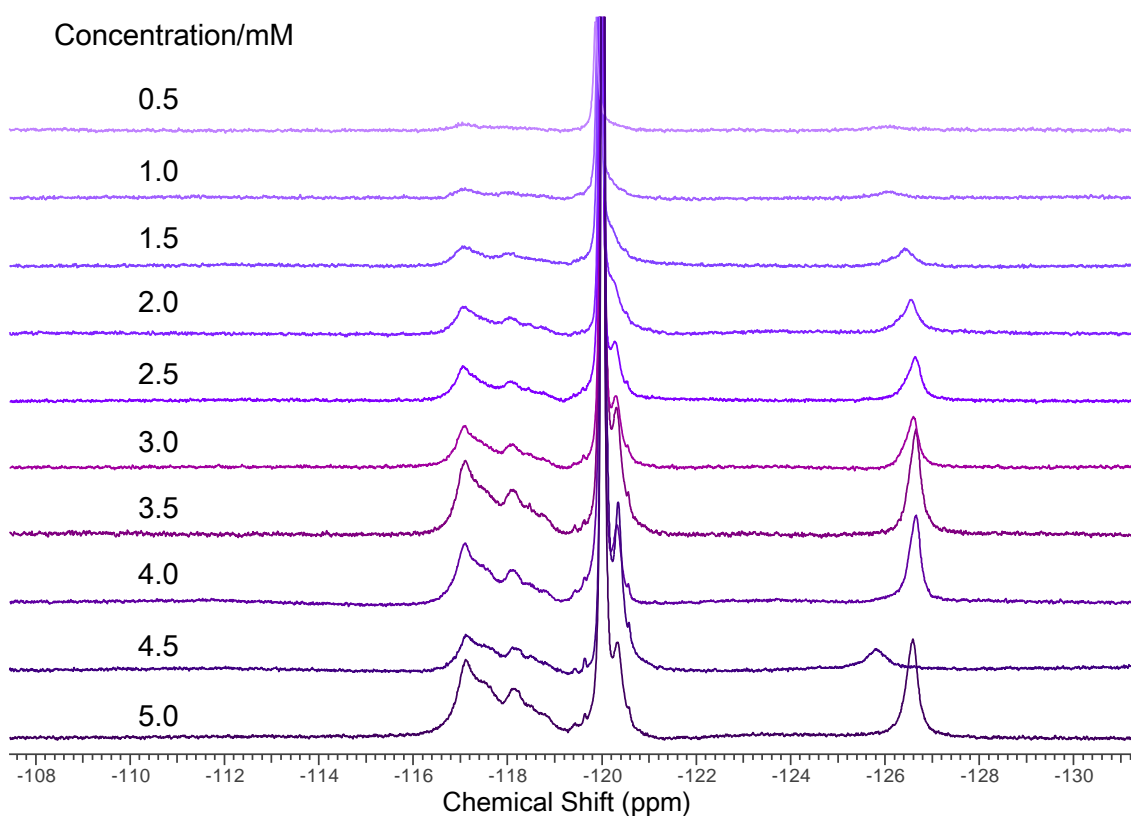


Figure 4.71 ^{19}F $\{^1\text{H}\}$ NMR spectra of $[\text{Pd}_3(\text{dppp})_3(\text{FL1})_2]^{6+}$ at 0.5 – 5.0 mM. (300 K, 282 MHz, d_3 -MeNO $_2$)

4.3.4 L1 + $[\text{Pd}(\text{dppp})]^{2+}$ Cryptophane Host-Guest Investigations

The $[\text{Pd}_3(\text{dppp})_3(\text{L1})_2] \cdot 6(\text{OTf})$ and $[\text{Pd}_3(\text{dppp})_3(\text{FL1})_2] \cdot 6(\text{OTf})$ cryptophanes underwent preliminary host-guest studies in d_6 -DMSO. This solvent was used as it was the only solvent in which L1 and FL1 complexes had successfully formed host-guest complexes in this work. Guests investigated included: SDS, adamantane-1-carboxylic acid,

biphenyl, 2-bromoadamantane and camphor-*D*. SDS was the only guest that showed any indication of a host-guest interaction.

4.4 Discussion

4.4.1 [Pd(dppp)]²⁺

Prior to investigating [Pd(dppp)]²⁺ as a *cis*-protected palladium(II) for use in cryptophane formation, it was studied in the range 0.5 – 5.0 mM, in *d*₆-DMSO, *d*₃-MeCN, and *d*₃-MeNO₂ by ¹H and ³¹P NMR spectroscopy to provide characterisation, and to compare to any cryptophanes formed (section 4.3.1). The ¹H NMR spectra of [Pd(dppp)]²⁺ in *d*₆-DMSO and *d*₃-MeNO₂ were similar in appearance, displaying five different proton environments. In *d*₃-MeCN only two multiplets were observed in the aromatic region, with the Ha and Hb protons resonating as one second-order multiplet. The ³¹P NMR spectra in *d*₃-MeCN and *d*₃-MeNO₂ each showed a single sharp resonance, indicating that the phosphorus spins were homotopic and experienced the same magnetic environment. The spectra of [Pd(dppp)]²⁺ in *d*₃-MeNO₂ were not affected in any way by varying the concentration. In *d*₃-MeCN, the phosphorus environment remains unchanged with varying concentration. However, small changes are seen to the Ha/Hb multiplet in the ¹H NMR spectra as the concentration was varied, but at no point between 0.5 and 5.0 mM were the resonances resolved. The concentration investigation in *d*₆-DMSO revealed a slightly different scenario, with two different conformations of [Pd(dppp)]²⁺ present. [Pd(dppp)]²⁺ has a central six-membered diphosphine ring that exchanges between two chair conformations (Figure 4.26). In *d*₆-DMSO this exchange was slow on the NMR timescale, resulting in

additional peaks in the ^1H NMR spectrum. These additional resonances consist of a small triplet in the aromatic region and two Hd proton resonances. The aromatic triplet is upfield to the other aromatic peaks and has the same couplings as seen for the Ha protons. The populations of the two chair conformations were unequal, with one conformation being preferred at room temperature. To further probe the exchange, the 0.5 and 5.0 mM of $[\text{Pd}(\text{dppp})]^{2+}$ in d_6 -DMSO samples were studied by VT ^1H NMR. The 5.0 mM sample did not vary at temperatures up to 75°C . The 0.5 mM sample however, showed a remarkable change when heated (Figure 4.29). The proportions of the two conformation populations were altered by heating. The conformation populations became equal at 55°C and as the temperature was increased, the chair conformation that was the minor conformation component at room temperature became the most populated conformation. When the sample had cooled, the spectrum showed that the conformation favoured at 75°C was retained, indicating that a meta-stable kinetic product had been formed.

4.4.2 L1 Cryptophanes

The ^1H NMR analysis of L1 and $[\text{Pd}(\text{dppp})]^{2+}$ at a ratio of 2:3 in d_6 -DMSO gave a broad spectrum indicative of complex formation. The 2-D ROESY data confirmed the complexation with through-space connections seen between the phenyl arms of $[\text{Pd}(\text{dppp})]^{2+}$ and the pyridyl coordinating groups of L1. No other rOes were observed, nor were they expected to be, as the protons that showed through-space connections were the only ones that were in close proximity to each other. This was similar to what was observed by Espinosa and co-workers who assembled cryptophanes from $[\text{Pd}(\text{dppp})]^{2+}$ and chiral nitrile-substituted cyclotribenzylenes (CTBs).⁸³ The CTBs are

similar to **L1** and **FL1**, however, they are shorter, as the only upper rim decoration comes from the nitrile group and a hydrogen or methoxy group (Figure 4.72). When cryptophanes were with formed with the nitrile/hydrogen decorated CTBs, no through-space connections were observed. When the nitrile/methoxy decorated CTB was used, through-space connections were observed between the benzyl arms of $[\text{Pd}(\text{dppp})]^{2+}$ and the methoxy group of the CTB, reaching as far as the protons of the CTB benzene rings. This is consistent with what was observed in this work.

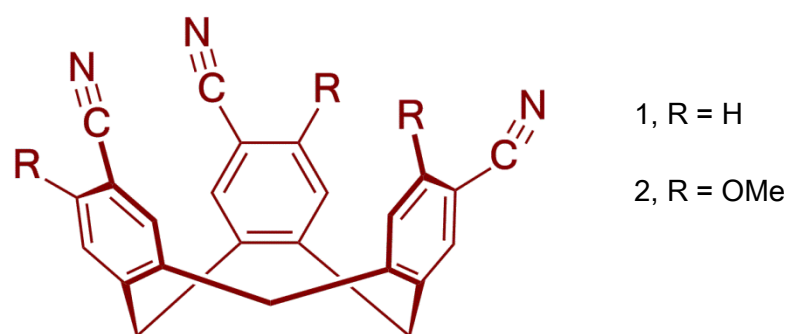


Figure 4.72 CTBs used by Espinosa and co-workers.⁸³

When $[\text{Pd}_3(\text{dppp})_3(\text{L1})_2] \cdot 6(\text{OTf})$ in d_6 -DMSO was investigated in the range 0.5 - 5.0 mM, it became clear that both *anti* and *syn* isomers of the $[\text{Pd}_3(\text{dppp})_3(\text{L1})_2] \cdot 6(\text{OTf})$ cryptophane were present in solution. From the intensities of the $[\text{Pd}(\text{dppp})]^{2+}$ H δ peaks, it was determined that the *anti* isomer is preferred and at very low concentrations (0.5 mM), the intensity of the *syn* peaks was so low that they could barely be discerned above the spectrum noise. This situation was repeated when these samples were analysed by ^{31}P NMR spectroscopy. Two clear phosphorous environments were observed, and at 0.5 mM $[\text{Pd}_3(\text{dppp})_3(\text{L1})_2] \cdot 6(\text{OTf})$, only one of these environments remained. It would be expected that if both *anti* and *syn* isomers were present in d_6 -DMSO, that three peaks would be observed; one that represented the homotopic *anti* phosphorus environment; and a pair of peaks that represented the diastereotopic *syn* phosphorus. However, the *anti* resonance displayed a clear

shoulder which could be the unseen *syn* resonance. The 0.5 and 5.0 mM $[\text{Pd}_3(\text{dppp})_3(\text{L1})_2]\cdot 6(\text{OTf})$ samples were studied with VT ^1H NMR spectroscopy. The 0.5 mM sample, which was mostly *anti* isomers showed no change between cryptophane isomers, although the populations of $[\text{Pd}(\text{dppp})]^{2+}$ chair conformations became equal at elevated temperatures. The 5.0 mM $[\text{Pd}_3(\text{dppp})_3(\text{L1})_2]\cdot 6(\text{OTf})$ sample however, showed a dramatic change with the peaks in the aromatic region sharpening considerably at 45 °C and above. At the same time, the $[\text{Pd}(\text{dppp})]^{2+}$ Hd peak became a single broad peak. This indicates that at 45°C and above, there was a highly symmetrical cryptophane in solution. The $[\text{Pd}(\text{dppp})]^{2+}$ Hd peak did have a very small *syn* resonance, but it was clear that at these elevated temperatures the *anti* cryptophane conformation is the preferred isomer. When the sample was cooled back down to room temperature, the original spectrum is restored; indicating that at room temperature there is a clear lack of thermodynamic preference between the two cryptophane isomers.

When **L1** and $[\text{Pd}(\text{dppp})]^{2+}$ were added together in a 2:3 ratio in d_3 -acetonitrile, a sharp well-resolved ^1H NMR spectrum was observed. The spectrum (Figure 4.39) was highly symmetrical, indicating that the complex formed from **L1** and $[\text{Pd}(\text{dppp})]^{2+}$ was also highly symmetrical. The $[\text{Pd}(\text{dppp})]^{2+}$ propylene bridge protons shifted downfield and broadened in comparison to uncomplexed $[\text{Pd}(\text{dppp})]^{2+}$ and there was only one peak each for the Hd and He protons, indicating that only the *anti* $[\text{Pd}_3(\text{dppp})_3(\text{L1})_2]\cdot 6(\text{OTf})$ cryptophane was formed. 2-D ROESY NMR analysis revealed through-space connections between the Ha/a' protons of the pyridyl arms of **L1** and the Hb and Hc protons of the phenyl arms of $[\text{Pd}(\text{dppp})]^{2+}$, indicating that a cryptophane complex had been formed. When the $[\text{Pd}_3(\text{dppp})_3(\text{L1})_2]\cdot 6(\text{OTf})$ cryptophane was studied in the range 0.5 – 5.0 mM, no changes in cryptophane conformation preference were observed in

the ^1H NMR spectra. The ^{31}P NMR spectra showed a second phosphorus environment at higher concentrations. This was not observed when $[\text{Pd}(\text{dppp})]^{2+}$ in $d_3\text{-MeCN}$ was studied in the same concentration range. This was attributed to the presence of a small amount of *syn* cryptophane isomers being present in $d_3\text{-MeCN}$ throughout the concentration range studied. This was discovered by further investigation of the ^1H NMR spectra. A small amount of *syn* cryptophane isomer was present; however, the peaks of the *syn* isomers were of a very low intensity, with very low signal to noise levels. The 5.0 mM sample of $[\text{Pd}_3(\text{dppp})_3(\text{L1})_2]\cdot 6(\text{OTf})$ was heated up to 65°C and was found to be stable up to this temperature and exhibited no change in conformation.

The 2:3 stoichiometric mixture of **L1** and $[\text{Pd}(\text{dppp})]^{2+}$ in $d_3\text{-nitromethane}$ yielded a broad, unsymmetrical ^1H NMR spectrum that was indicative of complexation formation. It could be seen from the He peaks of the $[\text{Pd}(\text{dppp})]^{2+}$ propylene bridge that both *anti* and *syn* were present, as there were three resonances: one large upfield *anti* resonance at 2.47 ppm and two smaller *syn* resonances 2.76 and 3.00 ppm (Figure 4.46). The 2-D ROESY NMR spectrum showed a single through-space connection between the Ha/a' protons of the pyridyl arm of **L1** and the Hb protons of the phenyl arms of $[\text{Pd}(\text{dppp})]^{2+}$, indicative of cryptophane formation. When the $[\text{Pd}_3(\text{dppp})_3(\text{L1})_2]\cdot 6(\text{OTf})$ cryptophane in $d_3\text{-MeNO}_2$ was studied in the concentration range 0.5 – 5.0 mM the ^1H and ^{31}P NMR spectra both showed that the two cryptophane conformations remained present throughout this concentration range at the same proportions, with an approximate ratio of 1:13 *syn:anti*. This indicated that at low concentrations there was hardly any *syn* conformation present. It could be seen in the ^1H NMR spectra (Figure 4.49), that the aromatic region of the spectra had changed considerably as the concentration of $[\text{Pd}_3(\text{dppp})_3(\text{L1})_2]\cdot 6(\text{OTf})$ was increased. This was attributed to the increasing amount of *anti* cryptophanes present in solution, relative to the small amount

of *syn* cryptophanes, resulting in the *anti* cryptophane peaks becoming more dominant in the spectra.

4.4.3 FL1 Cryptophanes

The 2:3 stoichiometric mixture of **FL1** and $[\text{Pd}(\text{dppp})]^{2+}$ in d_6 -DMSO resulted in sharp, well-resolved highly symmetrical ^1H NMR spectrum (Figure 4.51) indicative of highly symmetrical *anti* cryptophanes in solution. In the 2-D ROESY NMR analysis, through-space connections between the Hb of the phenyl arms of $[\text{Pd}(\text{dppp})]^{2+}$ and the Ha and Hb protons of the **FL1** ligands can be seen clearly, unlike the analogous **L1** $[\text{Pd}_3(\text{dppp})_3(\text{L1})_2]\cdot 6(\text{OTf})$ cryptophane. This was because there was no overlap of peaks in the aromatic region of in the ^1H NMR spectrum of $[\text{Pd}_3(\text{dppp})_3(\text{FL1})_2]\cdot 6(\text{OTf})$ cryptophane. As seen with the $[\text{Pd}_3(\text{dppp})_3(\text{L1})_2]\cdot 6(\text{OTf})$ cryptophanes in d_6 -DMSO, d_3 -MeCN and d_3 -MeNO₂, no other through-space connections were observed between **FL1** and $[\text{Pd}(\text{dppp})]^{2+}$. As the ligands **L1** and **FL1** are the same shape, this was to be expected. When the $[\text{Pd}_3(\text{dppp})_3(\text{FL1})_2]\cdot 6(\text{OTf})$ cryptophane in d_6 -DMSO was studied in the range 0.5 – 5.0 mM the ^1H NMR spectra revealed no changes; indicating that *anti* conformation was the only cryptophane conformation in this concentration range. This was confirmed by the ^{19}F and ^{31}P NMR analysis of these samples. There was only one fluorine environment observed, indicating that all of the fluorines in the $[\text{Pd}_3(\text{dppp})_3(\text{FL1})_2]\cdot 6(\text{OTf})$ cryptophane experienced a very similar magnetic environment. The ^{31}P NMR spectra had the same appearance as those recorded for uncomplexed $[\text{Pd}(\text{dppp})]^{2+}$ in d_6 -DMSO (Figure 4.27 and Figure 4.57 respectively). The $[\text{Pd}_3(\text{dppp})_3(\text{FL1})_2]\cdot 6(\text{OTf})$ cryptophane in d_6 -DMSO was analysed by ESI-MS. This analysis revealed a highly dynamic system. Whilst there were some mass peaks that

could be representative of an M_3L_2 type complex in solution, there were many other M_xL_y combinations observed. These results neither confirmed nor refuted that cryptophanes were present in solution.

$[Pd_3(dppp)_3(FL1)_2] \cdot 6(OTf)$ in d_3 -acetonitrile was studied by 1H , ^{19}F and ^{31}P NMR spectroscopy, in the range 0.5 – 5.0 mM. These analyses showed that the cryptophanes produced were *anti* isomers, with no evidence seen of the presence of *syn* isomers in solution. 2-D ROESY NMR analysis revealed no through-space connections between **FL1** and $[Pd(dppp)]^{2+}$. This is unusual when compared to the other **L1** and **FL1** cryptophanes in this study, which all show at least one through-space connection, however, this lack of through-space connections was observed by Espinosa and co-workers for their $[Pd(dppp)]^{2+}$ -mediated cryptophane as discussed above.⁸³

Producing crystals of both the $[Pd_3(dppp)_3(L1)_2] \cdot 6(OTf)$ and $[Pd_3(dppp)_3(FL1)_2] \cdot 6(OTf)$ cryptophanes that were of a suitable quality for X-ray crystallography analysis proved difficult. $[Pd_3(dppp)_3(FL1)_2] \cdot 6(OTf)$ in d_3 -acetonitrile solution was the only cryptophane/solvent system that yielded crystals that were suitable for analysis. This analysis revealed that the $[Pd_3(dppp)_3(FL1)_2] \cdot 6(OTf)$ cryptophanes had non-crystallographic C_3 symmetry, as indicated by the paddle-wheel shape seen in Figure 4.63 a) and b). Crystallographic symmetry was not observed, as the carbonyl groups of the **FL1** ligands are pointing in different directions. The cryptophanes were found to have a oblate spheroid shape with static dimensions of $15.6 \times 29.8 \text{ \AA}$. The crystals were formed in the achiral *meso* conformation, which consisted of an *M* and a *P* enantiomer of **FL1**. This was different to what was observed in solution, however it is possible that the predominant species in solution is not that same as that in the solid

state.¹⁵³ Mukherjee and Ghosh studied the self-assembly of molecular squares and triangles. They observed an equilibrium between the molecular squares and triangles in solution. However, only the molecular square was crystallised, even though for one system studied the molecular triangle was observed to be the dominant species in solution. This was attributed to the high lattice energy of formation for the molecular square when compared to the triangle in the solid state at room temperature.¹⁵⁴

When **FL1** and $[\text{Pd}(\text{dppp})]^{2+}$ were mixed in a 2:3 ratio in d_3 -nitromethane, a well-resolved ^1H NMR spectrum was observed, indicative of *anti* isomer cryptophanes in solution. 2-D ROESY NMR analysis showed through-space connections between the phenyl arms of the $[\text{Pd}(\text{dppp})]^{2+}$ and the pyridyl arms of **FL1**, indicative of cryptophane formation. When the $[\text{Pd}_3(\text{dppp})_3(\text{FL1})_2]\cdot 6(\text{OTf})$ cryptophane was studied in the range 0.5 -5.0 mM, no change in cryptophane conformation was observed. ^{31}P NMR analysis revealed that the phosphorus in the $[\text{Pd}_3(\text{dppp})_3(\text{FL1})_2]\cdot 6(\text{OTf})$ complex were homotopic with only one phosphorus environment observed. ^{19}F NMR analysis however, revealed the presence of multiple fluorine environments, which indicated a lack of symmetry about the position of the fluorines of the **FL1** pyridyl arms within the cryptophanes. This explained the broadness of the peaks in the aromatic region of the ^1H NMR spectra, which results from ^1H - ^{19}F spin-spin splitting, in addition to ^1H - ^1H spin-spin splitting.

Both the **L1** and **FL1** ligands have been shown to form M_3L_2 cryptophanes in polar aprotic solvents with the palladium(II) compound $[\text{Pd}(\text{dppp})]^{2+}$. Studying the cryptophanes in a small range of concentrations revealed additional information regarding their conformations. This additional knowledge would not have been found if only one concentration of cryptophane had been used in this work. The **L1** cryptophane in d_6 -DMSO was found to be a mixture of *anti* and *syn* cryptophane isomers at room

temperature. At very low concentrations [0.5 mM $[\text{Pd}_3(\text{dppp})_3(\text{L1})_2]\cdot 6(\text{OTf})$] only the *anti* isomer was observed. When 5.0 mM $[\text{Pd}_3(\text{dppp})_3(\text{L1})_2]\cdot 6(\text{OTf})$ was heated to 45°C, equilibria between *anti* and *syn* isomer shifted purely to the *anti* isomer. When the sample was cooled again, the equilibrium between isomers was restored. The **L1** cryptophane in d_3 -acetonitrile and d_3 -nitromethane were also found to be mixtures of *anti* and *syn* cryptophane isomers, with the *anti* isomer being the preferred cryptophane conformation. The **FL1** cryptophanes however, were observed to only form *anti* cryptophanes in solution.

4.5 Conclusions

Several routes to cryptophane formation have been investigated. This resulted in the production of new cryptophanes. Although the $[\text{Pd}_3(\text{bis-NHC-b})_3(\text{L1})_2]^{6+}$ complex was well characterised by ^1H NMR techniques, it was assessed not to be suitable for further host-guest studies due to the intramolecular exchange observed, which would complicate any host-guest analyses. Cryptophanes were successfully prepared from **L1** and $[\text{Pd}(\text{dppp})]^{2+}$ and from **FL1** and $[\text{Pd}(\text{dppp})]^{2+}$ in d_6 -DMSO, d_3 -acetonitrile and d_3 -nitromethane. These new systems were characterised by 1-D ^1H , ^{19}F and ^{31}P and 2-D ROESY NMR spectroscopy. The NMR analyses of these systems showed that the *anti* cryptophane conformation was preferred, with a small amount of *syn* isomer seen for the **L1** cryptophanes. The **FL1** cryptophanes were found to form enantiopure *anti* cryptophanes in solution. Attempts were made to analyse these systems by ESI-MS and X-ray crystallography. This was only achieved for $[\text{Pd}_3(\text{dppp})_3(\text{FL1})_2]\cdot 6(\text{OTf})$ in d_6 -DMSO and $[\text{Pd}_3(\text{dppp})_3(\text{FL1})_2]\cdot 6(\text{OTf})$ in d_3 -acetonitrile, respectively. The ESI-MS analysis was not particularly enlightening. However, the X-ray crystallographic analysis

did provide conformation of cryptophanes being formed, although the achiral *syn* isomer was the dominant species in the solid state. A limited amount of host-guest work was performed in solution. Now that these materials have been well characterised, further work into their host-guest capabilities should be undertaken.

Chapter 5 Conclusions

This work has demonstrated the usefulness of NMR spectroscopy in characterising and probing hosts and host guest systems and their interactions. NMR experiments including 1-D, DOSY and 2-D ROESY in particular have provided information on the chiralities and self-assembly of hosts. These techniques have also supplied information about the nature of host-guest interactions, including information regarding stoichiometries and binding, imparting a greater understanding of the complexes studied.

5.1 L1 Stella Octangula Cage

The host-guest relationship between the L1 stella octangula cage and sodium alkyl sulfate guests, SOS, SDS and STS has been firmly established at a host:guest ratio of 1:2. The sodium alkyl sulfate guests and L1 stella octangula cages were found to be in fast exchange with each other. 2-D ROESY NMR analysis revealed that the guest molecules enter the cage *via* the cage portals and that they are rotating about their long axis as they do so. The fitting of binding constants revealed that the shorter alkyl sulfate guests, the more tightly bound they were to the $[\text{Pd}_6(\text{L1})_8]^{12+}$ stella octangula cage.

During the host-guest investigation of the $[\text{Pd}_6(\text{L1})_8]^{12+}$ stella octangula cage, it became apparent that the self-sorting process of the cage was not as simple it had initially seemed. The most thermodynamically stable arrangement for the stella octangula cage was when each individual $[\text{Pd}_6(\text{L1})_8]^{12+}$ stella octangula cage self-assembled with eight ligand molecules of the same chirality. This resulted in a racemic mixture of both cage

enantiomers.¹¹⁰ The $[\text{Pd}_6(\text{L1})_8]^{12+}$ stella octangula cage was observed to initially form heterochiral assemblies; formed from a mixture of ligand enantiomers, which over time self-sorted into enantiopure cages. The d_6 -DMSO was found to compete with the **L1** ligand for the palladium(II), hindering the rate of self-sorting. When the similar polar aprotic solvent d_3 -acetonitrile was used instead of d_6 -DMSO, the stella octangula cage was observed to form instantly, with no evidence of self-sorting observed after the initial formation. The resulting ^1H NMR spectrum indicated heterochiral assemblies had been formed. The rate of self-sorting in d_6 -DMSO was also found to be affected by the concentration of the $[\text{Pd}_6(\text{L1})_8]^{12+}$ stella octangula cage in solution, with the optimum concentration being found to be between 0.2 and 0.5 mM.

5.2 FL1 Stella Octangula Cage

The novel **FL1** ligand was characterised by ^1H and ^{19}F NMR spectroscopy. The **FL1** ligand was found to have improved solubility when compared to **L1**. The **FL1** ligand was used to produce stella octangula cages in d_6 -DMSO and d_3 -acetonitrile. The self-sorting of the **FL1** stella octangula cage was found to be restricted in d_6 -DMSO and heterochiral cage assemblies were observed. The self-sorting process was aided by adding excess palladium(II) to the cage solutions. The host-guest interaction between the **FL1** stella octangula cage and SDS was investigated and was found to be weaker than that observed for the **L1** cage. However, the **FL1** host-guest investigation was not ideal, with the samples containing either excess ligand or excess palladium(II) salt. The **FL1** stella octangula cage in d_3 -acetonitrile was characterised by ^1H , ^{19}F , DOSY and 2-D ROESY NMR spectroscopy, ESI-MS and X-ray crystallography. Although the crystals produced were poorly diffracting, similarities between the $[\text{Pd}_6(\text{FL1})_8]^{12+}$ stella

octangula cage and the isostructural $[\text{Pd}_6(\text{L2})_8]^{12+}$ stella octangula cage allowed for a partially resolved structure to be obtained.¹¹³ It was found throughout this research that suitable crystals of CTV-derivative based metallo-cages were difficult to obtain and that when suitable crystals were grown, the X-ray crystallography data was poor. This system was found to be stable at room temperature for up to four months. Suitable guests for the **FL1** stella octangula cage in d_3 -acetonitrile were not found in this study, although the amount of host:guest work performed with this system was limited.

5.3 Cryptophanes

The **L1** and **FL1** ligands were used to construct new metallo-cryptophanes with $[\text{Pd}(\text{dppp})]^{2+}$ in d_6 -DMSO, d_3 -acetonitrile and d_3 -nitromethane. These cryptophanes were characterised in the range of 0.5 – 5.0 mM using ^1H , ^{19}F , ^{31}P and 2-D ROESY NMR spectroscopy and limited analyses with ESI-MS and X-ray crystallography. The **L1** cryptophanes were found to form mostly chiral *anti* isomers, with a small amount of the achiral *syn* isomer also present. At low concentrations, only the *anti* isomer was observed. The **FL1** cryptophanes only formed the chiral *anti* isomers. Crystals that were suitable for X-ray crystallography were difficult to produce, and only the **FL1** cryptophane in d_3 -MeCN yielded suitable crystals. The crystal structure revealed that the **FL1** cryptophane formed in the achiral *meso* conformation, in contrast to what was observed in the solution studies. Studying the cryptophanes over a small concentration range allowed for much more information to be collected about the cryptophanes than studying them at a single concentration would have allowed. Studying uncomplexed $[\text{Pd}(\text{dppp})]^{2+}$ in d_6 -DMSO in the same concentration range by ^1H and ^{31}P NMR revealed that the $[\text{Pd}(\text{dppp})]^{2+}$ could express two chair conformations; the exchange rate

between them in d_6 -DMSO being slow enough to be observed on the NMR timescale. This information was extremely useful during the analysis of the **L1** cryptophanes in d_6 -DMSO.

During the early investigations into cryptophane formation, (ethylenediamine)palladium(II) dinitrate was found not to form cryptophanes with either the **L1** or **FL1** ligand. The novel palladium tecton bis(acetonitrile)-1,1'-methylenebis(3-benzyl-imidazol-2-ylidene)palladium(II)tetrafluoroborate was found to successfully form cryptophanes. However, due to the exchange seen within the systems, they were ruled out as potential hosts for solution-phase host-guest chemistry.

5.4 Future Work

The aims of this research – the investigation of the host-guest chemistry of the $\text{Pd}_6\text{L1}_8$ stella octangula system and sodium alkyl sulfate salts, the application of the **FL1** ligand to stella octangula cages and the generation of the new cryptophanes – have been accomplished. However, there is plenty of scope for further work.

One recurring aspect of this research was that the self-assembly and self-sorting processes - along with chirality of the host molecules, complicated matters. This necessitated further studies of the host molecules to fully understand their behaviour in solution. This resulted in less time being devoted to the study of the host-guest chemistry of the host molecules, as it seemed senseless to conduct host-guest studies, whilst the solution behaviour of the host molecules had not been fully characterised. Accordingly, a dedicated study of potential guest molecules should be performed.

The **L1** and **FL1** stella octangula cages have potential applications in host-guest chemistry. The stella octangula cages have large, accessible cavities and have been shown to be capable of forming host-guest assemblies. However, the sodium alkyl sulfate guests used in this study were not the optimum guests for these hosts, as indicated by their low packing coefficients. This implies that a larger guest would be a better fit, meaning that there should be plenty of potential guest molecules from which to choose. However, it could also mean that Rebek's 55% rule³² is not suited for ionic guests. The rule was devised by studying small, hydrogen-bonded guests, with cavities an order of magnitude smaller than that of the stella octangula cage. The guests that were used were small organic liquids and adamantane derivatives. Further study is required to investigate if the 55% rule applies for much larger, metallo-coordinated host complexes, and also for ionic guests, as this would be of great value to the supramolecular scientist.

The $[\text{Pd}_3(\text{dppp})_3(\text{L1})_2]^{6+}$ and $[\text{Pd}_3(\text{dppp})_3(\text{FL1})_2]^{6+}$ cryptophanes also have potential applications in host-guest chemistry. The early cryptophanes had small cavities (in the region of 60 – 100 Å), which were suitable for encapsulating small guests.^{55, 73, 76} The cryptophanes produced in this study were much larger. It is reasonable to assume that their cavities are not dissimilar in size to Henkelis's bis-NHC-n cryptophanes, reported at 697 Å (refer to section 1.3.3).⁸⁸ Henkelis's bis-NHC-n cryptophanes were capable of sequestering 1,2-dichlorobenzene and I₂. Both of these guests had a 1:3 host:guest ratio. However, to achieve this, the cryptophanes were used in the solid state and the guest locations were found to be disordered about the cryptophanes. Although this is a less-than-ideal situation for the chemist studying these host-guest interactions, the uptake of I₂ into a solid-state matrix is of importance for nuclear fuel processing, where the removal of the I₂ is more important than nice data! It is feasible that both the

cryptophanes formed in this study with the bis-NHC-b and $[\text{Pd}(\text{dppp})]^{2+}$ palladium tectons could have applications in the solid state uptake of guests.

Chapter 6 Experimental

6.1 NMR Sample Preparation

6.1.1 Ligand Samples

The ligands **L1**, *tris*(isonicotinoyl)cyclotriguaiacylene, and **FL1**, *tris*(3-fluoropyridine)cyclotriguaiacylene were prepared in-house by the Hardie group in accordance with the literature.^{126,113} Ligand samples for NMR analysis were typically prepared at 4mM.

6.1.2 Cage Samples

The stella octangula cage assemblies were synthesised by first producing stock solutions of palladium salt and ligand in deuterated solvent. Then appropriate amounts of these stock solutions were added together to give a 3:4 metal:ligand ratio in accordance with the literature.¹¹⁰ To prepare 5 ml of 2 mM **L1** stella octangula cage, the following stocks were prepared: 16 mM **L1** in 2.5 ml (0.0289 g) and 12 mM Pd salt in 2.5 ml (0.0133 g). The two stocks were then added together in a 50:50 ratio to produce the desired stock solution. To produce a cage sample with a guest present, stock solutions of guests were produced at concentrations that when diluted would provide the required host:guest ratio when added directly to the NMR tube to make the volume of the solutions up to 600 μ l. As the solutions were made directly in the NMR tubes, the samples were vortexed until they became homogenous (Figure 6.1). The palladium solutions in DMSO-*d*₆ were a clear golden brown colour and the ligand was a very pale

creamy yellow colour, together these solutions had obvious stratifications when unmixed. When the solution was homogenised, the resulting solution was a clear, light yellow. Samples made up in acetonitrile- d_3 had the same colouration, but were lighter in hue. After vortexing the samples remained homogenous. Stock solutions of the **FL1** ligand had the appearance of an opaque milky suspension. When palladium salt stock was added to **FL1** ligand stock, complexation was observed instantly as the resulting solution no longer looked like a suspension; it becomes entirely clear with no precipitate and had a very light yellow colour. Cryptophanes were prepared by mixing metal to ligand at a 3:2 ratio. To prepare 5 ml of 5 mM **FL1** cryptophane with $[\text{Pd}(\text{dppp})]^{2+}$, the following stocks were prepared: 30 mM $[\text{Pd}(\text{dppp})]^{2+}$ in 2.5 ml (0.0613 g) and 20 mM **FL1** in 2.5 ml (0.0389 g). The two stocks were then added together in a 50:50 ratio to produce the desired stock solution. Cryptophanes were prepared in the same manner as stella octangula assemblies, unless otherwise stated. Samples prepared in nitromethane- d_3 had a similar appearance to those prepared in d_6 -DMSO.

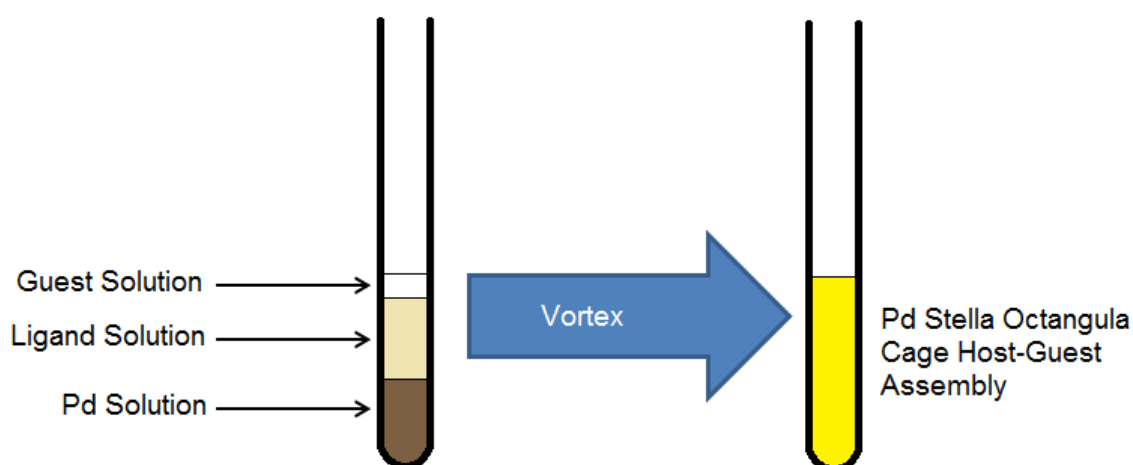


Figure 6.1 Schematic of Pd stella octangula cage host-guest synthesis.

6.1.3 Reagents

Palladium (II) nitrate hydrate ($\text{Pd}(\text{NO}_3)_2 \cdot x\text{H}_2\text{O}$) and acetonitrile- d_3 (CD_3CN) for NMR with 1% v/v TMS 99% D with D-enrichment $\geq 98.5\%$ were obtained from Acros Organics. Tetrakis(acetonitrile)palladium(II)tetrafluoroborate ($\text{Pd}(\text{CH}_3\text{CN})_4(\text{BF}_4)_2$) was obtained from Aldrich initially and then from Acros Organics with a purity of 99%, due to issues with purity and degradation. (Ethylenediamine)palladium(II) Dinitrate ($\text{C}_2\text{H}_8\text{N}_4\text{O}_6\text{Pd}$) $>98.0\%$ was obtained from Tokyo Chemical Industry. Toluene- d_6 ($\text{C}_5\text{D}_5\text{CD}_3$) 99.6% atom D, chloroform- d 99.8% atom D containing 0.03% v/v TMS, nitromethane- d_3 (CD_3NO_2) ≥ 99 atom%, fullerene- C_{60} , 98%, biphenyl ($\text{C}_{12}\text{H}_{10}$) 99.5%, 2-bromoadamantane ($\text{C}_{10}\text{H}_{15}\text{Br}$) 98%, [1,3-Bis(diphenylphosphino)propane]palladium(II)triflate ($[\text{Pd}(\text{dppp})]^{2+}$) ($\text{C}_{29}\text{H}_{26}\text{F}_6\text{O}_6\text{P}_2\text{PdS}_2$), camphor- D ($\text{C}_{10}\text{H}_{16}\text{O}$) $\geq 97\%$ and sodium tetradecyl sulfate ($\text{CH}_3(\text{CH}_2)_{13}\text{OSO}_3\text{Na}$) were obtained from Aldrich. Sodium octyl sulfate ($\text{CH}_3(\text{CH}_2)_7\text{OSO}_3\text{Na}$) $\sim 95\%$ was obtained from Sigma Aldrich. Sodium dodecyl sulfate ($\text{CH}_3(\text{CH}_2)_{11}\text{OSO}_3\text{Na}$) $>99\%$ at electrophoresis grade was obtained from Fisher Scientific. Dimethyl sulfoxide- d_6 ($(\text{CD}_3)_2\text{SO}$) 99.9% D was obtained from Goss Scientific. Adamantane-1-carboxylic acid ($\text{C}_{10}\text{H}_{16}\text{O}$) 99% was obtained from Alfa Aesar. All reagents were used as supplied with no further purification.

6.2 NMR Experiments

NMR experiments were performed using a Varian Unity Inova 500 Spectrometer (Varian Inc., Palo Alto, California, USA) operating at 499.97 MHz proton frequency with a 5 mm $^1\text{H}\{^{13}\text{C}, ^{15}\text{N}, ^{31}\text{P}\}$ ID/PFG VT probe. Additional NMR experiments were

performed using Bruker Avance 300 or 500 MHz spectrometers. Standard 5 mm Norell S500 NMR tubes containing 600 μ l of sample were used. All spectra were referenced to the solvent peak, unless otherwise stated. Experiments were performed at 293 K unless otherwise stated.

6.2.1 ^1H NMR Experiments

^1H NMR experiments were performed on the Varian Unity Inova 500 Spectrometer. A spectral width of 6000 Hz was collected in 8192 pairs of data points and experiments were recorded using 128 scans and a recycle delay of 5 seconds.

6.2.1.1 Diffusion-Ordered Spectroscopy Experiments

DOSY NMR measurements were performed on the Varian Unity Inova 500 Spectrometer, using the bipolar pulse pair stimulated echo (BPPSTE) operating in the ONESHOT experiment. Additional parameters: number of different gradient levels, 15; gradient stabilisation delay, 0.0025 s; gradient length, 0.004 s; diffusion delay, 0.05 s; relaxation delay, 10.5 s; Kappa (unbalancing factor), 0.2.

6.2.1.2 Rotational Overhauser Spectroscopy Experiments

Phase-sensitive 2-D ROESY experiments were performed on the Varian Unity Inova 500 Spectrometer, with a mixing time of 300 ms, 64 transients, a relaxation delay of 4.0 s, 256 increments (states phase cycling, so 512 increments in total) and a spectral width of 6000 Hz and 2K data points.

6.2.2 ¹⁹F NMR Experiments

¹⁹F NMR experiments were performed on Bruker Avance 300 and 500 MHz spectrometers, operating at 282 and 471 MHz respectively. The standard ¹⁹F NMR experiment was performed on the Bruker 300 Avance. Data was collected across a spectral width of 67000 Hz with 65536 data points, experiments were recorded using 16 scans. ¹⁹F broadband decoupled experiments were also performed on the Bruker 300 Avance. Data was collected across a spectral width of 109000 Hz with 65536 data points, experiments were recorded using 1024 scans.

6.2.3 ³¹P NMR Experiments

³¹P NMR experiments were performed on the Bruker Avance 300 MHz spectrometer, operating at 121 MHz. Data was collected across a spectral width of 7300 Hz with 4096 data points, experiments were recorded using 4096 scans.

6.2.4 Data Processing

1-D and 2-D NMR data were processed using ACD Spectrus Processor 2015 of the ACD labs 2015 software package from Advanced Chemistry Development, (Toronto, Canada). DOSY data was processed using the DOSYtoolbox, software version 2.5 developed by Mathias Nilsson of the University of Manchester.¹⁵⁵ Fitting of the association constants (K_a) was achieved using HypNMR 2008 software from Protonic Software.¹⁴²

6.3 Mass Spectroscopy

High resolution electrospray mass spectra (ESI-MS) were measured on a Bruker MaXis Impact spectrometer in positive ion mode by Dr Stuart L. Warriner of the University of Leeds.

6.4 X-ray Crystallography

6.4.1 FL1 Stella Octangula Cage in Acetonitrile

A crystal was mounted under oil on a MiTeGen tip and X-ray diffraction data were collected and solved by Dr Flora Thorp-Greenwood at 110(1) K with Cu- $K\alpha$ radiation ($\lambda = 1.54184 \text{ \AA}$) with an Agilent SuperNova diffractometer. Data were corrected for Lorentz and polarisation factors and an absorption correction was applied using a multi-scan method. The crystals were extremely weakly diffracting due to extensive inherent disorder. They are isostructural with a previously reported different $[\text{Pd}_6\text{L}_8].12\text{BF}_4$ complex of unit cell tetragonal / $a = 30.688(5)$, $c = 45.906(11) \text{ \AA}$,¹¹³ hence the published structure solution was used as a starting point for refinement of this data. The structure was refined by full-matrix least squares on F^2 by SHELXL-97.¹⁵⁶ Only Pd centres were refined anisotropically. The structure is highly disordered with averaged positions showing both ligand enantiomers superimposed on one another. All rings were refined with rigid body constraints and two rings were refined each with a group displacement parameter. One C-O bond length was restrained to be chemically reasonable. One fluoro-pyridyl was refined with the fluorine atom disordered across two positions due to ring rotation. While the gross structural features of the structure have been established, exact bond lengths and angles are not reliable due to the very low

resolution of the data obtained. Counter-anions could not be located and the modelled structure contained significant void space accounting for 69% of the unit cell volume. Hence the SQUEEZE¹⁵⁶ routine of PLATON¹⁵⁷ was employed. Details of data collections and structure refinements are given in Table 6.1

Table 6.1 Crystal data and structure refinement for the FL1 stella octangula cage

Empirical formula	$C_{312}H_{360}B_{12}N_{24}O_{60}F_{72}Pd_6$
Formula weight	7542.36
Temperature/K	110.15
Crystal system	tetragonal
Space group	$I4/mmm$
$a/\text{\AA}$	30.565(4)
$b/\text{\AA}$	30.565(4)
$c/\text{\AA}$	45.376(5)
$\alpha/^\circ$	90.00
$\beta/^\circ$	90.00
$\gamma/^\circ$	90.00
Volume/ \AA^3	42390(8)
Z	2
$\rho_{\text{calc}}/\text{g/cm}^3$	0.591
μ/mm^{-1}	1.407
F(000)	7728.0
Crystal size/ mm^3	$0.2 \times 0.2 \times 0.2$
Radiation	$\text{CuK}\alpha$ ($\lambda = 1.54184$)
2θ range for data collection/ $^\circ$	6.52 to 66.82
Index ranges	$-20 \leq h \leq 21, -21 \leq k \leq 17, -32 \leq l \leq 29$
Reflections collected	9278
Independent reflections	2306 [$R_{\text{int}} = 0.0703, R_{\text{sigma}} = 0.0647$]
Data/restraints/parameters	2306/5/75
Goodness-of-fit on F^2	1.898
Final R indexes [$I \geq 2\sigma(I)$]	$R_1 = 0.2392, wR_2 = 0.5458$
Final R indexes [all data]	$R_1 = 0.2810, wR_2 = 0.5837$
Largest diff. peak/hole / $e \text{\AA}^{-3}$	1.29/-0.66

6.4.2 $[\text{Pd}_3(\text{dppp})_3(\text{FL1})_2] \cdot 6(\text{OTf})$ Cryptophane in Acetonitrile

Crystals were mounted under inert oil on a MiTeGen tip and flash frozen to 120(1) K using an OxfordCryosystems low temperature device. X-ray diffraction data were collected and solved by Dr Flora Thorp-Greenwood using $\text{Cu-K}\alpha$ radiation ($\lambda = 1.54184 \text{\AA}$) using an Agilent Supernova dual-source diffractometer with Atlas S2 CCD detector

and fine-focus sealed tube generator. Data were corrected for Lorentzian and polarization effects and absorption corrections were applied using multi-scan methods. The structures were solved by direct methods using SHELXS-97 and refined by block-matrix on F2 using SHELXL-97.¹⁵⁶ The Pd, coordinating P atoms and non-hydrogen atoms of the **FL1** ligand were refined as anisotropic, with all other atoms refined with an isotropic model. Hydrogen positions were included at geometrically estimated positions. Crystals of $[\text{Pd}_3(\text{dppp})_3(\text{FL1})_2]\cdot 6(\text{OTf})$ were of poor quality, with poor internal consistency ($R_{int} = 0.1095$) and only exhibited weak diffraction, with no diffraction at high angles. Attempts to grow higher quality crystals were not successful. Only four of the six triflate counter-anions could be located in the difference map and refined, so two have been excluded from refinement but included in the formula. One aromatic ring was refined with a rigid body constraint, some interatomic distances were restrained to be chemically reasonable, and restraints were placed on some anisotropic displacement parameters. The structure contained significant void space (ca. 35% of unit cell volume) with residual electron density which could not be meaningfully modelled as solvent or counter-anions, hence the SQUEEZE routine of PLATON was employed in these structures.¹⁵⁸ Additional details of data collections and structure solutions are given in Table 6.2.

Table 6.2 Crystal data and structure refinement for $[Pd_3(dppp)_3(FL\ 1)_2] \cdot 6(OTf)$ Cryptophane in Acetonitrile

Empirical formula	$C_{171}H_{135}F_{24}N_6O_{36}P_6Pd_3S_6$
Formula weight	1029.21
Temperature/K	110.15
Crystal system	triclinic
Space group	$P-1$
$a/\text{\AA}$	18.8882(4)
$b/\text{\AA}$	22.7914(4)
$c/\text{\AA}$	28.1888(6)
$\alpha/^\circ$	102.532(2)
$\beta/^\circ$	10.5.751(2)
$\gamma/^\circ$	93.501(2)
Volume/ \AA^3	11307.7(4)
Z	2
$\rho_{\text{calc}}/\text{g/cm}^3$	1.176
θ range ($^\circ$)	3.29-65.0
No. data collected	89198
No. unique data	37073
Rint	0.1095
No. obs. Data ($I > 2\sigma(I)$)	17537
No. parameters	1516
No. restraints	9
R_1 (obs data)	0.1051
wR^2 (all data)	0.3059
S	0.955

6.4.3 X-ray Crystallography Sample Preparation

X-ray crystallography samples were prepared by slow vapour diffusion by either acetone or diethyl ether. A small vial containing the sample was placed inside a larger vial containing the diffusing solvent. The samples were prepared and stored at room temperature and crystal formation took 4-6 weeks.

Appendix

A.1 L1 + [Pd(dppp)]²⁺ Cryptophane in *d*₆-DMSO ¹H COSY

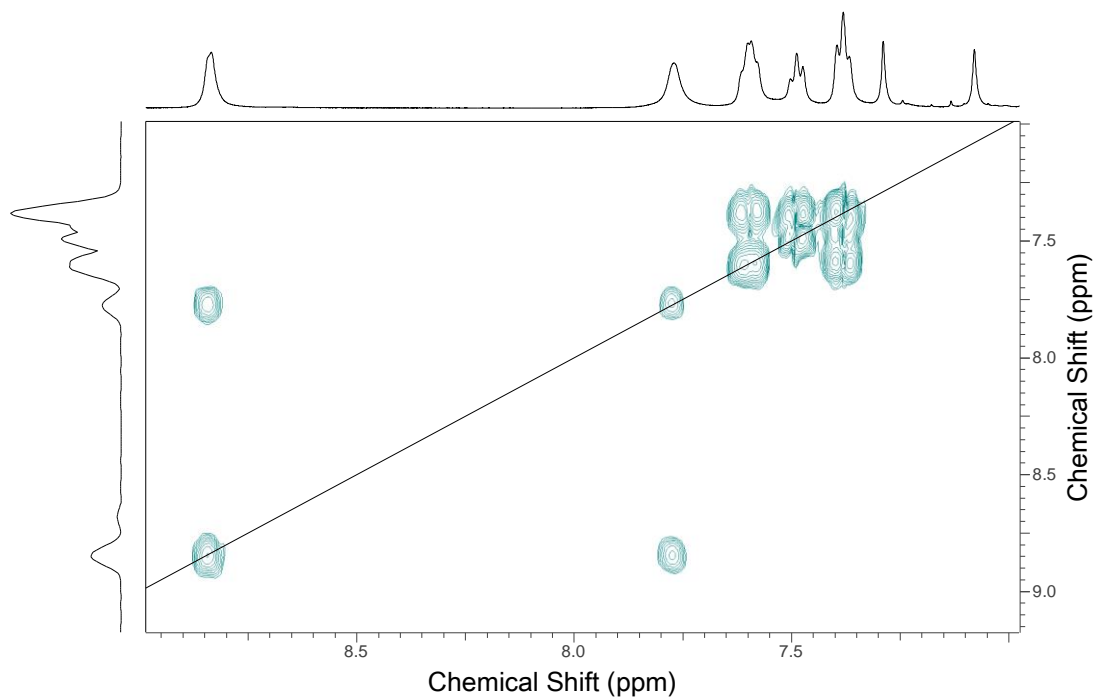


Figure A 1 Section of ¹H NMR COSY spectrum of [Pd₃(dppp)₃(L1)₂]⁶⁺.
(299 K, 500 MHz, *d*₆-DMSO)

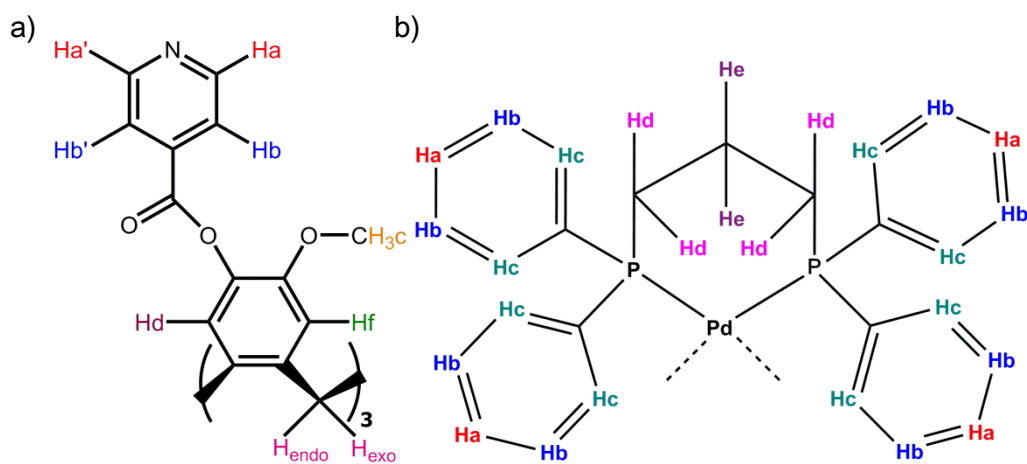


Figure A 2 Unique protons: a) L1 and b) 1,3-Bis(diphenylphosphino)propane]palladium(II).

Table A 1 Table of assignments for ¹H COSY of aromatic region of [Pd₃(dppp)₃(L1)₂](OTf)₆ cryptophane in d₆-DMSO. L1 listed in black and [Pd(dppp)]²⁺ listed in red.

Chemical Shift/ppm	Assignment
8.85	Ha/a'
7.77	Hb/b'
7.61	Hb
7.51	Ha
7.35	Hc

A.2 L1 & [Pd(dppp)]²⁺ in *d*₃-MeNO₂ ¹H-¹³C HMQC

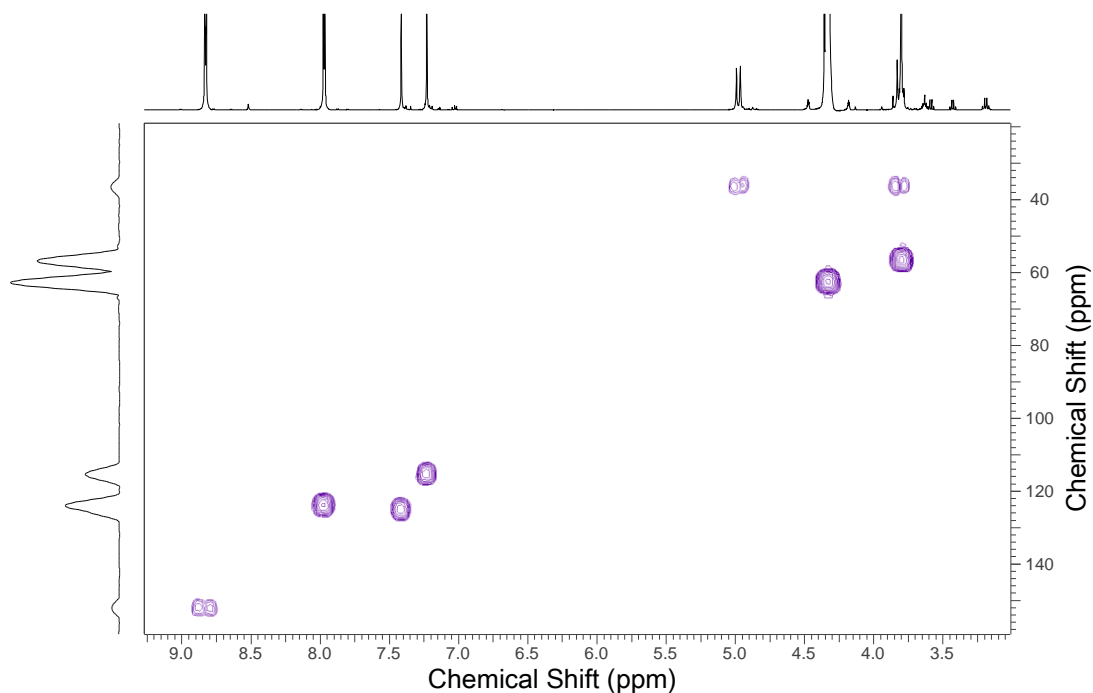
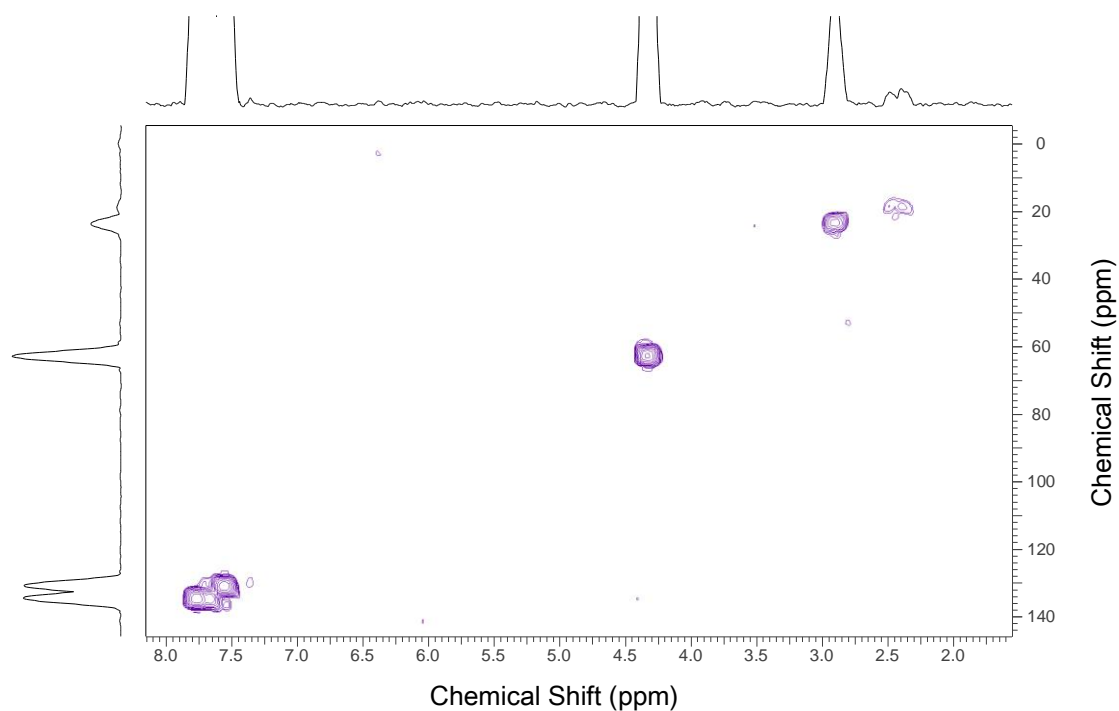


Figure A 3 Section of ¹H-¹³C NMR HMQC of L1. (299 K, 500 MHz, 125 MHz, *d*₃-MeNO₂)

Table A 2 Table of assignments for ¹H-¹³C NMR HMQC of L1 in *d*₃-MeNO₂.

Chemical Shift/ppm	Assignment
8.83/152.01	Ha/a'
7.97/123.91	Hb/b'
7.41/125.21	Hd
7.23/115.26	He
4.98/56.98	H _{endo}
3.82/36.55	Hc
3.64/56.98	H _{exo}



**Figure A 4 Section of ^1H - ^{13}C NMR HMQC of
1,3-Bis(diphenylphosphino)propane]palladium(II)triflate.
(293 K, 500 MHz, 125 MHz, d_3 -MeNO $_2$)**

Table A 3 Table of assignments for ^1H - ^{13}C NMR HMQC of $[\text{Pd}(\text{dppp})]^{2+}$ in d_3 -MeNO $_2$.

Chemical Shift/ppm	Assignment
7.77/134.39	Hb
7.66/134.39	Ha
7.55/130.61	Hc
2.91/23.50	He
2.44/18.93	Hd

A.3 FL1 & [Pd(dppp)]²⁺ in d₃-MeNO₂ ¹H-¹³C HMQC

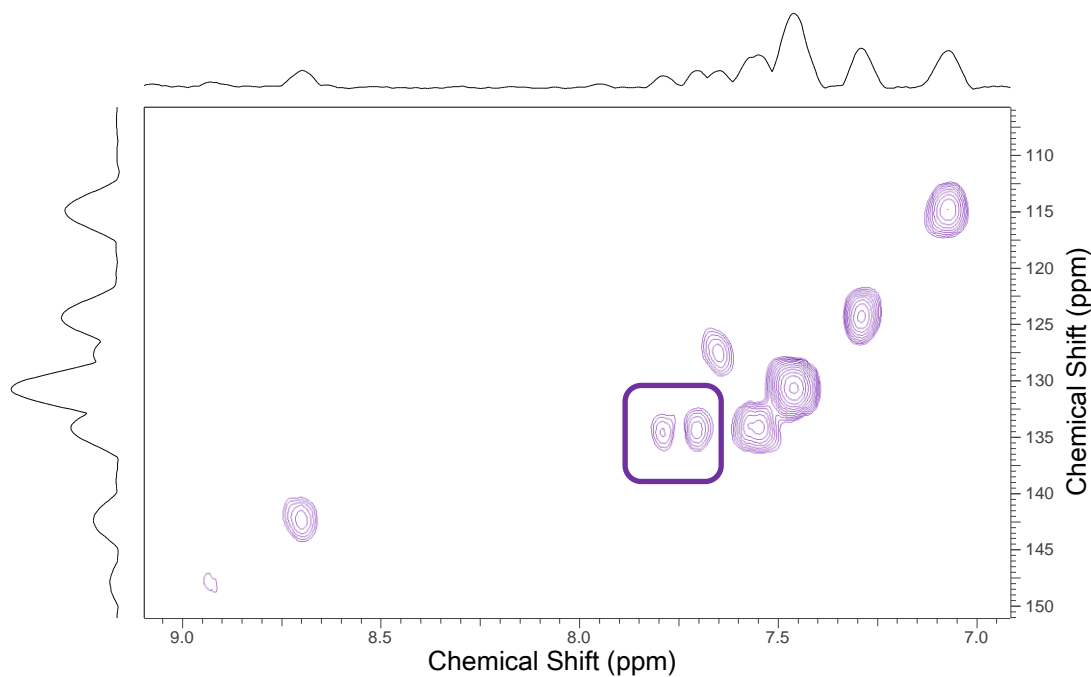


Figure A 5 Section of ¹H-¹³C NMR HMQC of [Pd₃(dppp)₃(FL1)₂]²⁺. The two [Pd(dppp)]²⁺ peaks are circled. (293 K, 500 MHz, 125 MHz, d₃-MeNO₂)

Table A 4 Table of assignments for ¹H-¹³C NMR HMQC of [Pd₃(dppp)₃(FL1)₂]²⁺ in d₃-MeNO₂. L1 listed in black and [Pd(dppp)]²⁺ listed in red.

Chemical Shift/ppm	Assignment
8.70/142.20	Hb
7.79/134.62	Hb
7.71/134.62	Hb
7.65/127.41	Hc
7.55/134.01	Ha
7.46/130.68	Hc
7.29/124.29	He
7.07/114.86	Hf

References

1. D. Su, X. Wang, M. Simard and J.D. Wuest, 'Molecular tectonics', *Supramolecular Chemistry*, 1995, **6**, 171-178.
2. J.-M. Lehn, 'Perspectives in Supramolecular Chemistry—From Molecular Recognition towards Molecular Information Processing and Self-Organization', *Angewandte Chemie International Edition in English*, 1990, **29**, 1304-1319.
3. J.W. Steed, D.R. Turner and K.J. Wallace, *Core Concepts in Supramolecular Chemistry and Nanochemistry*, Wiley, Chichester, UK, 1st ed., 2007.
4. J.W. Steed and J.L. Atwood, *Supramolecular Chemistry*, Wiley, Chichester, 1st ed., 2000.
5. M. Yoshizawa, J.K. Klosterman and M. Fujita, 'Functional Molecular Flasks: New Properties and Reactions within Discrete, Self-Assembled Hosts', *Angewandte Chemie-International Edition*, 2009, **48**, 3418-3438.
6. A.C. Schalley, *Analytical Methods in Supramolecular Chemistry*, Wiley-VCH, Berlin, 1st ed., 2007.
7. D. Philp and J.F. Stoddart, 'Self-Assembly in Organic Synthesis', *Synlett*, 1991, **1991**, 445-458.
8. D.L. Caulder and K.N. Raymond, 'Supermolecules by Design', *Accounts of Chemical Research*, 1999, **32**, 975-982.
9. B.H. Northrop, H.-B. Yang and P.J. Stang, 'Coordination-Driven Self-Assembly of Functionalized Supramolecular Metallacycles', *Chemical Communications*, 2008, 5896-5908.
10. N.C. Gianneschi, M.S. Masar and C.A. Mirkin, 'Development of a Coordination Chemistry-Based Approach for Functional Supramolecular Structures', *Accounts of Chemical Research*, 2005, **38**, 825-837.
11. J.D. Watson and F.H.C. Crick, 'Molecular Structure of Nucleic Acids - A Structure for Deoxyribose Nucleic Acid', *Nature*, 1953, **171**, 737-738.

12. C.J. Hastings, M.D. Pluth, R.G. Bergman and K.N. Raymond, 'Enzymelike Catalysis of the Nazarov Cyclization by Supramolecular Encapsulation', *Journal of the American Chemical Society*, 2010, **132**, 6938-6940.
13. Y. Nishioka, T. Yamaguchi, M. Yoshizawa and M. Fujita, 'Unusual [2+4] and [2+2] Cycloadditions of Arenes in the Confined Cavity of Self-Assembled Cages', *Journal of the American Chemical Society*, 2007, **129**, 7000-7001.
14. J.M. Kang and J. Rebek, 'Acceleration of a Diels-Alder Reaction by a Self-Assembled Molecular Capsule', *Nature*, 1997, **385**, 50-52.
15. F. Diederich, 'Molecular Recognition in Aqueous-Solution - Supramolecular Complexation and Catalysis', *Journal of Chemical Education*, 1990, **67**, 813-820.
16. I.A. Riddell, M.M.J. Smulders, J.K. Clegg and J.R. Nitschke, 'Encapsulation, Storage and Controlled Release of Sulfur Hexafluoride from a Metal-Organic Capsule', *Chemical Communications*, 2011, **47**, 457-459.
17. M.B. Duriska, S.M. Neville, J.Z. Lu, S.S. Iremonger, J.F. Boas, C.J. Kepert and S.R. Batten, 'Systematic Metal Variation and Solvent and Hydrogen-Gas Storage in Supramolecular Nanoballs', *Angewandte Chemie-International Edition*, 2009, **48**, 8919-8922.
18. P. Mal, B. Breiner, K. Rissanen and J.R. Nitschke, 'White Phosphorus Is Air-Stable Within a Self-Assembled Tetrahedral Capsule', *Science*, 2009, **324**, 1697-1699.
19. G. Whitesides, J. Mathias and C. Seto, 'Molecular Self-Assembly and Nanochemistry: A Chemical Strategy for the Synthesis of Nanostructures', *Science*, 1991, **254**, 1312-1319.
20. D.S. Lawrence, T. Jiang and M. Levett, 'Self-Assembling Supramolecular Complexes', *Chemical Reviews*, 1995, **95**, 2229-2260.
21. P. Baxter, J.-M. Lehn, A. DeCian and J. Fischer, 'Multicomponent Self-Assembly: Spontaneous Formation of a Cylindrical Complex from Five Ligands and Six Metal Ions', *Angewandte Chemie International Edition in English*, 1993, **32**, 69-72.

22. P. Atkins, *The Elements of Physical Chemistry*, Oxford Press, Oxford, 3rd ed., 2001.
23. G.M. Whitesides and B. Grzybowski, 'Self-Assembly at All Scales', *Science*, 2002, **295**, 2418-2421.
24. M.M.J. Smulders, I.A. Riddell, C. Browne and J.R. Nitschke, 'Building on Architectural Principles for Three-Dimensional Metallosupramolecular Construction', *Chemical Society Reviews*, 2013, **42**, 1728-1754.
25. S. De, K. Mahata and M. Schmittel, 'Metal-Coordination-Driven Dynamic Heteroleptic Architectures', *Chemical Society Reviews*, 2010, **39**, 1555-1575.
26. S. Sato, Y. Ishido and M. Fujita, 'Remarkable Stabilization of M₁₂L₂₄ Spherical Frameworks through the Cooperation of 48 Pd(II)-Pyridine Interactions', *Journal of the American Chemical Society*, 2009, **131**, 6064-6065.
27. A. Wu and L. Isaacs, 'Self-Sorting: The Exception or the Rule?', *Journal of the American Chemical Society*, 2003, **125**, 4831-4835.
28. D.J. Cram and J.M. Cram, eds. *Container Molecules and Their Guests*. 1st ed. Monographs in Supramolecular Chemistry, ed. F.J. Stoddart. 1994, The Royal Society of Chemistry Cambridge, UK. 223.
29. C.J. Pedersen, 'Cyclic Polyethers and their Complexes with Metal Salts', *Journal of the American Chemical Society*, 1967, **89**, 2495-2496.
30. C.J. Pedersen, 'Cyclic Polyethers and their Complexes with Metal Salts', *Journal of the American Chemical Society*, 1967, **89**, 7017-7036.
31. B. Dietrich, J.M. Lehn and J.P. Sauvage, 'Cryptates', *Tetrahedron Letters*, 1969, 2889-2892.
32. S. MeoZZi and J. Rebek, 'The 55% Solution: A Formula for Molecular Recognition in the Liquid State', *Chemistry-a European Journal*, 1998, **4**, 1016-1022.
33. M.D. Levin and P.J. Stang, 'Insights into the Mechanism of Coordination-Directed Self-Assembly', *Journal of the American Chemical Society*, 2000, **122**, 7428-7429.

34. P.J. Stang and B. Olenyuk, 'Self-Assembly, Symmetry, and Molecular Architecture: Coordination as the Motif in the Rational Design of Supramolecular Metallacyclic Polygons and Polyhedra', *Accounts of Chemical Research*, 1997, **30**, 502-518.
35. L.R. MacGillivray and J.L. Atwood, 'Structural Classification and General Principles for the Design of Spherical Molecular Hosts', *Angewandte Chemie International Edition*, 1999, **38**, 1018-1033.
36. G.M. Robinson, 'XXX.-A Reaction of Homopiperonyl and of Homoveratryl Alcohols', *Journal of the Chemical Society, Transactions*, 1915, **107**, 267-276.
37. A.J. Ewins, 'CLXVIII.-The Action of Phosphorus Pentachloride on the Methylene Ethers of Catechol Derivatives. Part V. Derivatives of Protocatechuyl Alcohol and Protocatechuonitrile', *Journal of the Chemical Society, Transactions*, 1909, **95**, 1482-1488.
38. A.S. Lindsey, '316. The Structure of Cyclotrimeratrylene (10,15-dihydro-2,3,7,8,12,13-hexamethoxy-5*H*-tribenzo[*a,d,g*]cyclononene) and Related Compounds', *Journal of the Chemical Society (Resumed)*, 1965, 1685-1692.
39. P. Lesot, D. Merlet, M. Sarfati, J. Courtieu, H. Zimmermann and Z. Luz, 'Enantiomeric and Enantiotopic Analysis of Cone-Shaped Compounds with C_3 and C_{3v} Symmetry Using NMR Spectroscopy in Chiral Anisotropic Solvents', *Journal of the American Chemical Society*, 2002, **124**, 10071-10082.
40. J.J. Henkelis, T.K. Ronson and M.J. Hardie, 'Lanthanide Coordination Polymers with Pyridyl-*N*-Oxide or Carboxylate Functionalised Host Ligands', *CrystEngComm*, 2014, **16**, 3688-3693.
41. A. Collet and G. Gottarelli, 'Circular Dichroism and Absolute Configuration of C_3 -Chiral Derivatives of Cyclotrimeratrylene', *Journal of the American Chemical Society*, 1981, **103**, 204-205.
42. R.C. Cookson, B. Halton and I.D.R. Stevens, 'Conformation in the Cyclotrimeratrylene Series', *Journal of the Chemical Society B: Physical Organic*, 1968, 767-774.
43. A. Collet, J. Gabard, J. Jacques, M. Cesario, J. Guilhem and C. Pascard, 'Synthesis and Absolute Configuration of Chiral (C_3) Cyclotrimeratrylene Derivatives. Crystal Structure of (*M*)-(-)-2,7,12-triethoxy-3,8,13-tris-[(*R*)-1-

- methoxycarbonylethoxy]-10,15-dihydro-5*H*-tribenzo[a,d,g]-cyclononene', *Journal of the Chemical Society, Perkin Transactions 1*, 1981, 1630-1638.
44. B. Miller and B.D. Gesner, 'Conformation of Cyclotrimeratrylene by Nuclear Magnetic Resonance Measurements', *Tetrahedron Letters*, 1965, **6**, 3351-3354.
 45. S. Winstein, P. Carter, F.A.L. Anet and A.J.R. Bourn, 'The Effects of Steric Compression on Chemical Shifts in Half-Cage and Related Molecules', *Journal of the American Chemical Society*, 1965, **87**, 5247-5249.
 46. T. Sato, K. Uno and M. Kainosho, 'A New Synthesis of Bridged Aromatics: 10,15-dihydro-5*H*-tribenzo[a,d,g]cyclononene and its Analogues', *Journal of the Chemical Society, Chemical Communications*, 1972, 579-580.
 47. A. Collet, ed. *Cryptophanes*. 1st ed. Comprehensive Supramolecular Chemistry ed. J. L. Atwood, J. E. D. Davies, D. D. Macnicol and F. Vogtle. Vol. 2. 1996, Pergamon: Exeter. 325-365.
 48. H. Zimmermann, P. Tolstoy, H.-H. Limbach, R. Poupko and Z. Luz, 'The Saddle Form of Cyclotrimeratrylene', *The Journal of Physical Chemistry B*, 2004, **108**, 18772-18778.
 49. H. Zimmermann, V. Bader, R. Poupko, E.J. Wachtel and Z. Luz, 'Mesomorphism, Isomerization, and Dynamics in a New Series of Pyramidic Liquid Crystals', *Journal of the American Chemical Society*, 2002, **124**, 15286-15301.
 50. A.D. McNaught and A. Wilkinson, *Compendium of Chemical Terminology (the "Gold Book")*, Blackwell Science Publications, Oxford, UK, 2nd ed., 1997.
 51. M.J. Hardie, 'Recent Advances in the Chemistry of Cyclotrimeratrylene', *Chemical Society Reviews*, 2010, **39**, 516-527.
 52. I.-I.C.o.B. Nomenclature, 'IUPAC Tentative Rules for the Nomenclature of Organic Chemistry. Section E. Fundamental Stereochemistry', *The Journal of Organic Chemistry*, 1970, **35**, 2849-2867.
 53. J. Canceill, A. Collet, J. Gabard, G. Gottarelli and G.P. Spada, 'Exciton Approach to the Optical Activity of C_3 -Cyclotrimeratrylene Derivatives', *Journal of the American Chemical Society*, 1985, **107**, 1299-1308.

54. V.K. Bhagwat, D.K. Moore, F.L. Pyman, C.H. Kao, S.-y. Ma, J.L. Simonsen, J.T. Hewitt and W. Lewcock, 'Notes - The Mechanism of the Oxidation of Laudanosine', *Journal of the Chemical Society (Resumed)*, 1931, 443.
55. A. Collet, J.P. Dutasta, B. Lozach and J. Canceill, 'Cyclotrimeratrylenes and Cryptophanes – Their Synthesis and Applications to Host-Guest Chemistry and to the Design of New Materials', *Topics in Current Chemistry*, 1993, **165**, 103-129.
56. A. Collet, 'Cyclotrimeratrylenes and Cryptophanes', *Tetrahedron*, 1987, **43**, 5725-5759.
57. J.W. Steed, P.C. Junk, J.L. Atwood, M.J. Barnes, C.L. Raston and R.S. Burkhalter, 'Ball and Socket Nanostructures: New Supramolecular Chemistry Based on Cyclotrimeratrylene', *Journal of the American Chemical Society*, 1994, **116**, 10346-10347.
58. J.T. Yu, Z.T. Huang and Q.Y. Zheng, 'Synthesis, Structure, Fullerene-binding and Resolution of C_3 -symmetric Cavitands with Rigid and Deep Cavities', *Organic & Biomolecular Chemistry*, 2012, **10**, 1359-1364.
59. J.L. Atwood, M.J. Barnes, M.G. Gardiner and C.L. Raston, 'Cyclotrimeratrylene Polarisation Assisted Aggregation of C_{60} ', *Chemical Communications*, 1996, 1449-1450.
60. E. Huerta, G.A. Metselaar, A. Frago, E. Santos, C. Bo and J. de Mendoza, 'Selective Binding and Easy Separation of C_{70} by Nanoscale Self-Assembled Capsules', *Angewandte Chemie International Edition*, 2007, **46**, 202-205.
61. E. Huerta, E. Cequier and J.d. Mendoza, 'Preferential Separation of Fullerene[84] from Fullerene Mixtures by Encapsulation', *Chemical Communications*, 2007, 5016-5018.
62. R.J. Blanch, M. Williams, G.D. Fallon, M.G. Gardiner, R. Kaddour and C.L. Raston, 'Supramolecular Complexation of 1,2-Dicarbododecaborane(12)', *Angewandte Chemie-International Edition in English*, 1997, **36**, 504-506.
63. M.J. Hardie, P.D. Godfrey and C.L. Raston, 'Self-Assembly of Grid and Helical Hydrogen-Bonded Arrays Incorporating Bowl-Shaped Receptor Sites That Bind Globular Molecules', *Chemistry – A European Journal*, 1999, **5**, 1828-1833.

64. M.J. Hardie and C.L. Raston, 'Confinement and Recognition of Icosahedral Main Group Cage Molecules: Fullerene C₆₀ and α -, m -, ρ -Dicarbadodecaborane(12)', *Chemical Communications*, 1999, 1153-1163.
65. C. Carruthers, J. Fisher, L.P. Harding and M.J. Hardie, 'Host-Guest Influence on Metallo-Supramolecular Assemblies with a Cyclotrimeratrylene-Type Ligand', *Dalton Transactions*, 2010, **39**, 355-357.
66. T.K. Ronson and M.J. Hardie, 'Extended 3⁶ and 6³ Arrays of Capsule Motifs Using Ligand Tris{4-(3-pyridyl)phenylester}cyclotriguaiacylene', *CrystEngComm*, 2008, **10**, 1731-1734.
67. C. Carruthers, T.K. Ronson, C.J. Sumbly, A. Westcott, L.P. Harding, T.J. Prior, P. Rizkallah and M.L. Hardie, 'The Dimeric "Hand-Shake" Motif in Complexes and Metallo-Supramolecular Assemblies of Cyclotrimeratrylene-Based Ligands', *Chemistry-a European Journal*, 2008, **14**, 10286-10296.
68. A. Westcott, J. Fisher, L.P. Harding, P. Rizkallah and M.J. Hardie, 'Self-Assembly of a 3-D Triply Interlocked Chiral [2]Catenane', *Journal of the American Chemical Society*, 2008, **130**, 2950-2951.
69. J.T. Yu, J.L. Sun, Z.T. Huang and Q.Y. Zheng, 'A Novel 1D Independent Metal-Organic Nanotube Based on Cyclotrimeratrylene Ligand', *CrystEngComm*, 2012, **14**, 112-115.
70. J.J. Henkelis and M.J. Hardie, 'Tuning the Coordination Chemistry of Cyclotrimeratrylene Ligand Pairs Through Alkyl Chain Aggregation', *CrystEngComm*, 2014, **16**, 8138-8146.
71. Z.L. Zhong, A. Ikeda, S. Shinkai, S. Sakamoto and K. Yamaguchi, 'Creation of Novel Chiral Cryptophanes by a Self-Assembling Method Utilizing a Pyridyl-Pd(II) Interaction', *Organic Letters*, 2001, **3**, 1085-1087.
72. C. Garcia, D. Humiliere, N. Riva, A. Collet and J.-P. Dutasta, 'Kinetic and Thermodynamic Consequences of the Substitution of SMe for OMe Substituents of Cryptophane Hosts on the Binding of Neutral and Cationic Guests', *Organic & Biomolecular Chemistry*, 2003, **1**, 2207-2216.
73. T. Brotin and J.-P. Dutasta, 'Cryptophanes and Their Complexes—Present and Future', *Chemical Reviews*, 2008, **109**, 88-130.

74. L. Garel, J.P. Dutasta and A. Collet, 'Complexation of Methane and Chlorofluorocarbons by Cryptophane-A in Organic Solution', *Angewandte Chemie International Edition in English*, 1993, **32**, 1169-1171.
75. C.E.O. Roesky, E. Weber, T. Rambusch, H. Stephan, K. Gloe and M. Czugler, 'A New Cryptophane Receptor Featuring Three *endo*-Carboxylic Acid Groups: Synthesis, Host Behavior and Structural Study', *Chemistry – A European Journal*, 2003, **9**, 1104-1112.
76. J. Canceill, L. Lacombe and A. Collet, 'New Cryptophane Forming Unusually Stable Inclusion Complexes with Neutral Guests in a Lipophilic Solvent', *Journal of the American Chemical Society*, 1986, **108**, 4230-4232.
77. G. Haberhauer, S. Woitschetzki and H. Bandmann, 'Strongly Underestimated Dispersion Energy in Cryptophanes and their Complexes', *Nat Commun*, 2014, **5**, 3542.
78. M.A. Little, J. Donkin, J. Fisher, M.A. Halcrow, J. Loder and M.J. Hardie, 'Synthesis and Methane-Binding Properties of Disulfide-Linked Cryptophane-0.0.0', *Angewandte Chemie International Edition*, 2012, **51**, 764-766.
79. O. Taratula, P.A. Hill, N.S. Khan, P.J. Carroll and I.J. Dmochowski, 'Crystallographic Observation of 'Induced Fit' in a Cryptophane Host–Guest Model System', *Nat Commun*, 2010, **1**, 148.
80. M.M. Spence, S.M. Rubin, I.E. Dimitrov, E.J. Ruiz, D.E. Wemmer, A. Pines, S.Q. Yao, F. Tian and P.G. Schultz, 'Functionalized Xenon as a Biosensor', *Proceedings of the National Academy of Sciences*, 2001, **98**, 10654-10657.
81. M.M. Spence, E.J. Ruiz, S.M. Rubin, T.J. Lowery, N. Winssinger, P.G. Schultz, D.E. Wemmer and A. Pines, 'Development of a Functionalized Xenon Biosensor', *Journal of the American Chemical Society*, 2004, **126**, 15287-15294.
82. K.T. Holman, S.D. Drake, J.W. Steed, G.W. Orr and J.L. Atwood, 'Anion Binding, Aryl-Extended Cyclotriguaiacylenes and an Aryl-Bridged Cryptophane that Provides Snapshots of a Molecular Gating Mechanism', *Supramolecular Chemistry*, 2010, **22**, 870-890.

83. A. Schaly, Y. Rousselin, J.-C. Chambron, E. Aubert and E. Espinosa, 'The Stereoselective Self-Assembly of Chiral Metallo-Organic Cryptophanes', *European Journal of Inorganic Chemistry*, 2016, **2016**, 832-843.
84. T.K. Ronson, H. Nowell, A. Westcott and M.J. Hardie, 'Bow-Tie Metallo-Cryptophanes from a Carboxylate Derived Cavitand', *Chemical Communications*, 2011, **47**, 176-178.
85. C.J. Sumby and M.L. Hardie, 'Capsules and Star-Burst Polyhedra: An [Ag₂L₂] Capsule and a Tetrahedral [Ag₄L₄] Metallosupramolecular Prism with Cyclotrimeratrylene-Type Ligands', *Angewandte Chemie-International Edition*, 2005, **44**, 6395-6399.
86. T.K. Ronson, J. Fisher, L.P. Harding, P.J. Rizkallah, J.E. Warren and M.J. Hardie, 'Stellated Polyhedral Assembly of a Topologically Complicated Pd₄L₄ 'Solomon Cube'', *Nature Chemistry*, 2009, **1**, 212-216.
87. J.J. Henkelis, T.K. Ronson, L.P. Harding and M.J. Hardie, 'M₃L₂ Metallo-Cryptophanes: [2]Catenane and Simple Cages', *Chemical Communications*, 2011, **47**, 6560-6562.
88. J.J. Henkelis, C.J. Carruthers, S.E. Chambers, R. Clowes, A.I. Cooper, J. Fisher and M.J. Hardie, 'Metallo-Cryptophanes Decorated with Bis-N-Heterocyclic Carbene Ligands: Self-Assembly and Guest Uptake into a Nonporous Crystalline Lattice', *Journal of the American Chemical Society*, 2014, **136**, 14393-14396.
89. M. Fujita, J. Yazaki and K. Ogura, 'Preparation of Macrocyclic Polynuclear Complex, [(en)Pd(4,4'-bpy)]₄(NO₃)₈, Which Recognizes an Organic Molecule in Aqueous Media', *Journal of the American Chemical Society*, 1990, **112**, 5645-5647.
90. M. Fujita, O. Sasaki, T. Mitsuhashi, T. Fujita, J. Yazaki, K. Yamaguchi and K. Ogura, 'On the Structure of Transition-Metal-Linked Molecular Squares', *Chemical Communications*, 1996, 1535-1536.
91. M. Fujita, M. Tominaga, A. Hori and B. Therrien, 'Coordination Assemblies from a Pd(II)-Cornered Square Complex', *Accounts of Chemical Research*, 2005, **38**, 369-378.

92. P. Mal, D. Schultz, K. Beyeh, K. Rissanen and J.R. Nitschke, 'An Unlockable-Relockable Iron Cage by Subcomponent Self-Assembly', *Angewandte Chemie-International Edition*, 2008, **47**, 8297-8301.
93. T.K. Ronson, S. Zarra, S.P. Black and J.R. Nitschke, 'Metal-Organic Container Molecules Through Subcomponent Self-Assembly', *Chemical Communications*, 2013, **49**, 2476-2490.
94. D. Ajami and J. Rebek, 'Gas Behavior in Self-Assembled Capsules', *Angewandte Chemie International Edition*, 2008, **47**, 6059-6061.
95. J.L. Bolliger, T.K. Ronson, M. Ogawa and J.R. Nitschke, 'Solvent Effects upon Guest Binding and Dynamics of a Fe^{II} ⁴L₄ Cage', *Journal of the American Chemical Society*, 2014, **136**, 14545-14553.
96. D.L. Caulder, R.E. Powers, T.N. Parac and K.N. Raymond, 'The Self-Assembly of a Predesigned Tetrahedral M₄L₆ Supramolecular Cluster', *Angewandte Chemie International Edition*, 1998, **37**, 1840-1843.
97. M.D. Pluth, R.G. Bergman and K.N. Raymond, 'Proton-Mediated Chemistry and Catalysis in a Self-Assembled Supramolecular Host', *Accounts of Chemical Research*, 2009, **42**, 1650-1659.
98. T. Kusukawa and M. Fujita, 'Self-Assembled M₆L₄-Type Coordination Nanocage with 2,2'-Bipyridine Ancillary Ligands. Facile Crystallization and X-ray Analysis of Shape-Selective Enclathration of Neutral Guests in the Cage', *Journal of the American Chemical Society*, 2002, **124**, 13576-13582.
99. M. Fujita, D. Oguro, M. Miyazawa, H. Oka, K. Yamaguchi and K. Ogura, 'Self-Assembly of Ten Molecules into Nanometre-Sized Organic Host Frameworks', *Nature*, 1995, **378**, 469-471.
100. T. Kusukawa, T. Nakai, T. Okano and M. Fujita, 'Remarkable Acceleration of Diels-Alder Reactions in a Self-Assembled Coordination Cage', *Chemistry Letters*, 2003, **32**, 284-285.
101. T. Murase, S. Horiuchi and M. Fujita, 'Naphthalene Diels-Alder in a Self-Assembled Molecular Flask', *Journal of the American Chemical Society*, 2010, **132**, 2866-2867.

102. H. Ito, T. Kusakawa and M. Fujita, 'Wacker Oxidation in an Aqueous Phase through the Reverse Phase-Transfer Catalysis of a Self-Assembled Nanocage', *Chemistry Letters*, 2000, 598-599.
103. M. Yoshizawa, Y. Takeyama, T. Kusakawa and M. Fujita, 'Cavity-Directed, Highly Stereoselective [2+2] Photodimerization of Olefins within Self-Assembled Coordination Cages', *Angewandte Chemie International Edition*, 2002, **41**, 1347-1349.
104. M. Yoshizawa, T. Kusakawa, M. Fujita and K. Yamaguchi, 'Ship-in-a-Bottle Synthesis of Otherwise Labile Cyclic Trimers of Siloxanes in a Self-Assembled Coordination Cage', *Journal of the American Chemical Society*, 2000, **122**, 6311-6312.
105. H. Takezawa, T. Murase and M. Fujita, 'Temporary and Permanent Trapping of the Metastable Twisted Conformer of an Overcrowded Chromic Alkene *via* Encapsulation', *Journal of the American Chemical Society*, 2012, **134**, 17420-17423.
106. Y. Kohyama, T. Murase and M. Fujita, 'Metal-Organic Proximity in a Synthetic Pocket', *Journal of the American Chemical Society*, 2014, **136**, 2966-2969.
107. D.K. Chand, K. Biradha, M. Fujita, S. Sakamoto and K. Yamaguchi, 'A Molecular Sphere of Octahedral Symmetry', *Chemical Communications*, 2002, 2486-2487.
108. M. Fujita, S. Nagao and K. Ogura, 'Guest-Induced Organization of a Three-Dimensional Palladium(II) Cagelike Complex. A Prototype for "Induced-Fit" Molecular Recognition', *Journal of the American Chemical Society*, 1995, **117**, 1649-1650.
109. D. Moon, S. Kang, J. Park, K. Lee, R.P. John, H. Won, G.H. Seong, Y.S. Kim, G.H. Kim, H. Rhee and M.S. Lah, 'Face-Driven Corner-Linked Octahedral Nanocages: M_6L_8 Cages Formed by C_3 -Symmetric Triangular Facial Ligands Linked *via* C_4 -Symmetric Square Tetratopic Pd^{II} Ions at Truncated Octahedron Corners', *Journal of the American Chemical Society*, 2006, **128**, 3530-3531.
110. T.K. Ronson, J. Fisher, L.P. Harding and M.J. Hardie, 'Star-burst Prisms with Cyclotriveratrylene-type Ligands: A $[Pd_6L_8]^{12+}$ Stella Octangular Structure', *Angewandte Chemie-International Edition*, 2007, **46**, 9086-9088.

111. N.J. Cookson, J.J. Henkelis, R.J. Ansell, C.W.G. Fishwick, M.J. Hardie and J. Fisher, 'Encapsulation of Sodium Alkyl Sulfates by the Cyclotrimeratrylene-Based, $[\text{Pd}_6\text{L}_8]^{12+}$ Stella Octangula Cage', *Dalton Transactions*, 2014, **43**, 5657-5661.
112. T.K. Ronson, C. Carruthers, J. Fisher, T. Brotin, L.P. Harding, P.J. Rizkallah and M.J. Hardie, 'Tripodal 4-Pyridyl-Derived Host Ligands and Their Metallo-Supramolecular Chemistry: Stella Octangula and Bowl-Shaped Assemblies', *Inorganic Chemistry*, 2010, **49**, 675-685.
113. J.J. Henkelis, J. Fisher, S.L. Warriner and M.J. Hardie, 'Solvent-Dependent Self-Assembly Behaviour and Speciation Control of Pd_6L_8 Metallo-supramolecular Cages', *Chemistry – A European Journal*, 2014, **20**, 4117-4125.
114. M. Fujita, K. Umemoto, M. Yoshizawa, N. Fujita, T. Kusukawa and K. Biradha, 'Molecular Paneling *Via* Coordination', *Chemical Communications*, 2001, 509-518.
115. Q.F. Sun, J. Iwasa, D. Ogawa, Y. Ishido, S. Sato, T. Ozeki, Y. Sei, K. Yamaguchi and M. Fujita, 'Self-Assembled $\text{M}_{24}\text{L}_{48}$ Polyhedra and Their Sharp Structural Switch upon Subtle Ligand Variation', *Science*, 2010, **328**, 1144-1147.
116. K. Harris, D. Fujita and M. Fujita, 'Giant Hollow M_nL_{2n} Spherical Complexes: Structure, Functionalisation and Applications', *Chemical Communications*, 2013, **49**, 6703-6712.
117. K. Suzuki, M. Tominaga, M. Kawano and M. Fujita, 'Self-Assembly of an M_6L_{12} Coordination Cube', *Chemical Communications*, 2009, 1638-1640.
118. M. Tominaga, K. Suzuki, M. Kawano, T. Kusukawa, T. Ozeki, S. Sakamoto, K. Yamaguchi and M. Fujita, 'Finite, Spherical Coordination Networks that Self-Organize from 36 Small Components', *Angewandte Chemie International Edition*, 2004, **43**, 5621-5625.
119. M. Yoneya, S. Tsuzuki, T. Yamaguchi, S. Sato and M. Fujita, 'Coordination-Directed Self-Assembly of $\text{M}_{12}\text{L}_{24}$ Nanocage: Effects of Kinetic Trapping on the Assembly Process', *Acs Nano*, 2014, **8**, 1290-1296.

120. T. Murase, S. Sato and M. Fujita, 'Nanometer-Sized Shell Molecules That Confine Endohedral Polymerizing Units', *Angewandte Chemie International Edition*, 2007, **46**, 1083-1085.
121. Q.-F. Sun, T. Murase, S. Sato and M. Fujita, 'A Sphere-in-Sphere Complex by Orthogonal Self-Assembly', *Angewandte Chemie International Edition*, 2011, **50**, 10318-10321.
122. C.J. Bruns, D. Fujita, M. Hoshino, S. Sato, J.F. Stoddart and M. Fujita, 'Emergent Ion-Gated Binding of Cationic Host-Guest Complexes within Cationic $M_{12}L_{24}$ Molecular Flasks', *Journal of the American Chemical Society*, 2014, **136**, 12027-12034.
123. D. Fujita, K. Suzuki, S. Sato, M. Yagi-Utsumi, Y. Yamaguchi, N. Mizuno, T. Kumasaka, M. Takata, M. Noda, S. Uchiyama, K. Kato and M. Fujita, 'Protein Encapsulation within Synthetic Molecular Hosts', *Nat Commun*, 2012, **3**, 1093.
124. T. Kikuchi, S. Sato, D. Fujita and M. Fujita, 'Stepwise DNA Condensation by a Histone-Mimic Peptide-Coated $M_{12}L_{24}$ Spherical Complex', *Chemical Science*, 2014, **5**, 3257-3260.
125. J. Bunzen, J. Iwasa, P. Bonakdarzadeh, E. Numata, K. Rissanen, S. Sato and M. Fujita, 'Self-Assembly of $M_{24}L_{48}$ Polyhedra Based on Empirical Prediction', *Angewandte Chemie International Edition*, 2012, **51**, 3161-3163.
126. M.J. Hardie and C.J. Sumbly, 'Interwoven 2-D Coordination Network Prepared from the Molecular Host *Tris*(isonicotinoyl)cyclotriguaiacylene and Silver(I) Cobalt(III) Bis(dicarbollide)', *Inorganic Chemistry*, 2004, **43**, 6872-6874.
127. Y. Cohen, L. Avram and L. Frish, 'Diffusion NMR spectroscopy in supramolecular and combinatorial chemistry: An old parameter - New insights', *Angewandte Chemie-International Edition*, 2005, **44**, 520-554.
128. N. Kamiya, M. Tominaga, S. Sato and M. Fujita, 'Saccharide-Coated $M_{12}L_{24}$ Molecular Spheres That Form Aggregates by Multi-interaction with Proteins', *Journal of the American Chemical Society*, 2007, **129**, 3816-3817.
129. P. Rovó, 'Project Report: Pd-based Metallo-Supramolecular Cage as a Potential Host', *MChem, University of Leeds*, 2009

130. H.R.W.J. Orville-Thomas, *Molecular Interactions*, Vol. 2, John Wiley & Sons, Michigan, 1st ed., 1981.
131. S. Nilsson, 'Interactions between Water-Soluble Cellulose Derivatives and Surfactants. 1. The HPMC/SDS/Water System', *Macromolecules*, 1995, **28**, 7837-7844.
132. D.K. Chand, K. Biradha and M. Fujita, 'Self-assembly of a novel macrotricyclic Pd(II) metallocage encapsulating a nitrate ion', *Chemical Communications*, 2001, 1652-1653.
133. S. Sato, J. Iida, K. Suzuki, M. Kawano, T. Ozeki and M. Fujita, 'Fluorous Nanodroplets Structurally Confined in an Organopalladium Sphere', *Science*, 2006, **313**, 1273-1276.
134. J.-M. Lehn, *Supramolecular Chemistry : Concepts and Perspectives; A Personal Account*, VCH, Weinheim, 1995.
135. V. Gutmann, 'Empirical Parameters for Donor and Acceptor Properties of Solvents', *Electrochimica Acta*, 1976, **21**, 661-670.
136. R.J. Abraham, J. Fisher and P. Loftus, *Introduction to NMR Spectroscopy*, John Wiley & Sons, Chichester, UK, 2nd ed., 1988.
137. C. Reichardt, *Solvents and Solvent Effects in Organic Chemistry*, Wiley-VCH, Weinheim, 3rd ed., 2003.
138. D. Martin, A. Weise and H.J. Niclas, 'The Solvent Dimethyl Sulfoxide', *Angewandte Chemie International Edition in English*, 1967, **6**, 318-334.
139. G.P. Cunningham, G.A. Vidulich and R.L. Kay, 'Several properties of acetonitrile-water, acetonitrile-methanol, and ethylene carbonate-water systems', *Journal of Chemical & Engineering Data*, 1967, **12**, 336-337.
140. D.A. Skoog, D.M. West and F.J. Holler, *Fundamentals of Analytical Chemistry*, Harcourt College, London, 7th ed., 1996.
141. P. Thordarson, 'Determining association constants from titration experiments in supramolecular chemistry', *Chemical Society Reviews*, 2011, **40**, 1305-1323.
142. C. Frassinetti, L. Alderighi, P. Gans, A. Sabatini, A. Vacca and S. Ghelli, 'Determination of protonation constants of some fluorinated polyamines by

- means of ^{13}C NMR data processed by the new computer program HypNMR2000. Protonation sequence in polyamines', *Analytical and Bioanalytical Chemistry*, 2003, **376**, 1041-1052.
143. T.D.W. Claridge, *High-Resolution NMR techniques in Organic Chemistry* Elsevier, Oxford, 1st ed., 1999.
144. F.A. Cotton, R. Francis and W.D. Horrocks, 'Sulfoxides as Ligands II. The Infrared Spectra of Some Dimethyl Sulfoxide Complexes', *The Journal of Physical Chemistry*, 1960, **64**, 1534-1536.
145. F.A. Cotton and R. Francis, 'Sulfoxides as Ligands. I. A Preliminary Survey of Methyl Sulfoxide Complexes', *Journal of the American Chemical Society*, 1960, **82**, 2986-2991.
146. J.J. Henkelis and M.J. Hardie, 'Controlling the assembly of cyclotrimeratrylene-derived coordination cages', *Chemical Communications*, 2015, **51**, 11929-11943.
147. R. Kulasekharan, N. Jayaraj, M. Porel, R. Choudhury, A.K. Sundaresan, A. Parthasarathy, M.F. Ottaviani, S. Jockusch, N.J. Turro and V. Ramamurthy, 'Guest Rotations within a Capsuleplex Probed by NMR and EPR Techniques', *Langmuir*, 2010, **26**, 6943-6953.
148. E. Pasgreta, R. Puchta, M. Galle, N.V. Hommes, A. Zahl and R. van Eldik, 'Ligand-exchange processes on solvated lithium cations: DMSO and water/DMSO mixtures', *Chemphyschem*, 2007, **8**, 1315-1320.
149. S.B. Lee, S. Hwang, D.S. Chung, H. Yun and J.-I. Hong, 'Guest-induced reorganization of a self-assembled Pd(II) complex', *Tetrahedron Letters*, 1998, **39**, 873-876.
150. J.J. Henkelis, 'Supramolecular Architectures with Functionalised Host Ligands', *PhD Thesis, University of Leeds*, 2014
151. D.K. Chand, R. Manivannan, H.S. Sahoo and K. Jeyakumar, 'Self-Assembly by Ligand-Exchange Reactions', *European Journal of Inorganic Chemistry*, 2005, **2005**, 3346-3352.

152. J.A. Mata, M. Poyatos and E. Peris, 'Structural and catalytic properties of chelating bis- and tris-N-heterocyclic carbenes', *Coordination Chemistry Reviews*, 2007, **251**, 841-859.
153. R. Chakrabarty, P.S. Mukherjee and P.J. Stang, 'Supramolecular Coordination: Self-Assembly of Finite Two- and Three-Dimensional Ensembles', *Chemical Reviews*, 2011, **111**, 6810-6918.
154. S. Ghosh and P.S. Mukherjee, 'Self-Assembled Pd(II) Metallocycles Using an Ambidentate Donor and the Study of Square-Triangle Equilibria', *Inorganic Chemistry*, 2009, **48**, 2605-2613.
155. M. Nilsson, 'The DOSY Toolbox: A new tool for processing PFG NMR diffusion data', *Journal of Magnetic Resonance*, 2009, **200**, 296-302.
156. G. Sheldrick, 'A short history of SHELX', *Acta Crystallographica Section A*, 2008, **64**, 112-122.
157. P. van der Sluis and A.L. Spek, 'BYPASS: an effective method for the refinement of crystal structures containing disordered solvent regions', *Acta Crystallographica Section A*, 1990, **46**, 194-201.
158. A. Spek, 'Structure validation in chemical crystallography', *Acta Crystallographica Section D*, 2009, **65**, 148-155.